EXPLORING THE ROLE OF MITOCHONDRIAL CHOLESTEROL IN NIEMANN-PICK TYPE C DISEASE

by

Barry E. Kennedy

Submitted in partial fulfilment of the requirements
for the degree of Doctor of Philosophy

at

Dalhousie University
Halifax, Nova Scotia
July 2014

TABLE OF CONTENTS

LIST OF FIGURES

LIST OF TABLES

ABSTRACT

Niemann-Pick type C (NPC) disease is an autosomal recessive neurodegenerative disorder caused by mutations in *Npc1* or *Npc2* gene. *Npc1* and *Npc2* encode a late-endosomal transmembrane and lumenal cholesterol-binding domain protein, respectively. Together NPC1 and NPC2 mediate the transport of endosomal cholesterol to the plasma membrane and endoplasmic reticulum. Loss of function mutations in NPC1 or NPC2 leads to cholesterol accumulation in late endosomes, neuronal dysfunction, neurodegeneration, and premature death. The link between cholesterol trafficking and NPC pathogenesis is unclear. I performed metabolomics analyses of different brain regions from wildtype and *Npc1*$^{-/-}$ mice at pre-symptomatic, early-symptomatic and late-stage disease by ^{1}H-NMR spectroscopy. Metabolic profiling revealed increased lactate and decreased acetyl-CoA levels in *Npc1*$^{-/-}$ cerebellum and cerebral cortex at all ages. Protein and gene expression analyses indicated a deficiency in the oxidative decarboxylation of pyruvate to acetyl-CoA, an upregulation of glycolytic gene expression, and alterations in glutamate oxidation at the early-symptomatic stage. I also observed a pre-symptomatic increase in several indicators of oxidative stress and antioxidant response systems in all *Npc1*$^{-/-}$ brain regions. Furthermore, mitochondrial cholesterol levels were increased in *Npc1*$^{-/-}$ murine brain and NPC1-deficient Chinese hamster ovary (CHO) cells. Using CHO cells that express CYP11A1 fusion protein that converts cholesterol to pregnenolone at the mitochondrial inner membrane I determined that the endosomal cholesterol-binding protein, metastatic lymph node protein 64 (MLN64) and NPC2 but not NPC1 were required for transport of endosomal cholesterol to mitochondria. To investigate the effects of elevated mitochondrial cholesterol levels on energy metabolism I manipulated mitochondrial cholesterol by genetic alterations of NPC1, MLN64, and NPC2. I found that the depletion of NPC1 increased lactate secretion, decreased glutamine-dependent mitochondrial respiration, and decreased ATP transport across mitochondrial membranes in CHO cells. These metabolic alterations did not occur when transport of endosomal cholesterol to mitochondria was blocked. Additionally, the elevated mitochondrial cholesterol levels in NPC1-depleted cells and in NPC2-depleted cells expressing mutant NPC2 that allows endosomal cholesterol trafficking to mitochondria were associated with increased expression of the antioxidant response factor *Nfe2l2*. These results suggest that mitochondrial cholesterol accumulation causes oxidative stress and mitochondrial dysfunction and contributes to NPC disease pathogenesis.

LIST OF ABBREVIATIONS USED

22-OH-Chol	22R-hydroxycholesterol
4-4-19	+-CHO cells that express a non-functional NPC1 protein
ABCA1	ATP-binding cassette A1
ACAT	Acyl-CoA: cholesterol acyltransferase
ACC	Acetyl-CoA carboxylase
AKT	Protein kinase B
AMPK	AMP kinase
ANOVA	Analysis of variance
ANT	Adenosine nucleotide translocase
AOA	Aminooxyacetate
ApoE	Apolipoprotein E
BCAT	Branched chain amino acid aminotransferase
BSA	Bovine serum albumin
BSO	Buthionine sulfoximine
CA	Cornu Ammonis
CHO	Chinese hamster ovary
CNS	Central nervous system
CoA	Coenzyme A
CYP11A1	P450 side chain cleavage enzyme
DCA	Dichloroacetate
DMEM	Dulbecco's modified eagle medium
E#	Embryonic day #
EAAT	Excitatory amino acid transporters
EDTA	Ethylenediaminetetraacetic acid
F2	Fusion protein of human CYP11A1, ferredoxin reductase, ferredoxin 1
FBS	Fetal bovine serum
FCCP	Carbonyl cyanide *p*-trifluoromethoxy-phenylhydrazone
FRET	Fluorescent resonance energy transfer
GABA	Gamma-aminobutyric acid
GAD	Glutamate decarboxylase
GFAP	Glial fibrillary acidic protein
GLUD	Glutamate dehydrogenase
GLUT	Glucose transporter
GOT2	Aspartate aminotransferase 2
GPT	Alanine transaminase
GS/*Glu1*	Glutamine synthetase
GSH	Glutathione
GSL	Phosphate-activated glutaminase
HBS	HEPES buffered saline
HDL	High density lipoprotein
HE1	Human epididymis 1
HEK	Human embryonic kidney cells

HEPES	4-(2-hydroxyethyl)-1-piperazineethanesulfonic acid
Hif1alpha	Hypoxia inducible factor 1 alpha subunit
HMGCR	3-hydroxy-3-methylglutaryl-CoA reductase
HO-1/*Hmox1*	Heme oxygenase 1
HPCD	2-hydroxypropyl-beta-cyclodextrin
HPLC	High-performance liquid chromatography
HRP	Horse radish peroxidase
HXK	Hexokinase
INSIG	Insulin-induced gene
JNK	Jun-N-terminal kinase
KGDH	Alpha-ketoglutarate dehydrogenase
LDH	Lactate dehydrogenase
LDL	Low density lipoprotein
LDLR	Low density lipoprotein receptor
LPDS	Lipoprotein-deficient serum
LRP1	LDLR-related protein-associated protein 1
LXR	Liver X receptor
MAM	Mitochondria-associated membrane
Map2	Microtubule-associated protein 2
MEM	Minimum essential medium
MENTHO	MLN64 N-terminal domain homologue
MI	Mitochondrial isolation
MLN64	Metastatic lymph node 64
mtDNA	Mitochondrial DNA
NAA	N-acetylaspartate
NAC	N-acetylcysteine
NADH	Nicotinamide adenine dinucleotide
NADPH	Nicotinamide adenine dinucleotide phosphate
NMR	Nuclear magnetic resonance
NPC	Niemann-Pick type C
NPC1	Niemann-Pick type C1
NPC2	Niemann-Pick type C2
Nrf2/*Nfe2l2*	Nuclear factor erythroid 2-related factor
NTD	N-terminal domain of NPC1
OCR	Oxygen consumption rates
PBS	Phosphate buffered saline
PCR	Polymerase chain reaction
PCX	Pyruvate carboxylase
PDH	Pyruvate dehydrogenase
PDK1/2	Pyruvate dehydrogenase kinase 1/2
PFK	Phosphofructokinase
PFK1	phosphofructokinase 1
PFK2	Phosphofructokinase 2
PGC1alpha	Peroxisome proliferator-activated receptor gamma coactivator-1 alpha
PKM	Pyruvate kinase
PPP	Pentose phosphate pathway

qPCR	Quantitative PCR
RIA	Radioimmunoassay
RNAi	RNA interference
ROS	Reactive oxygen species
RT-PCR	Reverse transcriptase PCR
SCAP	SREBP cleavage-activating protein
SDS	Sodium dodecyl sulfate
shNPC1	shRNA against NPC1
shNPC2	shRNA targeting NPC2
shNT	Non-targeting shRNA
shRNA	short hairpin RNA
SHSY	Human neuroblastoma SH-SY5Y cells
siMLN64	siRNA against MLN64
siNPC1	siRNA against NPC1
siNPC2	siRNA against NPC2
siNT	Non-targeting siRNA
siRNA	Small interfering RNA
SNP	Single-nucleotide polymorphisms
SOD1	Copper-zinc superoxide dismutase
SOD2	Manganese superoxide dismutase
SRE	Sterol regulatory element
SREBP	Sterol regulatory element binding protein
SSD	Sterol sensing domain
StAR	Steroidogenic acute regulatory
StARD3	StAR-related lipid transfer domain protein 3
START	StAR-related transfer
TCA	Tricarboxylic acid cycle
TCEP	Tris (2-carboxyethyl) phosphine
TNF-α	Tumour necrosis factor alpha
Tom20	Translocase of outer mitochondrial membrane 20
TSPO	Translocator protein
TTBS	Tris buffered saline with tween
UCP2	Uncoupling protein 2
VDAC	Voltage-dependent anion channel
VLDL	Very low density lipoprotein
WT	Wildtype

ACKNOWLEDGEMENTS

I would like to start by thanking my wonderful supervisor, Dr. Barbara Karten, for her expert advice and encouragement throughout this difficult project. Barbara has helped me with everything from experimental design, data interpretation, data analysis, understanding of complex scientific concepts, presentation skills, preparation for conferences, writing of grant, scholarships, and scientific papers. Additionally, she has helped prepare me for a long future in scientific research. Barbara first gave me an opportunity to work in her lab back in the summer of 2007 and for the past 7 years I have learned how to apply what I have learned in my undergraduate classes to real life scientific problems. Barbara always gave me the opportunity to explore areas in research that I found particularly interesting. For example, during our first meeting where we just discussed topics that I had found interesting such as cholesterol transport to mitochondria for an hour or two, from that meeting Barbara already had a project envisioned for me that eventually turned into the basis for my PhD. Barbara always had the interest of her students as her top priority, she provided the best opportunity for all of us to succeed. For me personally, I was able to achieve several accomplishments including publishing four (with one additional paper, close to submission) first author papers, won numerous awards including the Doug Hogue Award (awarded to the top graduate student), and poster awards at international conferences (Gordon Research conference, and the Canadian Lipoprotein conference), and received scholarships (NSERC and NSHRF). Without Barbara's encouragement, help, and high expectations of my capabilities I feel that I would not have this success.

I would also like to thank Barbara with her amazing help with guiding me through scientific writing. Writing was always a weak point for me but thanks to the countless hours that she has put into editing and teaching me, I have learned so much and am now at to a point in which I am much more confident in my abilities to write a scientific paper, grant, and thesis. In addition to working in the lab I will always remember our lab socials that Barbara hosted, our outdoor summer parties, and our Christmas parties were excellent bonding experiences. I will always remember the wonderful and academically stimulating times working with Barbara and I will be forever thankful for all of what she has taught me.

I would also like to thank everyone that I have ever worked with in the Karten lab. Being one of the first students in Barbara's lab I have crossed paths with many amazing people and I thank them for numerous things both scientific and scientific related. I am also grateful for the ever lasting friendships that I have established during my time here.

First off I would like to thank Mark Charman; Mark and I started working in Barbara's lab around the same time. In our studies, Mark and I worked closely together, elucidating the cholesterol trafficking pathway to mitochondria. He helped me out immensely with my studies, sharing tasks, combining our data, and bouncing ideas off of each other, we were able to publish two papers together. The thing that I will always remember about Mark, is that he was such a nice guy, who was always able to find joy and happiness in even the most monotonous tasks. He was the lab jokester, which really made the difficulties of graduate studies a little more fun. Finally, what Mark accomplished by completing a Master's degree while being a loving husband to his wife Julie and a wonderful father to his three daughters provided so much motivation for me to want to accomplish more both in and outside of the lab.

Next, I would like to thank Dr. Nolan Osborne, Nolan was a technician in the Karten lab when I first arrived and he quickly became my first friend in the intimidating world of a science laboratory. I was fortunate to follow Nolan for the first three months of my time in Barbara's lab. He was such an amazing teacher, with so much patience. Nolan never got mad or upset at me when I would make an error. He taught me several lab techniques that I still use to this day. Finally, the thing that I will always remember about Nolan was him as a person, he was so worldly, having traveled to six continents and living in a few of them, he became a person that I looked up to, and is a large part behind my motivation to travel myself after completing my doctorate.

I can't go any longer without thanking Debbie Fice, the Karten lab technician for the past five years. Debbie was another truly amazing person that I had the fortune of working with. Debbie in ways took a motherly role in the lab, always making sure that everything was okay, and if it wasn't she always seemed to have a way to fix things. I cannot thank her enough for all of the work that she did for me, many of the Western blots that are presented in this thesis are thanks to her hard work and precision when it

came to experiments. Without Debbie there was no way the lab would have run as smoothly as it did. She organized so much, including chores, ordering, and extra circular events, without Debbie I would not have been given the freedom to focus on experiments without worrying about prepping buffers or ordering items. I would also like to thank Debbie for all that she did for me personally, Debbie always went out of her way to help other. For example, when the buses went on strike I would have had no way of getting to work if it wasn't for Debbie's drives. Also, I can't thank her enough for the delicious goodies that she would often bring in just because. I learned so much from Debbie during our many years working side by side, and I thank her for the wonderful time together.

There have been so many other co-workers that I cannot thank enough. I would to thank, Matthew Taylor, Carolyn-Ann Robinson, Tiffany Mailman, Westley Reinhart-McMillian, Cory Hawes, Veronique LeBlanc, Nicole Marnet, Brandon Scott, Zeina Asyyed, Yijun Liu, Manoj Hariharan, Hana Wiemer, Laura Martin, Zhou Hui, Natalie Donaher, Bhavya Ojha, Wilson Chan, and everyone else that I crossed paths with in the Karten lab for their amazing help with my research project. I would also like to thank them for their great companionship during my time in the lab, their stories, jokes, and get-togethers. I will never forget any of you, as you were such a big and enjoyable part of my time in the Karten lab. I have learned so much from each and every one of you, I look forward to maintaining a lasting friendship wherever our paths take us.

I would like to thank all of my committee members Drs. Melanie Dobson, Roger McLeod, and Karen Bedard for their expert advice and numerous contributions to my research. Each and every one of them was always available for help with experiments and concepts. Together they played a large part in my research. I would also like to thank all of my collaborators, especially Dr. Tobias Karakach, Ian Burton, and Dr. Wolfgang Graier for their help and for the learning experiences that I gained from these projects.

I could not have performed any of my research if it wasn't for the generous funding provided to me and to my research over the years by Natural Sciences and Engineering Research Council of Canada (NSERC), Nova Scotia Health Research Foundation (NSHRF), Canadian Institutes of Health Research (CIHR), and the Ara Parseghian medical research foundation.

I would also like to thank the many people that I meet while working in the Sir Charles Tupper building. Just to name a few, Eric, Craig, Alexi, Dennis, Dale, Courtney, Vanessa, Brandon, Carolyn, Christina, Nicole, Anna, Michael, Dan, Adam, Simon, Drew, Ian, and so many more. I would like to thank all of them for the wonderful time that we spent together at various parties, sporting events, and trips. These events and get-togethers were a nice relaxation from the tough demands of grad studies and I will always remember these people with the hope that we will continue our friendship. I would also like to thank members of the Dal intramural softball, basketball, and football teams for great experiences and great fun running around.

I would also like to thank my family especially my parents, Ed and Paula Kennedy, for their constant support and encouragement during my graduate studies degree. I owe so much to all of their hard work and dedication that they instilled in me to provide the best foundations that I could ever ask for. Both of them always made sure that I put my education and studies as a top priority. They have each been there through every step of my life from helping me study throughout grade school to helping me adapt to the new experiences of university. Thank-you Mom and Dad.

Last but certainly not least, I probably owe my greatest gratitude to my wonderful wife of four years, Melina Kennedy MEd, BEd, BSc. Melina has been by my side throughout my best times and my worst times. She is the person that I can always talk to about the daily struggles of a graduate degree. She has always supported me and more than that encouraged me to always do my best and to not set any limitations. Melina encouraged me at every step of my university experience, while we attended Dalhousie together she encouraged me to major in Biochemistry, she helped me apply to my first job in science and after numerous rejections she did everything in her power to find me a job. Thanks to her encouragement I finally found an opportunity working with Dr. Melanie Dobson on Niemann-Pick type C disease in yeast. It was here that I was introduced to Barbara. Melina also encouraged me to attend graduate studies, and eventually convert to a PhD. I know the difficulties that a spouse of a graduate student goes through, for example I would often work late hours, weekends, and had to work many of our dates and time together around my experiments. Also during these last several weeks, I have been very busy writing my thesis and Melina has done everything

she could, while herself working a full time job, to make meals, take care of the house, to allow me to fully focus on my writing. She has made life so easy for me during my graduate studies and words cannot explain how grateful I am to have Melina in my life. Thank you, Melina, for all of your help, Love Barry.

CHAPTER 1 INTRODUCTION

1.1 Niemann-Pick type C disease

1.1.1 History of Niemann-Pick disease

Niemann-Pick disease was first described in the early 20th century by a German pediatrician, Dr. Albert Niemann, and a German pathologist, Dr. Ludwig Pick. Drs. Niemann and Pick studied infant patients who suffered from lipid accumulation and enlargement of the spleen, liver, and lymph nodes at birth, followed by severe damage to the central nervous system (CNS) and death at a young age [1].

In 1958, Crocker and Faber classified Niemann-Pick disease patients into four subgroups (A-D) based on genealogy, accumulated lipid, age of onset, and age of death [2-4]. The type C subgroup was characterized by a small increase in sphingomyelin levels, late age of onset, and CNS deterioration, distinguished from both type A (high sphingomyelin levels, early onset, and CNS involvement) and type B (high sphingomyelin levels, late onset, and no CNS involvement). Originally type D was distinguished by patients lineage to Yarmouth County, Nova Scotia, Canada, but was later reclassified as type C once the causative gene was determined to be identical [5].

It was not until the late 1990's when the causative genes were discovered. The genes responsible for Niemann-Pick type C (NPC) disease are *NPC1* (95% of cases) and *NPC2* (5% of cases), which encode a transmembrane (NPC1) and a lumenal (NPC2) endosomal protein, respectively [6-9]. The exact functions of NPC1 and NPC2 are still unknown; however, loss of function mutations in either protein cause accumulation of cholesterol and other lipids in endosomes [8, 10-13]. Because of this finding and others that will be discussed later, NPC disease was determined to be a disorder of cholesterol metabolism.

Conversely, type A and B are caused by mutations in the acid sphingomyelinase gene (*Smpd1*), which encodes the enzyme responsible for the breakdown of sphingomyelin to ceramide. Loss of function mutations in sphingomyelinase result in accumulation of sphingomyelin in endosomes/lysosomes [4, 14-21]. This thesis focused only on NPC disease.

1.1.2 Pathogenesis of NPC disease in humans

NPC disease is a rare, autosomal recessive, fatal neurodegenerative disease with a prevalence of approximately 1:120 000 live births [22]. Patient life span is variable, ranging from life into the sixth decade to death shortly after birth. The majority of patients die between the ages of 10-25 years [23-26]. NPC disease has a broad spectrum of symptoms, however there are many commonalities, including: visceral involvement shortly after birth (enlargement of the liver and spleen); neurological involvement (learning difficulties, difficulty in swallowing (dysphagia), loss of muscle coordination (ataxia), sudden muscle weakness (cataplexy), seizures, and impairment of eye movement (vertical gaze palsy)) [27-34]. Although visceral organs are affected, bone marrow and liver transplantation had no effects on the neurological symptoms and did not improve life span in human patients suggesting that the neuronal dysfunction is the cause of early death in NPC disease [35, 36].

The brain region most affected in NPC disease is the cerebellum, which is responsible for the regulation of motor control. It is the major site of neurodegeneration in NPC disease with massive loss of Purkinje cells, a subtype of neurons. Purkinje cell death causes most symptoms involving loss of muscle coordination. However, based on information from histological studies and the prevalence of non-cerebellar symptoms, for

example cognitive decline and seizures, other brain regions are also affected in NPC disease and contribute to the decline in health [37]. There are no known cures for NPC disease and current treatments only target symptoms such as seizures, cataplexy, dystonia, feeding difficulties [34].

1.1.3 Murine models of NPC disease

A breakthrough in the NPC disease field was the discovery of a Balb/c mouse strain with a viral sequence insertion in the *Npc1* gene causing a null phenotype (*Npc1*$^{-/-}$) similar in pathology to the human NPC disease [38-40]. Symptomatically, these mice have stunted growth (between postnatal day 25 and 35), progressive motor impairments (beginning at postnatal day 28), weight loss (after postnatal day 45), severe loss of myelin, learning difficulties, and premature death between 10-13 weeks [41-47]. *Npc1*$^{-/-}$ mice do not suffer from seizures unlike human patients. These mice suffer from visceral dysfunction such as enlargement of the liver. Expression of NPC1 exclusively in the brain prevents neurological symptoms and early death in *Npc1*$^{-/-}$ mice [48], supporting that NPC disease is mainly a disorder of the brain.

Similar to human patients, the brain region most affected in *Npc1*$^{-/-}$ mice is the cerebellum with progressive death of Purkinje cells [37, 49]. In *Npc1*$^{-/-}$ mice, Purkinje cell death begins at postnatal day 9 in a spatially and temporally specific pattern [42, 49, 50]. Neurodegeneration is evident at 5 weeks of age and is confined to the Purkinje cells in *Npc1*$^{-/-}$ mice; however, the numbers of neurons and synapses in the thalamus at 3 weeks of age and in CA2/3 regions of the hippocampus in 4-week-old *Npc1*$^{-/-}$ are decreased [37, 51, 52]. Additionally, morphological alterations include enlarged axons or storage in axons and alterations in dendrite formation and axomal degeneration, and

altered neurotransmission suggest that the hippocampus and cortex of *Npc1*$^{-/-}$ mice also contributes to cognitive decline and shortened life span [37, 53-57]. Furthermore, the other non-neuronal in the brain, astrocytes and microglia (collectively referred to as glia), are activated throughout *Npc1*$^{-/-}$ mouse brain as early as postnatal day 9 [58-60].

Recently, NPC2-deficient mice were generated; a hypomorph with 0-4% expression of NPC2 and *Npc2*-null [61, 62]. These NPC2-deficient mice have similar biochemical defects as *Npc1*$^{-/-}$ mice including endosomal cholesterol and glycolipid accumulation and suffer from weight loss, CNS motor defects, and died prematurely. Interestingly, these NPC2-deficient mice had delayed weight loss and survived slightly longer than *Npc1*$^{-/-}$ mice (110 days compared to 73 days) [63]. The exact reason for longer survival is unknown.

1.2 Cholesterol trafficking in NPC disease

1.2.1 Cholesterol metabolism

The connection between loss of function of NPC1 or NPC2 and brain dysfunction/neurodegeneration is largely unknown. One consequence of loss of NPC1 or NPC2 is the disruption of cholesterol homeostasis. Cholesterol is an essential structural component in all mammalian cellular membranes (reviewed by [64]). Additionally, cholesterol is the precursor for steroid and oxysterol biosynthesis. In most cells, cholesterol is acquired indirectly through the diet or synthesized *de novo*. The precursor for cholesterol biosynthesis is acetyl-CoA, which is derived from pyruvate or fatty acids in mitochondria. Acetyl-CoA is converted to cholesterol through a multi-step enzymatic pathway in the endoplasmic reticulum. The rate-limiting enzyme of cholesterol biosynthesis is 3-hydroxy-3-methylglutaryl-CoA reductase (HMGCR). HMGCR is

upregulated at the transcriptional level by the transcription factor sterol regulatory element binding protein (SREBP) [65, 66]. When endoplasmic reticulum cholesterol levels are low, the transmembrane precursor of SREBP (normally localized to endoplasmic reticulum) is escorted to the Golgi by SREBP cleavage-activating protein (SCAP). In the Golgi, the precursor of SREBP is cleaved by two proteases to release the transcription factor domain of SREBP. The transcription factor then translocates to the nucleus, interacts with a DNA octamer sequence called sterol regulatory element (SRE), and promotes transcription of target genes involved in cholesterol metabolism [66]. Conversely, when endoplasmic reticulum cholesterol levels are high, cholesterol binds SCAP, inducing it to bind to regulatory protein, insulin-induced gene (INSIG), thereby forming a stable complex and anchoring SREBP precursor in the endoplasmic reticulum. Thus, SREBP is not cleaved under these conditions and transcription of SRE-containing genes is not activated [67].

Alternatively, exogenous cholesterol is acquired in the form of lipoproteins. Lipoproteins are macromolecular assemblies comprised of a hydrophobic core containing triacylglycerols and cholesterol esters, and a hydrophilic coat that contains cholesterol, phospholipid and apolipoproteins that serve to transport lipids through circulatory system. There are several different lipoproteins found in the human circulation that are classified based on size, density, lipid and apolipoprotein content, and function. These lipoproteins are chylomicrons, very low density lipoprotein (VLDL), low density lipoprotein (LDL), and high density lipoprotein (HDL). Typically cells take up lipoproteins by receptor-mediated endocytosis [68]. There are several different receptors involved in this process but many are members of the LDL receptor (LDLr) family. Once

internalized, lipoproteins dissociate from the receptor due to acidification of endosomes and are moved through the endocytic pathway to late endosomes and lysosomes [69]. Cholesterol esters are hydrolyzed by lysosomal acid lipase, releasing cholesterol in the late endosomes and lysosomes [70]. Cholesterol is then transported to the plasma membrane, endoplasmic reticulum, and other sites. At the endoplasmic reticulum, cholesterol regulates SCAP, as discussed above, or is esterified by acyl-CoA: cholesterol acyltransferase (ACAT) for storage of cholesterol in lipid droplets [71](Figures 1.01 and 1.02 summarize cholesterol transport in cells).

1.2.2 Brain cholesterol metabolism

The highest levels of unesterified cholesterol are found in the brain (23 mg/g) and although the brain is only 2.1% total body weight it contains 23% of total cholesterol of the body [72]. The majority of brain cholesterol is part of myelin sheaths of oligodendroglia, which are essential for neuron signaling [73]. Cholesterol is also essential for growth of axons and synapse formation [74, 75]. Additionally, cholesterol is the precursor for neurosteroid biosynthesis, which are important for neurotransmission and gene expression in the brain [76]. Brain cholesterol metabolism differs from the rest of the body in several ways; for example, cholesterol does not cross the blood brain barrier, therefore all brain cholesterol is synthesized *de novo*. In mature CNS, the majority of cholesterol synthesis occurs in astrocytes [77]. Cholesterol is secreted from astrocytes in a lipoprotein with apolipoprotein E (ApoE) (apolipoproteins A-I, H, and D are also present in the brain in smaller concentrations) [78-81]. Several lipoprotein receptors are found in neurons including LDLR-related protein-associated protein 1 (LRP1) and LDLR in the cell body and proximal axons [72, 82, 83]. After endocytosis,

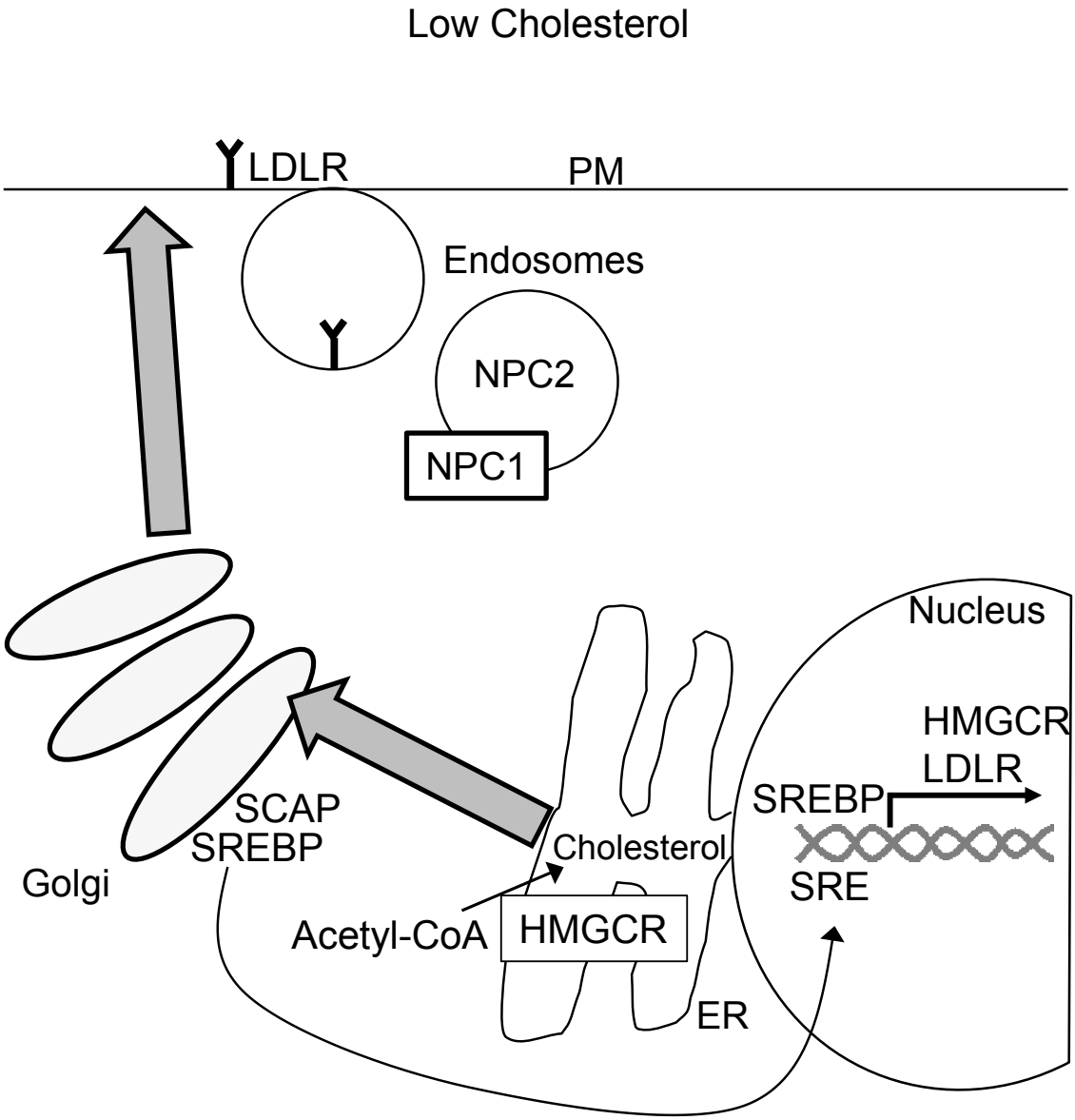

Figure 1.01 Overview of cholesterol metabolism when cellular cholesterol levels are low

When cholesterol levels are low, SCAP escorts SREBP to Golgi, where SREBP is cleaved by proteases. The cleaved SREBP translocates into nucleus, where it acts to upregulate the transcription of SRE targeted genes such as HMGCR. HMGCR is the rate-limiting enzyme in cholesterol biosynthesis. Newly synthesized cholesterol is transported to PM via Golgi. Large grey arrows represent the direction of newly synthesized cholesterol transport. PM: plasma membrane, ER: endoplasmic reticulum, grey double stranded helix: DNA. HMGCR: 3-hydroxy-3-methylglutaryl-CoA reductase, ACAT: Acyl-CoA: cholesterol acyltransferase, SREBP: sterol regulatory element binding protein, SCAP: SREBP cleavage-activating protein, INSIG: insulin-induced gene, SRE: sterol regulatory element, LDLR: low density lipoprotein receptor.

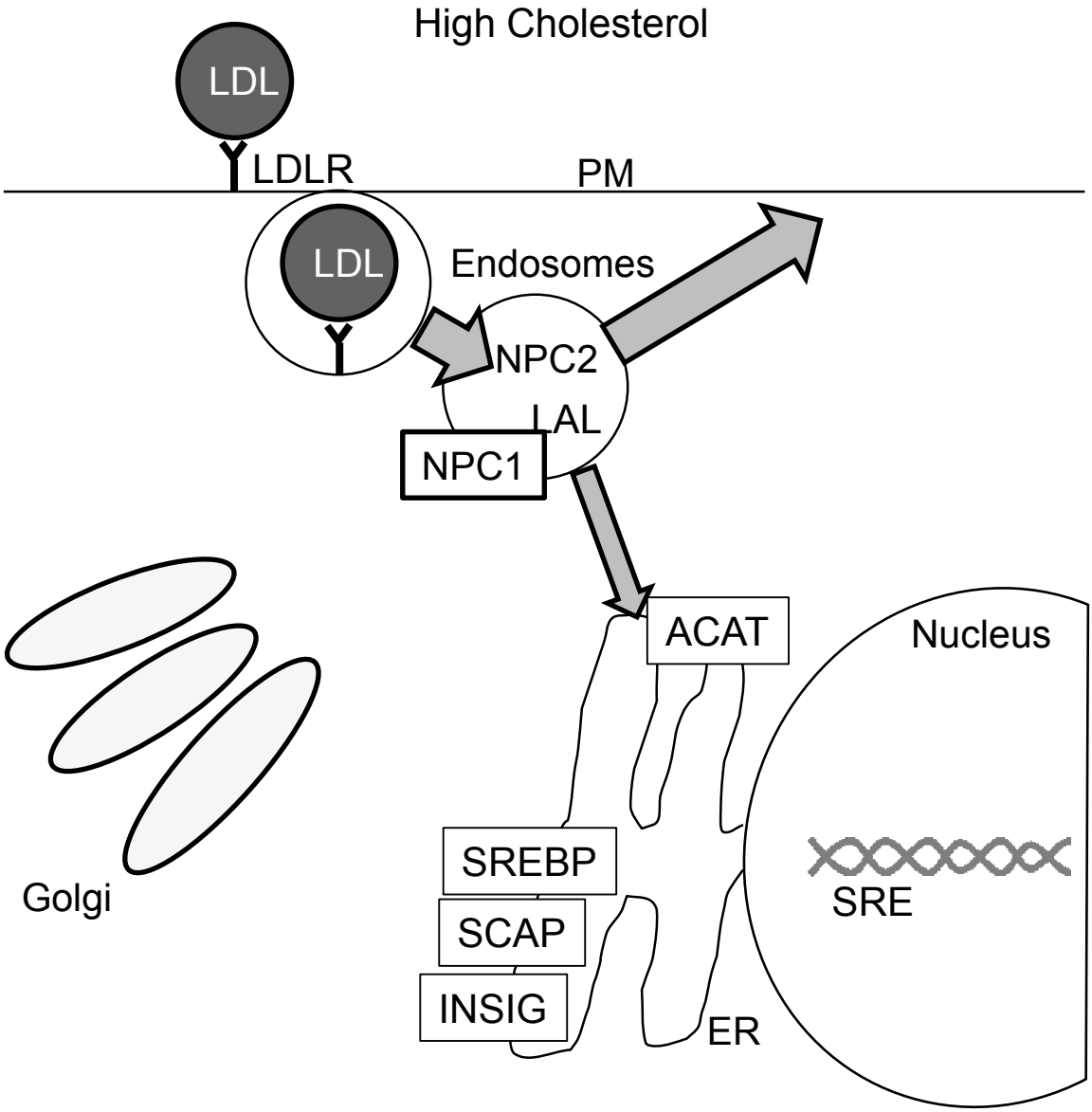

Figure 1.02 Overview of cholesterol metabolism when cellular cholesterol levels are high

In the presence of LDL, exogenously-derived cholesterol is endocytosed and transported to PM or ER. In ER, cholesterol binds INSIG, preventing the transport of SCAP and SREBP to Golgi, and the cleavage of SREBP. SREBP is degraded in the ER and SRE-targeted genes are not upregulated. Large grey arrows represent the direction of exogenously-derived cholesterol transport. PM: plasma membrane, ER: endoplasmic reticulum, grey double stranded helix: DNA. HMGCR: 3-hydroxy-3-methylglutaryl-CoA reductase, ACAT: Acyl-CoA: cholesterol acyltransferase, SREBP: sterol regulatory element binding protein, SCAP: SREBP cleavage-activating protein, INSIG: insulin-induced gene, SRE: sterol regulatory element, LDL: low density lipoprotein, LDLR: LDL receptor, LAL: lysosomal acid lipase.

cholesterol is distributed throughout neurons. The most common mechanisms for removal of cholesterol are by oxidation to membrane/blood-brain-barrier permeable 24-hydroxy cholesterol by members of the cytochrome P450 family or excretion with apoE [72, 84]. Figure 1.03 summarizes cholesterol transport in brain.

1.2.3 Cholesterol homeostasis in *Npc1*$^{-/-}$ cells

The trafficking of lipoprotein-derived cholesterol from lysosomes is a major area of focus in the field of intracellular cholesterol metabolism. In the 1980s and early 1990s several groups determined that NPC1 and NPC2 were involved. The biochemical hallmark of *Npc1*$^{-/-}$ cells is lipoprotein-derived unesterified cholesterol accumulation in endosomes/lysosomes, as demonstrated by filipin staining [10, 13, 58, 60, 85, 86]. Endosomal cholesterol accumulates by postnatal day 9 in *Npc1*$^{-/-}$ mouse brain, which precedes Purkinje cell death [60]. Despite massive endosomal cholesterol accumulation there is no increase in total cholesterol in *Npc1*$^{-/-}$ murine brain probably reflecting losses of cholesterol due to demyelination and neuronal death [87]. Delays in several aspects of cholesterol homeostasis, including the esterification of LDL-derived cholesterol (despite normal ACAT activity), downregulation of SREBP-mediated genes, and cholesterol delivery to the plasma membrane in *Npc1*$^{-/-}$cells, show that NPC1 is involved in the transport of endosomal cholesterol to the plasma membrane and the endoplasmic reticulum [10, 13, 88, 89]. Endosomal cholesterol accumulation and low cholesterol ester formation in *Npc2*$^{-/-}$ human fibroblasts in response to cholesterol refeeding shows that NPC2 is also involved in the transport of cholesterol to the endoplasmic reticulum [90](Figure 1.04 summarizes defects in cholesterol trafficking in NPC disease). In addition to cholesterol, sphingolipids, including gangliosides, accumulate in lysosomes

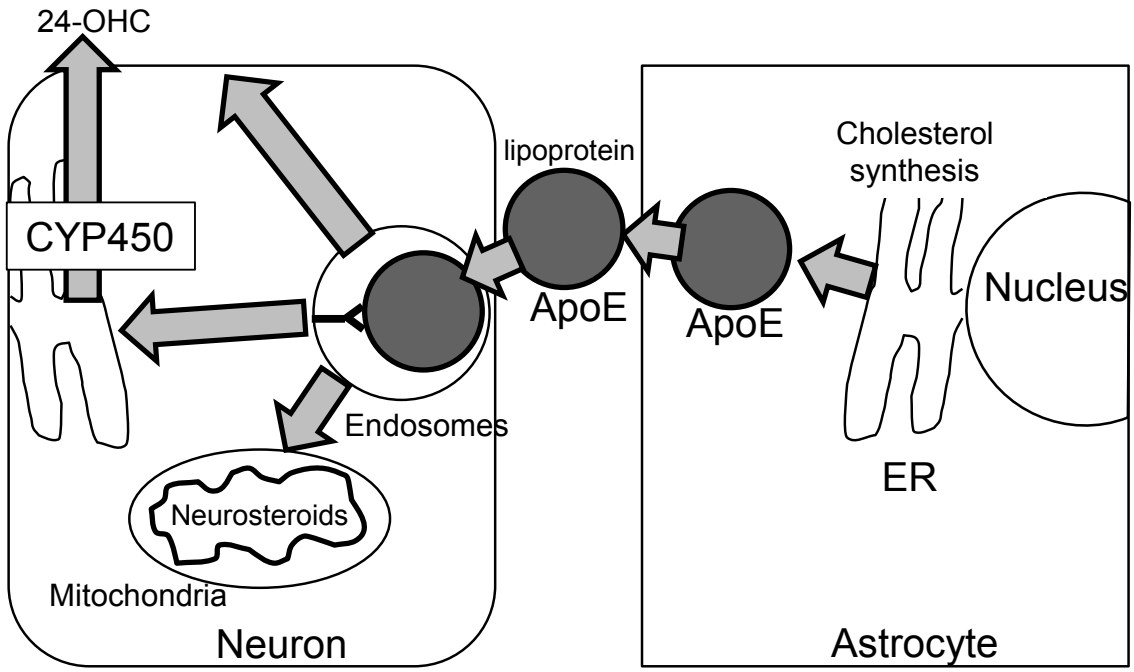

Figure 1.03 Overview of cholesterol metabolism in the brain
Majority of cholesterol synthesis in mature brain occurs in astrocytes. Newly synthesized cholesterol is packaged with ApoE and exported from the cell. ApoE lipoproteins are endocytosed by neurons and cholesterol is transported to membranes. One mechanism of cholesterol export from the brain is conversion of cholesterol to 24-OHC in ER. Large grey arrow represent the direction of cholesterol transport. ER: endoplasmic reticulum, ApoE: apolipoprotein E-containing glial lipoprotein, CYP450: cytochrome P450, 24-OHC: 24-hydroxyl cholesterol. Figure adapted from Benarroch [91].

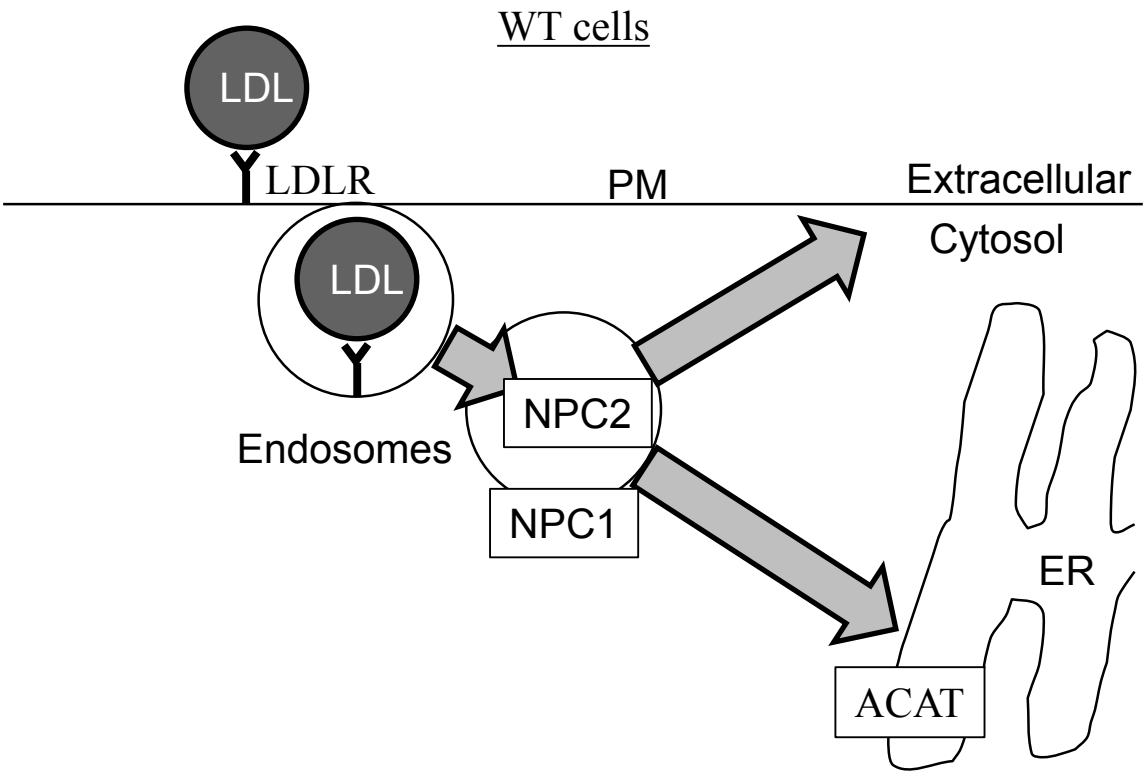
WT cells
LDL
LDLR
PM
Extracellular
Cytosol
LDL
NPC2
Endosomes
NPC1
ER
ACAT

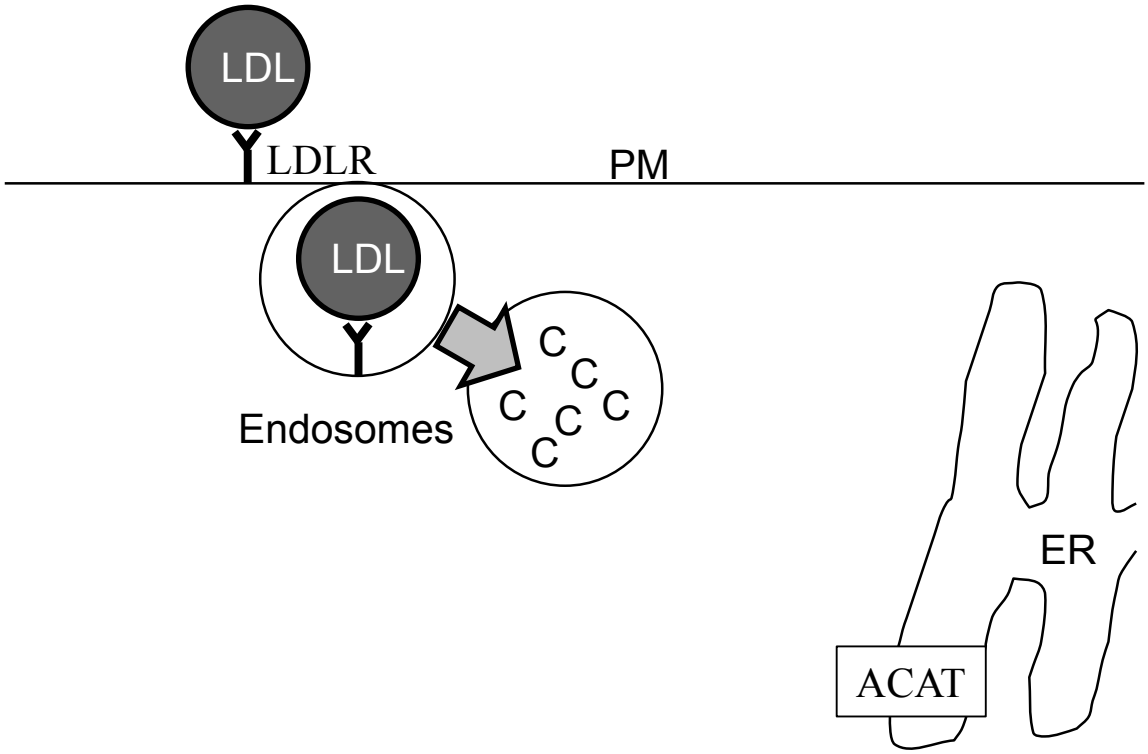
NPC1-/- or NPC2-/- cells
LDL
LDLR
PM
LDL
C
C
C
C
C
C
Endosomes
ER
ACAT

Figure 1.04 Summary of cholesterol metabolism in *Npc1*$^{-/-}$ cells
In wildtype (WT) cells, exogenously-derived cholesterol is endocytosed and transported to PM and ER in a NPC2-/NPC1-dependent mechanism. In *Npc1*$^{-/-}$ or *Npc2*$^{-/-}$ cells, exogenously-derived cholesterol is endocytosed and accumulates in endosomes. Large grey arrow represent the direction of cholesterol transport. ER: endoplasmic reticulum, PM: plasma membrane, LDL: low density lipoprotein, LDLR: LDL receptor, C: cholesterol, ACAT: Acyl-CoA: cholesterol acyltransferase.

by 3 weeks of age in *Npc1*$^{-/-}$ murine brain showing that sphingolipid homeostasis is also altered in NPC disease [92].

1.2.4 NPC1 structure, localization, and function

Although NPC1 is required for normal cholesterol metabolism, the exact function of the protein is unknown. NPC1 has orthologs in humans, mice, *C. elegans*, and *S. cerevisiae* and has homology with the resistance-nodulation-division (RND) family of prokaryotic proton permeases suggesting a conserved function throughout evolution [6, 93]. The NPC1 protein is a 1278 amino acid protein with a molecular weight of 142 kD [6]. Structurally, NPC1 contains a unique 112 amino acid N-terminal domain (NTD) with a leucine zipper motif, 13 transmembrane-spanning domains, and a C-terminal domain that contains a di-leucine (LLNF) lysosomal targeting motif [6, 40, 94]. In addition, NPC1 is contains 14 glycosylation sites conserved between human and mice [6]. Within NPC1 is a sterol sensing domain (SSD) similar to the cholesterol binding proteins SCAP, patched, and HMG-CoA reductase [40, 95]. Similar to these proteins, the SSD of NPC1 binds cholesterol [96] and specific point mutations in the NPC1 SSD domain increase or decrease transport of cholesterol to the plasma membrane and endoplasmic reticulum [97]. In addition to the SSD, the NTD (240 amino acid lumenal loop 1) also binds cholesterol and hydroxylated cholesterol derivatives including 24-, 25-, 27- hydroxyl cholesterol [98] (Figure 1.05 highlights structural features of NPC1). NPC1 localizes to late endosomes and lysosomes [99-101]. NPC1 is also found in synaptosomes isolated from mouse brain suggesting a role for NPC1 in axons [102]. NPC1 is ubiquitously

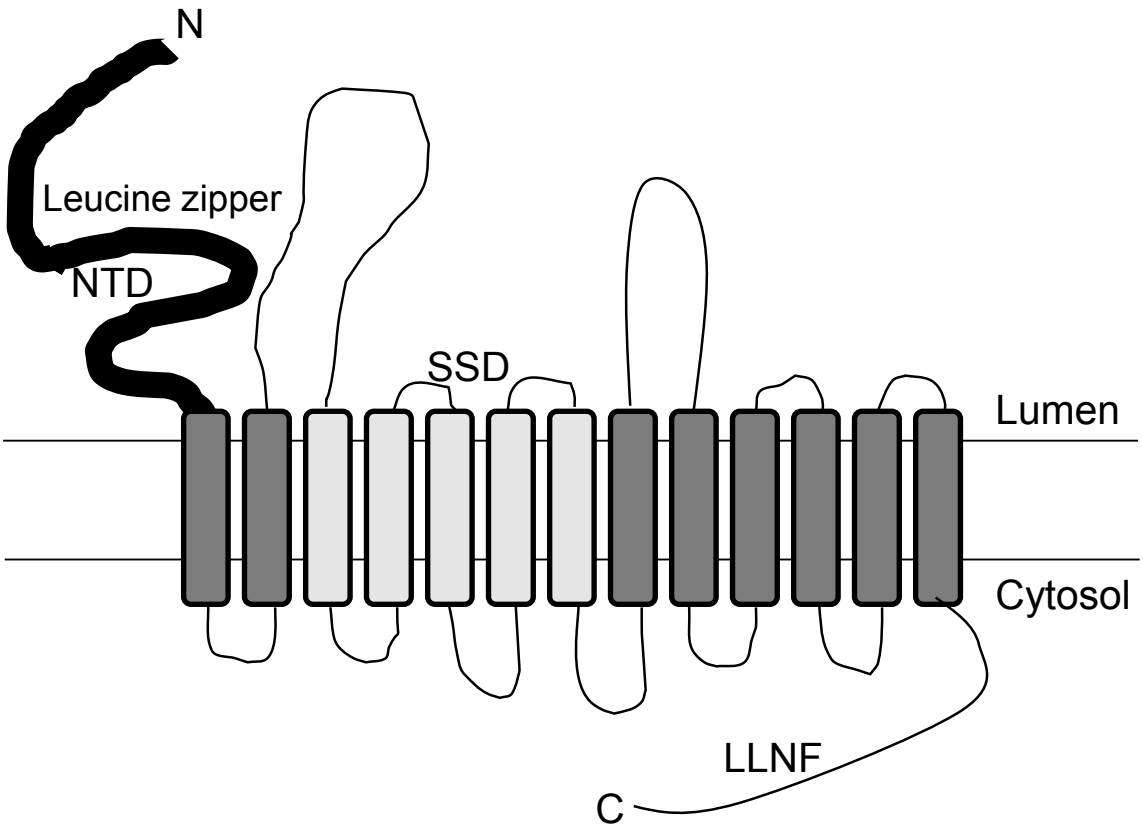

Figure 1.05 NPC1 structure
Two long horizontal lines represent the endosomal perimeter membrane. The dark and light grey rectangles represent transmembrane domains of NPC1. N: amino terminus, C: carboxyl-terminus, NTD: N-terminal domain, LLNF: lysosomal targeting motif, 5 light grey boxes represent the sterol-sensing domain (SSD) of NPC1.

expressed in all cells and tissues, with the highest expression in the cerebellum and pontine nuclei, two brain regions involved in motor activity [103]. Expression of NPC1 is detectable as early as embryonic day 15 and is maintained at similar levels throughout development in wildtype mice and rats [103, 104].

As of 2004 there were over 240 disease-causing mutations in NPC1 reported; likely in part responsible for the large heterogeneity of symptoms between patients [5, 6, 26, 105-113]. These mutations (nonsense, missense, insertions, and deletions) are spread throughout the gene and therefore, do not point to a single functionally significant domain. However, many mutations cluster in the NTD and SSD suggesting key functional roles for the cholesterol binding domains [95, 108, 114].

1.2.5 NPC2 structure and localization

NPC2 is an ubiquitous 151 amino acid protein localized to the lumen of lysosomes and is secreted into semen, milk, and also from cells when lysosomes are exocytosed [7, 115, 116]. NPC2 was originally cloned from the human epididymis and referred to as the major secretory protein of the human epididymis 1 (HE1). After the role in NPC disease was discovered, HE1 was named NPC2 [7, 115].

NPC2 binds cholesterol but not sphingolipids in a high affinity hydrophobic binding pocket at a 1:1 molar ratio as determined by crystal structure and mutation analysis [117-121]. NPC2 is capable of transferring cholesterol bidirectionally between phospholipid membranes or between phospholipid membranes and NPC1 [122, 123]. Mutation analysis of the N-terminal domain of NPC1 identified several amino acid residues necessary for the hydrophobic transfer of cholesterol from NPC2 [124, 125].

Additionally, three surface residues on NPC2 are required for transfer of cholesterol to the N-terminal domain of NPC1 [125]. Also required for the transfer of cholesterol between NPC2 and NPC1 is the second lumenal domain of NPC1, which directly binds NPC2 at acidic pH [126]. Together these findings suggest a model where NPC2 transfers cholesterol from the lumenal vesicles of multivesicular bodies to the perimeter membrane of endosomes or NTD of NPC1 in the perimeter membrane. Cholesterol is then transferred from the NTD to the SSD of NPC1 where it is presented to cytosolic transfer proteins that deliver cholesterol to other cellular membranes (A schematic of cholesterol transfer between NPC2 and NPC1 is presented in Figure 1.06).

1.2.6 Role of cholesterol in NPC disease pathogenesis

Because NPC1 and NPC2 both specifically bind cholesterol, which would suggest that NPC disease is a disease of cholesterol metabolism. However, sphingolipids accumulate in the endosomes of *Npc1*$^{-/-}$ and *Npc2*$^{-/-}$ cells. To further address the relative contribution of each lipid, several studies used genetic modification or pharmaceutical treatments to alter lipid metabolism and determine the effect on NPC pathogenesis. Genetic depletion of ganglioside (GM2/GD2 or GM3) synthase to decrease the synthesis of gangliosides a no effect on the endosomal cholesterol accumulation, had minimal effect on altered gene expression profile in the cerebellum, and did not improve lifespan of *Npc1*$^{-/-}$ mouse brain, indicating that ganglioside accumulation did not cause NPC pathogenesis [127]. The most convincing studies linking cholesterol to NPC pathogenesis were treatments with the soluble cholesterol-binding complex carbohydrate molecule, 2-hydroxypropyl-beta-cyclodextrin (HPCD). HPCD is a water-soluble structure that contains a hydrophobic pocket that binds cholesterol. HPCD is endocytosed into *Npc1*$^{-/-}$

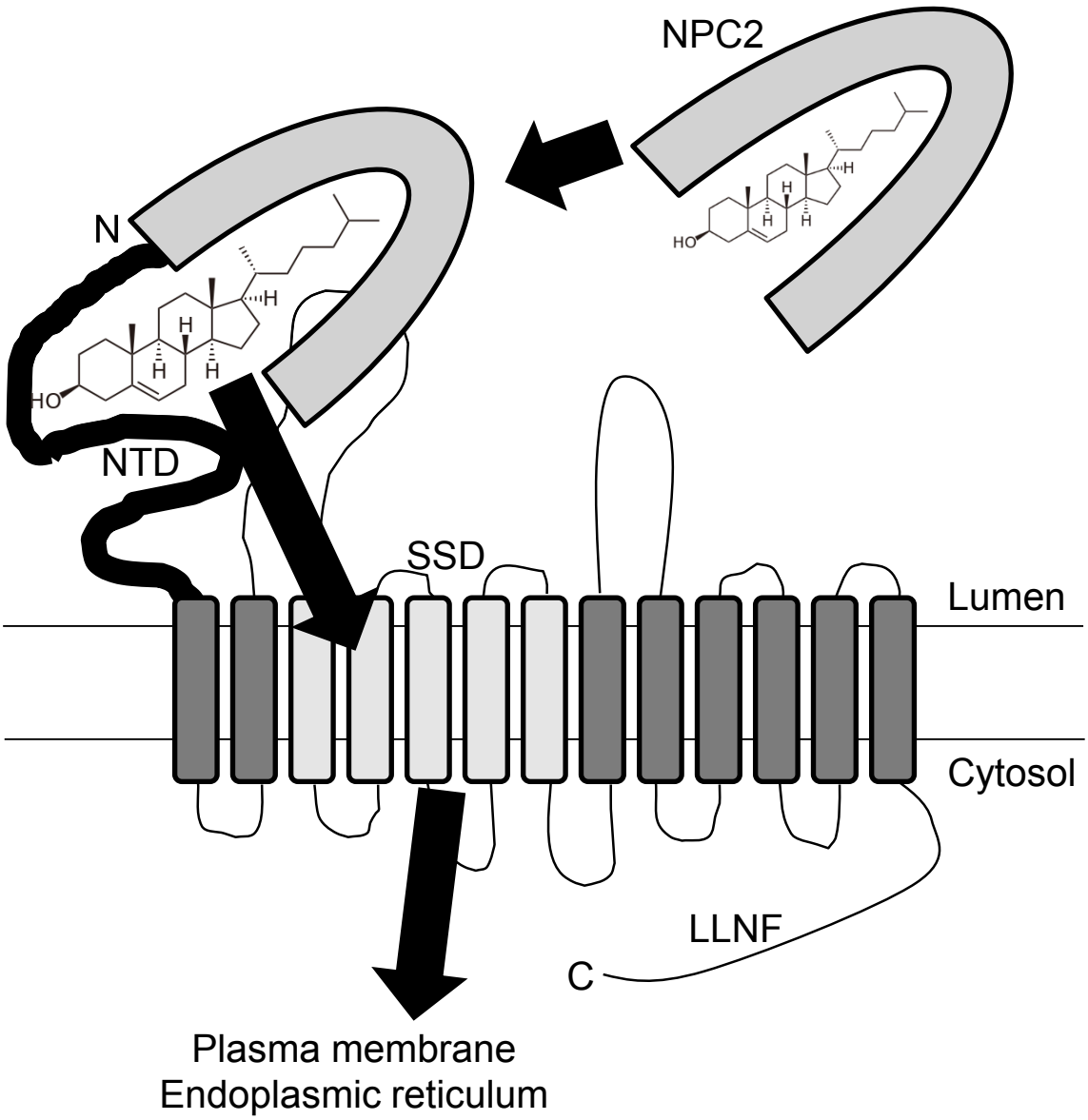

Figure 1.06 Model of cholesterol transfer between NPC2 and NPC1
NPC2 binds cholesterol in a hydrophobic pocket, interacts with the NTD and the second lumenal loop of NPC1. Cholesterol is transported from NPC2 to the NTD of NPC1, and in an unknown mechanism presented to cytosolic cholesterol carrier proteins, possibly through the SSD. Black arrows represent the proposed direction of cholesterol transport. Two long horizontal lines represent the endosomal perimeter membrane. The dark and light grey rectangles represent transmembrane domains of NPC1. The grey horse shoe represents NPC2 and the hydrophobic binding pocket of NPC2. N: amino terminus of NPC1, C: carboxyl-terminus of NPC1, NTD: N-terminal domain, LLNF: lysosomal targeting motif, 5 light grey boxes represent the sterol-sensing domain (SSD) of NPC1.

and *Npc2*$^{-/-}$ human fibroblasts where it mobilizes cholesterol, reducing endosomal cholesterol accumulation and increasing cholesterol ester formation in *Npc1*$^{-/-}$ and *Npc2*$^{-/-}$ human fibroblasts [128]. Multiple treatment conditions with HPCD at presymptomatic ages (e.g. a single injection at postnatal day 7 or continuous infusion into brain between 3 and 7 weeks) mobilized endosomal cholesterol, improved liver function, increased cholesterol ester formation, decreased neurodegeneration, and prolonged survival of *Npc1*$^{-/-}$ mice [129-132]. Recently, trials have begun to test the effect of HPCD as a treatment in human NPC patients [133]. Together these results show that the block of cholesterol transport out of endosomes is primarily responsible for neuron dysfunction, neurodegeneration, and early death of the animals.

The exact link between altered cholesterol homeostasis and NPC pathogenesis is unknown. Cholesterol is an essential component of all mammalian membranes, where the 3β-hydroxyl group interacts with polar head groups of surrounding phospholipids and the hydrophobic steroid ring is buried in the phospholipid bilayer. High cholesterol levels reduce the fluidity or motional freedom within a lipid bilayer, and vice versa [134]. Additionally, the cholesterol content in membranes affect a number of important membrane properties including membrane permeability, membrane enzyme activities, and conformation of membrane proteins [135, 136]. In *Npc1*$^{-/-}$ cells, plasma membrane and endoplasmic reticulum cholesterol levels are decreased and interestingly, as will be discussed in the following section, mitochondrial membrane cholesterol levels are increased. My research focused on the consequences of increased cholesterol levels on mitochondrial function in *Npc1*$^{-/-}$ cells.

1.3 Mitochondrial cholesterol

1.3.1 Decreased steroid production and increased mitochondrial cholesterol levels in *Npc1*$^{-/-}$ cells

The levels of cholesterol in mitochondria of *Npc1*$^{-/-}$ cells is a controversial topic. On the one hand because *Npc1*$^{-/-}$ cells had a block in cholesterol trafficking out of endosomes it was assumed that all membranes would have decreased cholesterol. In support of decreased mitochondrial cholesterol, steroid production was decreased in *Npc1*$^{-/-}$ cells. Cholesterol is a precursor for steroidogenesis, which is initiated by a member of the cytochrome P450 family of enzymes, Cyp11a1 (catalyzes the conversion of cholesterol to pregnenolone), located in the mitochondrial matrix [137, 138]. *Npc1*$^{-/-}$ male mice have decreased testosterone levels, and *Npc1*$^{-/-}$ mouse brain and *Npc1*$^{-/-}$ astrocytes have decreased expression of several steroidogenic enzymes and decreased production of neurosteroids [139-141]. Furthermore, treatment of *Npc1*$^{-/-}$ drosophila with 20-hydroxyecdysone and treatment with allopregnanolone or 17-beta-estradiol in *Npc1*$^{-/-}$ mice, delayed loss of motor control in mice and prolonged life span of both mice and drosophila [140-143]. However, the protein levels of two steroidogenic enzymes, 5-alpha-reductase and 3-alpha-hydroxysteroid dehydrogenase are reduced in *Npc1*$^{-/-}$ murine brain suggesting that steroid levels may not reflect mitochondrial cholesterol levels [140]. Noteworthy, the study that showed allopregnanolone improved *Npc1*$^{-/-}$ mouse life span was put into question because cyclodextrin was used as the vehicle [132].

Yu et al. reported increased mitochondrial cholesterol levels in 9-week-old *Npc1*$^{-/-}$ mouse brain [144]. Recently, several other groups, including our lab, have confirmed that mitochondrial cholesterol is increased in *Npc1*$^{-/-}$ murine brains and hepatocytes [145-

147]. Increased mitochondrial cholesterol levels could have several consequences on mitochondrial function in NPC disease. For example, Yu et al. showed that ATP synthase activity was decreased in mitochondria isolated from 9-week-old *Npc1*$^{-/-}$ mouse brain [144]. Furthermore reducing mitochondrial cholesterol levels by incubation with cyclodextrin partially restores activity, suggesting that increased mitochondrial cholesterol ATP synthase activity [144]. Additionally, accumulation of mitochondrial cholesterol occurs in pathological conditions including hepatic steatosis [145], myocardial cells after ischemia [148, 149], some cancers [150-155], and the brains of a murine model of Alzheimer disease [146]. In several of these models, accumulation of mitochondrial cholesterol correlated with mitochondrial dysfunction [148, 149, 154-157]. Increased mitochondrial cholesterol reduced membrane fluidity, increased reactive oxygen species production, and inhibited certain mitochondrial transporters (including the glutathione transporters) [144, 145, 154, 158, 159]. However, the extent to which increased mitochondrial cholesterol contributed to NPC disease pathogenesis was unclear and is a main focus of this thesis.

1.3.2 Cholesterol transport to mitochondria

The mechanisms of cholesterol transport to mitochondria are poorly understood. The best-described cholesterol transport pathway to mitochondria is mediated by the steroidogenic acute regulatory (StAR) protein in steroidogenic cells. The StAR protein contains a StAR-related transfer (START) domain that binds cholesterol. StAR expression is rapidly upregulated upon activation of steroidogenesis [160]. The mechanism of StAR-dependent cholesterol transport to mitochondria is incompletely understood; however, it appears that the StAR precursor is cleaved forming mature StAR

that transports cholesterol directly to the inner mitochondrial membrane (reviewed by Miller and Bose [161]). To deliver cholesterol to the mitochondria, StAR interacts with several mitochondrial proteins including translocator protein (TSPO) and voltage-dependent anion channel (VDAC) [162, 163].

In addition to steroidogenesis, the StAR/TSPO pathway regulates total mitochondrial membrane cholesterol [149, 155, 164]. Depletion of StAR prevented accumulation of mitochondrial cholesterol in hepatocellular carcinoma cells [155, 164], and treatment with the TSPO ligand, 4'-chlorodiazepam, prevented accumulation of mitochondrial cholesterol in cardiomyocytes after ischemia likely by blocking TSPO activity [149]. StAR is expressed in steroidogenic cells throughout the brain, however, StAR protein and mRNA levels are decreased in *Npc1*$^{-/-}$ astrocytes [141, 165, 166], suggesting that StAR does not cause increased mitochondrial cholesterol in the *Npc1*$^{-/-}$ brain.

Another member of the START domain-containing protein family is a late endosomal protein called metastatic lymph node 64 protein (MLN64) or StAR-related lipid transfer domain protein (StARD3). MLN64 contains a cytosolic C-terminal START domain with 37% homology to StAR and a four-transmembrane N-terminal domain homologous to MENTHO, a late endosomal transmembrane cholesterol-binding domain with unknown function [167-169]. Crystal structure of the MLN64 C-terminal START domain shows binding of one molecule cholesterol per protein molecule [169]. Expression of full length or C-terminal START domain, but not of the N-terminal domain of MLN64 stimulates steroidogenesis in cells that lack StAR, suggesting that MLN64 is capable of transporting cholesterol to mitochondria [170]. MLN64 is found in most human and mouse tissues

including the placenta. In the placenta, which lacks StAR, MLN64-mediated delivery of cholesterol to mitochondria may be the main pathway to support steroidogenesis [170]. Immunoblot analysis shows that the C-terminal domain of MLN64 is cleaved in placenta, suggesting that the C-terminus of MLN64 deliver cholesterol to mitochondria similarly to StAR [171].

MLN64 is expressed in all brain regions and in both neurons and glia; however, MLN64 was not expressed in StAR-expressing cells and had limited co-localization with *Cyp11a1*-expressing cells in human brain [172, 173]. This suggests that MLN64 does not transport cholesterol to mitochondria for neurosteroid synthesis in the brain. On the other hand, MLN64 may be involved in cholesterol transport to non-steroidogenic mitochondria (The transport of cholesterol to mitochondria is summarized in Figure 1.07). In the following thesis, I will determine the role of MLN64 in cholesterol delivery to mitochondrial in *Npc1*$^{-/-}$cells.

1.4 Energy metabolism and mitochondrial function in the brain

1.4.1 Glucose metabolism in the brain

In humans, approximately 20% of oxygen and 25% of glucose is consumed by the brain, emphasizing the importance of oxidative glucose metabolism. Maintenance and restoration of ion gradients and uptake/recycling of neurotransmitters are the main processes contributing to the high-energy demands [174, 175]. Glucose is the obligatory energy substrate; however, under certain circumstances where glucose is unavailable as an energy source such as fasting or in diabetics, the brain uses ketone bodies as energy substrates [176-179]. Glucose enters cells through specific glucose transporters (GLUTs) and is phosphorylated to glucose-6-phosphate by hexokinase. Glucose-6-phosphate is

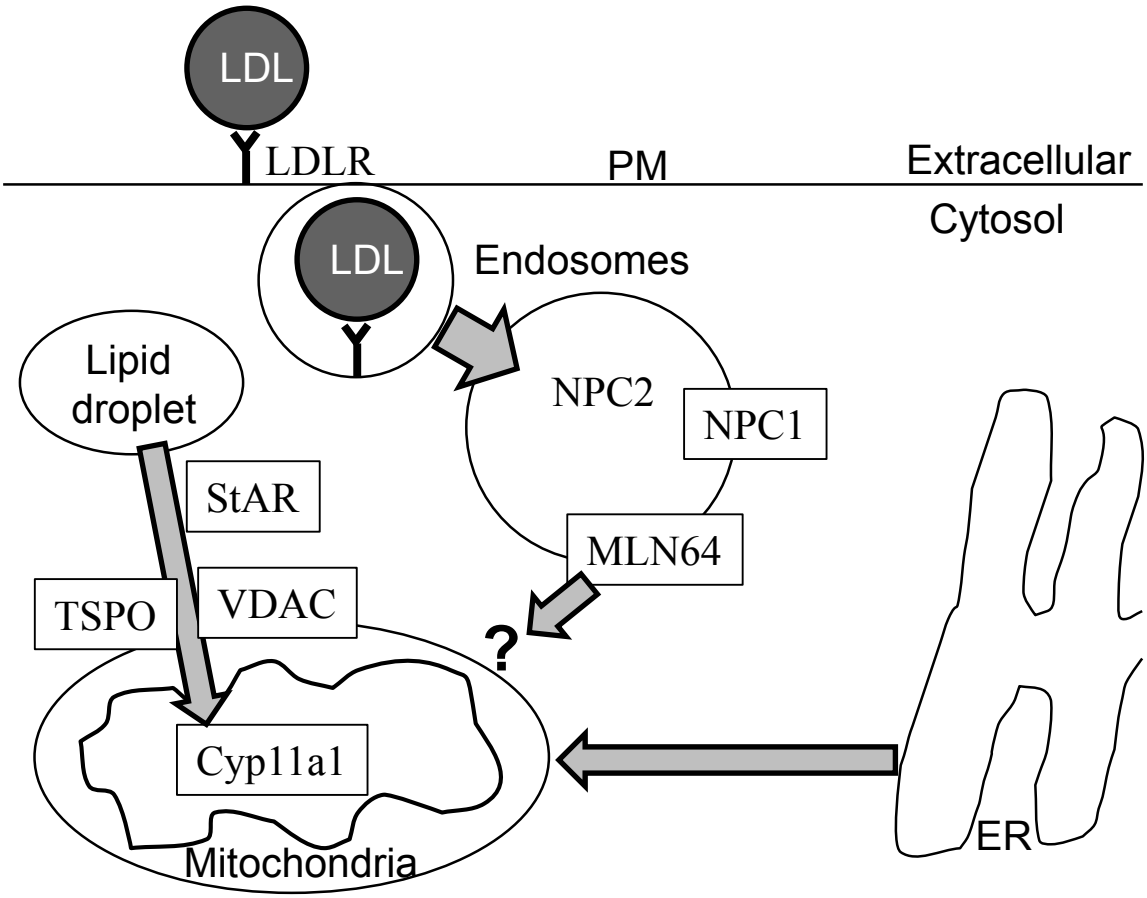

Figure 1.07 Overview of cholesterol transport to mitochondria
Exogenously-derived cholesterol is transported to mitochondria possibly through MLN64 to an unknown mitochondrial acceptor. Endogenously-derived cholesterol is transported from ER to mitochondria through an unknown mitochondrial acceptor (possibly via mitochondrial associated membrane). In steroidogenic cells, cholesterol from lipid droplets are transported to the inner mitochondrial membrane in an unknown mechanism that involves several proteins including StAR, TSPO, and VDAC. Large grey arrow represent the direction of cholesterol transport. ER: endoplasmic reticulum, PM: plasma membrane, LDL: low density lipoprotein, LDLR: LDL receptor, Cyp11a1: Cytochrome P450 side chain cleavage, StAR: steroidogenic acute regulatory protein, TSPO: translocator protein, VDAC: voltage-dependent anion channel, MLN64: metastatic lymph node 64.

then metabolized through glycolysis (leading to pyruvate) or the pentose-phosphate pathway (PPP, leading to the regeneration of NADPH and the production of nucleotides). Brain energy metabolism involves a complex interplay between neurons and astrocytes. Both cell types are capable of fully oxidizing glucose [178]; however, cell-specific expression of key glycolytic enzymes suggest that these cells use different metabolic pathways [180].

The majority of high-energy brain functions such as neurotransmission occur in neurons. Consistent with their high energy demand, neurons sustain a higher rate of oxidative metabolism than astrocytes [181, 182]. In contrast, glycolytic rates are likely lower in neurons than in astrocytes, partly due to constant proteasomal degradation of phosphofructokinase 2 (PFK2) in neurons [183]. PFK2 catalyzes the generation of fructose-2,6-bisphosphate, a potent activator of the glycolytic enzyme phosphofructokinase-1 (PFK1). In cultured neurons, the upregulation of glycolysis by PFK2 overexpression led to increased oxidative stress and eventually neurodegeneration, suggesting that neurons cannot sustain a high glycolytic rate [183, 184]. The probable reason behind increased oxidative stress is decreased flux of glucose-6-phosphate through PPP and thus decreased production of NADPH, which is required for the regeneration of the major cellular antioxidant glutathione [183, 185]. Interestingly, several studies show that neurons can efficiently use lactate as an energy source [186-188]. Therefore, the oxidation and release of lactate from astrocytes may provide neurons with energy without altering glucose usage by PPP [189]. The consequences of NPC1-deficiency for glycolysis were investigated in this thesis.

Although astrocytes display lower rates of oxidative metabolism compared to neurons, they take up large amounts of glucose and have a high glycolytic rate [190, 191]. The majority of glucose taken up by astrocytes is metabolized through glycolysis and converted to/released as amino acids or lactate [190, 192, 193]. Consistent with increased glycolysis and lactate production, astrocytes maintain high levels of PFK2 and inhibition of pyruvate dehydrogenase by phosphorylation, [190, 194].

To explain energy metabolism in the brain, Pellerin and Magistretti proposed the "astrocyte-neuron lactate shuttle" hypothesis [192]. This model proposes that neuronal activity increases glucose uptake and glycolysis in astrocytes resulting in increased production of lactate, which is then secreted by astrocytes and oxidized by neurons to provide energy [181, 195-198]. Support of this hypothesis stems from studies showing that glucose analogs are preferentially taken up by astrocytes as opposed to neurons in rat cortex following stimulation [199]. Furthermore, exposure to the major excitatory neurotransmitter glutamate stimulates glucose uptake and increases lactate production in astrocytes, whereas addition of glutamate decreases glucose uptake in neurons [192, 200, 201]. Additionally, delivery of glucose to astrocytes in hippocampal slices restored synaptic transmission in neighboring neurons during glucose deprivation [202]. Moreover, haploinsufficiency of neuron-specific GLUT3 did not cause any neurological or brain energy abnormalities. Haploinsufficiency of the astrocytic GLUT1 caused a severe neurological phenotype [203-205]. Furthermore, neurons express lactate dehydrogenase b (LDHb), which favours the conversion of lactate to pyruvate, which astrocytes express both LDHa, which favours the production of lactate and LDHb [206]. A schematic of glucose metabolism in the brain is shown in Figure 1.08.

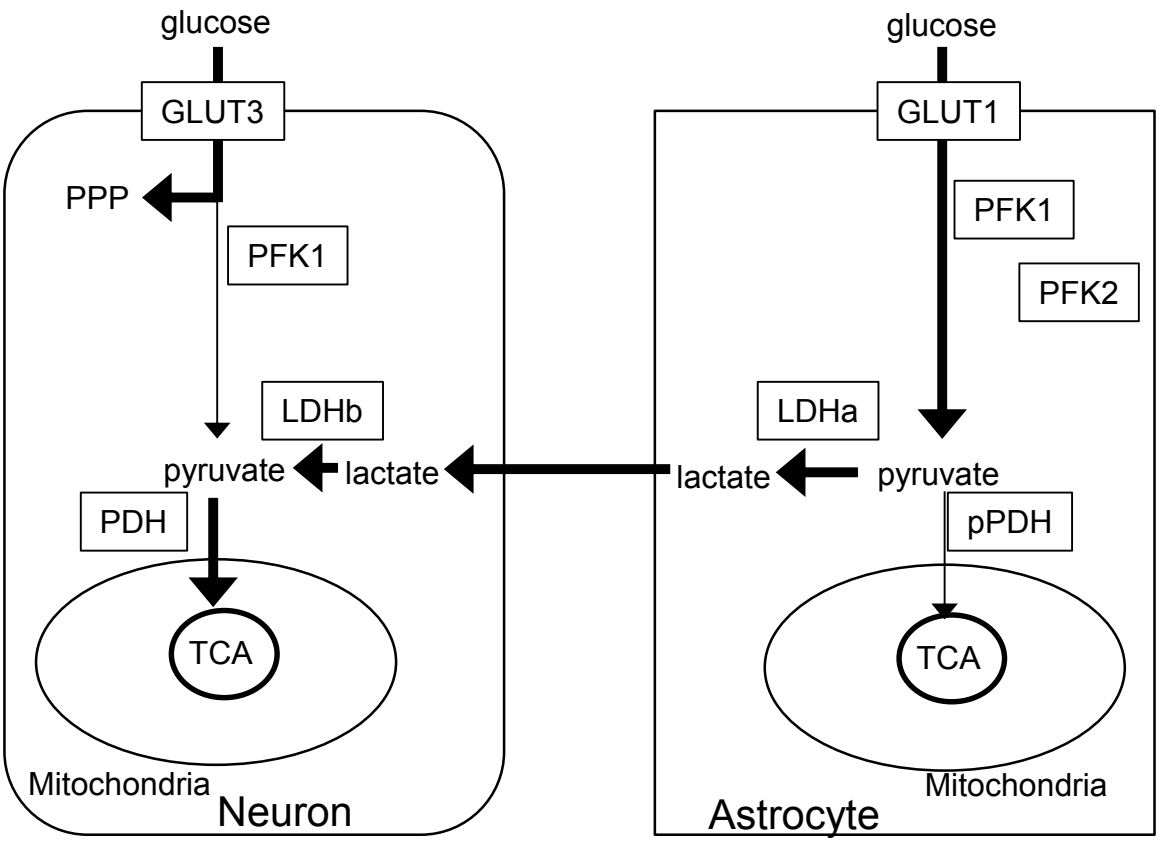

Figure 1.08 Overview of neuron-glia lactate shuttle hypothesis in brain
Glucose is taken up by both neurons and astrocytes, in neurons glucose is mainly metabolized in the PPP, in astrocytes glucose is metabolized to lactate via glycolysis. Lactate produced by astrocytes is released and taken up by neurons, where it is converted to pyruvate and oxidized for energy production in mitochondria. Black arrows represent metabolic flux, with the darker arrows representing the areas of greatest flux. Enzymes are shown in boxes. GLUT3: neuronal glucose transporter 3, GLUT1: astrocytic glucose transporter 3, PFK1: phosphofructokinase 1, PFK2: astrocytic phosphofructokinase 2, LDHa: astrocytic lactate dehydrogenase a, LDHb: neuronal lactate dehydrogenase b, PDH: pyruvate dehydrogenase, pPDH: phosphorylated/inhibited PDH, TCA: tricarboxylic acid cycle, PPP: pentose phosphate pathway.

1.4.2 Glutamate-glutamine cycle in brain

In addition to oxidation of pyruvate, neurons also oxidize amino acids, namely glutamate, for energy production. Glutamate is the major excitatory neurotransmitter in the brain [207] that is metabolized by both neurons and astrocytes [208-210]. It is released from glutamatergic neuronal synapses upon physiological stimulation [211]. High extracellular glutamate is excitotoxic and can induce seizures or neurodegeneration [212-214]. Glutamate metabolism in the brain follows a cycle that involves both neurons and astrocytes called the glutamate-glutamine cycle. Astrocytes control glutamate signaling and prevent excitotoxicity through glutamate uptake by excitatory amino acid transporters (EAATs) [215-219]. Glutamate is converted to glutamine by the astrocytic enzyme glutamine synthetase [220, 221]. Glutamine is subsequently released from astrocytes, and taken up by neurons [222, 223]. To complete this cycle, glutamine is hydrolyzed into glutamate and ammonia by phosphate-dependent glutaminase and stored in synaptic vesicles or metabolized further [224]. Under conditions such as energy deprivation, neurons convert glutamate to alpha-ketoglutarate through either oxidative deamination catalyzed by glutamate dehydrogenase through transamination by aminotransferases [178, 225, 226]. The tricarboxylic acid (TCA) cycle intermediate alpha-ketoglutarate is further metabolized as a mechanism to generate energy (Figure 1.09 summarizes glutamate metabolism in the brain).

1.4.3 Mitochondrial function and oxidative stress

Mitochondria are the central component of energy metabolism. Glycolysis on its own does not generate sufficient ATP in the brain; therefore, oxidative phosphorylation is required. Impaired oxidative phosphorylation is associated with most neurodegenerative

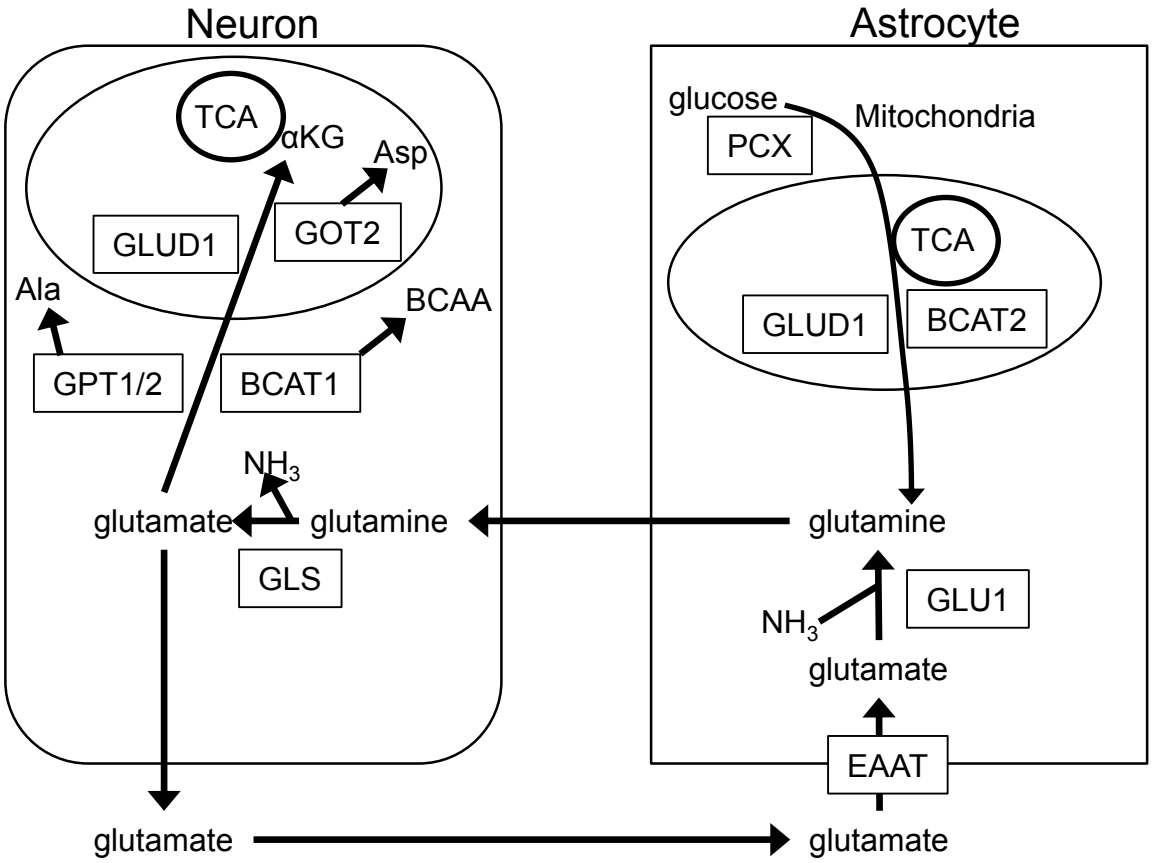

Figure 1.09 Summary of glutamate-glutamine cycle in brain
Glutamate released by neurons at synapses is taken up by astrocytes, converted to glutamine, and released. Glutamine is taken up by neurons, converted back to glutamate, and either used again as a neurotransmitter or oxidized (through conversion to αKG) as an energy source. Black arrows represent metabolic flux. Enzymes are shown in boxes. Glu1: glutamine synthetase, GLS: glutaminase, GOT2: aspartate aminotransferase, GLUD1: glutamate dehydrogenase, BCAT1/2: branched-chain aminotransferase 1/2, GPT1/2: alanine aminotransferase 1/2, EAAT: excitatory amino acid transporter, TCA: tricarboxylic acid cycle, αKG: alpha ketoglutarate, BCAA: branched chain amino acids, PCX: pyruvate carboxylase.

disorders including Alzheimer, Parkinson, Huntington, and Amyotrophic lateral sclerosis diseases as reviewed by Lin and Beal [227]. Another consequence of oxidative phosphorylation dysfunction is increased "leakage" of electrons from the electron transport chain [228-231]. These electrons generate potentially harmful reactive oxygen species (ROS). ROS are toxic to the cell due to their reactivity with proteins, lipids, and nucleotides [232]. Normally, an antioxidant defense system comprised of superoxide dismutase and glutathione is sufficient to prevent harmful accumulation of ROS. However, defects in the antioxidant defense system or in oxidative phosphorylation that cause very high ROS production/accumulation can lead to cellular dysfunction [233-238].

The brain is particularly sensitive to oxidative stress due to high concentrations of polyunsaturated fatty acids that are susceptible to lipid peroxidation, high rates of oxidative phosphorylation, lower antioxidant defense capacities, and increased longevity of neurons compared to cells in other organs (reviewed by Adibhatla and Hatcher [239]). Recently, several groups detected increased markers of oxidative stress in NPC disease. Oxidative stress markers in serum of human patients correlated with age and disease progression [240-243]. Also, 7-week-old *Npc1*$^{-/-}$ mouse liver and brain have decreased levels of glutathione, increased copper levels, decreased expression of antioxidant defense genes such as catalase, increased expression of genes that promote oxidative damage such as nitric oxide synthase, and increased oxidative stress markers such as nitrotyrosine and protein carbonyls [144, 241, 244-249]. Additionally, many NPC1-deficient cell lines show signs of oxidative stress, including *Npc1*$^{-/-}$ human fibroblasts, which produce increased levels of ROS, have increased lipid peroxidation and express a

gene profile indicative of increased oxidative stress [247, 250, 251]. Several NPC1-deficient neuronal cell lines (SHSY neuroblastoma cells and neuronal stem cells) also produce increased ROS and nitric oxide [251, 252]. Together these studies suggest that oxidative stress and mitochondrial dysfunction contributes to NPC pathogenesis. However, whether mitochondrial dysfunction occurs early in disease progression and what causes the initial defect remains unclear. The connection between mitochondrial dysfunction and disrupted cholesterol homeostasis in NPC disease is also unclear.

1.4.4 Neurodegeneration and energy deprivation in *Npc1*$^{-/-}$ brain

The precise connection between altered cholesterol homeostasis and brain dysfunction/neurodegeneration remains unknown. Alterations in energy metabolism and mitochondrial dysfunction could lead to some degree of energy deprivation in *Npc1*$^{-/-}$ murine brains. Energy deprivation would have several consequences including cell dysfunction and cell death. Several studies have proposed that programmed cell death by either apoptosis or autophagy or some combination of both, causes axonal degeneration and neurodegeneration in *Npc1*$^{-/-}$ mice [253, 254]. Apoptosis is a pathway that leads to cell death in response to an intrinsic signal such as energy deprivation or oxidative stress or an extrinsic signal such as tumour necrosis factor alpha (TNF-α). Several pro-apoptotic genes are upregulated in 7 to 9-week-old *Npc1*$^{-/-}$ mouse brain and many are involved in the extrinsic TNF-α death pathway [42, 254]. Additionally, inhibition of the TNF-α death pathway with weekly injections of imatinib (an inhibitor of pro-apoptotic protein c-Abl) resulted in delayed neurodegeneration, improvement in neurological symptoms, and increased survival of *Npc1*$^{-/-}$ mice [255]. These findings suggest that the extrinsic apoptotic pathway contributes to neurodegeneration in NPC disease.

Autophagy is a process of catabolic degradation of cellular material during energy deprivation. Under prolonged energy deprivation, autophagy leads to programmed cell death. Several studies have shown increased numbers of autophagic vesicles, upregulation of autophagic protein expression, and increased degradation of long-lived proteins in *Npc1*$^{-/-}$ human and mouse fibroblasts suggesting increased autophagy [253, 256, 257]. Conversely, *Npc1*$^{-/-}$ human stem cells that were differentiated into neurons had a blockage of autophagy, after initial activation leading to a defect in mitochondrial clearance and an accumulation of fragmented mitochondria [258]. Inhibition of autophagy or treatment with cyclodextrin rescued these phenotypes suggesting that autophagy was detrimental for *Npc1*$^{-/-}$ cells [258]. The extent that autophagy plays in *Npc1*$^{-/-}$ brain is unclear. Nevertheless, increased apoptosis and autophagy in *Npc1*$^{-/-}$ cells may be indicative of energy deprivation. In this thesis I investigated energy metabolism and mitochondrial function in *Npc1*$^{-/-}$ cells to determine a potential cause of brain dysfunction and neurodegeneration in NPC disease.

1.5 Conclusion

My research goals were to elucidate mechanisms of cholesterol transport to mitochondria and to characterize the effects of mitochondrial cholesterol accumulation on mitochondrial function and energy metabolism in NPC disease. We detected increased markers of oxidative stress and upregulation of antioxidant defense genes in presymptomatic *Npc1*$^{-/-}$ mouse brain. Moreover, metabolic profiling revealed increased lactate and decreased acetyl-CoA levels in 5-week-old *Npc1*$^{-/-}$ cerebellum and cortex. Furthermore, gene expression analysis indicated that oxidative pyruvate decarboxylation to acetyl-CoA was decreased, glycolysis was increased, and that oxidation of glutamate

was increased in early symptomatic *Npc1*$^{-/-}$ murine brain. Additionally, using NPC1-depleted CHO cells, we determined that NPC2 and MLN64 but not NPC1 were involved in the transport of endosomal cholesterol to mitochondria. By genetic manipulation of the expression of these proteins we showed a relation between mitochondrial cholesterol levels and several mitochondrial functions including increased oxidative stress, increased lactate production, decreased glutamate-dependent mitochondrial oxygen consumption, and decreased ATP transport across the mitochondrial membrane. Together these findings suggest that mitochondrial cholesterol accumulation contributes to mitochondrial dysfunction in NPC disease.

CHAPTER 2 Materials and Methods

2.1 Materials, animals, cell models

2.1.1 Materials

Cell culture media, B27, fetal bovine serum (FBS), and other media supplements were obtained from Life Technologies (Burlington, ON). Poly-D-lysine was obtained from Peptides International (Louisville, KY). [^{3}H]-2-deoxyglucose (2-[1,2-^{3}H(N)]; 1 mCi/ml; 25–50 Ci/mmol) and [7-^{3}H(N)]pregnenolone (1 mCi/ml and 11.5 Ci/mmol) were obtained from Perkin-Elmer (Waltham, MA). Geneticin was from Wisent Bioproducts (St. Bruno, QC). Trilostane and 22R-hydroxycholesterol (22-OH-Chol) were purchased from Steraloids (Newport, RI). Dynabeads M500 Subcellular were purchased from Invitrogen. Short interfering RNA (siRNA) sequences and transfection agent (dharmaFECT 4) were obtained from Thermo Scientific. Human LDL was isolated from EDTA-plasma of apparently healthy, normolipidemic volunteers by KBr density gradient ultracentrifugation [259]. Informed consent was obtained from all human volunteers, and the protocol was approved by the Human Research Ethics Board, Dalhousie University (protocol #2007-1493). Lipoprotein-deficient serum (LPDS) was prepared by density ultracentrifugation from FBS [259]. Other chemicals and buffers were obtained from Sigma (Oakville, ON) or Thermo Fisher Scientific (Ottawa, ON).

2.1.2 Mouse model

BALB/cNctr-Npcm1N/J mice heterozygous for a null mutation in *Npc1* are maintained as in-house breeding colony. Mice were fed a normal chow diet *ad libitum* (Prolab RMH 3000 5P00*, LabDiet). Mice originated from the Jackson Laboratory, Bar

Harbour, ME (stock number 003092). Only wildtype (WT) and mice homozygous for the mutation (*Npc1*$^{-/-}$) were used in this study. All animals were genetically identified by PCR using DNA prepared from ear tissue with primers (Table 2.1) as previously described [40]. Before dissection, mice were deeply anesthetized with halothane (Sigma, St. Louis, MO) and terminated by cervical dislocation. Cerebella, cerebral cortices, and hippocampi were removed rapidly and immediately used or snap-frozen in liquid nitrogen.

2.1.3 Ethics

All procedures were approved by the animal ethics committee of Dalhousie University (protocol numbers # 08-006, #10-102, and #10-030) based on the standards established by the Canadian Council of Animal Care.

2.1.4 Primary neuron and glia cultures

Primary cortical neurons were prepared from embryonic day 17 (E17) wildtype and *Npc1*$^{-/-}$ mice by a method adapted from Hawes et al. [55]. Briefly, murine cerebral cortices were placed in ice-cold Hibernate E medium (BrainBits) with 2% B27 supplement immediately after dissection, and kept at 4°C for not longer than 24 h while embryos were genotyped. WT and *Npc1*$^{-/-}$ cortices were digested with 0.03% trypsin in Hepes buffered saline (HBS, 124 mM NaCl, 3 mM KCl, 5 mM D-glucose, 10 mM Hepes, pH 7.4, 2 mM $CaCl_2$, 1 mM $MgCl_2$) for 9 minutes at 37°C. Dissociated neurons (35000 cells/ml) were plated in serum-free Neurobasal/MEM medium (1:1 v/v) and antibiotics onto dishes coated with 0.1% (w/v) poly-D-lysine and conditioned in Minimum Essential Medium (Invitrogen) medium with 7% FBS. After 3 h, medium was

Table 2.1 Primers for RT-PCR and qPCR

Target gene	Animal	Forward primer (5'→3')	Reverse primer (5'→3')	Annealing temperature (°C)
Actb	Mouse/ human/ hamster	AGCCTTCCTTCTTGGGTATGG	ACACAGAGTACTTGCGCTCAG	54.6
Bcat1	Mouse	ACGTGAAGCCCTGCTAGTGTTAAG	GGCAACAGAAAGGTGGACATAATC	55.5
Bcat2	Mouse	GGCAAGCAACTCCACATACCT	CCGTCACACCCGAAACA	56
Cdh1	Mouse	CACAAGGGCTTCGTGCAG	TCACGGCTACCAGATGACAAC	58.7
Eno1	Mouse	GTACATCACTCCCGACCAGC	CGCAGCCTTGGCAATC	58.6
Eno2	Mouse	AAGCCATCCAAGCGTGCAAGC	CGCCAGTCTTGATCTGGCCTGT	60
G6pd	Mouse	AGCCTCCTACAAGCACCTCA	TGGTTCGACAGTTCATTGGA	55.7
Gad1	Mouse	CTGATTACCTCTACGCCAAG	GTCGCTCAGGGCTATCTG	56.6
Gls1	Mouse	GACAAGATGGGCAACAGTG	CAGTGTATGCGGCAAAC	51.6
Gls2	Mouse	ATATGGAGCAGAAGGACTATGA	TTGAGTCTCAGAGAGCAAGTG	53.4
Glu1	Mouse	TCTCCGCCTCGCTCTCCTGAC	TACGGGTCTTGCAGCGCAGTC	59.8
Glud1	Mouse	CGCCAGCGAGAAGC	AAGTAGAGATCGGGAATAACC	53
Got2	Mouse	GCAGGTAGAGCGGCTGAC	ATGGCATGGGCAAGGTAG	56
Gpt1	Mouse	AGGCCGTAATCCGCTTTGC	TCGCCCATGTAGCCCTTAG	58.2
Gpt2	Mouse	TATGCGTTCCCTCGGATTC	ACTGCCAGGCACGACACAG	58
Hif1a	Mouse	CCTGCGTGCATGTCTAATC	ATGTGCCATGTACCAGAATC	53.2
Hmox1	Mouse	GGCGTCACTTCGTCAGAG	ACTGGAGGAGCGGTGTC	57.1
Hxk1	Mouse	TGGGCACCATGATGACTTGTG	TCGTCCAGACAGCCGTTGTC	57.2
Ldha	Mouse	TGGGAGAACATGGCGACTC	GCACCCGCCTAAGGTTCTTC	58.7
Me1	Mouse	ATTCGAGGCGTTTCGTTG	CTGTTGCGTTACTGGTTGAC	52.9
Me3	Mouse	CATGAGCGCCCTATCGTC	GATCCCACCAGCGATGAC	57.9
Mtco1	Mouse	TGCTAGCCGCAGGCATTAC	GGGTGCCCAAAGAATCAGAAC	60.0
Mtco2	Mouse	GAGTCGTTCTGCCAATAGA	ATGGGCATAAAGCCTATGGT	52.7
Ndu	Mouse	CTTCCCCACTGGCCTCAAG	CCAAAACCCAGTGATCCAGC	60.0
Nfe2l2	Mouse	TTGGCAGGAGCTATTTTCC	GAACAGCGGTAGTATCAGC	50.1
Npc1	Mouse	GGTGCTGGACAGCCAAGTA	GATGGTCTGTTCTCCCATG	53.0
Pcx	Mouse	TGGACGTGGCAGTAGACTC	CATGGTAGCCGTGCAATC	57.7
Pdha	Mouse	CTGGCATAAACCCTACGGAC	CGCCTTTCCCTTTAGCAC	56.4
Pdk1	Mouse	ATACACTGCCAATGATTGAC	GCCATGCCGCTGTAAC	53.1
Pdk2	Mouse	CTGGCTTTGGGTACGGAC	TGGACAGGGCCTTCAGATAG	56.2
Pfkl	Mouse	TTGACTGCAGGACCAATG	CGGTAGACATCACGTAGCTTC	55.4
Pfkm	Mouse	TAAGATGGGTGCTAAGGCTATG	GATCAATCTCGTACTTGGCTAGG	55.3
Pfkp	Mouse	AGCACCGTGTCCATTCGATAG	CTTCAGCTCTGCCACTGGTTG	55
Pkm	Mouse	TGCCGTGACTCGAAATCCC	GGCCAAGTTTACACGAAGGTC	55.0
Ppargc1a	Mouse	ATTGAGAGACCGCTTTGAAG	TCGACCTGCGTAAAGTATATCC	53.4

Target gene	Animal	Forward primer (5'→3')	Reverse primer (5'→3')	Annealing temperature (°C)
Ppia	Mouse/ human/ hamster	TCTTCTTGCTGGTCTTGC CATTCC	TCCAAAGACAGCAGAAAACTTTCG	55
Sod1	Mouse	ATGAAAGCGGTGTGCGTG	TGCTGGCCTTCAGTTAATCC	56.4
Ucp2	Mouse	TCCACGCAGCCTCTACAATG	TGGAAGCGGACCTTTACCAC	60.3
Nfe2l2	Hamster	GCTTCTTTCCATTCCCGAATTAC	TGAGCTGGCTGGCGTCTTC	
Npc2	Hamster	CTCAGGTTGGAATCTCGGC	GTCAGCCTCTTGTCGAGACGGT	
Npc2	human	CGACGGTCCTTTGCGTACCACCGCC CTAGGATAT	GTCTAGCAAAGAGTAGAGACTCTTA AGATAT	58.0

replaced with Neurobasal/MEM without serum. Five days after plating, neurons were treated with 2.5 μM cytosine arabinoside to prevent proliferation of glia. Neurons were cultured for 14–21 days *in vitro* before experiments were conducted. Primary *Npc1*$^{-/-}$ neurons E17 accumulated cholesterol even in cholesterol-free media [86]. *Npc1*$^{-/-}$ neurons were morphologically indistinguishable from wildtype neurons and did not die prematurely [260].

Primary cortical glia were prepared from 1- or 2-day-old WT and *Npc1*$^{-/-}$ mice in a method adapted from Karten et al. [261]. Similar to the neuron preparation, cortices where placed in ice-cold Hibernate E medium with 2% B27 supplement immediately after dissection, and kept at 4°C for not longer than 24 h while tail clippings were genotyped. WT and *Npc1*$^{-/-}$ cortices were digested in PBS (137 mM NaCl, 2.7 mM KCl, 10 mM Na_2HPO_4, 2 mM KH_2PO_4, pH 7.4) containing trypsin (0.1%) and DNase I (0.36 mg/ml) for 15 minutes at 37°C. Additionally, trypsinized tissue was mechanically broken apart by trituration before being added to 10 cm dishes in DMEM 10% FBS. Medium was replaced every three days and glia were subcultured once at a 1:2.5 split ratio after reaching confluency before use for experiments.

2.1.5 CHO, SHSY, HEK cell culture conditions

Wildtype Chinese hamster ovary (CHO) and NPC1-deficient 4-4-19 CHO cell lines were a generous gift from Laura Liscum (Tufts University, Boston, MA). The 4-4-19 cells were originally discovered in a screen for cells unable to mobilize LDL-derived cholesterol from endosomes to plasma membrane and endoplasmic reticulum [262]. Later, 4-4-19 cells were found to express a non-functional NPC1 protein with a point mutation (Gly660Arg) in the sterol-sensing domain (L. Liscum, personal communication

and [263]). CHO and 4-4-19 cells were maintained in Ham's F12 medium (Invitrogen) supplemented with 5% (v/v) FBS, penicillin (100 U/ml), and streptomycin (100 μg/ml) in a humidified atmosphere (5% CO_2) at 37°C. Cells were subcultured every 4 days at a 1:5 split ratio.

Human neuroblastoma SH-SY5Y cells (SHSY) and human embryonic kidney 293T (HEK) cells were cultured in DMEM supplemented with 10% FBS and antibiotics. Cells were maintained in a humidified atmosphere (5% CO_2) at 37°C and subcultured every 4 days at a 1:5 split ratio for continuous growth.

2.2 Molecular Biology

2.2.1 Vectors and vector construction

Generation of pcDNA3.1-F2: The expression vector pcDNA3-F2 encodes a fusion protein (F2) of human CYP11A1 (P450 side chain cleavage complex), ferredoxin reductase, and ferredoxin 1, which together catalyze the conversion of cholesterol to pregnenolone [264, 265]. The vector was a kind gift from Dr. W. L. Miller (University of California, San Francisco, CA). The open reading frame was excised from the pcDNA3 backbone using the restriction enzymes EcoRI and KpnI and inserted into the pcDNA3.1(+) backbone (Life Technologies). Hereafter, cells stably expressing the F2-fusion protein will be designated with the prefix "F2."

NPC2 point mutations: V81A, V81D, and Y119S mutations (corresponding to mutations in V62 and Y100 in mature NPC2, respectively) were introduced into human NPC2 (pYFP-NPC2 vector obtained from Dr. Heiko Runz (University of Heidelberg, Heidelberg, Germany) by an overlap-extension PCR procedure using Platinum® Pfx polymerase (Life Technologies) [266]. These mutations have been described previously

[125, 267]. Briefly, two separate PCR reactions were set up for each target mutation with the human NPC2 as a template. The first PCR reaction used a common forward flanking primer and an upper mutagenesis primer unique for each mutation (Table 2.2). The second PCR reaction used a common reverse flanking primer and a lower mutagenesis primer unique for each mutation (Table 2.2). The two PCR reactions were combined with fresh polymerase and nucleotides for 10 cycles, then forward and reverse flanking primers were added to amplify the full length cDNA with restriction sites and point mutation but without YFP tag. Amplicons were cloned into the BamHI/EcoRI site of pcDNA3.1(+) (Life Technologies). To generate mutant human NPC2 with a linker and flag tag (GSGGSDYKDDDDK) at the C-terminus, NPC2 was amplified using primers (Table 2.2) and cloned into the BamHI/EcoRI restriction sites of pcDNA3.1 (zeocin resistance).

Generation of pLKO-TRC-mCherry: A CMV-mCherry-polyA cassette flanked by EcoRI restriction sites was generated by PCR amplification using pmCherry-C1 (Clontech) as a template and primers (TRC1-F) and (TRC1-R). The unique AgeI restriction site in pmCherry-C1 was destroyed by fill-in and self-ligation prior to the vector being used as template. The amplified CMV-mCherry-polyA cassette was digested with EcoRI and inserted in EcoRI-digested pLKO1-TRC (Addgene 10878) in the forward direction to create pLKO-TRC-mCherry. The BamHI site in pLKO1-TRC was destroyed by fill-in and self-ligation prior to insertion of the cassette.

shRNA sequences: Duplex DNAs encoding shRNA hairpins targeting hamster NPC1, hamster NPC2, or a non-targeting shRNA hairpin (MWG Operon, Huntsville, AL), each with 5'AgeI and 3'MluI overhangs, were created by annealing

Table 2.2 Primers for cloning of vectors

Target	Forward primer	Reverse primer
forward flanking and upper mutagenesis V81A	3'-TATAGGATCCACCATGCGTTTCCTGGCAGC-5'	3'- GGAACTGGGGCGCCCATCAG-5'
forward flanking and upper mutagenesis V81D	3'-TATAGGATCCACCATGCGTTTCCTGGCAGC-5'	3'-GGAACTGGGTCGCCCATCAG-5'
forward flanking and upper mutagenesis Y119S	3'-TATAGGATCCACCATGCGTTTCCTGGCAGC-5'	3'-GAGGGCGATTCGCTTTTCAC-5'
reverse flanking and lower mutagenesis V81A	3'-TATAGAATTCTTAGAGATGAGAAACGATCTG-5'	3'-GCGCCCCAGTTCCCTTTCC-5'
reverse flanking and lower mutagenesis V81D	3'-TATAGAATTCTTAGAGATGAGAAACGATCTG-5'	3'- GCGACCCAGTTCCCTTTCC-5'
reverse flanking and lower mutagenesis Y119S	3'-TATAGAATTCTTAGAGATGAGAAACGATCTG-5'	3'- GTGAAAAGCGAATCGCCCTC-5'
Forward Reverse with FLAG tag	3'-TATAGGATCCCGCCACCATGCGTTTCCTGGCAGC-5'	3'-TATAGAATTCTCACATCTTATCGTCGTCATCCTTGTAATCGCTACCTCCACTTCCGAGATGAGAAACGATCTG-5'
TRC1	5'-TATAGAATTCATACGCGTAATGTATTACCGCCATGCATTAG-3'	5'-TATAGAATTCCGTTAAGATACATTGATGAG-3'
shNT	5'-CCGGGCAACAAGATGAAGAGCACCGACGAGTGCTCTTCATCTTGTTGCTTTTTT-3'	5'-CGCGAAAAAAGCAACAAGATGAAGAGCACTCGTCGGTGCTCTTCATCTTGTTGC-3'
shNPC1- (hamster)	5'-CCGGCGAGTAAGCCGAGCAGAAGACTGCAGTCTTCTGCTCGGCTTACTCGGTTTTT-3'	5'-CGCGAAAAACCGAGTAAGCCGAGCAGAAGACTGCAGTCTTCTGCTCGGCTTACTCGCCGG-3'
shNPC2- (hamster)	5'-CCGGGGTTGTAAGTCTGGAATCAACTGCAGTTGATTCCAGACTTACAACCTTTTTT-3'	5'-CGCGAAAAAAGGTTGTAAGTCTGGAATCAACTGCAGTTGATTCCAGACTTACAACC-3'

oligonucleotides shNPC1-F with shNPC1-R, shNPC2-F with shNPC2-R, and shNT-F with shNT-R, respectively (sequences available in Table 2.2). The duplexes were ligated with AgeI-MluI-digested pLKO1-mCherry vector to create shRNA-expressing plasmids pLKO1-mCherry-shNPC1, pLKO1-mCherry-shNPC2, or pLKO1-mCherry-shNT, respectively.

Generation of pLKO1-NPC2-shNPC2: cDNA sequences encoding FLAG-tagged human $NPC2^{wt}$, $NPC2^{V81D}$, or $NPC2^{Y119S}$ were amplified by PCR using the previously described pcDNA3.1-NPC2 vectors as templates, and primers that introduced an upstream NheI restriction site and a downstream BamHI site. PCR-amplified NPC2 cDNAs were digested with NheI and BamHI and ligated with NheI- and BamHI-digested plasmid pLKO1-mCherry-shNPC2, to create plasmids pLKO1-$NPC2^{wt}$, shNPC2, pLKO1-$NPC2^{V81D}$, shNPC2, and, pLKO1-$NPC2^{Y119S}$ shNPC2-mCherry.

2.2.2 Microporation and stable cell line generation

To generate cell lines stably expressing F2-pcDNA3.1, shNT, or shNPC1 vectors, CHO or SHSY cells were transfected by electroporation according to manufacturer's protocol (Microporator; Life Technologies). Briefly, 1 x 10^5 cells and 0.5 µg DNA were added to 12 µl Buffer R (Life Technologies) and electroporated at 1620 volts for 10 ms three times for CHO cells or 1200 volts for 20 ms three times for SHSY cells. Electroporated cells were plated into a 24 well plate in serum-containing, antibiotic-free medium. Seven day post electroporation cells were selected for survival in 500 µg/ml geneticin or 2 µg/ml puromycin depending on vector following serial dilution. These stable cell lines were maintained in medium containing 300 µg/ml geneticin or 2 µg/ml puromycin.

2.2.3 Lentivirus generation and infection

Stable NPC1-deficient cell lines, and NPC2-deficient cell lines expressing human NPC2 mutants were generated by lentivirus-mediated transduction of wildtype CHO cells with shRNA expression vectors described above.

pLKO.1 (3.3 μg), psPAX2/packaging (2 μg), and pMD.2G/envelope (1 μg) (amounts based on transfection of one 10 cm dish of HEK293T cells) were incubated with polyethyleneimine (PEI, 18 μg/ml) in 1 ml OptiMEM medium. For transfection, the DNA-PEI complex was added to 7 ml serum-free DMEM and incubated with HEK293T cells (grown to 80% confluency on a 10 cm dish) for 6 hours in a humidified atmosphere (5% CO_2) at 37°C. The transfected HEK293T cells were grown in DMEM supplemented with 10% FBS for 24 hours post-transfection. Subsequently, full growth medium was exchanged for viral collection medium (Ham's F12 with 2% FBS) for 24 hours before collection. Virus-containing medium was filtered using a 0.45 sterile μm filter, supplemented with 0.5 μg/ml polybrene to improve infection, and added to 80% confluent CHO cells for 24 hours. Monoclonal colonies were selected for their survival in 3 μg/ml puromycin following serial dilution.

2.2.4 RNA isolation and cDNA synthesis

Total RNA was extracted from snap-frozen brain tissue, primary cells, or CHO cells with Trizol (BioRad, Mississauga, ON). Briefly, tissue or cells were lysed in Trizol: chloroform (5:1 v/v) and centrifuged at 12000 g at 4°C. The resulting aqueous phase was incubated with isopropanol at a 1:1 ratio on ice to precipitate RNA. Precipitated RNA was collected by centrifugation at 12000 g at 4°C, washed in ice-cold ethanol, and

resuspended in water. One µg of RNA was used to prepare cDNA using iScript reverse transcriptase kit (BioRad) according to manufacturer's instructions.

2.2.5 qPCR

Quantitative PCR (qPCR) was performed on 0.66 ng of reverse transcribed RNA using the iSYBR Green Mastermix (BioRad) according to manufacturer's instructions. Specificity of the amplification reaction was tested by melt curve analysis in all cases, and in some cases by agarose gel electrophoresis and sequencing of the amplicon. Data were calculated by the Pfaffl method with cyclophilin (*Ppia*) or β-actin as housekeeping genes and standardized to the wildtype samples of the same age and the same run of the qPCR analysis [268]. *Ppia* and *β-Actin* were not differentially expressed between wildtype and *Npc1*$^{-/-}$ murine brain when calculated relative to each other, and gave similar results when used as housekeeping genes for expression analyses of target genes (Primers are listed in Table 2.1). Murine brain data was derived from 8 to 15 mice of each genotype and age.

2.2.6 PCR of mutant human NPC2

Reverse transcriptase (RT)-PCR was performed on 100 ng of reverse transcribed RNA using Taq recombinant polymerase according to manufacturer's protocol (Life Technologies). Briefly, cDNA was combined with 400 µM of each deoxy nucleotide (dATP, dGTP, dCTP, dTTP), 1.5 mM $MgCl_2$, 300 µM of both forward and reverse primers targeting human *Npc2* or *Ppia* (Primers are listed in table 2.1), 50 U/ml Taq polymerase in PCR buffer (20 mM Tris-HCl pH 8.4, 50 mM KCl). PCR reactions incubated in a thermal cycler for 3 minutes at 94°C, a cycle of 45 s at 94°C, 30 s at the primer specific annealing temperature (annealing temperatures and sequences of primers

are provided in Table 2.1), 1 minute at 72°C repeated 25 times for *Npc2* and 20 times for *Ppia*. The resulting PCR products were separated on a 1.5% agarose gel and visualized with GelRed (Biotium, Hayward, CA). The band density of amplicons was quantified by VersaDoc analyzer (Biorad).

2.2.7 DNA isolation for mtDNA

DNA was isolated from 5-week-old wildtype and *Npc1*$^{-/-}$ cerebellum by phenol-chloroform-isoamyl extraction adapted from Guo et al. [269]. Briefly, mouse brain tissue was homogenized in lysis buffer (10 mM Tris pH 8.0, 1 mM EDTA, 0.1% SDS and protease inhibitors) using a Dounce homogenizer and subsequent incubation with 0.13 mg/ml proteinase K for 3 hours at 55°C. The soluble fraction of lysed brain tissue was mixed with Trizol at 1:1 (v/v) and centrifuged at 12000 g at 4°C. The resulting supernatant was combined with chloroform at 1:1 (v/v) and centrifuged at 12000 g at 4°C. For precipitation of DNA, the supernatant was combined with sodium acetate (3 M) and isopropanol at 1:0.1:1 (v/v), incubated at -20°C for 10 minutes, and centrifuged at 12000 g at 4°C. The resulting DNA pellet was washed in ice-cold ethanol and resuspended in water. The cytochrome *c* oxidase subunit I (*Mtco1*) gene of mitochondrial DNA and the NADH dehydrogenase ubiquinone flavoprotein 1 (*Ndufv1*) gene of nuclear DNA were amplified by qPCR of 0.1 ng DNA using SYBR Green. Primers were first described by Amthor et al. [270] and are listed in Table 2.1. Data were calculated by the Pfaffl method using *Ndufv1* as standard and *Mtco1* as target gene [268]. Data were derived from 10 mice of each genotype.

2.2.8 siRNA transfection

All siRNAs were purchased from Thermo Fisher Scientific. For pre-designed siRNA sequences, the catalog numbers of the Thermo Scientific Dharmacon siRNA are listed (Table 2.3). The MLN64 siGENOME sequences 1 and 3, predesigned against mouse MLN64, were effective against hamster MLN64. Three siRNAs against hamster NPC1 was designed based on NPC1 hamster mRNA sequence. Three siRNA against hamster NPC2 were designed based on the cDNA sequence of hamster NPC2 (siRNA sequences/catalog number are provided in Table 2.3) [267]. We used two different transfection reagents. Initially for all cholesterol transport assays CHO cells were transfected with DharmaFECT 4 (Dharmacon, Lafayette, CO) transfection reagent. For the subsequent energy metabolism, CHO cells were transfected with JetPRIME (Polyplus Transfection, New York, NY) transfection reagent. No difference in transfection efficiency was observed, however, viability was greater in CHO cells transfected with JetPRIME compared to DharmaFECT. Briefly, siRNAs were complexed with a transfection reagent (jetPRIME or DharmaFECT) and added to cells in normal FBS-containing growth medium according to manufacturer's instructions. Unless otherwise indicated, multiple siRNAs were used in combination to effectively deplete target mRNA. To target NPC1, three siRNAs (siNPC) were used at a final concentration of 16.6 nM each; for MLN64, two siRNAs (siMLN64) were used at a final concentration of 25 nM each; for NPC2, three siRNAs (siNPC2) were used at a final concentration of 16.6 nM each; for co-depletion of NPC1 and MLN64, three siRNAs against NPC1 at final concentration of 16.6 nM each and two siRNA against MLN64 at a final concentration of 25 nM each. For non-targeting siRNA, a final concentration of 50 nM was used. Medium containing siRNA complexes was replaced 24 hours post-transfection and all

Table 2.3 siRNAs

Target	Sense (5' to 3')	Product #
hamster NPC1 -1	GGAAAGAGUUCAUG AAAUUUU	
hamster NPC1 -2	GGGAAAGAGUUCAU GAAAUUU	
hamster NPC1 -3	CCGAGUAAGCCGAG CAGAAUU	
MLN64 – 1	CUGCUGAGCUGGUG UAUCAUU	siGENOME duplex (1), D-048833-01
MLN64 – 3	GCGCAGAGACCGAU ACCUGUU	siGENOME duplex (3), D-048833-03
Non-targeting		siCONTROL non-targeting siRNA #1, D-001210-01-05
Hamster NPC2-1	CCUUAAAGCUGGUG GUGAAUU	
Hamster NPC2-2	ACUCAUAAAGGAAG UGAAUUU	
Hamster NPC2-3	GGUUGUAAGUCUGG AAUCAUU	

experiments were completed 72 hours post-transfection. The degree of protein depletion was tested by immunoblotting and qPCR. For cotransfections, 1 ng/µl plasmid DNA was added together with the siRNA complexed with JetPrime according to manufacturer's instructions.

2.3 Isolation of mitochondria

2.3.1 Percoll gradient ultracentrifugation isolation of mitochondria

Cells were harvested into cold mitochondria isolation (MI) buffer (220 mM mannitol, 7 mM sucrose, 20 mM Hepes, pH 7.2, 1 mM EGTA, 0.1% bovine serum albumin (Fraction V, fatty acid free) and protease inhibitors) and ruptured by nitrogen cavitation (1500 psi, 11 min on ice, cell disruption bomb 4639; Parr Instrument Company) in a method adapted from Kristian et al. [271]. Cerebella, cerebral cortices and hippocampi were dissected from 3-, 5-, or 7-week-old wildtype and *Npc1*$^{-/-}$ mice and homogenized together or separately in cold MI buffer. Unbroken cells were removed by centrifugation at 800 g at 4°C for 10 min. Centrifugation of the supernatant for 15 min at 4°C at 12000 g yielded a crude mitochondrial and a cytosolic fraction. Where indicated, crude mitochondria were treated with 0.1% (w/v) trypsin (T9935; Sigma) for 10 min at room temperature followed by addition of soybean trypsin inhibitor (Sigma, 0.5 mg/ml) to neutralize the trypsin. Crude mitochondria were overlaid on 30% (v/v) Percoll in MI buffer and subjected to ultracentrifugation for 30 min at 4°C at 95000 g in an SW61 rotor (Beckman). The mitochondria band was collected, diluted with MI buffer, and subjected to centrifugation at 12000 g at 4°C for 15 min to remove Percoll to yield purified mitochondria. A band visible at lower densities of the Percoll gradient was collected as an endosome/lysosome-enriched fraction. The purity of the fractions was tested by

immunoblotting using antibodies against endosomal and mitochondrial markers, as indicated.

2.3.2 Sucrose gradient mitochondria isolation

Crude mitochondria from 2 WT or *Npc1*$^{-/-}$ murine brains were overlaid on a continuous 20-55% (w/v) sucrose gradient in MI buffer and subjected to centrifugation for 20 hours at 4°C at 95000 g in an SW41 rotor (Beckman). The resulting gradient was collected from the top in 24, 500 µL fractions.

2.3.3 Immunoisolation of mitochondria

A purified mitochondrial fraction was isolated by Percoll gradient ultracentrifugation as described above from 7-week-old WT or *Npc1*$^{-/-}$ murine brain. Mitochondrial fractions (100 µg) were incubated with 4 µg rabbit anti-Tom20 antibodies or unspecific control antibodies (rabbit anti-flag; Sigma F7425) in 800 µl MI buffer at 4°C overnight. Samples were centrifuged at 14000 g for 20 min at 4°C, and the resulting pellets of mitochondria bound to antibodies were washed, resuspended in 300 µl MI buffer, and incubated at 4°C overnight in a total volume of 1 ml with 10^7 Dynabeads M-500 Subcellular (coated with secondary anti-rabbit antibodies according to the manufacturer's protocol). Beads were washed in MI buffer and transferred to a fresh tube prior to elution of bound material (pure mitochondria) into PBS with 0.1% (w/v) SDS. Data were derived from three independent experiments.

2.3.4 Electron microscopy

For electron microscopy, mitochondria bound to beads were resuspended in fixative (2% paraformaldehyde, 1.5% glutaraldehyde, 2.5% sucrose in 0.2 M cacodylate

buffer pH 7.2). Subsequent sample preparation was completed by Mary-Ann Trevors of the electron microscopy CORES facility (Dalhousie University). Images were acquired by a 120 kV JEOL 1230 TEM equipped with a cryo-stage and a 4 megapixel CCD camera at the electron microscopy CORES facility (Dalhousie University).

2.3.5 Synaptic mitochondria isolation

Cerebella, cerebral cortices and hippocampi were dissected from 5-week-old wildtype and *Npc1*$^{-/-}$ mice and homogenized together in cold SH buffer (320 mM sucrose, 20 mM Hepes, pH 7.4). The homogenates were centrifuged at 800 g for 10 min at 4°C to remove unbroken cells and the resulting supernatants were centrifuged at 12000 g for 10 min at 4°C to pellet mitochondria, lysosomes, and synaptosomes. This fraction was then centrifuged over a Percoll step-gradient (23, 10, and 4% Percoll (v/v) in SH buffer) in an SW41 rotor at 57270 g for 13 min at 4°C. The band at the 10/23% interface was collected as synaptosomes. Synaptosomes were then subjected to hypoosmotic shock by incubation in 30 ml of ice cold water for 30 min. After a light homogenization, and addition of Hepes (final concentration = 2.4 mM, pH 7.4), synaptic membranes were isolated by centrifuging the lysed synaptosomes at 12000 g for 15 min at 4°C in a SS34 Sorvall rotor. Synaptic membranes were subjected to ultracentrifugation for 30 min, 4°C at 95000 *g* in an SW61 rotor (Beckman) over a 30% Percoll gradient in MI buffer. The mitochondria band was collected, diluted with MI buffer, and subjected to centrifugation at 12000 *g* at 4°C for 15 min to remove Percoll and yield purified synaptic mitochondria.

2.4 Mitochondrial assays

2.4.1 Cholesterol Mass Assay

Cholesterol was measured with an Amplex Red assay kit (Life Technologies). Mitochondria or endosomes were incubated with reaction mixture (37.5 µg/ml Amplex red, 1 U/ml HRP, 1 U/ml cholesterol oxidase, 0.1 M potassium phosphate pH 7.4, 0.05 M NaCl, 0.1% TritonX-100) for 30 minutes at 37°C. Cholesterol in the sample was oxidized to cholest-4-ene-3-one by cholesterol oxidase in a reaction that also generates hydrogen peroxide at a 1 to 1 molar ratio. Hydrogen peroxide reacts with amplex red in a 1:1 stoichiometry to produce fluorescent resorufin in a reaction catalyzed by horse radish peroxidase (HRP). Resorufin fluorescence was measured at an excitation wavelength of 570 nm and emission wavelength of 585 nm over 15 minutes with one reading every five minutes using a FLUOStar Optima plate reader (BMG Labtech). The average of the three fluorescent reading was calculated and a standard curve of cholesterol was used to determine cholesterol concentration in samples. In the following, all data reported for cholesterol represents unesterified cholesterol because cholesterol esterase was not added.

2.4.2 Glutathione measurement

Glutathione in crude mitochondria or cytosolic fractions isolated from CHO cells or mouse brain tissue was measured using a commercially available kit (Promega GSH-Glo™ Glutathione Assay). This assay is based on the conversion of a luciferin derivative (luciferin-NT, Promega) to luciferin in the presence of glutathione catalyzed by glutathione-S-transferase. Luminescence, generated in a coupled reaction with firefly luciferase, is proportional to the amount of glutathione in each sample. Luminescence was detected by FLUOStar Optima plate reader (BMG Labtech) as the average of three readings over 88 s at 0.8 s integration time. Glutathione was expressed per protein. Total

glutathione was detected by a 30 min preincubation of sample with the reducing agent, 0.5 mM tris (2-carboxyethyl) phosphine (TCEP).

2.4.3 ATP production by isolated mitochondria

ATP production was measured by the luciferase-luciferin method as described [272]. Briefly, mitochondria (100 or 50 µg) were incubated with energy substrates (pyruvate (1 mM), malate (1 mM), glutamate (1 or 5 mM) and/or 5 mM succinate), ATP detection buffer (40 µM luciferin, 1/3000 (v/v) luciferase, Biotium) and ADP (300 or 750 µM) in Tris buffer (150 mM KCl, 25 mM Tris pH 7.4, 2 mM EDTA, 0.1% (w/v) fatty acid free BSA, 10 mM KH_2PO_4, and 0.1 mM $MgCl_2$) at 37°C. Luminescence was measured with a FLUOStar Optima plate reader (BMG Labtech) for 20 readings at one second integration time. The rate of ATP generation was calculated as the luminescence increase during the measurement period of 20 s as luminescence per second per mitochondrial protein, and expressed as a percent of the average of wildtype samples in the same experiment. Addition of NaN_3 (10 mM), rotenone (2 µg/ml), or antimycin A (50 µg/ml) during ATP measurements was used as negative controls.

2.4.4 Hydrogen peroxide production by isolated mitochondria

ROS production was measured by the amplex red method as described by [273]. Briefly, crude mitochondria (100 or 50 µg) were incubated with 5 mM succinate, 300 µM ADP, 50 µM amplex red, 0.1 U/ml HRP in Krebs-Ringer Phosphate buffer (145 mM NaCl, 5.7 mM sodium phosphate pH 7.35, 4.86 mM KCl, 0.54 $CaCl_2$, 1.22 mM $MgSO_4$, 5.5 mM Glucose). H_2O_2 produced by mitochondria reacts with Amplex red to form water and fluorescent resorufin in a reaction catalyzed by HRP. Fluorescence was measured every 2 min for 30 min in a FLUOStar Optima plate reader (BMG Labtech) at 544

nm (excitation) and 590 nm (emission). ROS generation was linear over 30 minutes and was calculated as the fluorescence increase over 30 min and standardized to mitochondrial protein. Fluorescence was only detected in the presence of energy metabolites and ADP.

2.4.5 Nonyl acridine orange fluorescence in isolated mitochondria

To verify mitochondrial polarization, an aliquot of each mitochondrial preparation was incubated with 2 μM nonyl acridine orange in MI buffer (Biotium, Hayward, CA) for 30 min at 37°C. Mitochondria were washed by centrifugation at 12000 g at 4°C twice. Fluorescence was measured at 488/520 nm excitation/emission and standardized to mitochondrial protein.

2.5 Protein and Metabolite analysis

2.5.1 Immunoblot blot analysis

Snap-frozen tissue was homogenized in ice-cold HEPES buffer (10 mM HEPES, 1 mM EDTA, 1 mM EGTA, 1% Triton X-100, 0.5% Nonidet 40), with freshly added protease inhibitors (5 μg/ml leupeptin, 5 μg/ml aprotinin, 50 μM PMSF and 1 μM pepstatin) and phosphatase inhibitors (2 mM ortho-vanadate and 1 mM sodium fluoride) using a motor-driven pestle, followed by slow trituration through a syringe fitted with a 26 gauge needle. Cell lysates were prepared in 0.1% SDS in PBS with protease and phosphatase inhibitors. Protein content was determined by a bicinchoninic acid-based photometric assay (Thermo Fisher Scientific). Proteins were separated by sodium dodecyl sulfate polyacrylamide gel electrophoresis (SDS-PAGE) and transferred to polyvinylidene fluoride membranes. For detection of nitrotyrosine, lysates were directly added to nitrocellulose membranes by slot-blotting. Membranes were blocked in 5%

(w/v) skim milk powder for most antibodies, 2% (w/v) bovine serum albumin (BSA) for detection of NPC2 (because of the presence of NPC2 in milk [116]) or 2% (w/v) polyvinylpyrrolidone and phosphatase inhibitors for detection of anti-phospho antibodies in Tris buffered saline with 5% (v/v) Tween (TTBS, pH 7.4). Primary antibodies used in this study are listed in Table 2.4. Secondary horseradish peroxidase (HRP)-conjugated donkey anti-rabbit, anti-mouse, anti-chicken, or anti-goat antibodies (Jackson Immunoresearch, West Grove, PA) were diluted 1:10000 in TTBS, and detected by enhanced chemiluminescence (Roche). Actin or tubulin were used as a loading control. Imaging and analysis of band density was performed by VersaDoc imaging (BioRAD). Unless otherwise indicated, immunoblot of murine brain proteins was performed with samples from at least 6 mice of each genotype and age.

2.5.2 NMR Spectrum deconvolution

Metabolites were extracted for ^{1}H-NMR spectroscopy essentially as described [274]. Briefly, tissues were mixed with methanol to a final methanol/water ratio of 3.2:1 (v/v) and homogenized via ultra-sonication in a FastPrep®-24 instrument for 40 seconds at 6 m/s (MP Biomedicals Inc., Solon, OH). Homogenates were extracted with chloroform and water in a final chloroform/methanol/water ratio of 1:1:0.81 (v/v). Aqueous extracts were dried under nitrogen, re-dissolved in 700 µL of phosphate buffer (1 mM NaH_2PO_4, pH 7.2) with 172.2 mg/mL of sodium 3-trimethylsilyl-2,2,3,3-d_4-propionate (TMSP, Cambridge Isotope Laboratories, Andover, MA) in D_2O as internal reference standard, and stored in liquid nitrogen until analysis. 1D-^{1}H-NMR spectra were

Table 2.4 Antibodies

Target	**Company (catalog #)**
ACC	Cell Signaling (3676)
Actin	Santa Cruz Biotechnology (sc1616)
Alpha Tubulin	Sigma (T 6074)
AMPK alpha	Cell Signaling (2603)
AMPK beta ½	Cell Signaling (4150)
Cytochrome c Oxygenase	Molecular Probes (A6403)
GLUT1	Santa Cruz Biotechnology (sc-7903)
Hexokinase 1 (Hxk1)	Santa Cruz (sc46695)
JNK	Cell Signaling (9252)
KGDH	Santa Cruz Biotechnology (sc-49589)
Lamp1	Abcam (ab24170)
MLN64	Affinity Bioreagents (PA1-562) or Abcam (ab3478)
Nitrotyrosine (Ntyr)	StressMarq (SMC-154 C/D)
NPC1	Novus Biologicals (NB400-148)
NPC2	gift from Peter Lobel, Rutgers University, Piscataway, NJ
pACC	Cell Signaling (3661)
pAMPK alpha (Thr172)	Cell Signaling (2535)
pAMPK beta (Ser108)	Cell Signaling (4181)
Phosphofructokinase P (PFK-P)	Santa Cruz Biotechnology (sc130227)
Phosphorylated JNK (Thr183/Tyr185)	Cell Signaling (9255)
Phosphorylated PDH E1α (Ser232)	Calbiochem (AP1063)
Pregnenolone	MP Biomedical (07172016)
Protein disulphide isomerase	Assay Designs (1D3)
Pyruvate dehydrogenase E1α (PDH)	Cell Signaling (2784)
Pyruvate kinase M1/2 (PKM1/2)	Cell Signaling (3190)
Pyruvate kinase M2 (PKM2)	Cell Signaling (3198)
Superoxide oxide dismutase 2 (SOD2)	Novus Biologicals (NB100-1992)
Tom20	Santa Cruz Biotechnologies (sc-11415)
VDAC1	Abcam (ab15895)

acquired using a 5 mm TCI CryoProbe™ (Bruker Biospin) on a Bruker Avance III spectrometer (Bruker Biospin) operating at 700 MHz proton resonance frequency [275].

Samples were added to 5 mm NMR sample tubes in a SampleJetTM sample changer (Bruker Biospin, Fällanden, Switzerland) pre-chilled SampleJetTM to 4°C. In automation, each sample was pre-warmed to 298.2 K for 5 min before acquisition of 1D-^{1}H-NMR spectra at 25°C using a 5 mm TCI CryoProbe™ (Bruker Biospin) with automatic tuning and matching and a z-axis gradient amplifier and digital lock on a Bruker Avance III spectrometer (Bruker Biospin) operating at 700 MHz proton resonance frequency. Tuning and matching to 50 Ω resistive impedance as well as shimming was applied under automation to each sample while the receiver gain was held constant for all samples. 1D ^{1}HNMR spectra were acquired using a 12 μs (90°) pulse calibrated in automation using the pulsecal macro, 10 kHz spectral width and a 2 s relaxation delay with residual water presaturation (PS) using a continuous wave irradiation attenuation of 60 dB during the relaxation delay, with 128 transients and 8 dummy scans collected into 32k data points. These were later zero-filled to 64k 2 and an exponential line-broadening of 0.3 Hz applied before Fourier transformation. Following manual zero- and first-order phasing, as well as manual baseline correction using TopSpinTM 2.1 (Bruker Biospin) the resulting spectra were calibrated (TMSP at $\delta = 0.0$ ppm), also using TopSpinTM 2.1, before being exported to MATLAB 7.1 (MathWorks®, Natick, MA) using ProMetab 1.0 software 26 for further processing. Data were derived from 6 to 13 mice of each genotype and each age.

2.5.3 HPLC measurement of free amino acids

Aqueous extracts were prepared from brain tissue by homogenization of tissue/water/methanol mixtures in a final methanol/water ratio of 3.2:1 (v/v) via ultra-sonication in a FastPrep®-24 instrument (MP Biomedicals Inc., Solon, OH), followed by extraction with chloroform and water in a final chloroform/methanol/water ratio of 1:1:0.81 [274]. Amino acids were analyzed in the Advanced Protein Technology Centre of the Sick Kids Hospital, Toronto, ON. Briefly, aqueous extracts were treated with trichloroacetic acid to remove residual proteins, and free amino acids were analyzed by reverse-phase high performance liquid chromatography with UV-detection of the absorption at 254 nm following pre-column derivatization with phenyl isothiocyanate at room temperature. Data were derived from 6 to 9 mice of each genotype and each age.

2.6 Immunostaining and cellular functional assays

2.6.1 Filipin stain

Cells cultured on glass coverslips were fixed and stained with 50 μg/ml filipin in PBS to visualize unesterified cholesterol as described [260]. Briefly, cells were fixed in 4% (w/v) paraformaldehyde in PBS, stained with 50 μg/ml Filipin III complex (Sigma), mounted in AquaMount (Thermo Fisher Scientific), and images were acquired on a Nikon TE2000 epifluorescence microscope with CCD camera at filter settings of 387/11 nm (excitation) and 447/60 nm (emission) using a 20× objective.

2.6.2 ROS assay cells

Cellular reactive oxygen species (ROS) production was measured using an Amplex-Red based fluorometric assay (Life Technologies). Briefly, cells were grown in a 96-well clear bottom plate, washed with glucose-free HBS and incubated at 37°C in 200

µl reaction mix (HBS with 2.5 mM glucose, 12.5 µg/ml Amplex Red, 0.3 U/ml horseradish peroxidase (HRP)). HRP catalyzes the conversion of hydrogen peroxide and Amplex red to water and fluorescent resorufin [276]. Fluorescence was measured every 2 min for 30 min in a FLUOStar Optima plate reader (BMG Labtech) at 544 nm (excitation) and 590 nm (emission). ROS generation was calculated as the fluorescence increase over 30 min and standardized to cell protein.

2.6.3 Lactate production cells

Primary cells, SHSY, and CHO cells were washed and incubated in glucose-free HBS for 30 min, followed by a 30 min incubation in phenol-red-free DMEM without glucose, pyruvate, or glutamine, but supplemented with the indicated metabolites (incubation medium). Incubation medium was collected after 30 min. The lactate assay was adapted from [277]. Briefly, 50 µl incubation medium were added to a reaction mix (2 mM NAD^+, 48 µM resazurin, 1 U/ml diaphorase, and 18.5 U/ml L-lactate dehydrogenase) in Tris buffer (75 mM Tris/HCl pH 8.9, 100 mM KCl, 0.0004% TritonX-100) for 30 min. Lactate in the incubation medium is converted with added NAD^+ to pyruvate and NADH by lactate dehydrogenase. NADH is measured in a diaphorase catalyzed reaction of NADH + H^+ + resazurin (blue fluorescence) to NAD^+ + resorufin (red fluorescence). Fluorescence was measured at 544/590 nm (excitation/emission) and lactate concentrations were calculated based on a calibration curve on the same assay plate. Cellular protein was collected into 0.1% (w/v) SDS/PBS containing protease and phosphatase inhibitors, and determined with the BCA assay. Data are derived from triplicate incubations in at least 4 independent experiments.

2.6.4 2-Deoxyglucose uptake

For measurement of glucose uptake, neurons were incubated with osmolarity-adjusted HEPES-buffered saline (10 mM HEPES, 124 mM NaCl, 3 mM KCl, 2 mM $CaCl_2$, 1 mM $MgCl_2$; osmolarity 270 to 290 mOsm), containing 2 mM glucose and 2 µCi/ml (0.08 mM) [^{3}H]-deoxyglucose for 30 min. CHO cells were incubated with 2-[1,2-^{3}H(N)]-deoxyglucose (2 µCi, 0.08 mM) in incubation medium (described above) for 30 min after 30 min pre-incubated in glucose-free HBS. Cell-associated radioactivity was determined by scintillation counting and standardized to cellular protein. Data were derived from three independent experiments in triplicate for CHO cells or three independent experiments in duplicate for primary neurons.

2.6.5 ATP levels in cells

SHSY or CHO cells were scraped into ice-cold PBS (200 µl/24 well plate well), and total cellular ATP was immediately measured using the ATP-GloTM bioluminometric assay kit according to manufacturer's protocol (Biotium, Hayward, CA). Briefly, 100 µl of cells in PBS were lysed in detergent-containing ATP-Glo assay buffer leading to conversion of ATP and added D-luciferin (0.4 mg/ml) to AMP, oxidized luciferin, and light by *Firefly* luciferase (Biotium, unknown concentration). Light/luminescence was measured with a FLUOStar Optima plate reader (BMG Labtech) for 20 readings at one second integration time. The rate of ATP generation was calculated as the luminescence increase during the measurement period of 20 s as luminescence per second per cellular protein, and expressed as a percent of the average of control samples of the same experiment. Data were derived from at least three independent experiments in triplicate.

2.6.6 Pregnenolone Radioimmunoassay

Pregnenolone generation by adherent F2-CHO cells: Forty-eight hours post siRNA transfection, F2-CHO cells were washed twice in phenol red-free, serum-free Ham's F12/DMEM (1:1, v/v) (import medium) and incubated for 24 hours in import medium containing 10 μM trilostane. Trilostane (10 μM) was added during all incubations for pregnenolone measurement to inhibit to inhibit 3 β-hydroxysteroid dehydrogenase, which catalyzes the conversion of pregnenolone to downstream steroids [278]. In experiments to determine the maximum rate of pregnenolone formation, 5 μM 22-OH-Cholesterol was added to the import medium.

Pregnenolone generation by F2-CHO and CHO cell homogenates: CHO and F2-CHO cells were harvested into PBS and homogenized in 1 ml ice-cold MI buffer with 30 strokes in a Dounce homogenizer. Cell homogenates were centrifuged at 800 g, 4°C for 5 min to remove nuclei and unbroken cells, followed by centrifugation of the supernatant at 12000 g, 4°C for 15 min to yield crude mitochondria. Samples were used immediately. CYP11A1 activity was determined essentially as described [279]. Cell homogenates, crude mitochondria, or the 12000 g supernatant (cytosol) were incubated for 1 h at 37°C in reaction buffer (250 mM sucrose, 20 mM KCl, 15 mM Tris-EDTA-HCl, 10 mM KH_2PO_4, and 5 mM $MgCl_2$, pH 7.2) with 2 mM NADPH, 2 mM malate/pyruvate, 5 μM 22-OH-Cholesterol, 10 μM trilostane, 0.3% (v/v) Tween, and an NADPH regenerating system (BD Biosciences). Data were derived from quadruplicate measurements.

Radioimmunoassay (RIA): Reaction mixtures or import medium were assayed for pregnenolone by radioimmunoassay (RIA) according to the protocol provided by MP Biomedicals (Solon, OH). Briefly, reaction mixtures or import medium were incubated with anti-pregnenolone antibody (1:810)(MP Biomedicals #07172016) and with ^{3}H-

radiolabelled pregnenolone (100 dpm/µl, 10000 dpm/166.6 bq pregnenolone total per reaction) in 700 µl phosphate buffer (60 mM sodium phosphate dibasic, 40 mM sodium phosphate monobasic pH 7.0, 15 mM sodium azide, 155 mM sodium chloride, 0.2% gelatin) for 24 h at 4°C. After antibody incubation, each reaction was incubated with 200 µl of charcoal-dextran (6.88 mg/ml) for 30 min on ice and centrifuged at 2000 rpm at 4°C for 15 min. The resulting supernatants were transferred into scintillation vials along with 4 mL of EcoLite, vortexed, and the radioactivity was determined with a preset time of 5 min. Each assay included a standard curve of known amounts of pregnenolone and a positive control of import medium with trilostane spiked with 300 pg pregnenolone to test recovery. A negative control of import medium (containing trilostane) that was not incubated with cells was routinely included but did not give readings above background.

2.6.7 Cholesterol ester formation

Cholesterol transport to the endoplasmic reticulum was measured as the incorporation of radiolabeled [^{3}H]oleate into cholesterol esters in the presence of FBS [280, 281]. CHO cells cultured overnight in LPDS containing medium were incubated for 4 h in medium containing FBS and [^{3}H]oleate complexed to BSA. Cellular lipids were extracted with hexane/isopropanol (3:2, v/v), dried under nitrogen, separated by thin-layer chromatography, and [^{3}H]oleate incorporation into cholesterol esters and triglycerides was quantified by scintillation counting. Data are derived from two independent experiments in triplicate.

2.6.8 Oxygen consumption analysis by Seahorse bioanalyzer

Three days after transfection with siRNA against NPC1 or MLN64 or with a mixture of siRNAs against both proteins, CHO cells were plated in XF96 polystyrene cell

culture microplates (Seahorse Bioscience) at a density of 35000 cells/well. After an overnight incubation, cells were washed and pre-incubated for 30 min in unbuffered XF assay medium (Seahorse Bioscience, 100965-000) with or without glutamine [2 mM] supplemented with 5.5 mM D-glucose and 1 mM sodium pyruvate at 37 °C in a non-CO_2 environment. Oxygen consumption rates (OCR) were measured every 7 min using an XF96 extracellular flux analyzer (Seahorse Bioscience) during consecutive addition of 1 μM oligomycin, 2 μM carbonyl cyanide *p*-trifluoromethoxy-phenylhydrazone (FCCP) and 2.5 μM antimycin A.

2.6.9 ATP FRET sensors

CHO cells stably expressing non-targeting shRNA or shRNA targeting NPC1 were transiently transfected with the fluorescence resonance energy transfer (FRET)-based ATP indicator mtAT1.03 [282]. The sensor was excited at 430 nm using a high-speed polychromator system VisiChrome (Visitron Systems, Puchheim, Germany) and emission was measured at 535 and 480 nm (Versatile Filter Wheel Systems, Visitron Systems), to measure FRET-dependent and cyan fluorescent protein (CFP)-dependent fluorescence, respectively, as previously described [283]. Data were derived from three independent experiments.

2.7 Statistics

For comparison of two groups, student's two-tailed t-test was used. For comparison of three or more groups, significance was calculated using ANOVA. Significance was assumed for $p < 0.05$. The Shapiro-Wilk test was used to verify the normality of the distribution of all qPCR murine brain data sets [284]. All *Npc1*$^{-/-}$ and

age-matched wildtype control data sets satisfied the conditions of a normal data distribution according to the Shapiro-Wilk Test for thresholds $p = 0.01$, $p = 0.05$ and $p = 0.1$, with the exception of the qPCR analysis of mRNA levels of *Gfap*. A student's two-tailed t-test was used for the comparison of normally distributed data from *Npc1*$^{-/-}$ and age-matched wildtype control, and the Mann-Whitney U test was used for the comparison of mRNA levels of *Gfap*. Statistical significance was assumed as $p<0.05$.

CHAPTER 3 Results

3.1 Mitochondrial dysfunction in *Npc1*$^{-/-}$ murine brain

With the exception of some preliminary data or data not published, the work in chapter 3.1 was published in PLoS One. 2013 Dec 18;8(12):e82685 [285]. In addition to myself, Dr. Barbara Karten, Debra Fice, Tiffany Mailman, Nicole Marnet, and Veronique LeBlanc contributed to the work presented. I was involved in the conceptualization of all data and performed the experiments in figures 3.02, 3.03 A, 3.04, 3.05, and 3.06 B.

Several studies have shown increased markers of oxidative stress in 7-week-old *Npc1*$^{-/-}$ mice, which is indicative of mitochondrial dysfunction [144, 241, 244-249]. Whether mitochondrial dysfunction occurred early in NPC disease progression and which aspects of mitochondrial function are altered was unclear. Hence, we performed an extensive characterization of mitochondrial function at different disease stages [presymptomatic (3 weeks), early (5 weeks), and late symptomatic (7 weeks)] in *Npc1*$^{-/-}$ mouse brain regions.

3.1.1 Oxidative stress in presymptomatic *Npc1*$^{-/-}$ mouse brain

Mitochondrial dysfunction leads to oxidative stress; a late stage marker of oxidative damage is the nitration of tyrosine residues in proteins (nitrotyrosine). Immunoreactivity of nitrotyrosine was increased in 7-week-old *Npc1*$^{-/-}$ cortex and cerebellum compared to wildtype, suggesting that oxidative damage occurred at least during late stages of NPC disease (Figure 3.01 A).

To determine whether oxidative stress occurred at presymptomatic ages we measured oxidative stress-regulated gene expression. One gene that is activated by mild

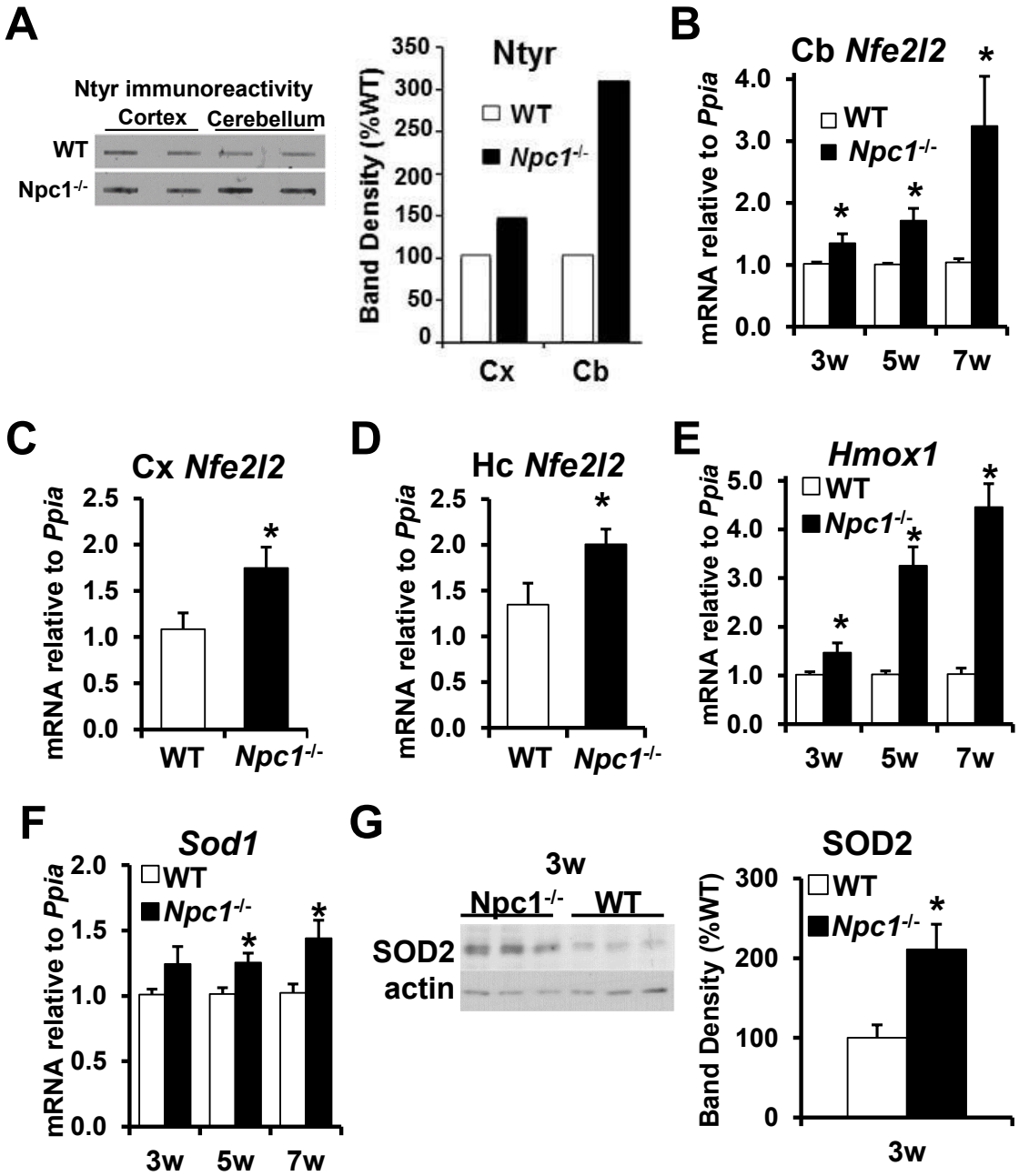
A
Ntyr immunoreactivity
Cortex
Cerebellum
WT
Npc1-/-
Ntyr
WT
Npc1-/-
Band Density (%WT)
350
300
250
200
150
100
50
0
Cx
Cb
B
Cb Nfe2l2
mRNA relative to Ppia
4.0
3.0
2.0
1.0
0.0
3w
5w
7w
C
Cx Nfe2l2
mRNA relative to Ppia
2.5
2.0
1.5
1.0
0.5
0.0
WT
Npc1-/-
D
Hc Nfe2l2
mRNA relative to Ppia
E
Hmox1
mRNA relative to Ppia
5.0
F
Sod1
mRNA relative to Ppia
G
3w
Npc1-/-
WT
SOD2
actin
SOD2
Band Density (%WT)
300
200
100
0

Figure 3.01 Increased oxidative stress and upregulation of genes involved in the antioxidant defense system in *Npc1*$^{-/-}$ brain

A) Slot blot analysis of cerebellum (Cb) and cortex (Cx) homogenates from 7-week-old WT and *Npc1*$^{-/-}$ mice using antibodies against nitrotyrosine (Ntyr). Bar graphs show band intensity of nitrotyrosine expressed as percent WT. B, E, F) Cerebellar RNA was prepared from 3-, 5-, and 7-week-old mice. C) Cerebral cortex RNA was prepared from 5-week-old mice. D) Hippocampal (HC) RNA was prepared from 5-week-old mice. B-F) Target gene mRNA levels were analyzed by qPCR using primers against Nuclear factor (erythroid-derived 2)-like 2 (*Nfe2l2*), heme oxygenase 1 (*Hmox1*), and superoxide dismutase 1 (*Sod1*), standardized to cyclophilin (*Ppia*). G) Immunoblot analysis of tissue homogenates of cerebellum from 3-week-old WT and *Npc1*$^{-/-}$ mice using antibodies against superoxide dismutase 2 (SOD2) and actin as a loading control. Bar graphs show the ratio of band intensity of SOD2 to actin expressed as percent WT. All bar graphs show the mean ± SEM. * $p<0.05$, *Npc1*$^{-/-}$ vs. WT.

increases in oxidative stress is the antioxidant transcription factor nuclear factor erythroid 2-related factor (*Nfe2l2*, protein name is Nrf2) [286]. Increased *Nfe2l2* expression in 3-, 5-, 7-week-old *Npc1*$^{-/-}$ cerebellum, 5 week *Npc1*$^{-/-}$ cortex, and 5 week *Npc1*$^{-/-}$ hippocampus suggested that oxidative stress increased before onset of symptoms in all brain regions measured (Figure 3.01 B-D). Nrf2 increases the expression of several antioxidant proteins including: heme oxygenase 1 (HO-1, gene is *Hmox1*), cytosolic copper-zinc superoxide dismutase (SOD1), and mitochondrial manganese superoxide dismutase (SOD2) [287, 288]. HO-1 breaks down heme, forming the potential radical scavenger bilirubin, while SOD1 and SOD2 detoxify superoxide to hydrogen peroxide and water. Consistent with increased *Nfe2l2* expression, *Hmox1* and *Sod1* mRNA levels were increased at all ages and SOD2 protein levels were increased at 3 weeks in *Npc1*$^{-/-}$ cerebellum (Figure 3.01 E-G).

Jun-N-terminal kinase (JNK) is activated by phosphorylation; JNK phosphorylation is regulated by JNK phosphatases. JNK phosphatases are inhibited by oxidative stress; therefore, in conditions of high oxidative stress JNK will be phosphorylated/activated [289-291]. Additionally, JNK is activated by the MAP kinase cell signaling cascade, which is also activated by oxidative stress [292]. Consistent with high oxidative stress, JNK phosphorylation was increased in 3- and 5-week-old *Npc1*$^{-/-}$ cerebellum (Figure 3.02 A). Another mechanism to decrease electron flux is by disruption of the mitochondrial proton gradient through the action of uncoupling proteins. Uncoupling protein 2 (*Ucp2*) mRNA increased progressively with age in *Npc1*$^{-/-}$ cerebellum (Figure 3.02 B). Altogether, these results suggest that oxidative

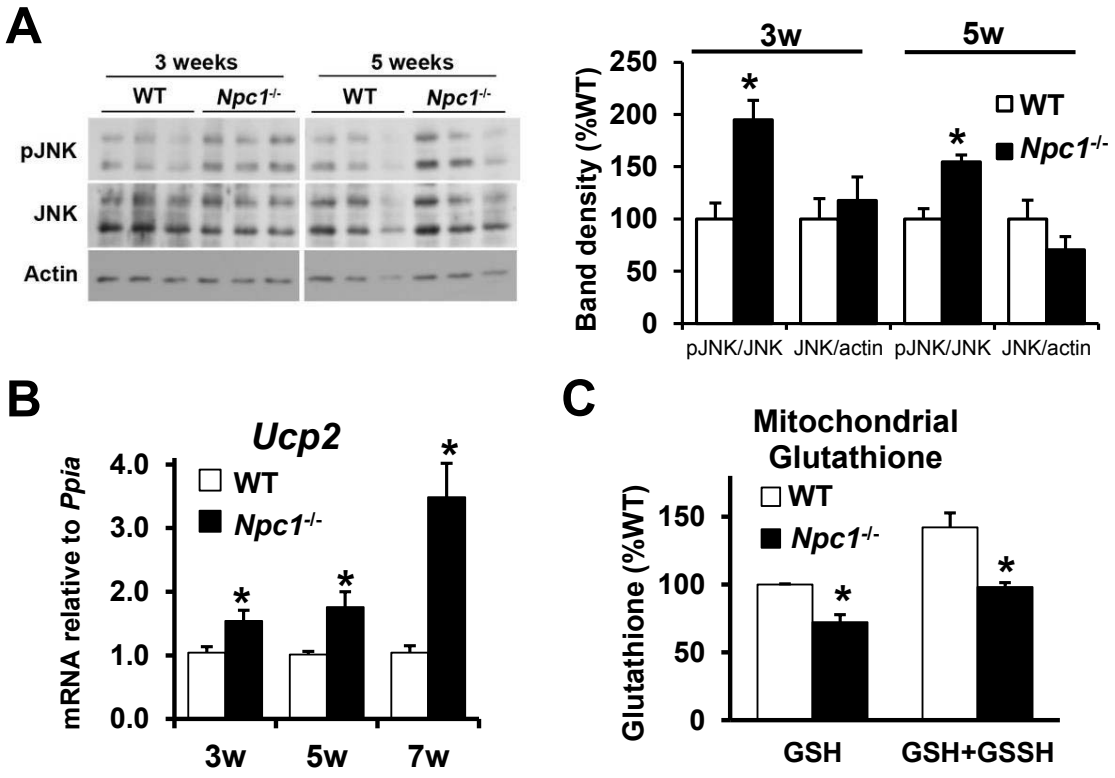

Figure 3.02 Increased phosphorylation of JNK and upregulation of UCP2 in *Npc1*$^{-/-}$ cerebellum

A) Immunoblot analysis of tissue homogenates of cerebellum from 3-, and 5- week-old WT and *Npc1*$^{-/-}$ mice using antibodies against phosphorylated c-Jun N-terminal kinase (pJNK), c-Jun N-terminal kinase (JNK), and actin as a loading control. Bar graphs show the ratio of band intensity of pJNK or JNK to actin expressed as percent WT. B) Cerebellar RNA was prepared from 3-, 5-, and 7-week-old mice. Target gene mRNA levels were analyzed by qPCR using primers against uncoupling protein 2 (*Ucp2*) standardized to *Ppia*. C) Reduced (GSH) and total (GSH+GSSH) glutathione levels in mitochondria isolated from 7-week-old WT and *Npc1*$^{-/-}$ murine brain expressed as percent WT. All bar graphs show the mean ± SEM. * $p<0.05$, *Npc1*$^{-/-}$ vs. WT.

A common contributor of increased oxidative stress are a defects in the antioxidant defense systems. One major cellular antioxidant is glutathione which is synthesized in the cytosol and imported into mitochondria [236-238]. In preliminary work (2 independent experiments) I detected decreased total and reduced glutathione levels in mitochondria isolated from 7-week-old *Npc1*$^{-/-}$ whole mouse brain (Figure 3.02 C). Whether decreased mitochondrial glutathione levels are responsible for increased oxidative stress in *Npc1*$^{-/-}$mouse brain will require further investigation.

3.1.2 Decreased levels of mitochondrial DNA and increased expression of the mitochondrial biogenesis regulator PGC1alpha in *Npc1*$^{-/-}$ cerebellum

We measured two consequences of oxidative stress in NPC disease, one being the levels of mitochondrial DNA (mtDNA) and the other being mRNA levels of proliferator-activated receptor gamma coactivator-1 alpha (*Ppargc1a*, protein is PGC1alpha) a gene involved in mitochondrial biogenesis. An essential component of mitochondria is mtDNA, which contains 37 genes that encode 13 mitochondrial protein all involved in the electron transport chain [293]. Each mitochondrion maintains 2-10 copies of mtDNA [294]. The copy number of mtDNA is decreased by oxidative stress by mutation of the D-loop, a mtDNA sequence involved in the initiation of replication [295-297]. Measurement of the ratio of mtDNA to nuclear DNA by qPCR revealed a two-fold decrease in mtDNA levels in 5-week-old *Npc1*$^{-/-}$ cerebellum (Figure 3.03 A). Consistent with the decreased mtDNA levels, 5- and 7-week-old *Npc1*$^{-/-}$ cerebellum had decreased mRNA levels of the mtDNA encoded cytochrome c oxygenase subunit 2 (mtCOX2) (Figure 3.03 B).

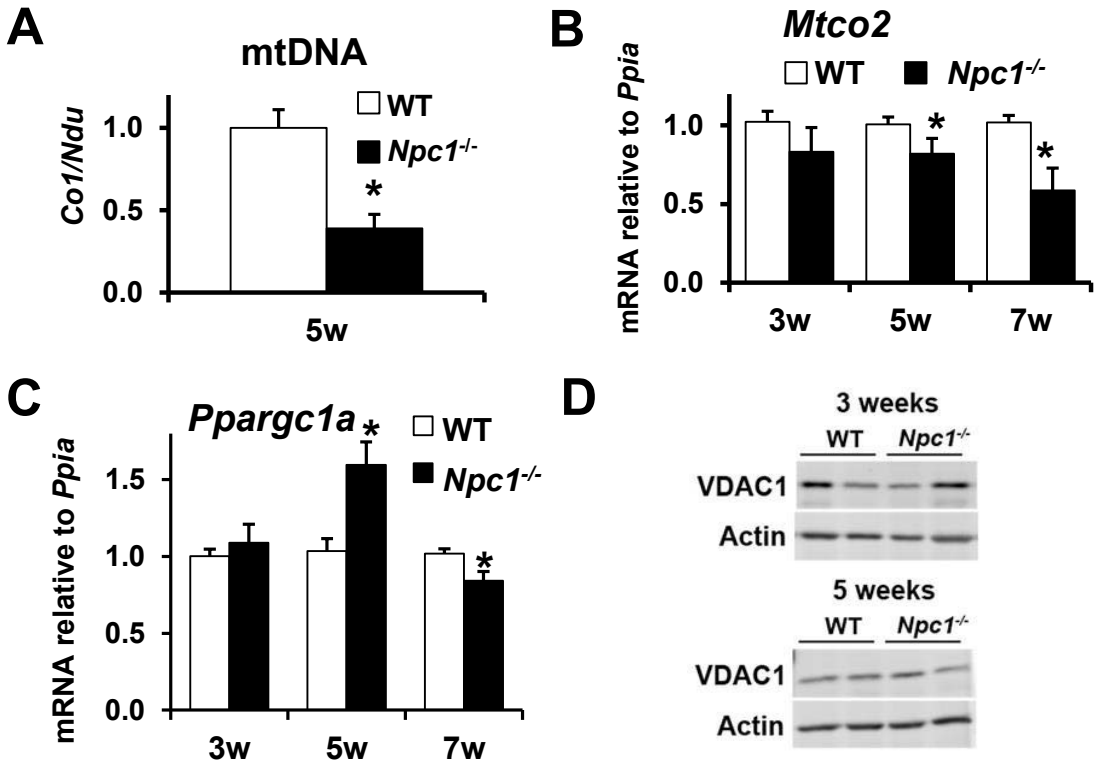

Figure 3.03 Decreased mitochondrial DNA and altered expression of mitochondrial biogenesis gene in *Npc1*$^{-/-}$ cerebellum

A) Cerebella DNA was prepared from 5-week-old mice. Target gene levels were analyzed by qPCR using primers against mtDNA-encoded cytochrome c oxidase subunit 1 (*Co1*) standardized to nuclear-encoded NADH dehydrogenase ubiquinone (*Ndu*). Data expressed as ratio of *Co1* per *Ndu*. B, C) Cerebellar RNA was prepared from 3-, 5-, and 7-week-old mice. Target gene mRNA levels were analyzed by qPCR using primers against mitochondrial cytochrome c oxidase subunit II (*MtCo2*), peroxisome proliferator-activated receptor gamma coactivator 1 alpha (*Ppargc1a*) standardized to *Ppia*. D) Immunoblot of tissue homogenates of cerebellum from 3-, and 5- week-old WT and *Npc1*$^{-/-}$ mice using antibodies against voltage-dependent anion channel (VDAC) and actin as a loading control. All bar graphs show the mean ± SEM. * $p<0.05$, *Npc1*$^{-/-}$ vs. WT.

The major regulator of mitochondrial biogenesis is PGC1alpha [298]. *Ppargc1a* mRNA was unchanged at 3 weeks, markedly increased at 5 weeks, and decreased at 7 weeks in *Npc1*$^{-/-}$ cerebellum (Figure 3.03 B). Although increased PGC1alpha expression suggested increased mitochondrial biogenesis at 5 weeks of age, we detected no change in mitochondrial voltage dependent anion channel 1 (VDAC1) protein levels per actin between *Npc1*$^{-/-}$ and wildtype cerebellum at 3 or 5 weeks of age indicating mitochondrial mass was unchanged (Figure 3.03 D). Together these results suggested a similar number of mitochondria per cell, however, these mitochondria have decreased mtDNA and that there was an initiation of mitochondrial biogenesis at 5 weeks in *Npc1*$^{-/-}$ cerebellum.

3.1.3 ROS production and ATP generation by mitochondria isolated from *Npc1*$^{-/-}$ mouse brain

To explore mitochondrial function in *Npc1*$^{-/-}$ mouse brain I measured reactive oxygen species (ROS) and ATP generation by isolated mitochondria in the presence of various energy metabolites. Even though nitrotyrosine modification had indicated greater oxidative damage there was no difference in the rate of H_2O_2 production per mitochondrial protein by mitochondria isolated from 3- or 7-week-old wildtype and *Npc1*$^{-/-}$ total brain in the presence of succinate as an energy source suggesting that ROS was not increased or that antioxidant enzymes masked increased ROS production (Figure 3.04 A, B). Succinate is oxidized directly in the electron transport chain through complex II and unlike pyruvate, had no antioxidant side effects. The rate of hydrogen peroxide production by isolated mitochondria was constant over 30 minutes indicating viability of the mitochondria over time. Additionally, the rate of hydrogen peroxide production by mitochondria isolated from WT of *Npc1*$^{-/-}$ brain was increased 20-40 fold by inhibition of

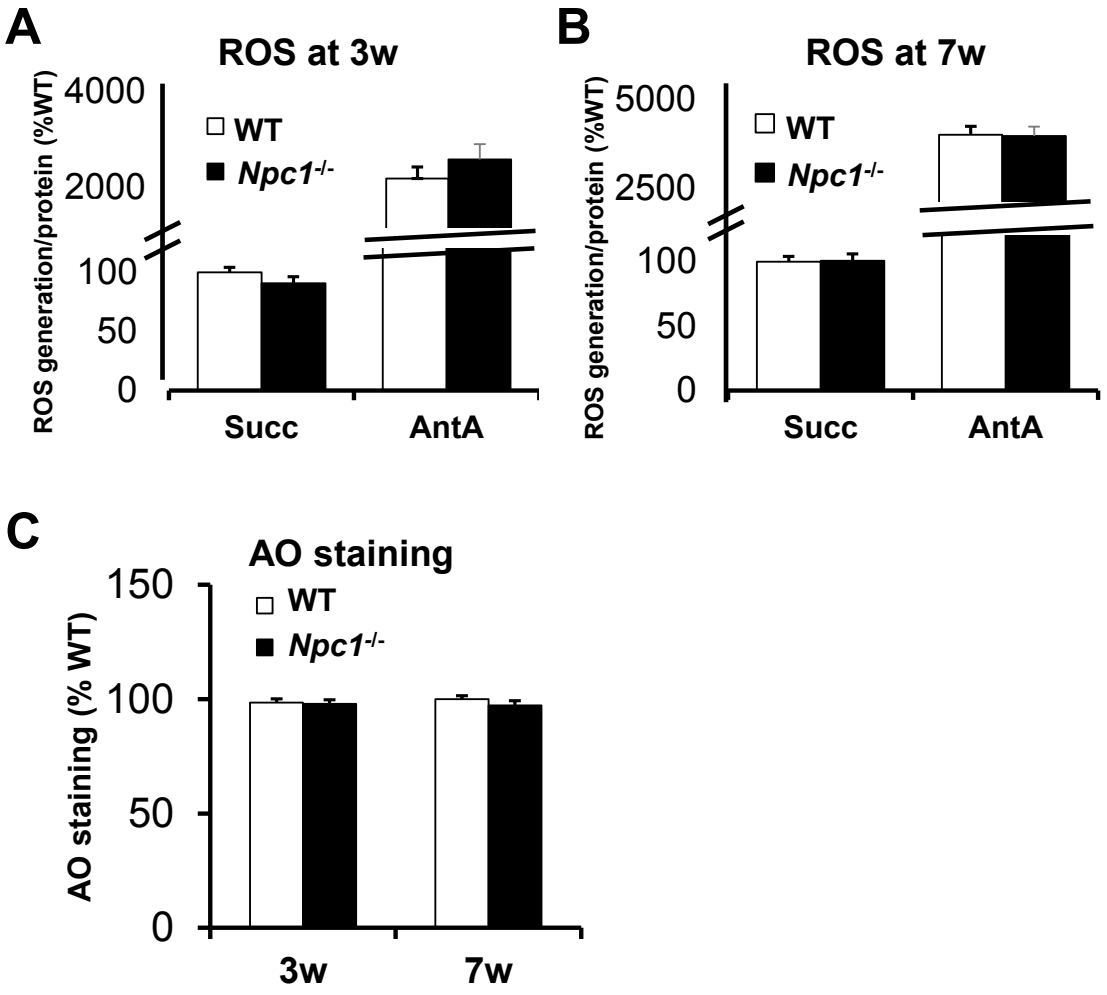

Figure 3.04 Normal ROS generation by mitochondria isolated from *Npc1*$^{-/-}$ mouse brain

A-C) Mitochondria were isolated by differential centrifugation from combined homogenates of the cerebella, hippocampi, and cerebral cortices of 3-, or 7-week-old WT and *Npc1*$^{-/-}$ mice. A, B) The rate of ROS generation was measured in the presence of 5 mM succinate (Succ) and ADP (300 μM) as fluorescence generated by amplex red reaction as fluorescence unit per second per protein. Antimycin A (AntA) was used as positive control. C) Mitochondria were stained with nonyl acridine orange (AO) to determine mitochondrial mass per sample. Data are expressed as percent of WT of the same experiment, and are derived from three independent experiments each with two independent preparations of each genotype and each age. All bar graphs show the mean ± SEM. * $p<0.05$, *Npc1*$^{-/-}$ vs. WT.

complex III with antimycin A and was prevented by the antioxidant N-acetylcysteine (NAC). Nonyl acridine orange fluorescence was similar, indicating that there were no differences in mitochondrial mass between genotypes (Figure 3.04 C).

Another measure of mitochondrial function is the production of ATP from ADP by ATP synthase, which requires numerous steps including the oxidation of energy metabolites, electron transport chain activity, ADP/ATP exchange, and ATP synthase activity. Mitochondria isolated from 3-week-old *Npc1*$^{-/-}$ whole brains produced less ATP in the presence of pyruvate and malate as energy sources (Figure 3.05 A). In the presence of succinate, there was no difference in the rate of ATP production, suggesting that the electron transport chain downstream of complex II functioned normally (Figure 3.05 A). The rate of ATP production was similar between mitochondria isolated from 7-week-old *Npc1*$^{-/-}$ and wildtype whole brains in the presence of either pyruvate/malate or succinate (Figure 3.05 B). To test whether normalization of ATP production at 7 weeks was due to isolation from whole brain I measured ATP from mitochondria isolated from 7-week-old cerebellum or cortex. Mitochondria isolated from 7-week-old wildtype or *Npc1*$^{-/-}$ cerebellum or cortex produced ATP at similar rates to wildtype in the presence of ADP, pyruvate, malate, and/or glutamate (Figure 3.05 C, D). Pyruvate is oxidized through conversion to acetyl-CoA by pyruvate dehydrogenase and subsequent conversion with oxaloacetate (generated from malate mediated by malate dehydrogenase) to citrate mediated by citrate synthase. Glutamate is oxidized through conversion to alpha-ketoglutarate. Further work is required to determine in which brain region the defect in ATP generation at 3 weeks of age was the strongest, and to determine why at 7 weeks of age the mitochondria displayed normal function. Complex I inhibitor rotenone (2 μg/ml)

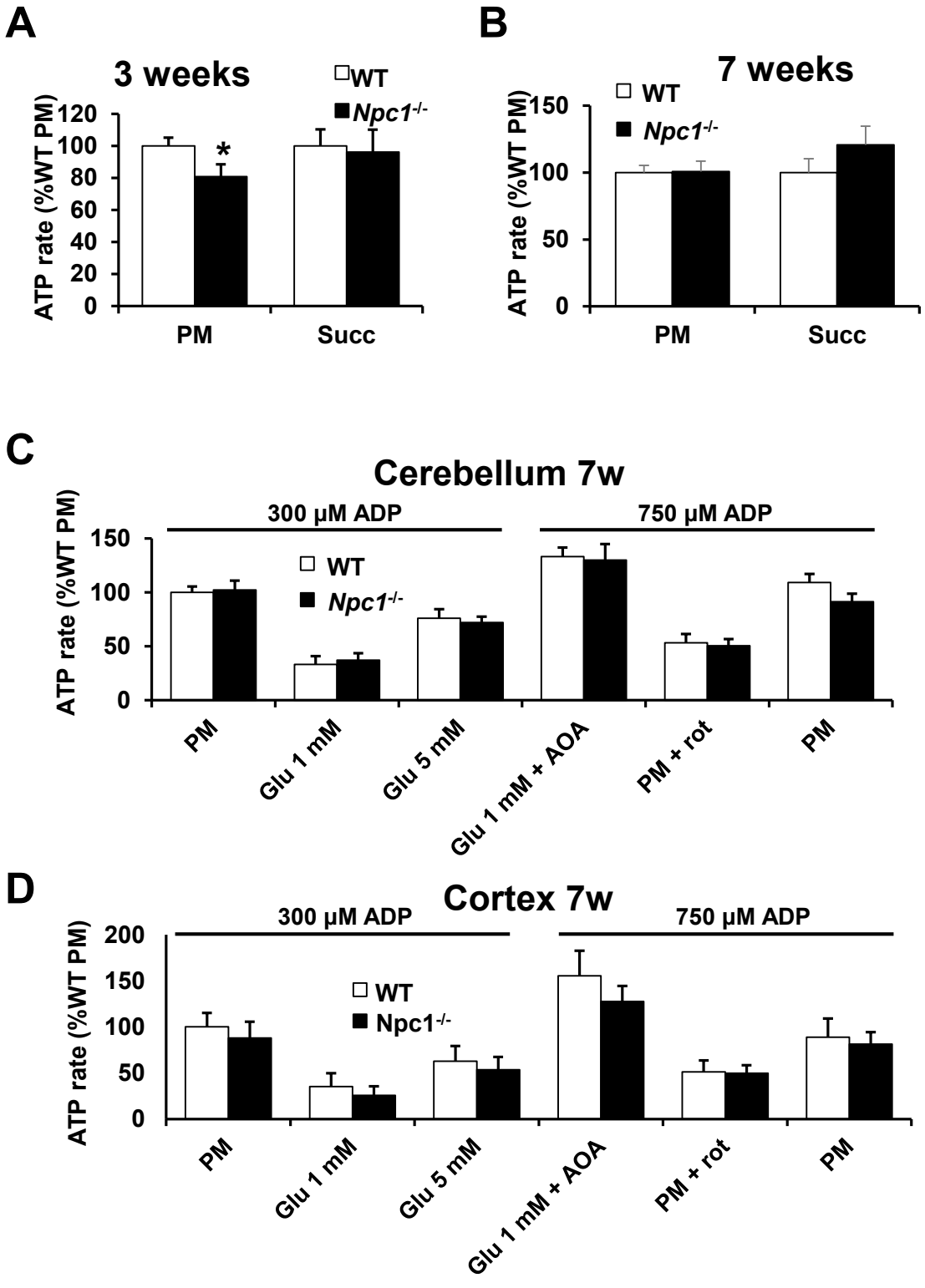
A
3 weeks
WT
Npc1-/-
ATP rate (%WT PM)
120
100
80
60
40
20
0
*
PM
Succ
B
7 weeks
WT
Npc1-/-
ATP rate (%WT PM)
150
100
50
0
PM
Succ
C
Cerebellum 7w
300 µM ADP
750 µM ADP
WT
Npc1-/-
ATP rate (%WT PM)
150
100
50
0
PM
Glu 1 mM
Glu 5 mM
Glu 1 mM + AOA
PM + rot
PM
D
Cortex 7w
300 µM ADP
750 µM ADP
WT
Npc1-/-
ATP rate (%WT PM)
200
150
100
50
0
PM
Glu 1 mM
Glu 5 mM
Glu 1 mM + AOA
PM + rot
PM

Figure 3.05 ATP generation by mitochondria isolated from *Npc1*$^{-/-}$ brain
A-D) Mitochondria were isolated by differential centrifugation from whole brain (A-B) of 3-, or 7-week-old WT and *Npc1*$^{-/-}$ mice, cerebellum (C) or cerebral cortices (D) of 7-week-old WT and *Npc1*$^{-/-}$ mice. The rate of ATP generation was measured in the presence of 1 mM pyruvate and 1 mM malate (PM), 1 or 5 mM glutamate (Glu), or 5 mM succinate (Succ) and 300 or 750 µM ADP as luminescence generated by the ATP-dependent D-luciferin/luciferase reaction per second per protein. Data are expressed as percent of WT in presence of PM of the same experiment, and are derived from three independent experiments each with two independent mitochondria preparations of each genotype and each age. All bar graphs show the mean ± SEM. * $p<0.05$, *Npc1*$^{-/-}$ vs. WT.

in the presence of pyruvate/malate, complex IV inhibitor sodium azide (NaN_3, 10 mM) in the presence of succinate, and the malate aspartate shuttle inhibitor aminooxyacetate (AOA, 0.5 mM) in the presence of glutamate all inhibited ATP generation.

3.1.4 Increased phosphorylation of pyruvate dehydrogenase in *Npc1*$^{-/-}$ cerebellum

To investigate the defect in pyruvate/malate oxidation by mitochondria isolated from 3-week-old *Npc1*$^{-/-}$ brain we analyzed the expression and phosphorylation/inhibition of pyruvate dehydrogenase (PDH, gene is *Pdha*). Consistent with a defect in pyruvate oxidation, *Npc1*$^{-/-}$ cerebellum had decreased *Pdha* mRNA and protein levels at 3 and 5 weeks, respectively (Figure 3.06 A, B). PDH is phosphorylated and inhibited by pyruvate dehydrogenase kinases (PDK1 and PDK2) or JNK [299, 300]. The ratio of phosphorylated PDH per total PDH protein levels was increased in 5-week-old *Npc1*$^{-/-}$ cerebellum, supporting the hypothesis that PDH was inhibited (Figure 3.06 B). Increased *Pdk1* and *Pdk2* mRNA levels at 5 weeks of age in *Npc1*$^{-/-}$ cerebellum coincided with increased phosphorylation of PDH (Figure 3.06 C, D). *Pdk1* and *Pdk2* mRNA levels were unchanged at 3 and 7 weeks in *Npc1*$^{-/-}$ cerebellum. Together these results suggested decreased conversion of pyruvate to acetyl-CoA at 5 weeks in *Npc1*$^{-/-}$ cerebellum. Given that *Pdk1* and *Pdk2* are predominantly expressed in neurons and astrocytes, respectively, it is likely that PDH inhibition occurred in both cell types in *Npc1*$^{-/-}$ cerebellum [194].

Additionally, I measured protein levels of alpha-ketoglutarate dehydrogenase (KGDH), which catalyzes the conversion of alpha-ketoglutarate to succinyl-CoA. I investigated KGDH because it is particularly sensitive to oxidative stress [301-303]. Five-week-old *Npc1*$^{-/-}$ cerebellum had similar protein levels of KGDH compared to

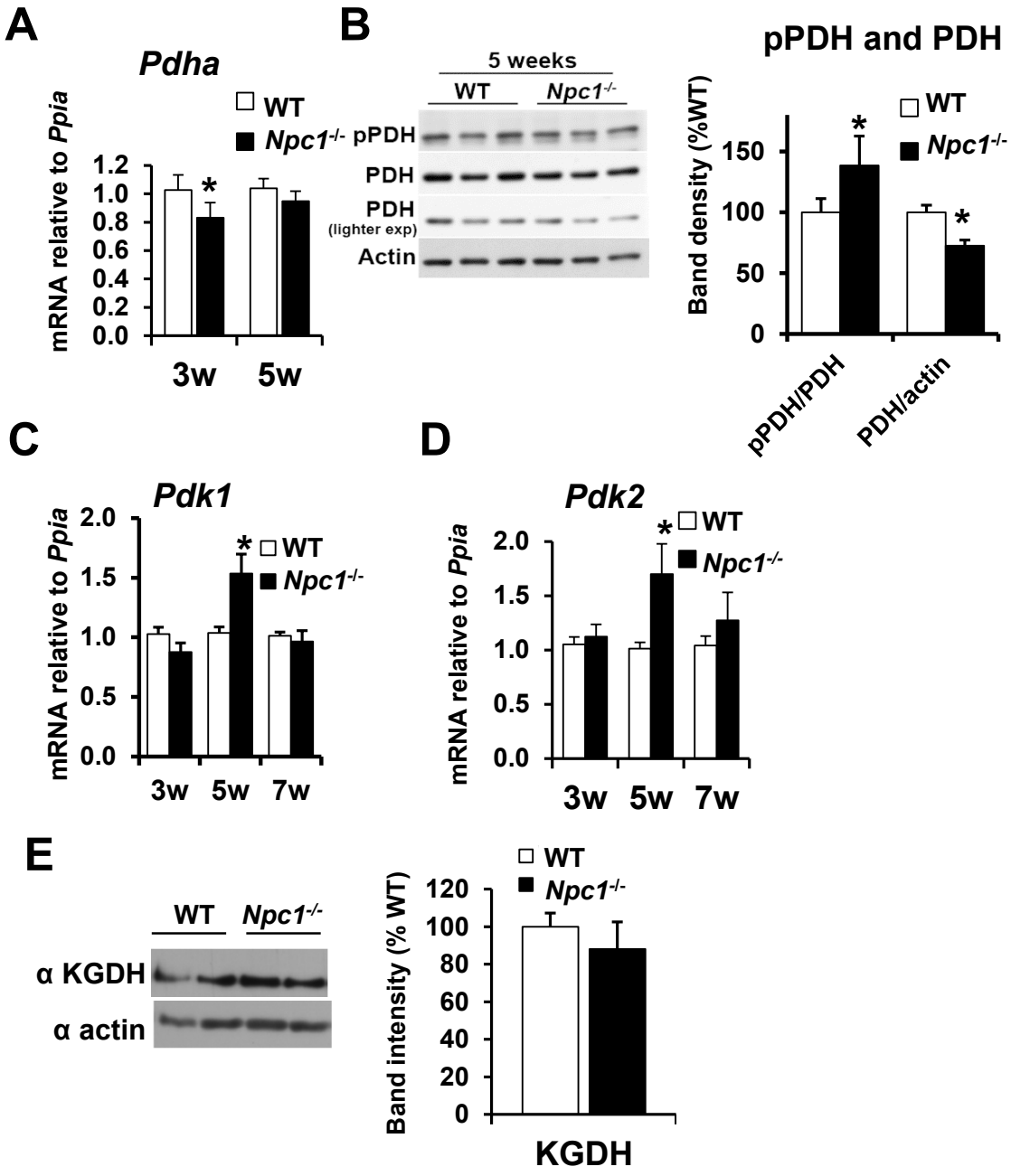
A
Pdha
WT
Npc1-/-
mRNA relative to Ppia
1.2
1.0
0.8
0.6
0.4
0.2
0.0
*
3w
5w
B
5 weeks
WT
Npc1-/-
pPDH
PDH
PDH
(lighter exp)
Actin
pPDH and PDH
WT
Npc1-/-
Band density (%WT)
150
100
50
0
*
*
pPDH/PDH
PDH/actin
C
Pdk1
mRNA relative to Ppia
2.0
1.5
1.0
0.5
0.0
*
WT
Npc1-/-
3w
5w
7w
D
Pdk2
mRNA relative to Ppia
2.0
1.5
1.0
0.5
0.0
*
WT
Npc1-/-
3w
5w
7w
E
WT
Npc1-/-
α KGDH
α actin
Band intensity (% WT)
120
100
80
60
40
20
0
WT
Npc1-/-
KGDH

Figure 3.06 Increased phosphorylation of PDH in *Npc1*$^{-/-}$ cerebellum.
A, C, D) Cerebellar RNA was prepared from 3-, 5-, and/or 7-week-old mice. Target gene mRNA levels were analyzed by qPCR using primers against pyruvate dehydrogenase (*Pdha*), pyruvate dehydrogenase kinases 1 (*Pdk1*), and 2 (*Pdk2*) standardized to *Ppia*. B, E) Immunoblot analysis of tissue homogenates of cerebellum from 5- week-old WT and *Npc1*$^{-/-}$ mice using antibodies against phosphorylated pyruvate dehydrogenase (pPDH), pyruvate dehydrogenase (PDH), α ketoglutarate dehydrogenase (KGDH), and actin as a loading control. Bar graphs show the ratio of band intensity of pPDH to PDH or PDH to actin expressed as percent WT. All bar graphs show the mean ± SEM. * $p<0.05$, *Npc1*$^{-/-}$ vs. WT.

wildtype suggesting that protein levels were not affected by oxidative stress (Figure 3.06 E). However, whether oxidative stress decreased KGDH function either through oxidation of the cofactor thiamine or modification of KGDH would require further investigation.

3.2 Glucose and glutamate metabolism in *Npc1*$^{-/-}$ murine brain and cultured cells

With the exception of some preliminary data or data not published, the work in chapter 3.2 was published in PLoS One. 2013 Dec 18;8(12):e82685 [285]. In addition to myself, Dr. Barbara Karten, Dr. Tobias Karakach, Ian Burton, Debra Fice, Tiffany Mailman, Nicole Marnet, and Veronique LeBlanc contributed to the work presented. I was involved in the conceptualization of all data and the NMR sample preparation and deconvolution (Figures 3.07-3.10) and performed the experiments in figures 3.12 A, D, G, 3.13 D, 3.15, 3.16, 3.20, 3.21, 3.24 A, 3.25, 3.26, 3.27B, and part of figure 3.18.

The results above suggested mitochondrial dysfunction and decreased pyruvate oxidation in *Npc1*$^{-/-}$ murine cerebellum. To further explore energy metabolism and to determine other pathways that may be affected in *Npc1*$^{-/-}$ mice we characterized metabolite levels and mRNA and protein levels of several key proteins involved in glycolysis and amino acid metabolism.

3.2.1 Metabolomics analysis of *Npc1*$^{-/-}$ brain

To identify altered energy metabolic pathways we conducted an unbiased metabolomics analysis on *Npc1*$^{-/-}$ brains regions in collaboration with Dr. Tobias Karakach (Nation research council, Halifax, Nova Scotia). Aqueous extracts of 3-, 5-, and 7-week-old cerebellum, cortex, and hippocampus were analyzed using proton NMR

spectroscopy. Figure 3.07 shows a typical proton NMR spectrum from this analysis. Principle component analysis performed by Dr. Karakach revealed significant differences between wildtype and *Npc1*$^{-/-}$ cerebellum beginning at 4 weeks of age [285]. Deconvolution and integration to quantify individual metabolites revealed differences in the levels of several metabolites even at 3 weeks of age, when the overall pattern was not statistically different. Lactate levels were increased in 3-, 5-, and 7-week-old *Npc1*$^{-/-}$ cerebellum compared to wildtype (Figure 3.08). The chemical shift of the $-CH_3$ group of both acetate and acetyl-CoA overlap at 1.92 ppm and therefore cannot be distinguished in the NMR spectrum. Acetate/acetyl-CoA levels were decreased at 3 and 7 weeks in *Npc1*$^{-/-}$ cerebellum (Figure 3.08). The increased lactate levels and decreased acetate/acetyl-CoA levels were consistent with decreased PDH activity in *Npc1*$^{-/-}$ cerebellum. Furthermore, increased alanine levels in 7-week-old *Npc1*$^{-/-}$ cerebellum suggested increased conversion of pyruvate to alanine by transamination at this age (Figure 3.08).

Similar changes as in *Npc1*$^{-/-}$ cerebellum were observed in *Npc1*$^{-/-}$ murine cortex including increased lactate levels at 3, 5, and 7 weeks of age; decreased acetate/acetyl-CoA levels at 3 and 7 weeks of age; increased alanine levels at 5 weeks of age (Figure 3.09). Conversely, in *Npc1*$^{-/-}$ hippocampus, lactate and alanine levels did not change compared to wildtype at 3 and 5 weeks (Figure 3.10). Surprisingly, even though lactate levels were normal, acetate/acetyl-CoA levels were decreased in both 3- and 5-week-old *Npc1*$^{-/-}$ hippocampus (Figure 3.10).

The levels of the neurotransmitter glutamate and of glutamine were similar between wildtype and *Npc1*$^{-/-}$ cerebellum at all ages (Figure 3.08). However, the levels of gamma-aminobutyric acid (GABA), an inhibitory neurotransmitter and downstream

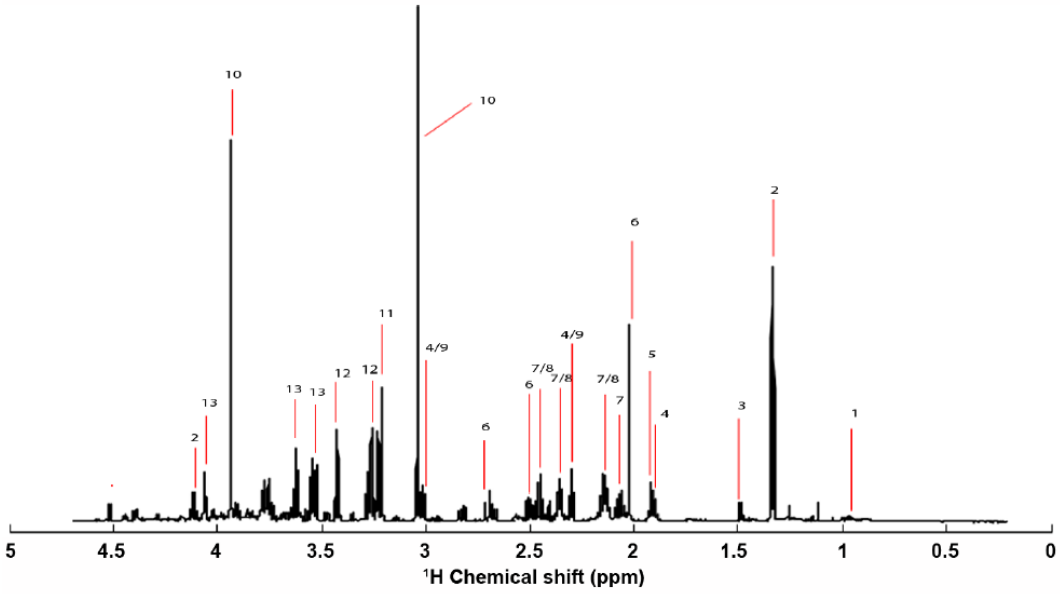

Figure 3.07 Sample ^{1}H NMR spectrum of wildtype murine cerebellum
^{1}H-NMR spectroscopy of aqueous extracts from WT cerebellum. Peaks: 1) Branched chain amino and ketoacids, 2) Lactate, 3) Alanine, 4) GABA, 5) Acetate/acetyl-CoA, 6) NAA, 7) Glutamate, 8) Glutamine, 9) α-ketoglutarate, 10) Creatine, 11) Choline, 12) Taurine, and 13) myo-Inositol.

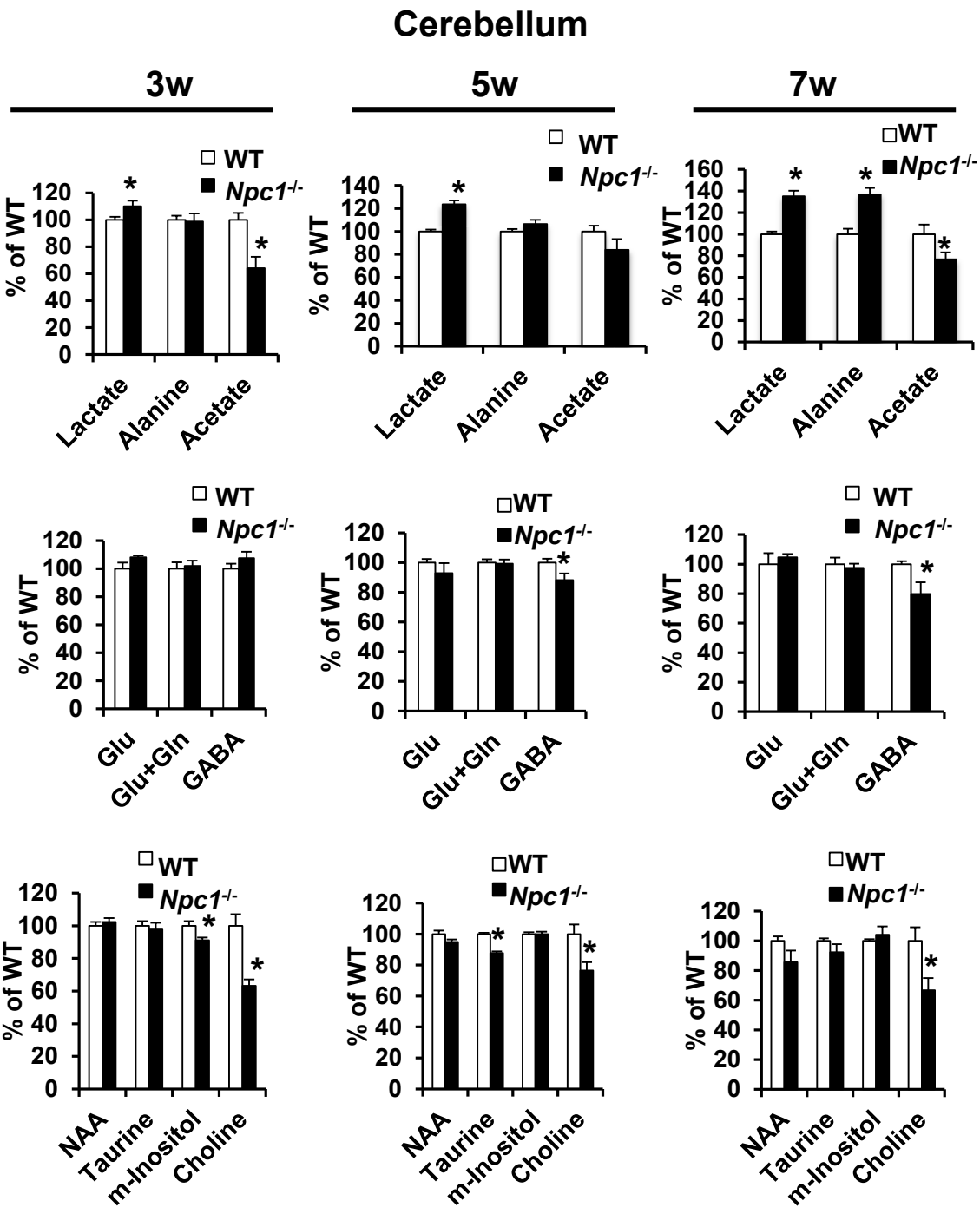
Cerebellum
3w
5w
7w
WT
Npc1-/-
% of WT
Lactate
Alanine
Acetate
Glu
Glu+Gln
GABA
NAA
Taurine
m-Inositol
Choline

Figure 3.08 Altered energy metabolite levels in *Npc1*$^{-/-}$cerebellum
Aqueous extracts of the cerebella from 3-, 5-, or 7-week-old wildtype (WT) and *Npc1*$^{-/-}$ mice were analyzed by ^{1}H-NMR spectroscopy. Spectra were deconvolved and integrated. Peak areas were standardized to total peak area. Glu: glutamate, Glu+Gln: glutamate and glutamine summed together, GABA: gamma-aminobutyric acid, NAA: N-acetylaspartate, m-Inositol: myo-Inositol. Graphs in each column show data from the same set of WT and *Npc1*$^{-/-}$ mice of one age. Data are expressed as percent of the average of WT samples of the same age. Shown are the mean ± SEM. * $p<0.05$, *Npc1*$^{-/-}$ vs. WT.

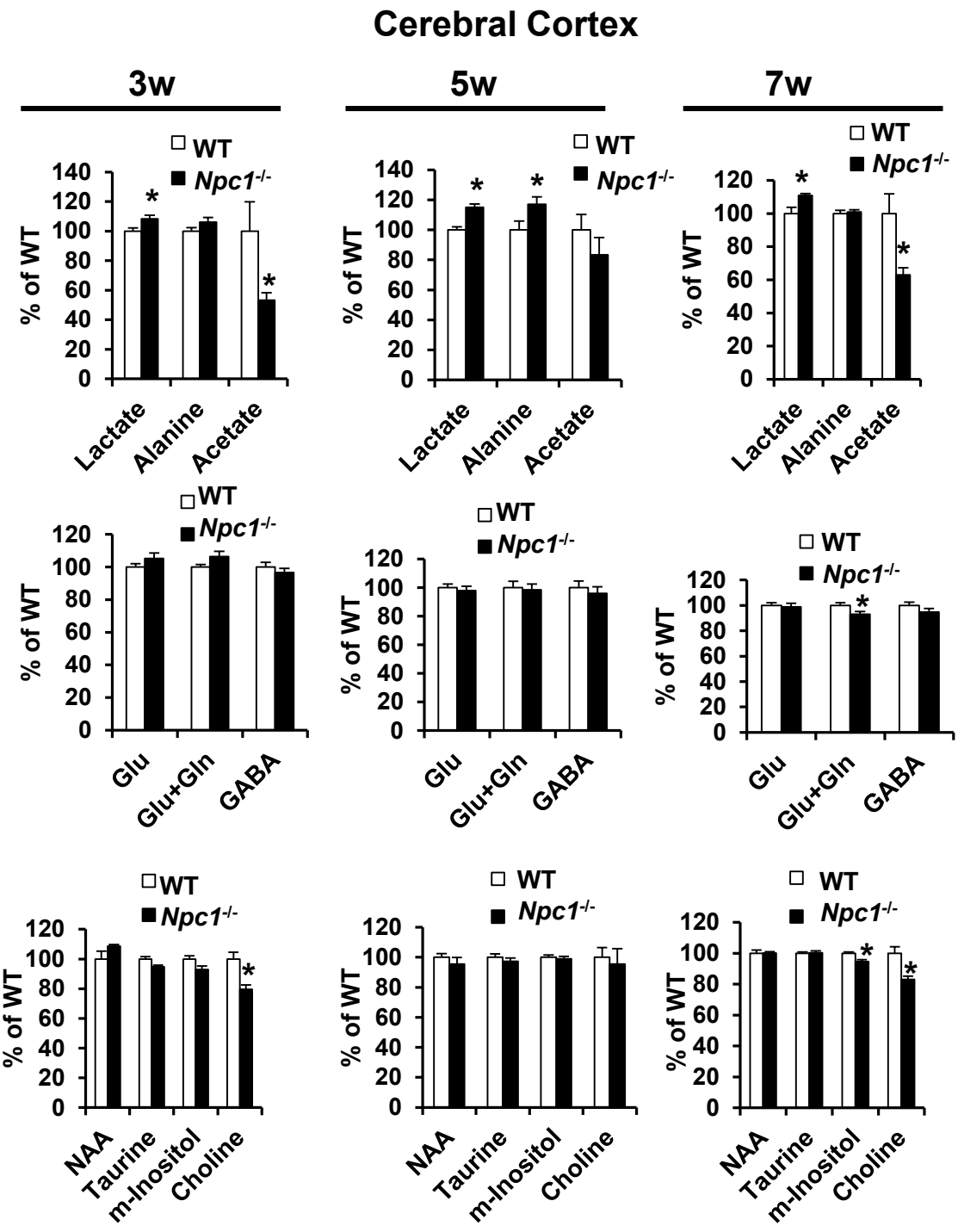
Cerebral Cortex
3w
5w
7w
WT
Npc1-/-
% of WT
Lactate
Alanine
Acetate
Glu
Glu+Gln
GABA
NAA
Taurine
m-Inositol
Choline

Figure 3.09 Altered energy metabolite levels in *Npc1*$^{-/-}$ cerebral cortex
Aqueous extracts of the cerebral cortex from 3-, 5-, or 7-week-old wildtype (WT) and *Npc1*$^{-/-}$ mice were analyzed by ^{1}H-NMR spectroscopy. Spectra were deconvolved and integrated. Peak areas were standardized to total peak area. Glu: glutamate, Glu+Gln: sum of glutamate and glutamine, GABA: gamma-aminobutyric acid, NAA: N-acetylaspartate, m-Inositol: myo-Inositol. Graphs in each column show data from the same set of WT and *Npc1*$^{-/-}$ mice of one age. Data are expressed as percent of the average of WT samples of the same age. Shown are the mean ± SEM. * $p<0.05$, *Npc1*$^{-/-}$ vs. WT.

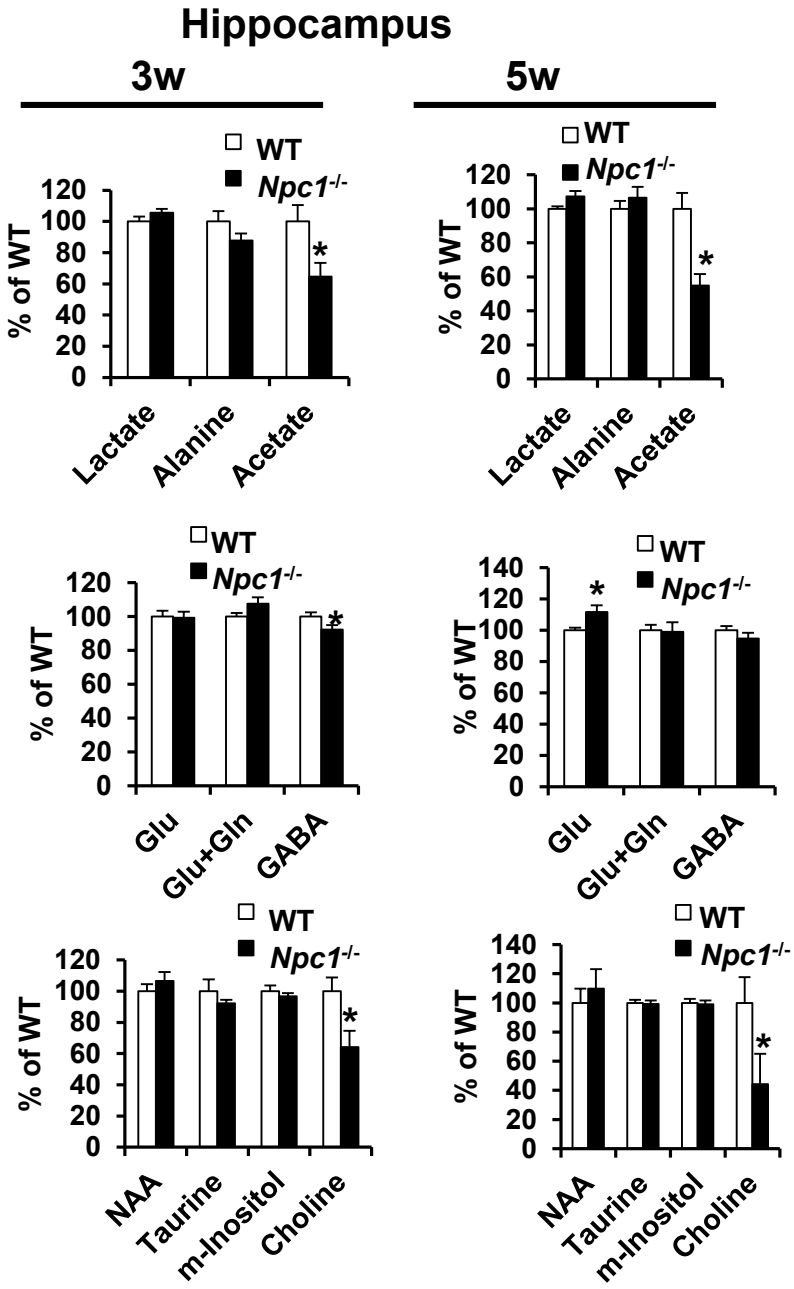

Figure 3.10 Altered energy metabolite levels in *Npc1*$^{-/-}$ hippocampus
Aqueous extracts of the hippocampus from 3-, or 5-week-old wildtype (WT) and *Npc1*$^{-/-}$ mice were analyzed by ^{1}H-NMR spectroscopy. Spectra were deconvolved and integrated. Peak areas were standardized to total peak area. Glu: glutamate, Glu+Gln: glutamate and glutamine summed together, GABA: gamma-aminobutyric acid, NAA: N-acetylaspartate, m-Inositol: myo-Inositol. Graphs in each column show data from the same set of WT and *Npc1*$^{-/-}$ mice of one age. Data are expressed as percent of the average of WT samples of the same age. Shown are the mean ± SEM. * $p<0.05$, *Npc1*$^{-/-}$ vs. WT.

metabolite of glutamate was decreased in 5- and 7-week-old *Npc1*$^{-/-}$ (Figure 3.08). Furthermore, in the cortex, glutamate and GABA levels were similar at all ages (Figure 3.09). *Npc1*$^{-/-}$ hippocampus had increased glutamate levels at 5 weeks of age and decreased GABA levels at 3 weeks of age (Figure 3.10).

Despite the loss of Purkinje cells, the levels of neuronal metabolite N-acetylaspartate (NAA) was similar at all ages between wildtype and *Npc1*$^{-/-}$ cerebellum (Figure 3.08). NAA levels were also similar at all ages in *Npc1*$^{-/-}$ and wildtype cortex and hippocampus (Figure 3.09 and 3.10). The osmolytes myo-inositol and taurine were decreased in *Npc1*$^{-/-}$ cerebellum at 3 and 5 weeks of age, respectively and myo-inositol was decreased at 7 weeks of age in *Npc1*$^{-/-}$ cortex (Figure 3.08). All brain regions at all ages (with the exception of *Npc1*$^{-/-}$ cortex at 5 weeks) had decreased levels of choline (Figure 3.08-10). Choline plays a key role in brain development as a precursor for one-carbon metabolism and phospholipid metabolism [304]. The consequences of decreased choline on DNA methylation are still under investigation and are not the topic of this thesis.

3.2.2 Increased expression of glycolytic enzymes in *Npc1*$^{-/-}$ brain

Mitochondrial dysfunction is typically accompanied by an upregulation of glycolysis to compensate for decreased ATP production. To determine whether glycolysis increased in *Npc1*$^{-/-}$ brain, we measured mRNA and/or protein levels of several enzymes involved in glycolysis. Figure 3.11 shows an overview of glycolytic enzymes and metabolites. The glucose transporter 1 (GLUT1) is a major glucose transporter in brain capillaries and glia [305, 306]. Preliminary measurements indicates that *Npc1*$^{-/-}$

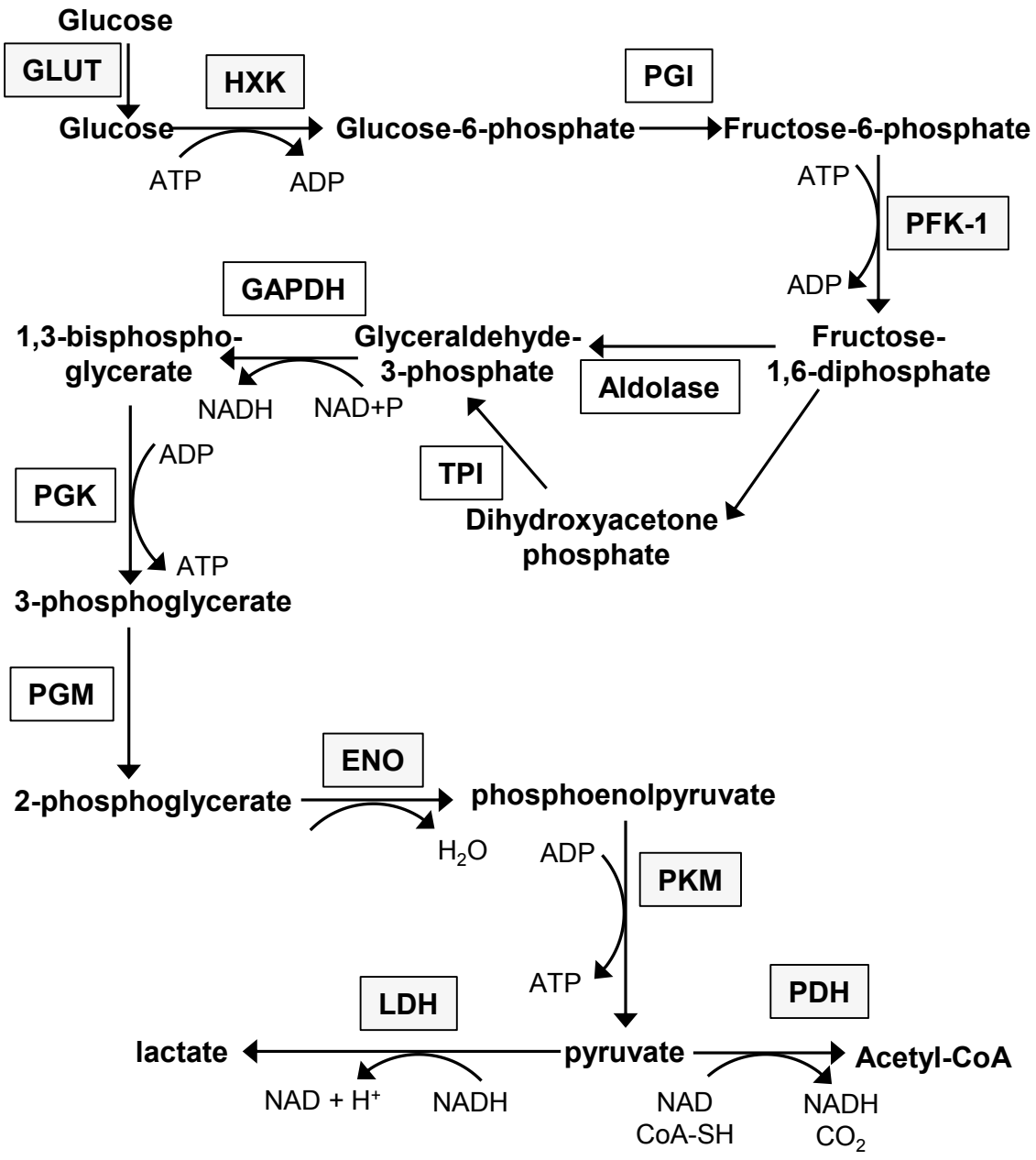

Figure 3.11 Glycolysis
A schematic of glycolysis. Grey boxes represent those genes/proteins that we measured. Hxk: hexokinase, PGI: phosphoglucose isomerase, PFK-1: phosphofructokinase 1, TPI: trisephosphate isomerase, GAPDH: glyceraldehyde phosphate dehydrogenase, PGK: phosphoglycerate kinase, PGM: phosphoglycerate mutase, ENO: enolase, PKM: pyruvate kinase, LDH: lactate dehydrogenase, PDH: pyruvate dehydrogenase.

cerebellum had increased GLUT1 protein levels at 7 weeks of age (Figure 3.12 A). The glycolytic enzyme, hexokinase, mediates phosphorylation of glucose at the carbon-6 position. Hexokinase 1 (*Hxk1*), the main isoform in brain, mRNA and protein levels were similar in 3- and 5-week-old wildtype and *Npc1*$^{-/-}$ cerebellum (Figure 3.12 B, C). However, HXK1 activity is also regulated by cellular localization; HXK1 is less active in the cytosol and more active when bound to mitochondria [307]. Mitochondria-bound HXK1 levels are increased in fraction enriched with synaptic mitochondria isolated from 7-week-old *Npc1*$^{-/-}$ brain (Figure 3.12 D). The main rate determining enzyme in glycolysis is phosphofructokinase 1 (PFK1), which catalyzes the conversion of fructose 6-phosphate to fructose 1, 6-bisphosphate. *Npc1*$^{-/-}$ cerebellum had similar mRNA levels of two isoforms of PFK1, *Pfkl* and *Pfkp*, and decreased mRNA levels of a third isoform, *Pfkm* at 3 weeks of age (Figure 3.12 E). However, at 5 weeks of age, mRNA levels of all three isoforms of PFK1 were increased markedly in *Npc1*$^{-/-}$ cerebellum (Figure 3.12 E). Consistent with the mRNA analysis, PFK-P protein levels were increased in 5-week-old but not 3-week-old *Npc1*$^{-/-}$ cerebellum (Figure 3.12 G). PFK1 is activated by fructose 2, 6-bisphosphate, the generation of which is catalyzed by phosphofructokinase-2 (PFK-2) [308]. PFK-2 protein levels are negatively regulated by protein degeneration mediated by the E3 ligase, *Cdh1* [309]. However, *Cdh1* mRNA levels were unchanged, suggesting that PFK-2 expression did not differ between wildtype and *Npc1*$^{-/-}$ cerebellum (Figure 3.12 F).

Enolase catalyzes the conversion of 2-phosphoglycerate to phosphoenolpyruvate, the ninth and penultimate step of glycolysis. In *Npc1*$^{-/-}$ cerebellum, mRNA levels of the

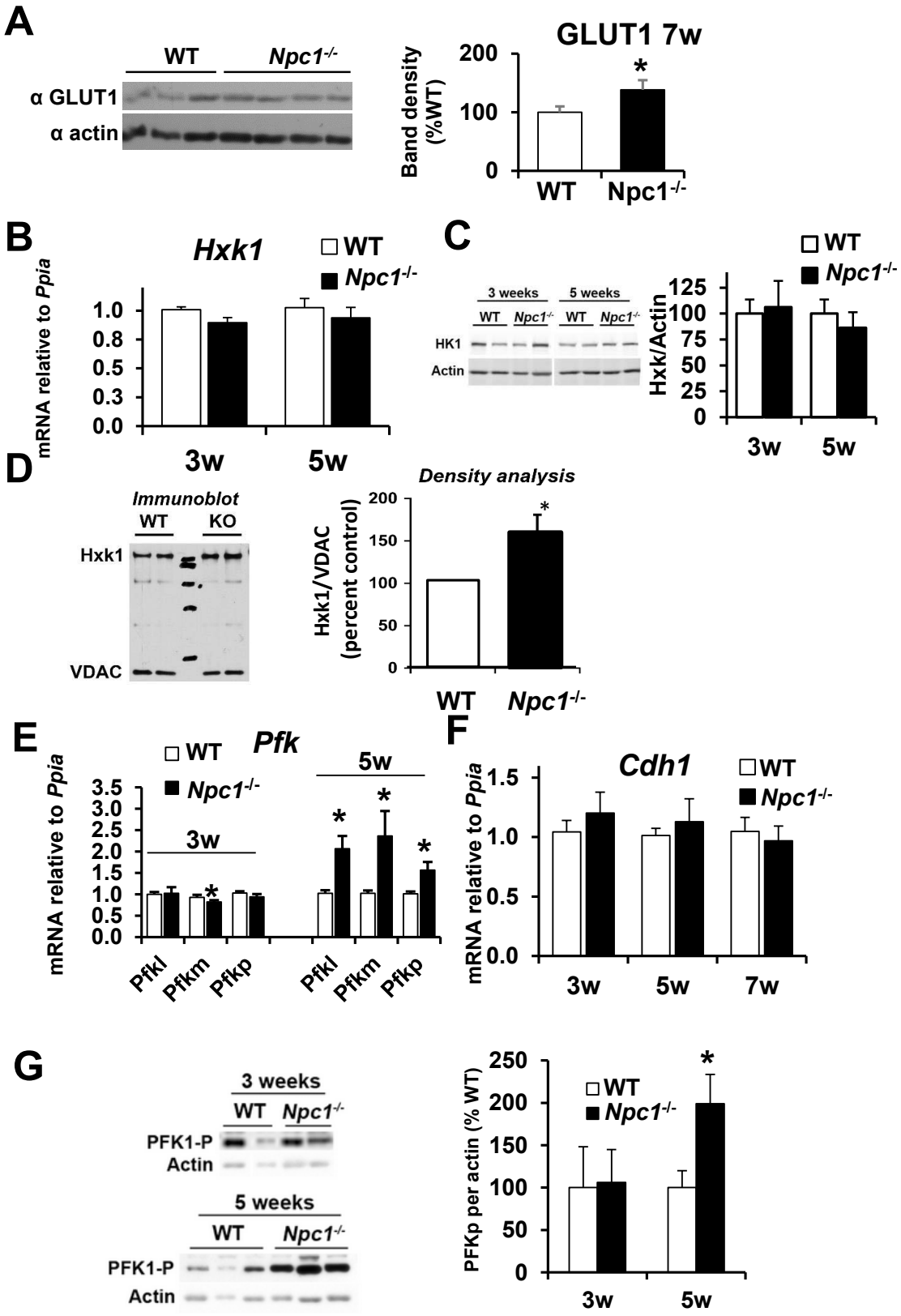
A
WT
Npc1-/-
α GLUT1
α actin
GLUT1 7w
Band density (%WT)
200
100
0
*
WT
Npc1-/-
B
Hxk1
WT
Npc1-/-
mRNA relative to Ppia
1.0
0.8
0.5
0.3
0.0
3w
5w
C
3 weeks
5 weeks
WT
Npc1-/-
HK1
Actin
Hxk/Actin
125
100
75
50
25
0
3w
5w
D
Immunoblot
WT
KO
Hxk1
VDAC
Density analysis
Hxk1/VDAC (percent control)
200
150
100
50
0
*
WT
Npc1-/-
E
Pfk
WT
Npc1-/-
mRNA relative to Ppia
3w
5w
3.5
3.0
2.5
2.0
1.5
1.0
0.5
0.0
*
Pfkl
Pfkm
Pfkp
F
Cdh1
WT
Npc1-/-
mRNA relative to Ppia
1.5
1.0
0.5
0.0
3w
5w
7w
G
3 weeks
WT
Npc1-/-
PFK1-P
Actin
5 weeks
WT
Npc1-/-
PFK1-P
Actin
PFKp per actin (% WT)
250
200
150
100
50
0
*
WT
Npc1-/-
3w
5w

Figure 3.12 Upregulation of glycolytic proteins and genes in *Npc1*$^{-/-}$ cerebellum
A, C, G) Immunoblot analysis of tissue homogenates of cerebellum from 3-, 5-, or 7-week-old WT and *Npc1*$^{-/-}$ mice using antibodies against glucose transporter 1 (Glut1), hexokinase 1 (HK1), phosphofructokinase-P (PFK1-P) and actin as a loading control. Bar graphs show the ratio of band intensity of protein target to actin expressed as percent WT. B, E, F) Cerebellar RNA was prepared from 3-, 5-, and/or 7-week-old mice. Target gene mRNA levels were analyzed by qPCR using primers against hexokinase 1 (*Hxk1*), phosphofructokinase isoforms (*Pfkl*, *Pfkm*, *Pfkp*) and anaphase-promoting complex activator protein (*Cdh1*) standardized to *Ppia*. D) Immunoblot analysis of mitochondria isolated from 7- week-old WT and *Npc1*$^{-/-}$ murine brain using antibodies against hexokinase 1 (Hxk1) and VDAC as a loading control. Bar graph shows the ratio of band intensity of Hxk1 to VDAC expressed as percent WT. All bar graphs show the mean ± SEM. * $p<0.05$, *Npc1*$^{-/-}$ vs. WT.

glial enolase 1 but not the neuronal enolase 2 were increased at 3 and 5 weeks of age and both decreased at 7 weeks of age in *Npc1*$^{-/-}$ cerebellum (Figure 3.13 A, B). The final step of glycolysis is the transfer of a phosphate from phosphoenolpyruvate to ADP generating ATP and pyruvate catalyzed by pyruvate kinase (PKM). *Npc1*$^{-/-}$ cerebellum had similar total pyruvate kinase mRNA and protein levels as WT cerebellum at 3 and 5 weeks of age (Figure 3.13 C, D). However, increased protein levels of pyruvate kinase 2 (PKM2) in both 3- and 5-week-old *Npc1*$^{-/-}$ cerebellum (Figure 3.13 D). PKM2 is commonly expressed in embryonic and cancer tissues and in contrast to PKM1 is under a complex allosteric regulation to control the flux of glycolysis into biosynthetic pathways [310, 311]. The consequences of increased expression of PKM2 in *Npc1*$^{-/-}$ cerebellum are unknown. The increased mRNA levels of astrocytic lactate dehydrogenase in 3- and 5-week-old *Npc1*$^{-/-}$ cerebellum were consistent with the increased lactate levels (Figure 3.13 E). Altogether, these findings suggested an increase in glycolysis in *Npc1*$^{-/-}$ cerebellum.

Glucose is a precursor for the pentose phosphate pathway and other biosynthetic pathways. In the first step of the pentose phosphate pathway, glucose-6-phosphate dehydrogenase catalyzes the oxidation of glucose-6-phosphate and reduction of NADP+. Glucose-6-phosphate dehydrogenase mRNA levels were decreased at 3 weeks of age, however, expression was normal at 5 and 7 weeks of age in *Npc1*$^{-/-}$ cerebellum (Figure 3.13 F).

To determine whether these alterations in energy metabolism alter the overall energy status of *Npc1*$^{-/-}$ cerebellum we measured the phosphorylation of AMP kinase

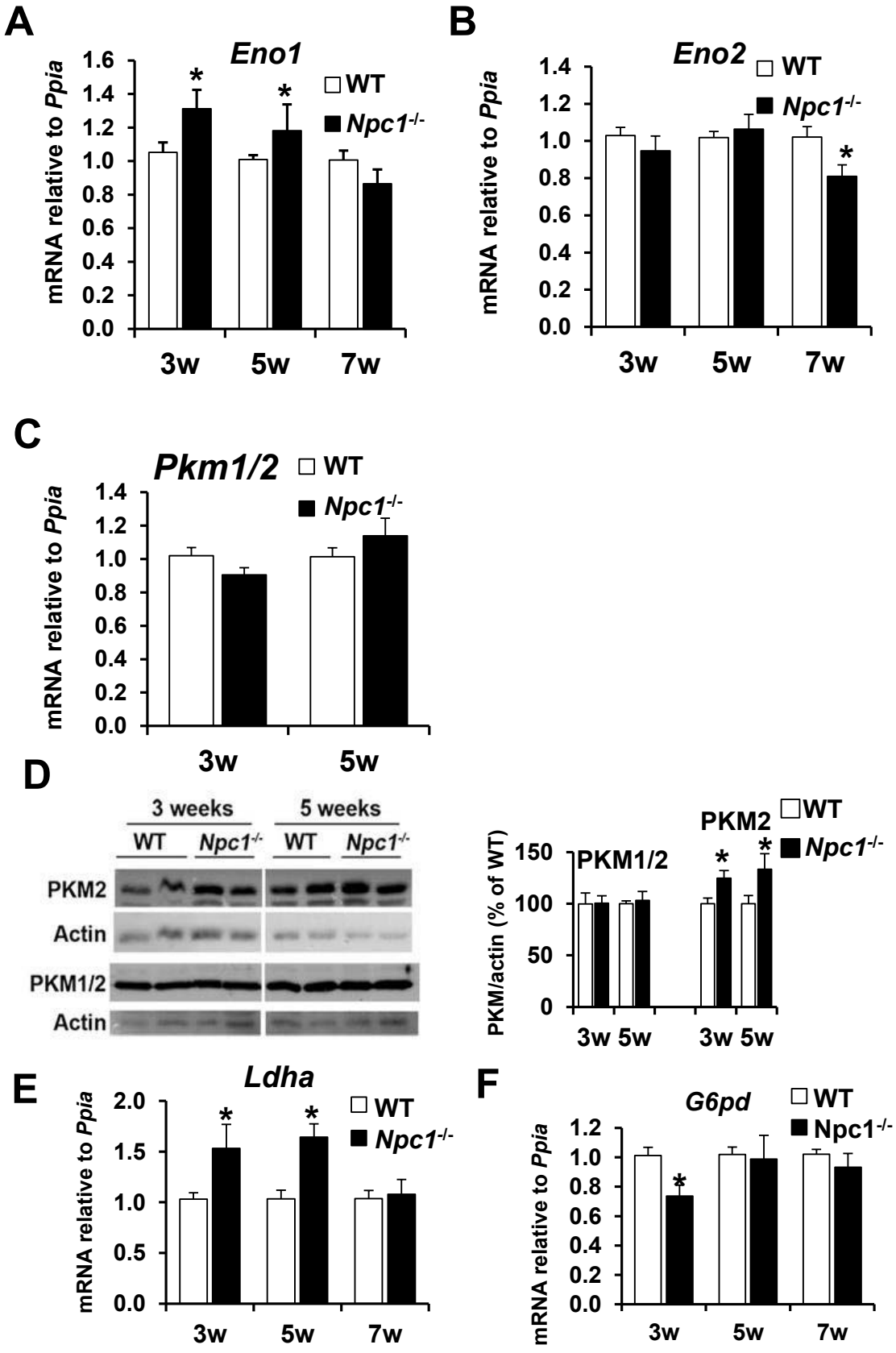
A
Eno1
WT
Npc1-/-
mRNA relative to Ppia
1.6
1.4
1.2
1.0
0.8
0.6
0.4
0.2
0.0
3w
5w
7w
B
Eno2
WT
Npc1-/-
mRNA relative to Ppia
1.4
1.2
1.0
0.8
0.6
0.4
0.2
0.0
3w
5w
7w
C
Pkm1/2
WT
Npc1-/-
mRNA relative to Ppia
1.4
1.2
1.0
0.8
0.6
0.4
0.2
0.0
3w
5w
D
3 weeks
5 weeks
WT
Npc1-/-
WT
Npc1-/-
PKM2
Actin
PKM1/2
Actin
PKM2
WT
Npc1-/-
PKM1/2
PKM/actin (% of WT)
150
100
50
0
3w 5w
3w 5w
E
Ldha
WT
Npc1-/-
mRNA relative to Ppia
2.0
1.5
1.0
0.5
0.0
3w
5w
7w
F
G6pd
WT
Npc1-/-
mRNA relative to Ppia
1.2
1.0
0.8
0.6
0.4
0.2
0.0
3w
5w
7w

Figure 3.13 Upregulation of glycolytic proteins and genes in *Npc1*$^{-/-}$ cerebellum
A-C, E, F) Cerebellar RNA was prepared from 3-, 5-, and/or 7-week-old mice. Target gene mRNA levels were analyzed by qPCR using primers against enolase 1 (*Eno1*), enolase 2 (*Eno2*), pyruvate kinase (*Pkm*), lactate dehydrogenase a (*Ldha*), glucose-6-phosphate dehydrogenase (*G6pd*), standardized to *Ppia*. D) Immunoblot analysis of tissue homogenates of cerebellum from 3-, 5- week-old WT and *Npc1*$^{-/-}$ mice using antibodies against total pyruvate kinase (PKM1/2), pyruvate kinase M2 (PKM2) and actin as a loading control. Bar graphs show the ratio of band intensity of protein target to actin expressed as percent WT. All bar graphs show the mean ± SEM. * $p<0.05$, *Npc1*$^{-/-}$ vs. WT.

(AMPK), which is increased during energy deprivation. Levels of phosphorylated alpha and beta AMPK were similar in 3- and 5-week-old *Npc1*$^{-/-}$ cerebellum compared to wildtype suggesting normal energy levels (Figure 3.14 A-C). Glycolytic gene expression are also induced by activation of hypoxia inducible factor 1 alpha subunit (*Hif1a*, protein is Hif1alpha). However, mRNA levels of *Hif1a* were unchanged at all ages in *Npc1*$^{-/-}$ cerebellum and we were unable to reliably detect HIF-1alpha by immunoblotting (Figure 3.14 D).

Brain areas have distinct metabolic patterns and are differently affected by NPC1-deficiency as seen in NMR study. To compare them, we measured expression of key glycolytic genes in *Npc1*$^{-/-}$ cortex and hippocampus. Consistent with the increased lactate levels found by NMR, 5-week-old *Npc1*$^{-/-}$ cortex had increased *Pfkp* and *Pdk1* mRNA levels and increased phosphorylation of PDH (Figure 3.15 A-C). Together these results suggested increased glycolysis to lactate in *Npc1*$^{-/-}$ cortex at 5 weeks of age. KGDH protein levels were similar between *Npc1*$^{-/-}$ and wildtype *Npc1*$^{-/-}$ cortex (Figure 3.15 C).

In 5-week-old *Npc1*$^{-/-}$ hippocampus mRNA levels of *Pfkm* and protein levels of PKM2 were increased (Figure 3.16 A, B). In contrast to cerebellum, total PKM protein levels were also increased in *Npc1*$^{-/-}$ hippocampus (Figure 3.16 B). Furthermore, mRNA levels of *Pdha* were unchanged, PDH protein levels were increased, and the ratio of pPDH per PDH was decreased in 5-week-old *Npc1*$^{-/-}$ hippocampus compared to wildtype (Figure 3.16 C-D). Unlike cortex or cerebellum, preliminary results found that *Npc1*$^{-/-}$ hippocampus had decreased protein levels of KGDH (Figure 3.16 E). Together these findings suggest that glycolysis was increased in all brain regions but pyruvate oxidation was inhibited only in cerebellum and cortex of *Npc1*$^{-/-}$ mice.

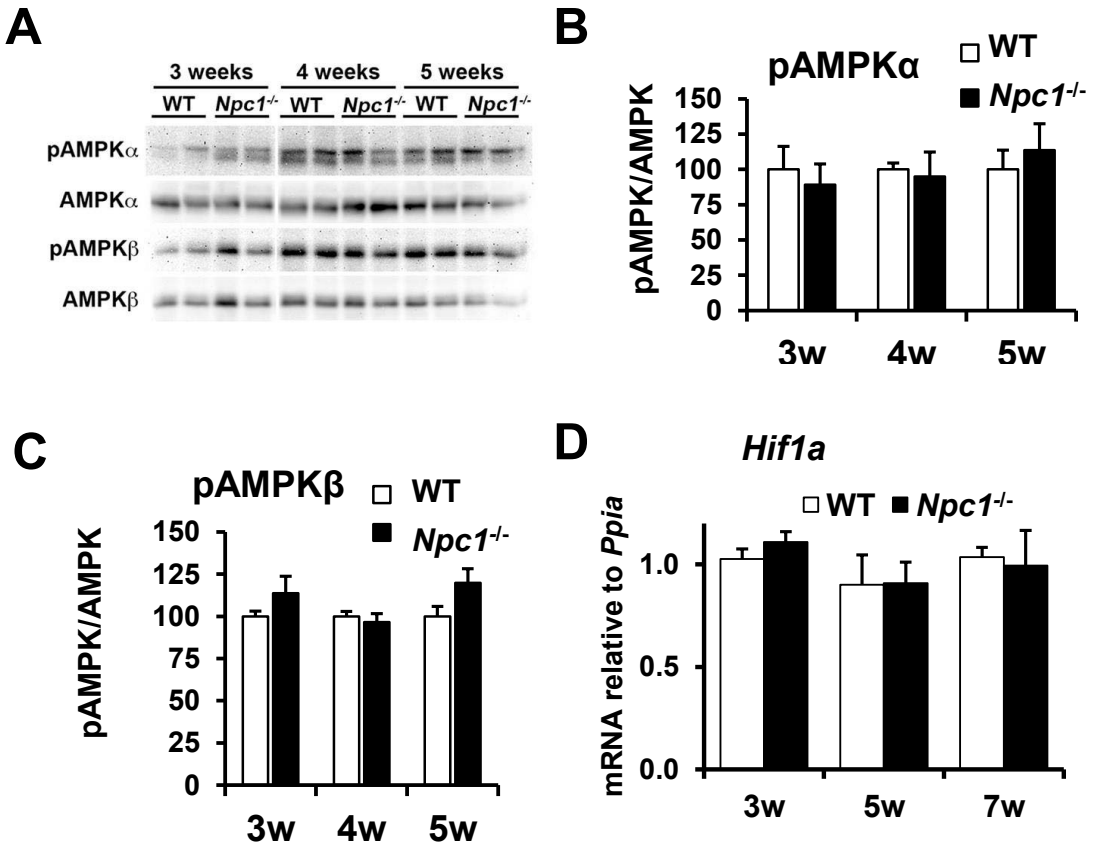

Figure 3.14 Normal phosphorylation of AMP kinase and expression of Hif1alpha in *Npc1*$^{-/-}$ cerebellum

A-C) Immunoblot analysis of tissue homogenates of cerebellum from 3-, 4-, 5- week-old WT and *Npc1*$^{-/-}$ mice using antibodies against phosphorylated AMP-activated protein kinase α (pAMPKα), AMP-activated protein kinase α (AMPKα), phosphorylated AMP-activated protein kinase β (pAMPKβ), AMP-activated protein kinase β (AMPKβ). Bar graphs show the ratio of band intensity of phosphorylated AMPK to total AMPK expressed as percent WT. D) Cerebella RNA was prepared from 3-, 5-, and 7-week-old mice. Target gene mRNA levels were analyzed by qPCR using primers against hypoxia-induced factor 1-α (*Hif1a*) standardized to *Ppia*. All bar graphs show the mean ± SEM. * $p<0.05$, *Npc1*$^{-/-}$ vs. WT.

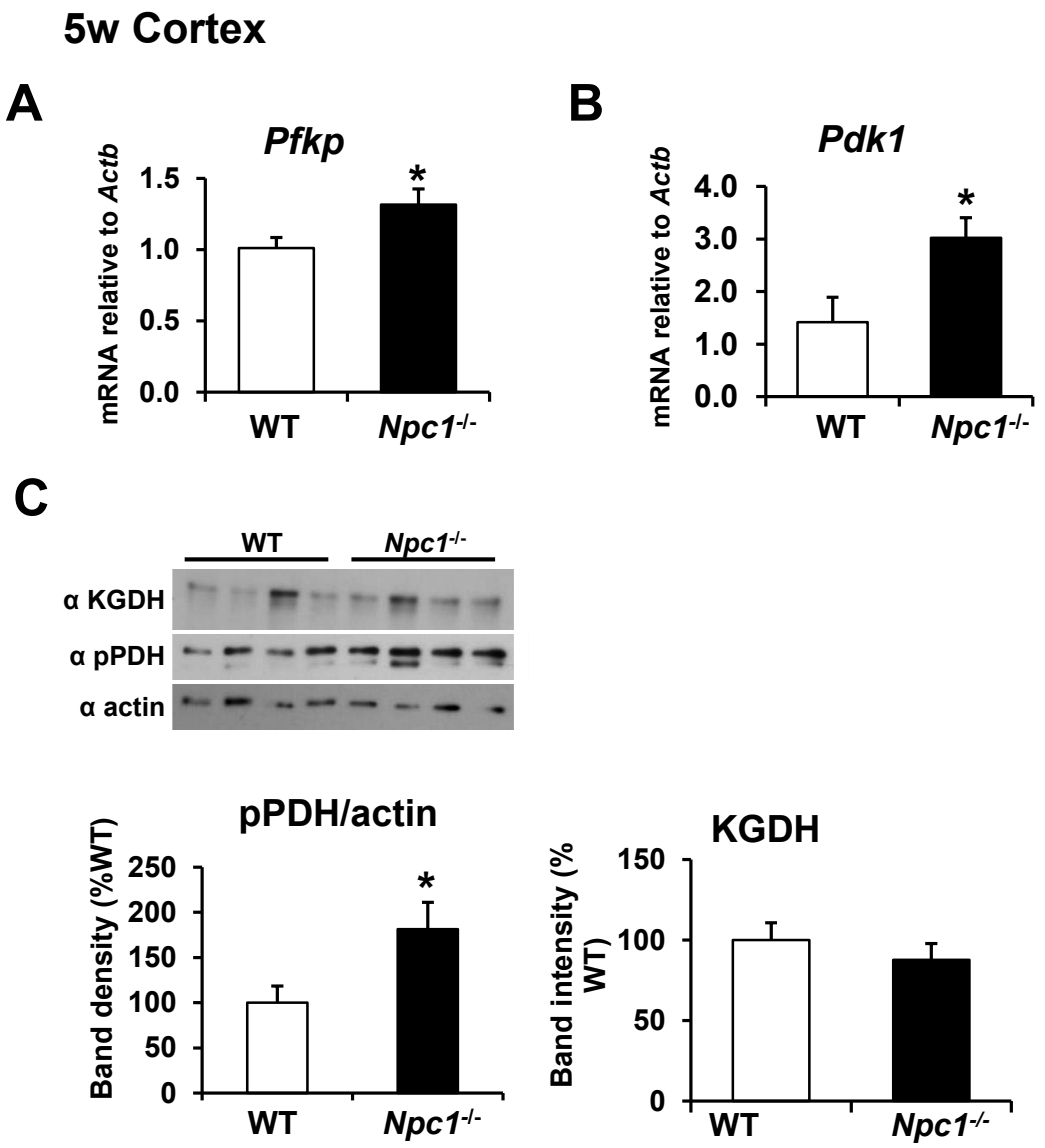

Figure 3.15 Upregulation of glycolytic genes and increased phosphorylation of PDH in *Npc1*$^{-/-}$ cortex

A, B) Cerebral cortical RNA was prepared from 5-week-old mice. Target genes mRNA levels were analyzed by qPCR using primers against phosphofructokinase platelet (*Pfkp*), pyruvate dehydrogenase kinase 1 (*Pdk1*), standardized to *actin*. C) Immunoblot analysis of tissue homogenates of cerebral cortex from 5- week-old WT and *Npc1*$^{-/-}$ mice using antibodies against α ketoglutarate (KGDH), phosphorylated pyruvate dehydrogenase (pPDH) and actin as a loading control. Bar graphs show the ratio of band intensity of protein target to actin expressed as percent WT. All bar graphs show the mean ± SEM. * $p<0.05$, *Npc1*$^{-/-}$ vs. WT.

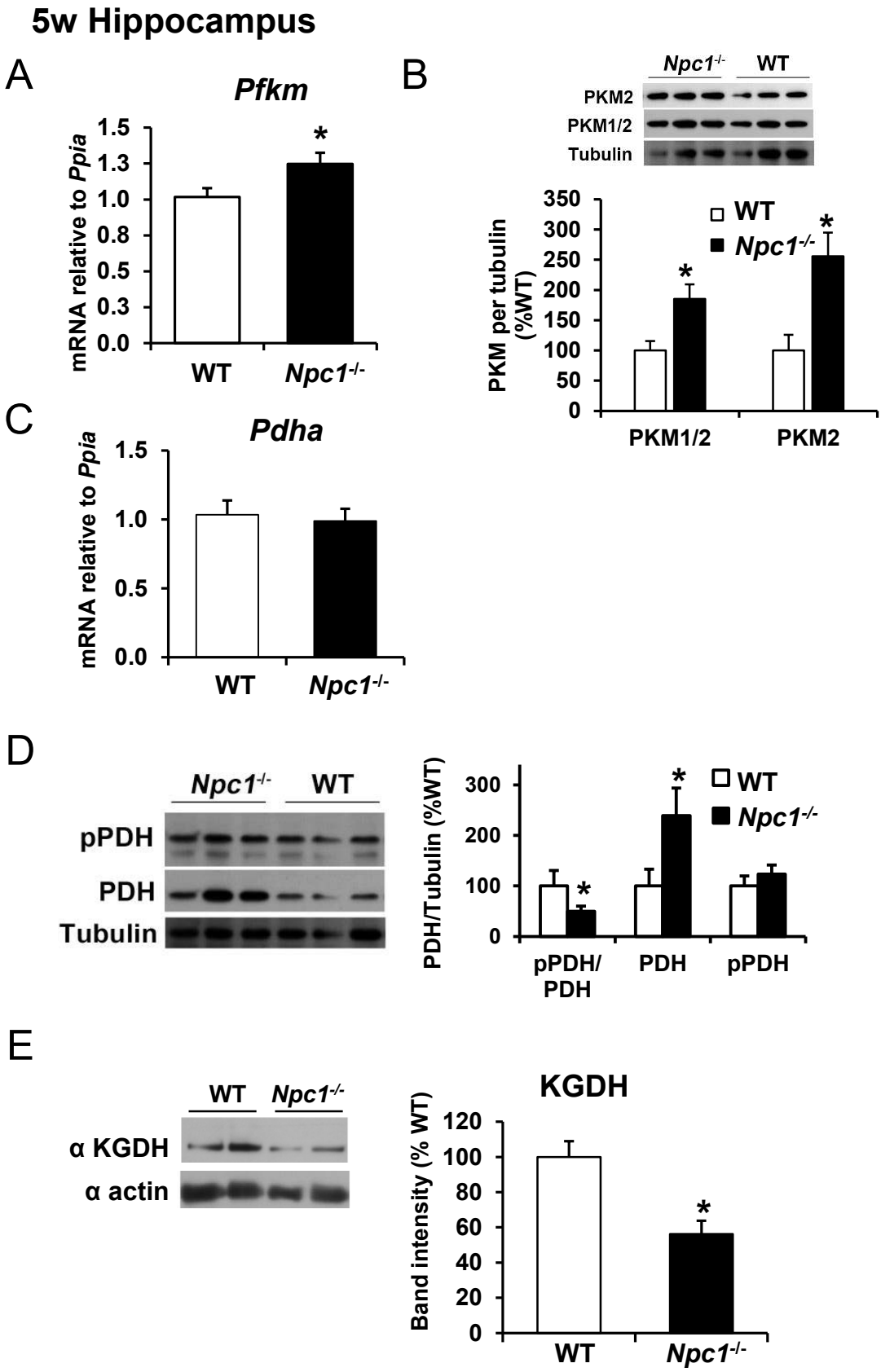
5w Hippocampus
A
Pfkm
mRNA relative to Ppia
1.5
1.3
1.0
0.8
0.5
0.3
0.0
*
WT
Npc1-/-
B
Npc1-/-
WT
PKM2
PKM1/2
Tubulin
PKM per tubulin (%WT)
350
300
250
200
150
100
50
0
WT
Npc1-/-
*
*
PKM1/2
PKM2
C
Pdha
mRNA relative to Ppia
1.5
1.0
0.5
0.0
WT
Npc1-/-
D
Npc1-/-
WT
pPDH
PDH
Tubulin
PDH/Tubulin (%WT)
300
200
100
0
*
*
WT
Npc1-/-
pPDH/ PDH
PDH
pPDH
E
WT
Npc1-/-
α KGDH
α actin
KGDH
Band intensity (% WT)
120
100
80
60
40
20
0
*
WT
Npc1-/-

Figure 3.16 Upregulation of glycolytic genes, increased protein levels of PDH, and decreased KGDH protein levels in *Npc1*$^{-/-}$ hippocampus

A, C) Hippocampal RNA was prepared from 5-week-old mice. Target gene mRNA levels were analyzed by qPCR using primers against phosphofructokinase muscle (*Pfkm*), pyruvate dehydrogenase (*Pdha*), standardized to *Ppia*. B, D) Immunoblot analysis of tissue homogenates of hippocampus from 5- week-old WT and *Npc1*$^{-/-}$ mice using antibodies against pyruvate kinase M2 (PKM2), total pyruvate kinase (PKM1/2), phosphorylated pyruvate dehydrogenase (pPDH), pyruvate dehydrogenase (PDH), and tubulin as a loading control. Bar graphs show the ratio of band intensity of pPDH to PDH or protein target to tubulin expressed as percent WT. E) Immunoblot analysis of tissue homogenates of hippocampus from 5- week-old WT and *Npc1*$^{-/-}$ mice using antibodies against alpha ketoglutarate (KGDH). Bar graphs show the ratio of band intensity of KGDH as percent WT. All bar graphs show the mean ± SEM. * $p<0.05$, *Npc1*$^{-/-}$ vs. WT.

3.2.3 Altered glutamate metabolism in *Npc1*$^{-/-}$ brain

Glutamate is the major excitatory neurotransmitter in the brain. When glucose oxidation is insufficient, glutamate can also be an energy source through conversion to alpha-ketoglutarate and entry into the TCA cycle (Figure 3.17). Next we asked whether *Npc1*$^{-/-}$ brains increased the oxidation of glutamate to compensate for decreased pyruvate oxidation. Astrocytes take up glutamate after its synaptic release. Subsequently, astrocytic glutamine synthetase (GS, gene is *Glu1*) mediates the conversion of glutamate to glutamine. *Glu1* mRNA levels were increased in 3-, 5-, and 7-week-old *Npc1*$^{-/-}$ cerebellum (Figure 3.18). Glutamine is secreted and taken up by neurons where phosphate-activated glutaminases (GLS1 and 2) convert glutamine to glutamate (Figure 1.09). *Gls1* mRNA levels were unchanged at all ages, whereas *Gls2* mRNA levels were increased at 5 weeks, and decreased at 7 weeks in *Npc1*$^{-/-}$ cerebellum (Figure 3.18). In GABAergic neurons (such as Purkinje cells) glutamate decarboxylase (GAD1) converts glutamate to GABA. *Gad1* mRNA levels were only non-significantly decreased at 3 weeks in *Npc1*$^{-/-}$ cerebellum (Figure 3.18).

The conversion of glutamate to alpha-ketoglutarate can be catalyzed by mitochondrial glutamate dehydrogenase (GLUD1) or one of several aminotransferases [312]. *Glud1* mRNA levels were unchanged at 3 and 5 weeks of age and increased at 7 weeks of age in *Npc1*$^{-/-}$ cerebellum (Figure 3.18). Another mechanism of conversion of glutamate to alpha-ketoglutarate is by transamination reactions with aspartate, alanine, or branched chain amino acids. Mitochondrial aspartate aminotransferase (*Got2*) mRNA levels were increased at all ages, mRNA levels of both the cytosolic/neuronal (*Bcat1*) and mitochondrial/astrocytic (*Bcat2*) branched chain amino acid aminotransferase were

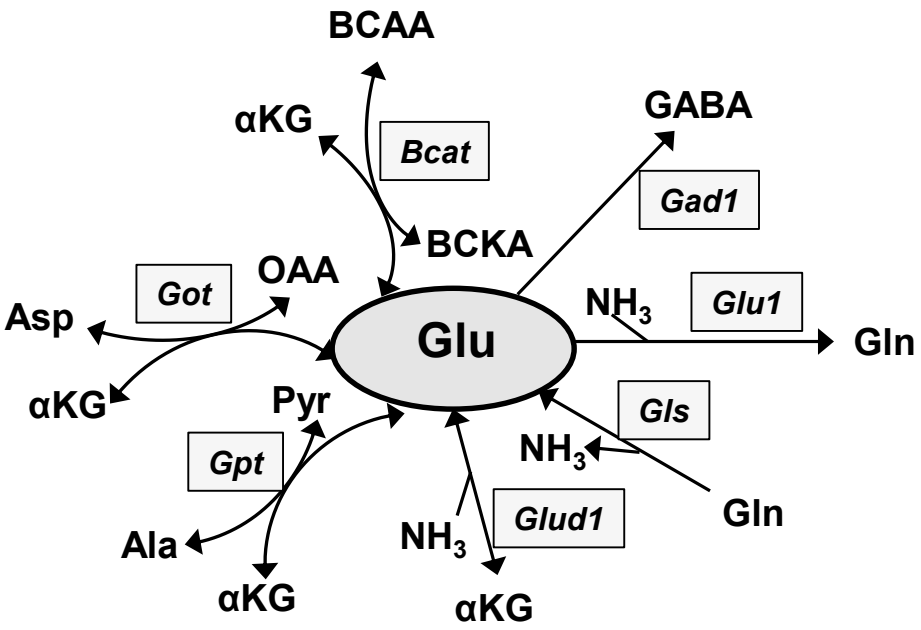

Figure 3.17 Glutamate metabolism
Schematic of glutamate metabolism. Enzymes are in grey boxes. Glu: glutamate, GABA: gamma-aminobutyric acid, Gln: glutamine, NH_3: ammonia, αKG: alpha ketoglutarate, Ala: alanine, Pyr: pyruvate, Asp: aspartate, OAA: oxaloacetate, BCAA: branched-chain amino acids, BCKA: branched-chain ketoacids. Gad1: glutamate decarboxylase 1, Glu1: glutamine synthetase 1, Gls: glutaminase, Glud1: glutamate dehydrogenase, Gpt: alanine aminotransferase, Got: aspartate aminotransferase, Bcat: branched-chain aminotransferase.

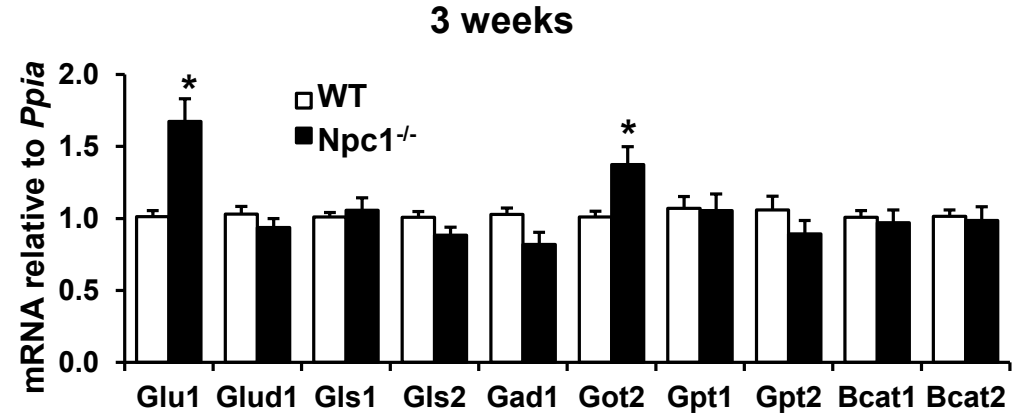
3 weeks
mRNA relative to Ppia
2.0
1.5
1.0
0.5
0.0
WT
Npc1-/-
Glu1 Glud1 Gls1 Gls2 Gad1 Got2 Gpt1 Gpt2 Bcat1 Bcat2

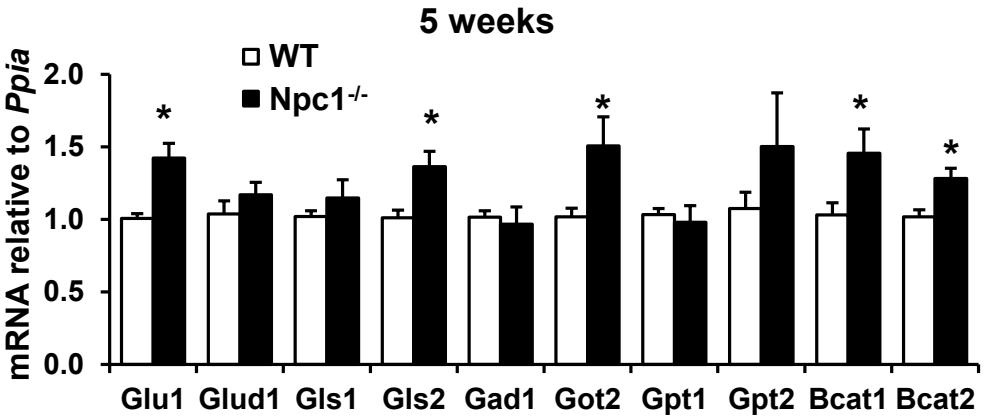
5 weeks
mRNA relative to Ppia
2.0
1.5
1.0
0.5
0.0
WT
Npc1-/-
Glu1 Glud1 Gls1 Gls2 Gad1 Got2 Gpt1 Gpt2 Bcat1 Bcat2

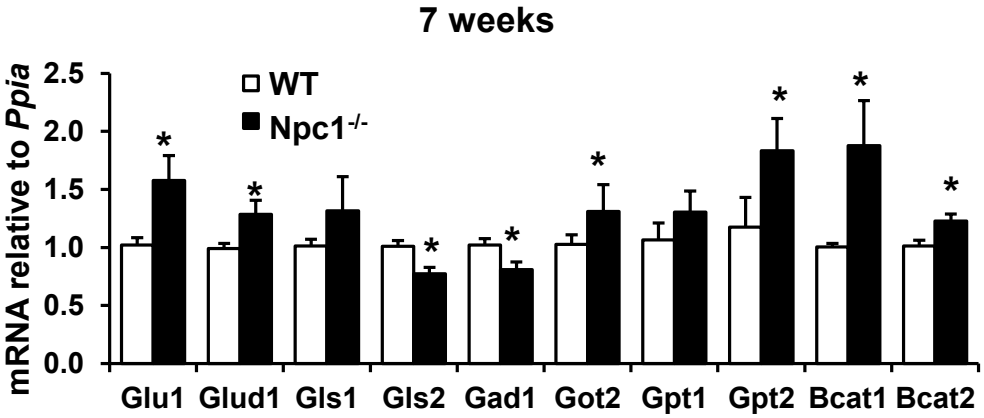
7 weeks
mRNA relative to Ppia
2.5
2.0
1.5
1.0
0.5
0.0
WT
Npc1-/-
Glu1 Glud1 Gls1 Gls2 Gad1 Got2 Gpt1 Gpt2 Bcat1 Bcat2

Figure 3.18 Altered expression of glutamate metabolism-related genes in *Npc1*$^{-/-}$ cerebellum

A-F) Cerebellar RNA was prepared from 3-, 5-, 7-week-old mice. Target gene mRNA levels were analyzed by qPCR using primers against glutamine synthetase 1 (*Glu1*), glutamate dehydrogenase (*Glud1*), glutaminase 1 (*Gls1*), glutaminase 2 (*Gls2*), glutamate decarboxylase 1 (*Gad1*), aspartate aminotransferase 2 (*Got2*), alanine aminotransferase 1 (*Gpt1*), alanine aminotransferase 2 (*Gpt2*), branched-chain aminotransferase 1 (*Bcat1*), branched-chain aminotransferase 2 (*Bcat2*), standardized to *Ppia*. All bar graphs show the mean ± SEM. * $p<0.05$, *Npc1*$^{-/-}$ vs. WT.

increased at 5 and 7 weeks of age in *Npc1*$^{-/-}$ cerebellum, and alanine transaminase (*Gpt1* and *Gpt2*) mRNA levels were unchanged (Figure 3.18). Increased expression of GLUD1, GOT2, and BCAT1/2 would support increased glutamate conversion to alpha ketoglutarate.

Pyruvate carboxylase (PCX), which converts pyruvate into oxaloacetate in astrocytes and is required for the *de novo* synthesis of glutamate from glucose-derived carbons [313, 314]. *Pcx* mRNA levels were increased in 3- and 5-week-old *Npc1*$^{-/-}$ cerebellum (Figure 3.19 A). Malic enzyme, which catalyzes the reversible conversion of malate to pyruvate and carbon dioxide; is required for full oxidation of glutamate in neurons [315]. The cytosolic malic enzyme 1 mRNA levels were decreased in 3-week-old *Npc1*$^{-/-}$ cerebellum and unchanged at 5 and 7 weeks of age (Figure 3.19 B). Meanwhile, mRNA levels of the neuronal/mitochondrial malic enzyme 3 were similar at all ages in *Npc1*$^{-/-}$ cerebellum (Figure 3.19 C).

In the cortex, *Glu1* mRNA levels were decreased and *Gls2* mRNA levels were unchanged in 5-week-old *Npc1*$^{-/-}$ cortex (Figure 3.20 A, B). *Glud1* and *Bcat2* mRNA levels were increased in 5-week-old *Npc1*$^{-/-}$ cortex (Figure 3.20 C, E). Additionally, *Gpt2* and *Gad1* mRNA levels were unchanged in 5-week-old *Npc1*$^{-/-}$ cortex (Figure 3.20 D, G). Furthermore, unlike cerebellum, *Pcx* mRNA levels were decreased in 5-week-old *Npc1*$^{-/-}$ cortex (Figure 3.20 F). Together these results show that glutamate metabolism is clearly altered but the pattern is more difficult to interpret.

Gene expression analysis of 5-week-old *Npc1*$^{-/-}$ hippocampus also revealed altered glutamate metabolism. *Glu1* mRNA levels were increased while *Gls1* and *Gls2* mRNA levels were unchanged in 5-week-old *Npc1*$^{-/-}$ hippocampus (Figure 3.21 A-C).

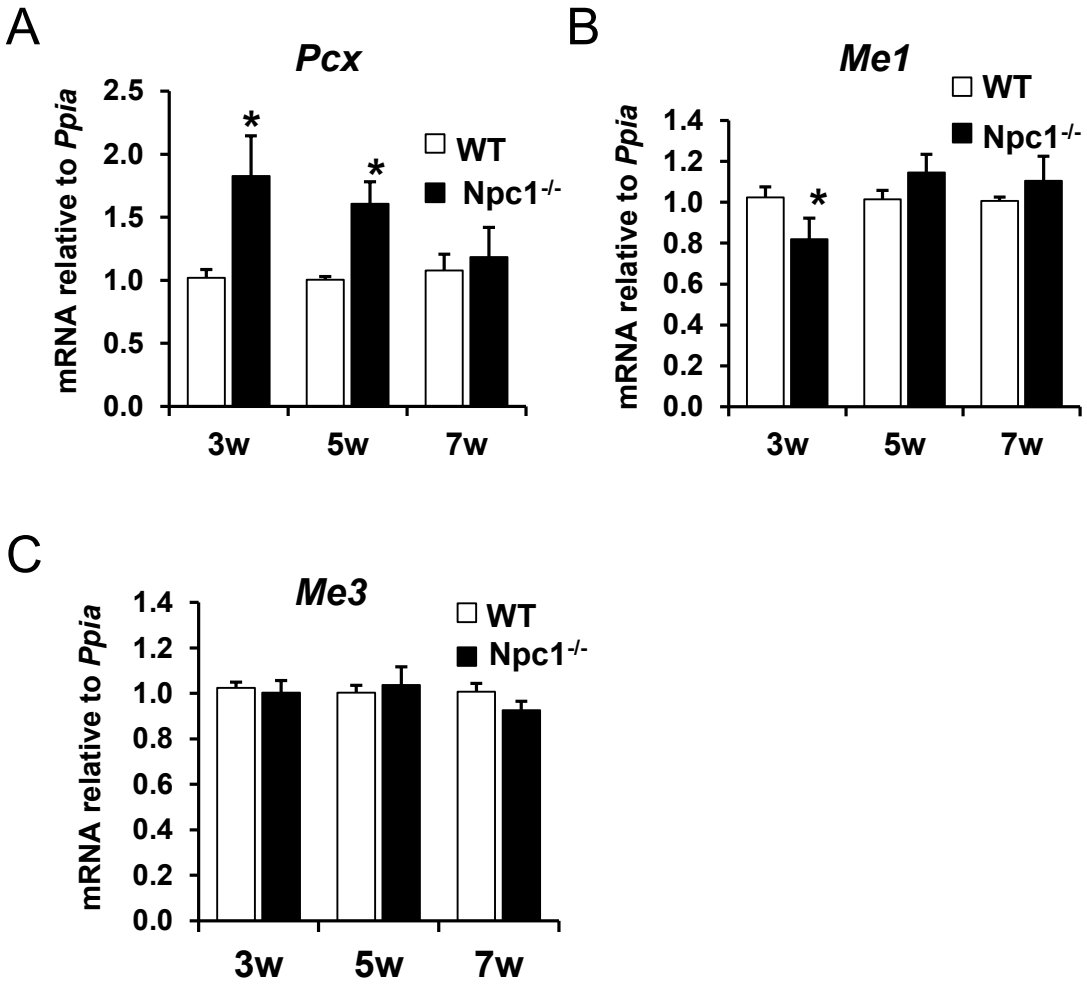

Figure 3.19 Altered expression of pyruvate metabolism-related genes in *Npc1*$^{-/-}$ cerebellum

A-F) Cerebella RNA was prepared from 3-, 5-, 7-week-old mice. Target genes mRNA levels were analyzed by qPCR using primers against pyruvate carboxylase (*Pcx*), malic enzyme 1 (*Me1*), malic enzyme 3 (*Me3*), standardized to *Ppia*. All bar graphs show the mean ± SEM. * $p<0.05$, *Npc1*$^{-/-}$ vs. WT.

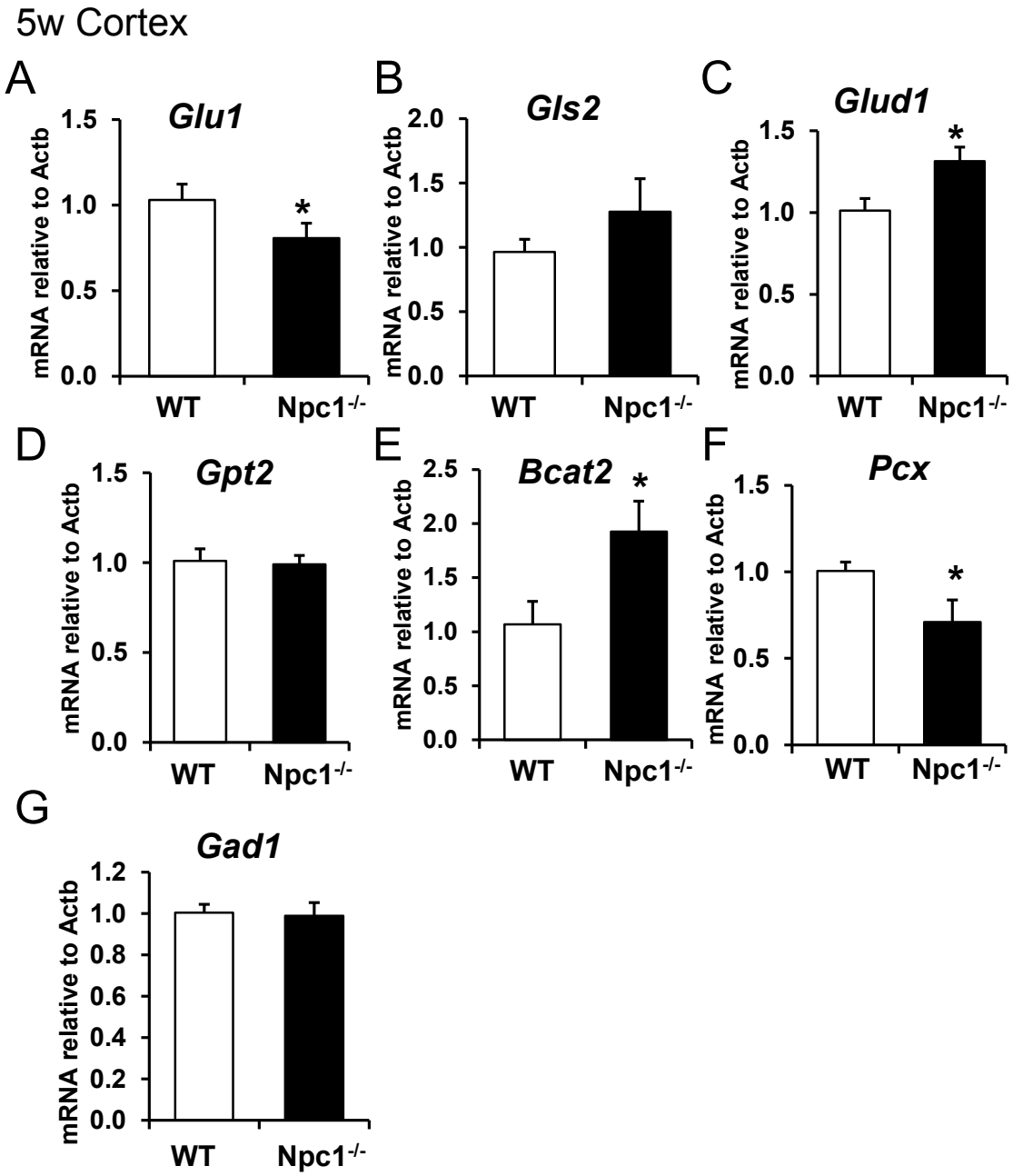

Figure 3.20 Altered expression of glutamate metabolism-related genes in *Npc1*$^{-/-}$ cerebral cortex

A-F) Cerebral cortex RNA was prepared from 5-week-old mice. Target genes mRNA levels were analyzed by qPCR using primers against glutamine synthetase 1 (*Glu1*), glutaminase 2 (*Gls2*), glutamate dehydrogenase (*Glud1*), alanine aminotransferase 2 (*Gpt2*), branched-chain aminotransferase 2 (*Bcat2*), pyruvate carboxylase (*Pcx*), glutamate decarboxylase 1 (*Gad1*), standardized to *Ppia*. All bar graphs show the mean ± SEM. * $p<0.05$, *Npc1*$^{-/-}$ vs. WT.

5w Hippocampus

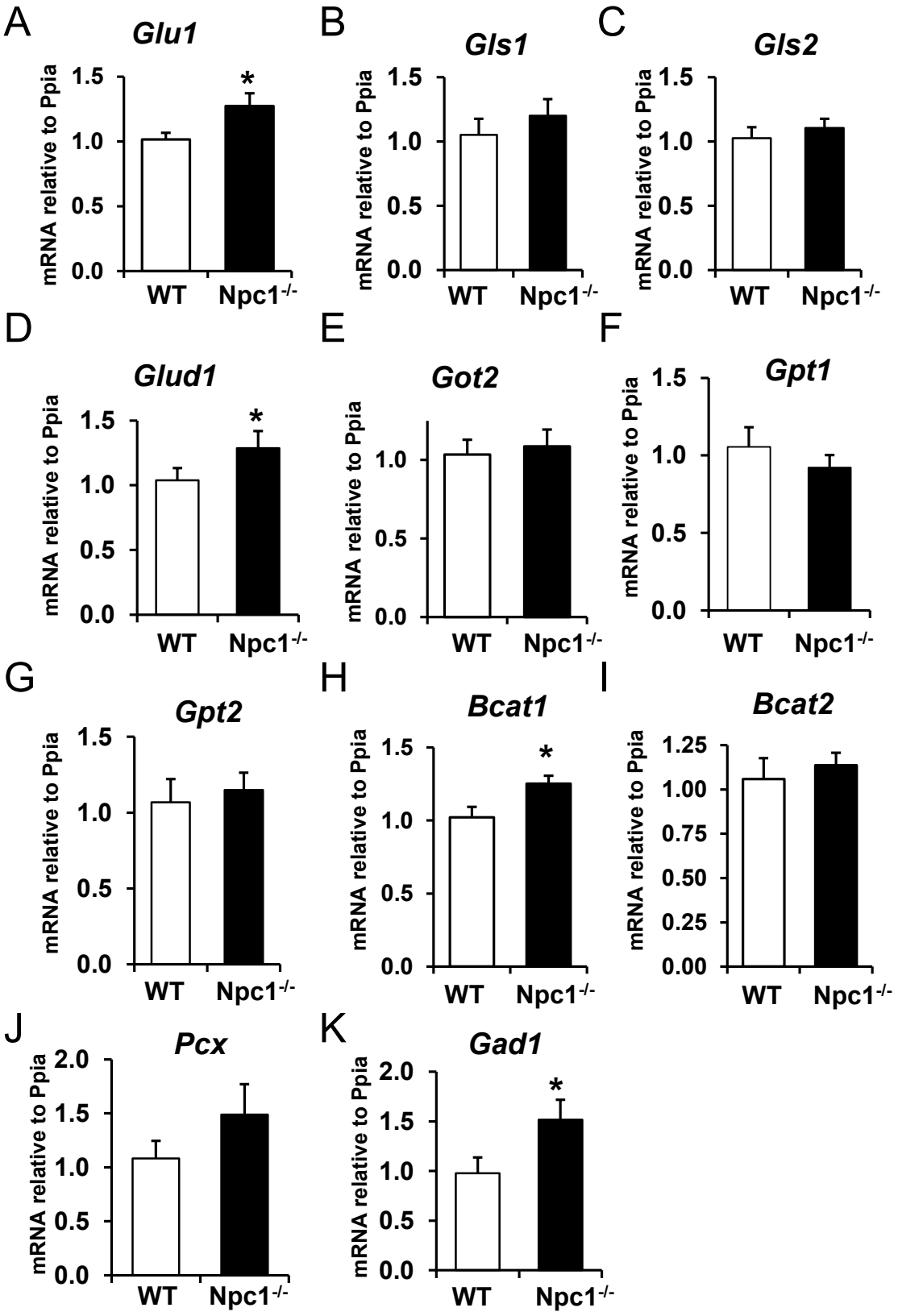

Figure 3.21 Altered expression of glutamate metabolism-related genes in *Npc1*$^{-/-}$ hippocampus

A-K) Hippocampal RNA was prepared from 5-week-old mice. Target genes mRNA levels were analyzed by qPCR using primers against glutamine synthetase 1 (*Glu1*), glutaminase 1 (*Gls1*), glutaminase 2 (*Gls2*), glutamate dehydrogenase (*Glud1*), aspartate aminotransferase (*Got2*), alanine aminotransferase 1 (*Gpt1*), alanine aminotransferase 2 (*Gpt2*), branched-chain aminotransferase 1 (*Bcat1*), branched-chain aminotransferase 2 (*Bcat2*), pyruvate carboxylase (*Pcx*), glutamate decarboxylase 1 (*Gad1*), standardized to *Ppia*. All bar graphs show the mean ± SEM. * $p<0.05$, *Npc1*$^{-/-}$ vs. WT.

Glud1 and *Bcat1* mRNA levels were increased in 5-week-old *Npc1*$^{-/-}$ hippocampus; whereas mRNA levels of other aminotransferases *Got2*, *Gpt1/2*, and *Bcat2* were unchanged (Figure 3.21 D-I). Furthermore, *Pcx* mRNA levels were unchanged and *Gad1* mRNA levels were increased in 5-week-old *Npc1*$^{-/-}$ hippocampus (Figure 3.21 J, K). Similar to the cortex, these results show a clear alteration in glutamate metabolism, however the pattern is difficult to interpret.

3.2.4 Altered levels of amino acids in *Npc1*$^{-/-}$ brain

The increased expression of aminotransferases in all brain regions suggested alterations in transamination of glutamate to alpha-ketoglutarate. However, because most enzymes catalyze reversible reactions it is impossible to draw conclusions by measuring mRNA. Therefore, we determined the concentrations of free amino acids in 3- and 5-week-old *Npc1*$^{-/-}$ cerebellum and hippocampus by high performance liquid chromatography (HPLC) (Hospital for Sick Children, Toronto). No changes were observed in glutamate, glutamine, and GABA levels in 3- and 5-week-old *Npc1*$^{-/-}$ cerebellum compared to wildtype (Figure 3.22). The levels of branched chain amino acids (valine, leucine, and isoleucine) were increased in 3- and 5-week-old *Npc1*$^{-/-}$ cerebellum (Figure 3.22). The levels of alanine and aspartate, which are also key transamination substrates, were unaltered in *Npc1*$^{-/-}$ cerebellum (Figure 3.22). However, asparagine, which is formed from aspartate, levels were increased in 3 and 5-week-old *Npc1*$^{-/-}$ cerebellum (Figure 3.22). Additionally, phenylalanine levels were increased at 3 and 5 weeks of age and tyrosine levels were increased at 3 weeks of age in *Npc1*$^{-/-}$ cerebellum (Figure 3.22).

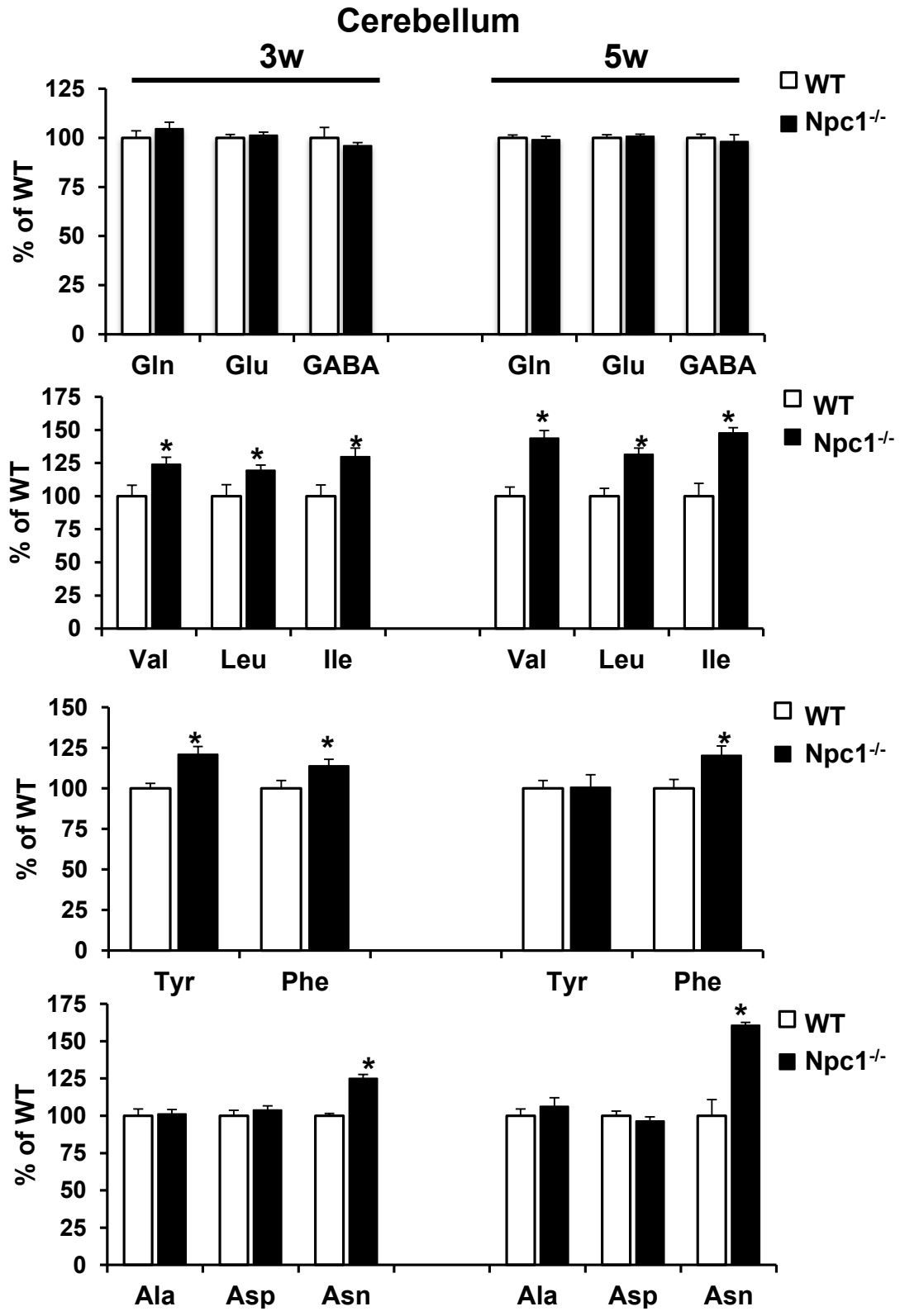
Cerebellum
3w
5w
WT
Npc1-/-
% of WT
Gln
Glu
GABA
Val
Leu
Ile
Tyr
Phe
Ala
Asp
Asn

Figure 3.22 Altered amino acid levels in *Npc1*$^{-/-}$ cerebellum
A-D) Aqueous extracts were prepared from snap-frozen cerebella of 3- or 5-week-old wildtype (WT) and *Npc1*$^{-/-}$ mice. Free amino acids were analyzed by reverse-phase HPLC and absorbance detection following pre-column derivatization with phenylisothiocyanate. Data are expressed as mole percent of each amino acid per total free amino acids expressed per the average of all WT samples of the same age. Gln: glutamine, Glu: glutamate, GABA: gamma-aminobutyric acid, Val: valine, Leu: leucine, Ile: isoleucine, Tyr: tyrosine, Phe: phenylalanine, Ala: alanine, Asp: aspartate, Asn: asparagine. Shown are means ± SEM, of 6 to 8 mice each genotype each age. * $p < 0.05$.

Glutamate, glutamine, and GABA levels were unaltered in 3- and 5-week-old hippocampus (Figure 3.23). Branched chain amino acid levels were unchanged at 3 weeks and at 5 weeks of age leucine and isoleucine levels were increased but valine levels were unchanged in *Npc1*$^{-/-}$ hippocampus (Figure 3.23). Furthermore, alanine levels were unchanged at 3 and 5 weeks of age and aspartate was unchanged at 3 weeks but decreased at 5 weeks of age in *Npc1*$^{-/-}$ hippocampus (Figure 3.23). Even though aspartate levels were decreased, asparagine levels were increased in 3- and 5-week-old *Npc1*$^{-/-}$ hippocampus (Figure 3.23). Furthermore, phenylalanine levels were increased at 3 and 5 weeks of age and tyrosine levels were not significantly different in *Npc1*$^{-/-}$ hippocampus (Figure 3.23). Together, increased branched chain amino acids and asparagine support increased conversion of glutamate to alpha ketoglutarate by aminotransferases in *Npc1*$^{-/-}$ cerebellum and hippocampus. Table 3.1 presents a summary of changes in metabolite, mRNA, and protein levels in *Npc1*$^{-/-}$ brain regions.

3.2.5 Altered glycolysis and mitochondrial dysfunction in NPC1-deficient neuroblastoma cells, primary neurons, and primary astrocytes

Except for cell-specific isoforms, it was unclear whether changes occurred in neurons or astrocytes. To further explore energy metabolic alterations in each cell type, I used two neuronal models: primary cortical neurons from embryonic day 17 *Npc1*$^{-/-}$ mice grown in culture for 14 days and a human neuroblastoma (SHSY) cell line that stably expressed shRNA targeting NPC1 (shNPC1). Primary cortical astrocytes were prepared from 3-day-old *Npc1*$^{-/-}$ and wildtype mice.

Primary neurons from *Npc1*$^{-/-}$ mice showed increased mRNA levels of the antioxidant defense gene, *Nfe2l2*, and increased nitrotyrosine immunoreactivity (Figure

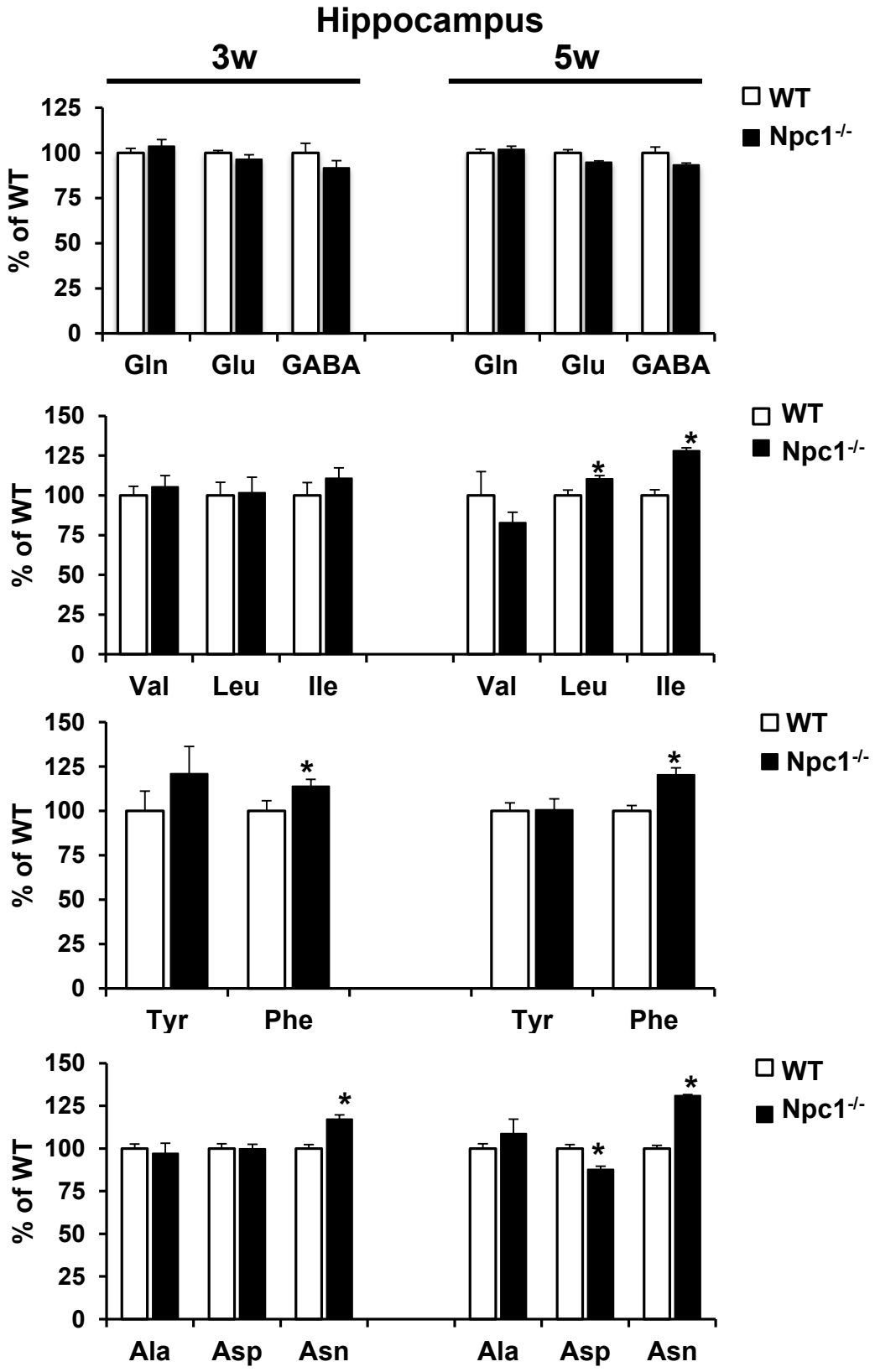
Hippocampus
3w
5w
WT
Npc1-/-
% of WT
125
100
75
50
25
0
Gln
Glu
GABA
150
Val
Leu
Ile
Tyr
Phe
Ala
Asp
Asn
*

Figure 3.23 Altered amino acid levels in *Npc1*$^{-/-}$ hippocampus
A-D) Aqueous extracts were prepared from snap-frozen hippocampi of 3- or 5-week-old wildtype (WT) and *Npc1*$^{-/-}$ mice. Free amino acids were analyzed by reverse-phase HPLC and absorbance detection following pre-column derivatization with phenylisothiocyanate. Data are expressed as mole percent of each amino acid per total free amino acids expressed per the average of all WT samples of the same age. Shown are means ± SEM, of 6 to 8 mice each genotype each age. * $p < 0.05$.

Table 3.1. Summary of metabolite, mRNA, and protein levels in *Npc1*$^{-/-}$ brain

	Cerebellum			Cortex			Hippocampus	
	3w	5w	7w	3w	5w	7w	3w	5w
Ntyr			↑			↑		
Nfe2l2	↑	↑	↑		↑			↑
Hmox1	↑	↑	↑					
Sod1	↑	↑	↑					
SOD2	↑							
pJNK	↑	↑						
Ucp2	↑	↑	↑					
mtDNA		↓						
Mtco2	N.S.	↓	↓					
Ppargc1a	N.S.	↑	↓					
Pdha	↓	N.S.						N.S.
pPDH		↑			↑			↓
PDH		↓						↑
Pdk1/2	N.S.	↑	N.S.		↑			
KGDH		N.S.			N.S.			↓
GLUT1			↑					
Pfk1	N.S.	↑			↑			↑
PFK1p	N.S.	↑						
Eno1	↑	↑	N.S.					
Eno2	N.S.	N.S.	↓					
PKM1/2	N.S.	N.S.						↑
PKM2	↑	↑						↑
Ldha	↑	↑	N.S.					
G6pd	↓	N.S.	N.S.					
Glu1	↑	↑	↑		↓			↑
Glud1	N.S.	N.S.	↑		↑			
Gls1	N.S.	N.S.	N.S.					N.S.
Gls2	N.S.	↑	↓		N.S.			N.S.
Gad1	N.S.	N.S.	↓		N.S.			↑
Got2	↑	↑	↑					N.S.
Gpt1	N.S.	N.S.	N.S.					N.S.
Gpt2	N.S.	N.S.	↑		N.S.			N.S.
Bcat1	N.S.	↑	↑					↑
Bcat2	N.S.	↑	↑		↑			N.S.
Pcx	↑	↑	N.S.		↓			N.S.
Me1	↓	N.S.	N.S.					
Me3	N.S.	N.S.	N.S.					
Lactate	↑	↑	↑	↑	↑	↑	N.S.	N.S.
Alanine	N.S.	N.S.	↑	N.S.	↑	N.S.	N.S.	N.S.
Acetyl-CoA	↓	N.S.	↓	↓	N.S.	↓	↓	↓
Valine	↑	↑					N.S.	N.S.

	Cerebellum			Cortex			Hippocampus	
	3w	5w	7w	3w	5w	7w	3w	5w
Leucine	↑	↑					N.S.	↑
Isoleucine	↑	↑					N.S.	↑
Tyrosine	N.S.	↑					N.S.	N.S.
Phenylalanine	↑	↑					↑	↑
Aspartate	N.S.	N.S.					N.S.	↓
Asparagine	↑	↑					↑	↑

Not significantly different (N.S.)
Non-measured are blank squares

3.24 A, B). In SHSY cells, immunoblotting for NPC1 and filipin staining confirmed the depletion of NPC1 and accumulation of endosomal cholesterol by expression of shNPC1 (Figure 3.25 A, B). SHSY cells expressing shNPC1 produced more hydrogen peroxide than cells transfected with non-targeting shRNA (Figure 3.25 C). Preliminary results show decreased cytosolic and mitochondrial levels of reduced glutathione in NPC1-depleted SHSY cells (Figure 3.25 D). Together these results suggest that oxidative stress is at least in part neuronal-derived.

Lactate levels are increased in *Npc1*$^{-/-}$ cerebellum and cortex and mRNA of several glycolytic enzymes are increased in all brain regions. To determine whether *Npc1*$^{-/-}$ cerebral cortical astrocytes produced different amounts of lactate, astrocytic lactate production was measured. *Npc1*$^{-/-}$ astrocytes produced more lactate than wildtype astrocytes suggesting that loss of NPC1 in astrocytes caused increased lactate production (Figure 3.26 A).

To investigate whether glycolysis was increased in neurons we used NPC1-deficient SHSY cells and primary cortical neurons from *Npc1*$^{-/-}$ mice. Preliminary results show that NPC1-deficient SHSY cells produced increased lactate compared to controls suggesting that NPC1-deficiency caused increased glycolysis in a neuronal cell line (Figure 3.26 B). Preliminary results show that ATP levels were increased in NPC1-deficient SHSY cells compared to SHSY cells transfected with non-targeting shRNA, which would further support the hypothesis that glycolysis is increased in NPC1-deficient SHSY cells (Figure 3.26 C). Furthermore preliminary results show that supplementation of medium with lactate, increased ATP levels in control but not NPC1-depleted SHSY cells suggesting that NPC1-deficient SHSY cells do not use lactate as an energy source

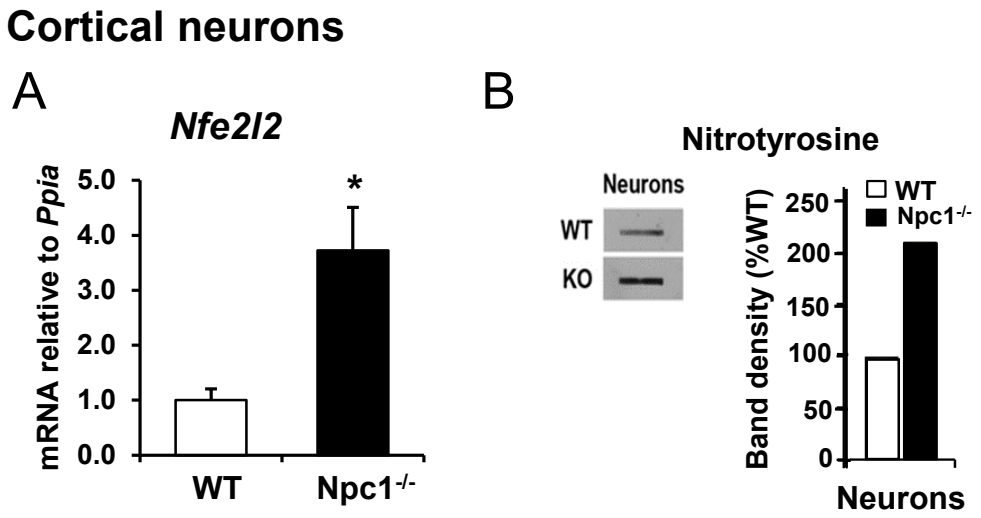

Figure 3.24 Increased oxidative stress in *Npc1*$^{-/-}$ primary cortical neurons
A) RNA was prepared from primary *Npc1*$^{-/-}$ cortical neuron. Nuclear factor (erythroid-derived 2)-like 2 (*Nfe2l2*) mRNA levels were analyzed by qPCR standardized to *Ppia*. Bar graph shows the mean ± SEM. * $p<0.05$, *Npc1*$^{-/-}$ vs. WT. Data were derived from five different neuron preparations per genotype. B) Preliminary immunoblot analysis of homogenates of primary WT and *Npc1*$^{-/-}$ cortical neurons using antibodies against nitrotyrosine. Bar graph shows the mean ratio of band intensity of nitrotryosine expressed as percent WT.

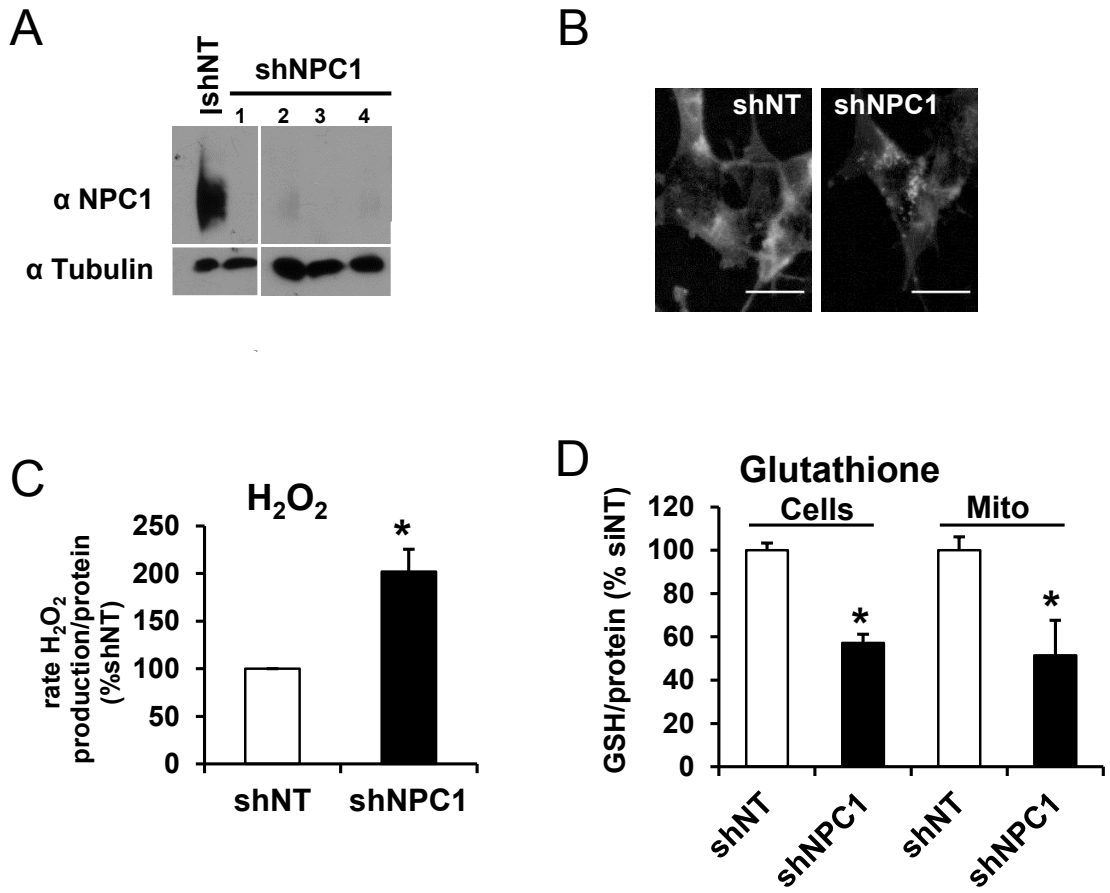

Figure 3.25 Increased ROS production and decreased glutathione levels in NPC1-depleted SHSY neuroblastoma cells

A) Immunoblot of homogenates of SHSY stably transfected with non-targeting shRNA (shNT) or 4 independent SHSY clones (1-4) transfected with shRNA against NPC1 (shNPC1) using antibodies against NPC1 and tubulin as a loading control. B) Filipin stain of SHSY cells transfected with shNT or shNPC1. Scale bar = 50 μm. C) Rate of ROS generation measured as fluorescence generated by amplex red reaction per second per protein. Data are expressed as percent of SHSY cells transfected with shNT of the same experiment, and are derived from three independent experiments. D) Reduced glutathione (GSH) levels in cellular homogenates (cells) or mitochondria (mito) isolated from SHSY cells transfected with shNT or shNPC1 expressed as percent control (shNT). Data were derived from two independent experiments in duplicate. All bar graphs show the means ± SEM. * $p<0.05$, shNPC1 vs. shNT.

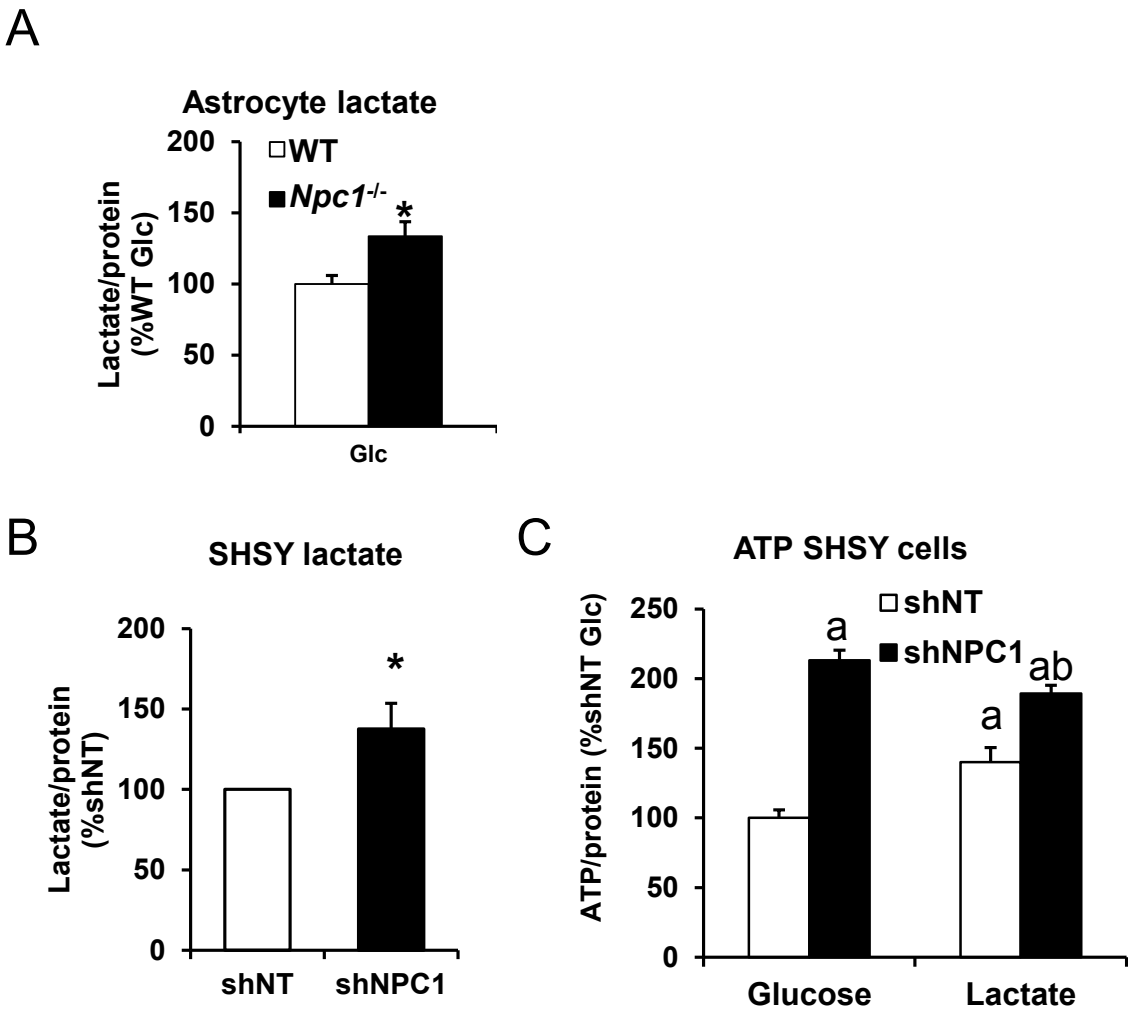

Figure 3.26 Increased lactate production by *Npc1*$^{-/-}$ primary astrocytes and NPC1-depleted SHSY neuroblastoma cells

A) Lactate production by primary WT and *Npc1*$^{-/-}$ astrocytes in the presence of glucose (Glc) alone. Data expressed as percent of WT the same experiment, and are derived from three independent experiments. B) Lactate production by SHSY cells transfected with non-targeting shRNA (shNT) or shRNA against NPC1 (shNPC1) in the presence of glucose alone. Data were derived from two independent experiments. C) ATP levels in SHSY cells transfected with shNT or shNPC1 in the presence of glucose or glucose and lactate. Bar graphs shows the mean ± SEM. Data is derived from two independent experiments in quadruplicate. * $p<0.05$, *Npc1*$^{-/-}$ vs. WT or shNPC1 vs. shNT. [a] $p < 0.05$ vs. siNT Glucose; [b] $p < 0.05$ vs. siNT Lactate

(Figure 3.26 C). Together these results suggest that NPC1-deficient SHSY cells have increased glycolysis, which results in increased ATP levels. Additionally, because lactate addition did not increase ATP levels, this may suggest that NPC1-deficient SHSY cells do not oxidize pyruvate (which is derived from lactate).

Primary neurons did not produce measurable amounts of lactate, in line with their metabolic profile in the brain. Therefore to investigate glycolysis in primary neurons we measured uptake of [^{3}H]-2-deoxyglucose in neurons from wildtype and *Npc1*$^{-/-}$ mouse cerebral cortex. [^{3}H]-2-deoxyglucose is taken through GLUT and phosphorylated by hexokinase. When glucose was the only energy substrate provided, *Npc1*$^{-/-}$ neurons took up more [^{3}H]-2-deoxyglucose than wildtype (Figure 3.27 A). Addition of glutamine decreased [^{3}H]-2-deoxyglucose uptake by *Npc1*$^{-/-}$ neurons, but had no effect on glucose uptake in wildtype neurons suggesting that *Npc1*$^{-/-}$ neurons preferred glutamate over glucose as an energy source (Figure 3.27 A). Measurements of glucose uptake in astrocytes was more variable between preparations. In two individual experiments glucose uptake was increased and in the other two experiments glucose uptake was decreased in *Npc1*$^{-/-}$ astrocytes compared to wildtype astrocytes. Therefore on average there were no significant differences between wildtype and *Npc1*$^{-/-}$ glia in the presence of glucose and/or glutamate (Figure 3.27 B). Further work is required to determine the reason for high variability in glucose uptake measurements in glia, such as the activation state or composition of cells between experiments.

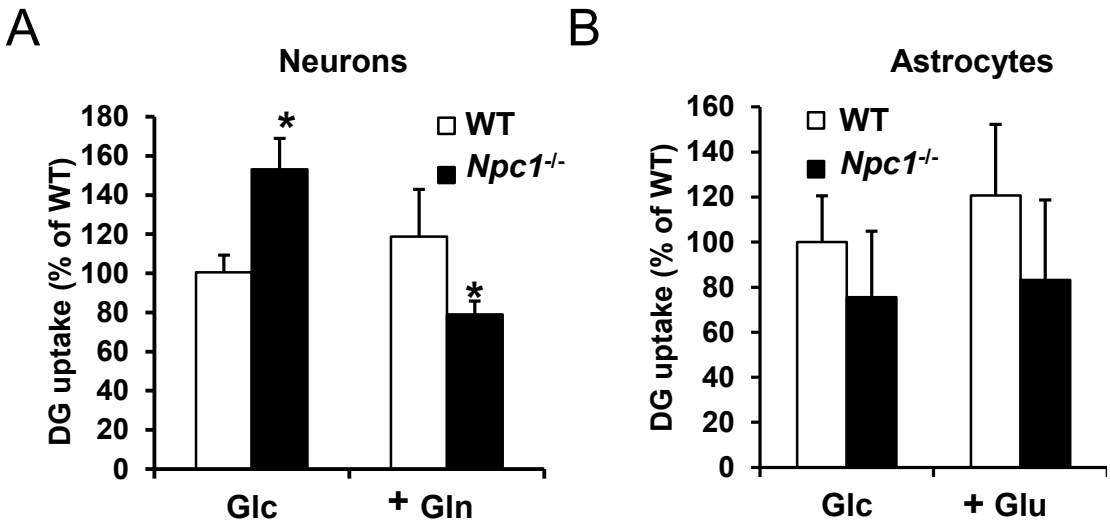

Figure 3.27 Altered glucose uptake by *Npc1*$^{-/-}$ neurons in the presence or absence of glutamine

A) ^{3}H-2-deoxyglucose uptake by primary cortical WT and *Npc1*$^{-/-}$ neurons in the presence of glucose alone (Glc) or glucose and glutamine (Gln). B) ^{3}H-2-deoxyglucose uptake by primary cortical WT and *Npc1*$^{-/-}$ astrocytes in the presence of glucose alone (Glc) or glucose and glutamate (Glu). Data expressed as percent of WT of the same experiment, and are derived from at least three independent experiments. Bar graphs shows the mean ± SEM. * $p<0.05$, *Npc1*$^{-/-}$ vs. WT or shNPC1 vs. shNT.

3.3 Mitochondrial cholesterol in Npc1-/- cells

With the exception of some preliminary data or data not published, the work in chapter 3.3 was published in three papers 1) J Lipid Res. 2010 May;51(5): 1023-34 [147] 2) J Lipid Res. 2012 Dec;53(12):2632-42 [267] and 3) J Biol Chem. 2014 Jun 6;289(23):16278-16289 [316]. In addition to myself, Dr. Barbara Karten, Mark Charman, and Dr. Nolan Osborne contributed to the work presented. I was involved in the conceptualization of all data and performed the experiments in all figures with the exception of figure 3.34 D, which was performed by Dr. Barbara Karten.

The disruption in cholesterol homeostasis in *Npc1*$^{-/-}$ cells could affect mitochondrial cholesterol levels which could lead to mitochondrial dysfunction. One previous report had found increased mitochondrial cholesterol levels in 9-week-old *Npc1*$^{-/-}$ mouse brain [144]. However, the lack of endosomal membrane markers used in that study cast some doubt on the purity of mitochondria isolated by density gradient ultracentrifugation. To address these concerns we isolated mitochondria by density gradient ultracentrifugation or immunoisolation and used endosomal membrane markers to show purity of mitochondrial fractions. Additionally, we identified proteins involved in the transport of cholesterol to mitochondria.

3.3.1 Increased cholesterol levels in mitochondrial isolated from *Npc1*$^{-/-}$ mouse brain

At 9 weeks of age, *Npc1*$^{-/-}$ mice are at an advanced stage of disease. To determine whether cholesterol accumulates in mitochondria at earlier stages of disease, I isolated mitochondria from 7-week-old *Npc1*$^{-/-}$ murine brain. The absence of an

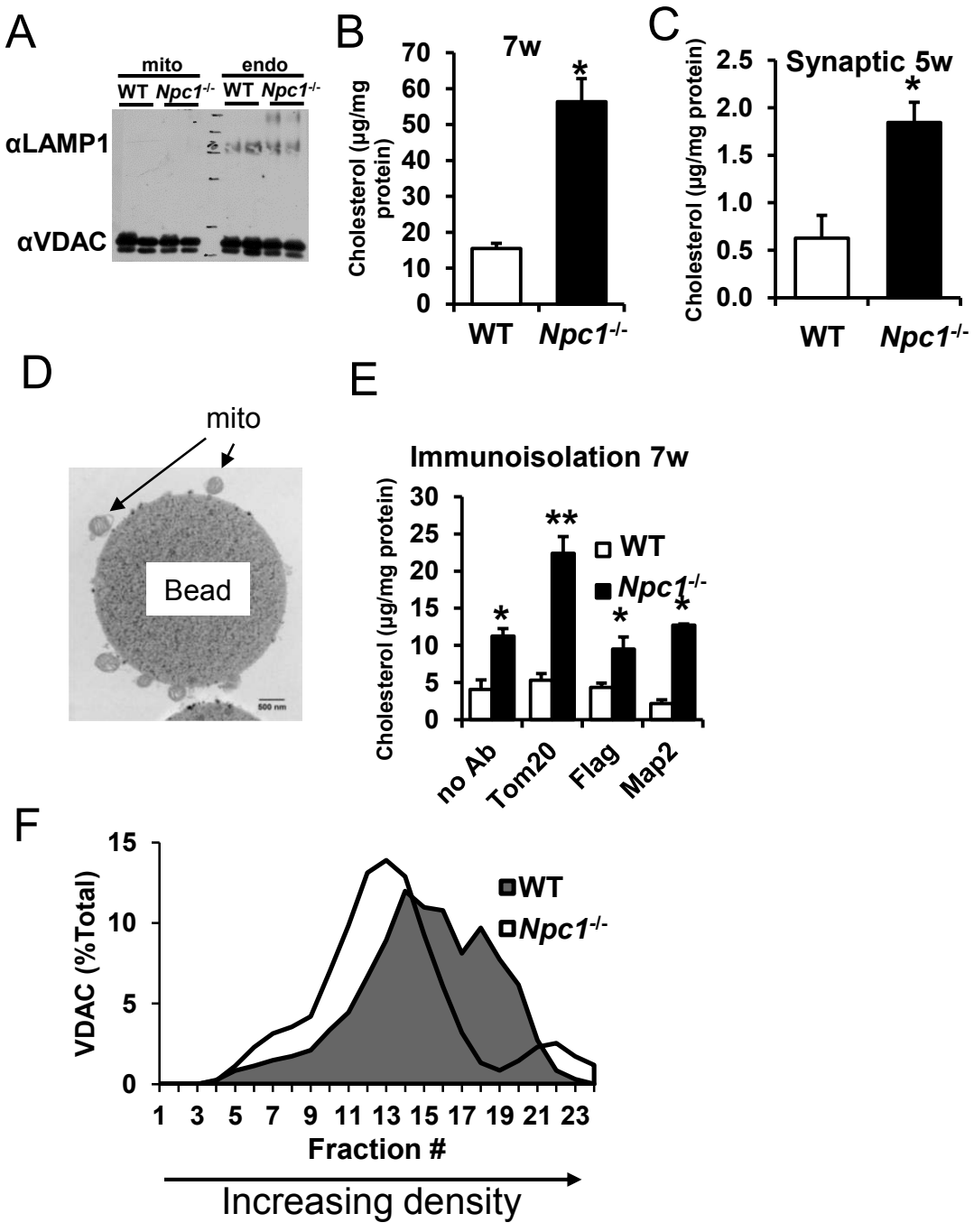
A
mito
endo
WT Npc1-/- WT Npc1-/-
αLAMP1
αVDAC
B
7w
Cholesterol (µg/mg protein)
70
60
50
40
30
20
10
0
*
WT
Npc1-/-
C
Synaptic 5w
Cholesterol (µg/mg protein)
2.5
2.0
1.5
1.0
0.5
0.0
*
WT
Npc1-/-
D
mito
Bead
500 nm
E
Immunoisolation 7w
Cholesterol (µg/mg protein)
30
25
20
15
10
5
0
**
*
*
*
WT
Npc1-/-
no Ab
Tom20
Flag
Map2
F
VDAC (%Total)
15
10
5
0
WT
Npc1-/-
1 3 5 7 9 11 13 15 17 19 21 23
Fraction #
Increasing density

Figure 3.28 Increased mitochondrial cholesterol in *Npc1*$^{-/-}$ murine brain
A-B) Mitochondria were isolated from 7-week-old wildtype (WT) and *Npc1*$^{-/-}$ murine brain by density gradient ultracentrifugation. A) Mitochondria (mito) and endosomes/lysosomes (endo) were analyzed by immunoblotting with antibodies against mitochondrial marker voltage-dependent anion channel (VDAC) and endosomal/lysosomal marker lysosomal-associated membrane protein 1 (LAMP1). B) Unesterified cholesterol determined with the Amplex Red assay. C) Synaptic mitochondria were isolated from 5-week-old WT and *Npc1*$^{-/-}$ murine brain by density gradient ultracentrifugation. Unesterified cholesterol determined with the Amplex Red assay. D, E) Mitochondria were isolated from 7-week-old wildtype and *Npc1*$^{-/-}$ murine brain by immunoisolation using anti-Tom20 antibodies (Tom20) bound to magnetic beads. No antibodies (no ab), anti-Flag (Flag), or anti-Map2 (Map2) were used as negative controls. D) Electron micrograph of immunoisolated mitochondria using anti-Tom20, 40000× magnification. Scale bar = 500 nm. E) Unesterified cholesterol determined with the Amplex Red assay. Cholesterol data are standardized to mitochondrial protein and represent means ± SEM of three independent experiments. Immunoblots are representative of three independent experiments. F) Mitochondria were isolated from 7-week-old WT and *Npc1*$^{-/-}$ murine brain by sucrose density gradient ultracentrifugation. Graphs show the ratio of band intensity of VDAC expressed as percent total VDAC per genotype. Data are representative of three independent experiments. Bar graphs shows the mean ± SEM. * $p<0.05$, *Npc1*$^{-/-}$ vs. WT. ** $p<0.05$ *Npc1*$^{-/-}$vs. WT and all *Npc1*$^{-/-}$ negative controls.

endosome/lysosome marker (LAMP1) by immunoblot analysis confirmed the purity of mitochondria isolated by ultracentrifugation on a Percoll gradient (Figure 3.28 A). Mitochondrial cholesterol levels in *Npc1*$^{-/-}$ mouse brain were increased three-fold compared to wildtype at 7 weeks of age (Figure 3.28 B). The mitochondria isolated above were from whole brain and included mitochondria from glia, neuronal cell bodies, and neuronal synapses from multiple brain regions. In a preliminary experiment, I isolated synaptic mitochondria from whole brain by ultracentrifugation over a Percoll gradient. Synaptic mitochondria isolated from 5-week-old *Npc1*$^{-/-}$ mouse had three-fold higher cholesterol levels compared to wildtype control mitochondria (Figure 3.28 C).

Although immunoblots showed a lack of contamination by other organelles, small amounts of membrane contamination could have remained undetected. In view of the massive accumulation of cholesterol in *Npc1*$^{-/-}$ endosomes, even a small contamination could have a large effect on cholesterol measurements of mitochondria. To address this concern I established an immunoisolation procedure on enriched mitochondrial fractions from brain lysates using magnetic beads bound to antibodies that specifically recognize a cytosolic epitope of the outer mitochondrial membrane protein Tom20 (anti-Tom20). Immunoisolation does not rely on the density of organelles and therefore is less prone to contamination with other membranes. We confirmed the purity of mitochondria by electron microscopy of the immunoisolation, which showed no other organelles bound to the beads (Figure 3.28 D). Although negative controls (beads ± antibodies (anti-Map2, anti-Flag) that do not target mitochondrial proteins) had small amounts of cholesterol, bound mitochondria isolated by anti-Tom20 immunoisolation from 7-week-old *Npc1*$^{-/-}$

mouse brain had higher cholesterol levels compared to wildtype and controls (Figure 3.28 E).

The higher cholesterol content was also reflected in preliminary experiments that showed a shift to lower density of mitochondria from 7-week-old *Npc1*$^{-/-}$ mouse brain compared to wildtype mitochondria. This result was evident by VDAC immunoreactivity in lower density fractions of a sucrose gradient after ultracentrifugation (Figure 3.28 F).

3.3.2 Increased mitochondrial cholesterol in NPC1 deficient CHO cells

The brain is not suitable for determining the transport of cholesterol to mitochondria therefore we used Chinese hamster ovary (CHO) cells. CHO were previously established as a model to study transport of cholesterol to mitochondria in our lab and are a commonly used model in for the study of NPC disease. To determine whether mitochondrial cholesterol accumulated in 4-4-19 cells we isolated mitochondria by ultracentrifugation over a Percoll gradient. The lack of endosomal protein markers confirmed the purity of mitochondria isolated by ultracentrifugation over a Percoll gradient from wildtype and 4-4-19 cells (Figure 3.29 A). Similar to mouse brain, mitochondria isolated from 4-4-19 cells had three-fold higher cholesterol levels compared to wildtype CHO cells (Figure 3.29 C). In a second purification approach, crude mitochondrial were trypsinized to break any potential protein-to-protein interactions between mitochondria and other membranes to further ensure that non-mitochondrial membranes did not contaminate the mitochondrial fraction. A brief trypsinization had no effect on mitochondrial structure (Figure 3.29 B). Similar to non-trypsinized mitochondria, trypsinized mitochondria isolated from 4-4-19 cells had higher mitochondrial cholesterol levels than wildtype CHO cells (Figure 3.29 C). Additionally, I

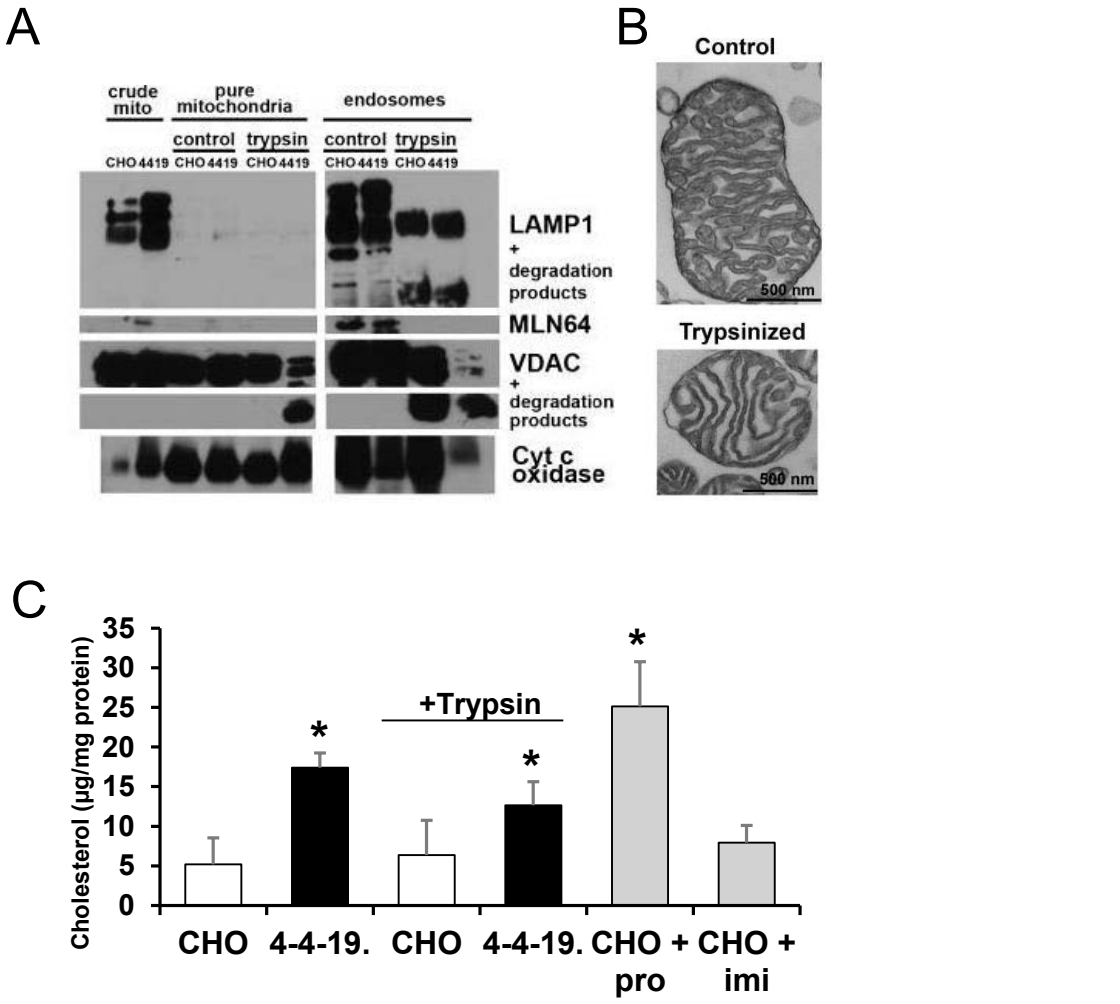

Figure 3.29 Increased mitochondrial cholesterol levels in NPC1-deficient CHO cells

A, B, C) Mitochondria were isolated from CHO and 4-4-19 cells grown in serum-containing medium by Percoll density ultracentrifugation following brief incubation with or without trypsin. A) Crude mitochondria (crude mito), purified-mitochondrial fraction (pure mito), endosomes analyzed by immunoblotting with antibodies against mitochondrial markers voltage-dependent anion channel (VDAC) and cytochrome c oxidase (Cyt c oxidase) and endosomal/lysosomal markers lysosomal-associated membrane protein 1 (LAMP1), and metastatic lymph node 64 (MLN64). B) Electron micrograph of non-trypsinized and trypsinized mitochondria, 40,000× magnification. Bars = 500 nm. C) Unesterified cholesterol in mitochondria determined with the Amplex Red assay. Where indicated, CHO cells were treated with 40 µM imipramine (imi) or 20 µM progesterone (pro) for 48 h prior to analysis. Cholesterol data are standardized to mitochondrial protein and represent means ± SEM of three independent experiments (* $P < 0.05$).

measured mitochondrial cholesterol levels in wildtype CHO cells that were treated with progesterone or imipramine to induce endosomal cholesterol accumulation [317, 318]. Progesterone but not imipramine treatment increased mitochondrial cholesterol levels (Figure 3.29 C). The normal mitochondrial cholesterol levels in the presence of endosomal cholesterol accumulation in imipramine-treated cells underlined the lack of contamination of the mitochondrial fraction with endosomes, but further investigation regarding the difference between progesterone and imipramine is required.

The Liscum lab established 4-4-19 cells nearly 2 decades ago and therefore these cells may have accumulated secondary mutations that affect mitochondrial cholesterol levels. To determine whether mitochondrial cholesterol accumulates in a short-term model of NPC1-deficiency, I isolated mitochondria from CHO cells transfected with non-targeting shRNA (shNT) or shRNA targeting NPC1 (shNPC1). NPC1 protein levels were reduced and cholesterol accumulated in endosomes by transfection with shNPC1 (Figure 3.30 A). The lack of endosomal protein markers showed purity of mitochondria isolated by ultracentrifugation over a Percoll gradient from shNT or shNPC1 transfected cells (Figure 3.30 B). As expected cholesterol levels were increased in the endosomal fraction isolated from NPC1-depleted CHO cells compared to control cells ten day post-transfection (Figure 3.30 C). Even after such brief periods of NPC1-depletion, mitochondrial cholesterol levels were three times higher in cells transfected with shNPC1 than shNT (Figure 3.30 D).

3.3.3 Normal cholesterol transport to the inner mitochondrial membrane in NPC1-deficient cells

To determine mechanisms of cholesterol transport to mitochondria in NPC1-deficient CHO cells we used a previously established system to measure arrival of

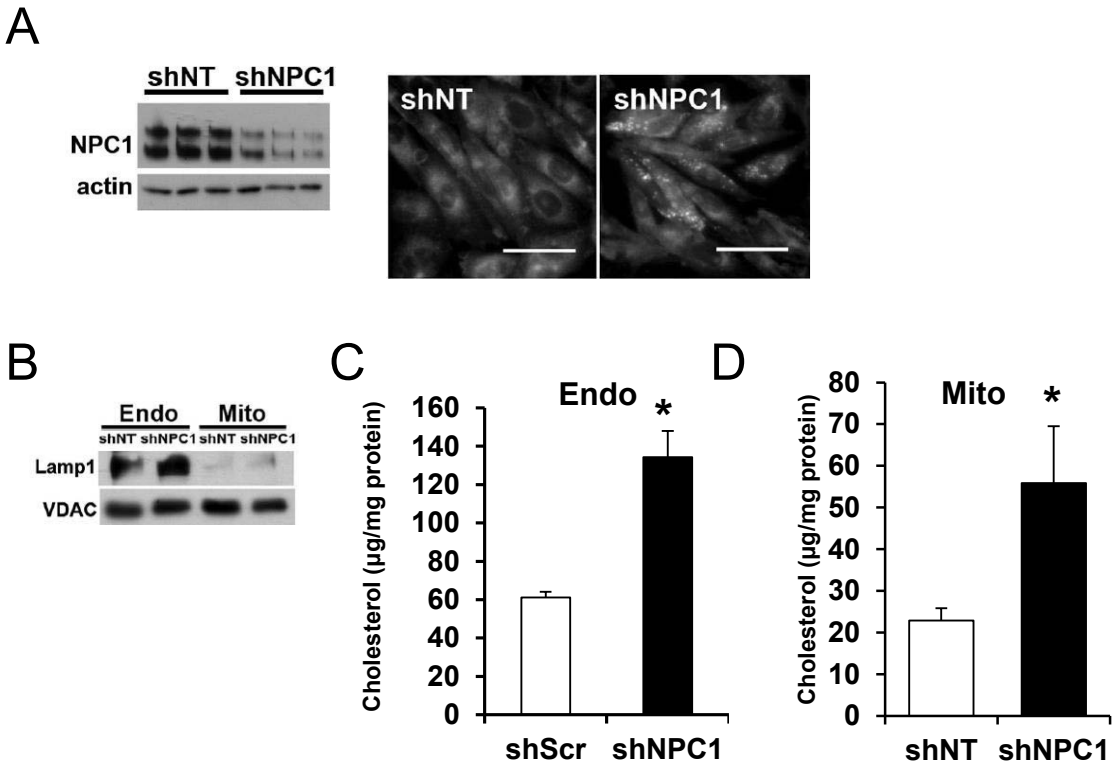

Figure 3.30 Increased mitochondrial cholesterol levels in NPC1-depleted CHO cells

A-D) Mitochondria were isolated from CHO cells transfected with non-targeting shRNA (shNT) or shRNA targeting NPC1 (shNPC1) grown in serum-containing medium by Percoll density ultracentrifugation following brief incubation with trypsin. A) Filipin stain and NPC1 immunoblot with actin as a loading control. Scale bars: 50 µm. B) Immunoblot of endosomes (endo) and purified mitochondria (mito) prepared from CHO cells expressing shNT or shNPC1 with antibodies against endosomal lysosomal-associated membrane protein 1 (LAMP1) and mitochondrial voltage-dependent anion channel 1 (VDAC1). C, D) Unesterified cholesterol in endosomes (endo) and mitochondria (mito) isolated from CHO cells expressing shNT or shNPC1 determined with the Amplex Red assay. Cholesterol data are standardized to mitochondrial protein and represent means ± SEM of three independent experiments (* $P < 0.05$). Data are derived from three independent experiments. Immunoblots are representatives of three independent experiments.

cholesterol at the inner mitochondrial membrane. Briefly, CHO cells were transfected with an expression vector encoding a mitochondrial-targeted fusion protein (F2) (consistent of a human P450 side chain cleavage enzyme (CYP11A1), ferredoxin reductase, and ferredoxin I) that catalyzes the conversion of cholesterol to pregnenolone [264]. Because CYP11A1 is the only enzyme capable of generating pregnenolone and it localizes to the inner mitochondrial membrane, pregnenolone formation by F2-CHO cells is a measure for cholesterol arrival at inner mitochondrial membrane. Immunofluorescence using antibodies against ferredoxin reductase co-localized with MitoTracker® Red [147]. Moreover, crude mitochondrial fractions but not cytosolic fractions produced pregnenolone (Figure 3.31 A), demonstrating that the F2 complex specifically localized to mitochondria. Additionally, non-transfected CHO cells did not express anti-ferredoxin reductase and produced virtually no pregnenolone in either cytosolic or mitochondrial fractions (Figure 3.31 A)[147]. To confirm that the F2 enzyme complex activity was not rate limiting, F2-CHO cells were treated with 22R-OH Cholesterol, which is converted to pregnenolone by the F2 complex, and is membrane-permeable so that pregnenolone formation is not dependent on transport mechanisms [264, 319, 320]. Addition of 5 μM 22R-OH cholesterol increased pregnenolone production 10-fold confirming that transport of cholesterol to the inner mitochondrial membrane and not enzymatic activity of the F2 protein was the rate-limiting step in the F2-CHO model (Figure 3.31 B).

Transfected with siRNA targeting NPC1 (siNPC1) lead to a 95% reduction of NPC1 protein levels and endosomal cholesterol accumulation in F2-CHO cells

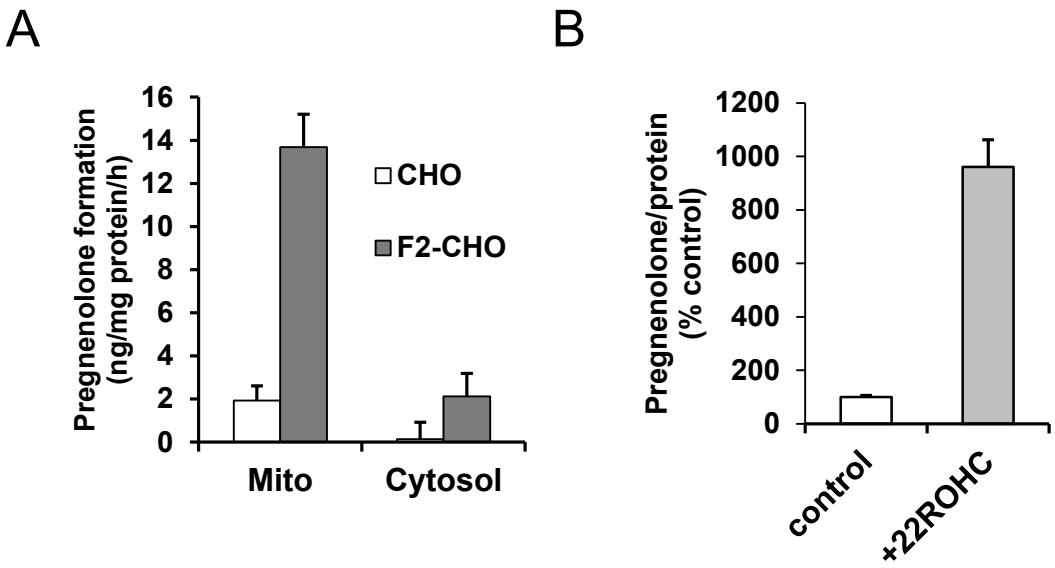

Figure 3.31 Expression of F2-fusion protein of CYP11A1 complex confers the ability to convert cholesterol to pregnenolone in mitochondria

A) CYP11A1 enzymatic activity was determined in crude mitochondria (mito) and in the remaining cell fraction (cytosol) from CHO and F2-CHO cells as pregnenolone production from 22-OH-Cholesterol in the presence of detergent and an NADPH regenerating system. Data represent means ± SEM of quadruplicate measurements. B) Pregnenolone formation from endogenous cholesterol sources (control) or maximum rate of pregnenolone formation from excess membrane-permeable precursor 22-OH-Cholesterol (+22ROHC) during 24 h in intact, adherent F2-CHO cells. Data are expressed as percent of WT ± SEM and are derived from at least three independent experiments.

(Figure 3.32 A). Pregnenolone production did not differ between cells transfected with siNT or with siNPC1 demonstrating that NPC1 is not required for the transport of cholesterol to the inner mitochondrial membrane (Figure 3.32 C). Together with the earlier findings that NPC1-deficiency caused elevated mitochondrial cholesterol levels, the lack of increased cholesterol transport to the inner mitochondrial membrane suggested that cholesterol accumulates in the outer mitochondrial membrane in NPC1-deficient CHO cells. Moreover, imipramine treatment, which failed to increase total mitochondrial cholesterol levels (Figure 3.32 C), did however increase pregnenolone production, suggesting that imipramine activated cholesterol transport to the inner mitochondrial membrane and thus prevented accumulation (Figure 3.32 C).

3.3.4 MLN64 transports cholesterol between endosome and mitochondria

To determine the mechanism of cholesterol transport to mitochondria in *Npc1*$^{-/-}$ cells we depleted several target proteins using RNA interference and measured the effect on mitochondrial cholesterol levels. Because the greatest increase in cholesterol levels is in endosomes we hypothesized that endosomes seemed to be the likely source of cholesterol.

One candidate protein for the transport of cholesterol from endosomes to mitochondria was the cholesterol-binding endosomal transmembrane protein, MLN64. Transfection of CHO cells with two different siRNAs against MLN64 reduced MLN64 protein levels in wildtype CHO cells and in CHO cells co-depleted of NPC1 (Figure 3.32 B). Depletion of MLN64 alone reduced pregnenolone production by 50% in both wildtype cells and cells depleted of NPC1 (Figure 3.32 C). Together these results

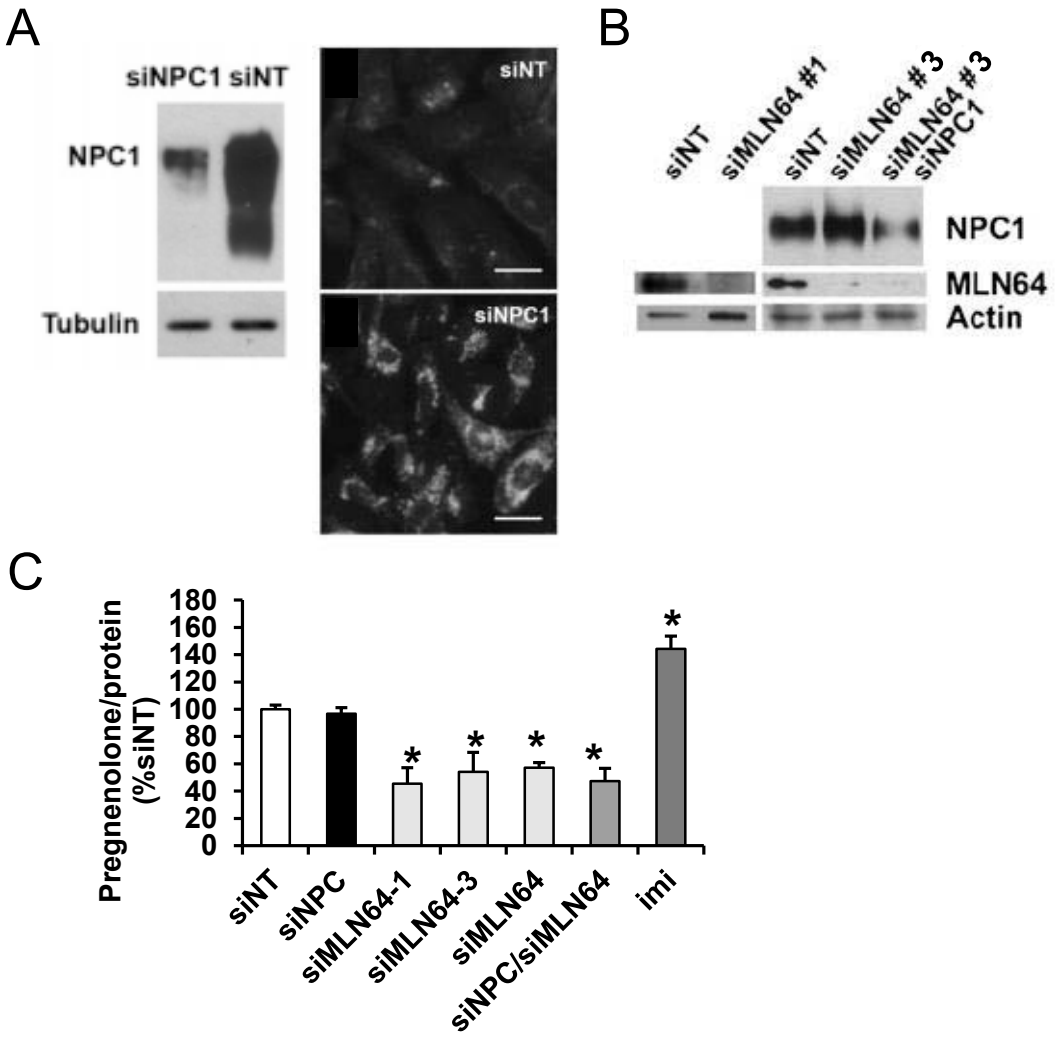
A
siNPC1 siNT
NPC1
Tubulin
siNT
siNPC1
B
siNT
siMLN64 #1
siNT
siMLN64 #3
siMLN64 #3
siNPC1
NPC1
MLN64
Actin
C
Pregnenolone/protein (%siNT)
180
160
140
120
100
80
60
40
20
0
siNT
siNPC
siMLN64-1
siMLN64-3
siMLN64
siNPC/siMLN64
imi

Figure 3.32 Levels of cholesterol transported to the inner mitochondrial membrane are unchanged by siRNA-mediated depletion of NPC1 and decreased by siRNA-mediated depletion of MLN64

A) NPC1 protein levels in F2-CHO cells transfected with non-targeting siRNA (siNT) or siRNA directed against NPC1 (siNPC1), analyzed by immunoblotting. Tubulin was used as a loading control. Shown is one representative blot of five independent experiments. F2-CHO cells transfected with siNT or siNPC1 were stained with filipin to visualize cholesterol accumulation. Scale bars = 40 μm. B) F2-CHO cells transfected with siNT or siMLN64 were analyzed by immunoblotting with antibodies directed against MLN64, NPC1, and actin was used as loading control. C) Pregnenolone formed during 24 h from endogenous cholesterol sources in intact, adherent F2-CHO cells grown in the presence of serum and transfected with siNT, siNPC1, siRNA directed against MLN64 (single siRNA sequence siMLN64 -1 or siMLN64-3, or combined siRNA sequences siMLN64) and/or siNT and treated with 40 μM imipramine for 48 hrs (imi). Data are expressed as percentage of the average of siNT (measured as ng pregnenolone per mg cell protein), means ± SEM, at least four independent experiment with duplicate or triplicate measurements. * $P < 0.05$ compared with siNT.

suggested that MLN64 transported cholesterol to mitochondria in wildtype and in NPC1-depleted CHO cells.

To determine whether depletion of MLN64 could decrease total mitochondrial cholesterol levels in NPC1-deficient cells, I transfected wildtype and 4-4-19 CHO cells with non-targeting siRNA or siRNA targeting MLN64. Depletion of MLN64 reduced MLN64 protein levels in wildtype and 4-4-19 CHO cells (Figure 3.33 A). Endosomal cholesterol levels in 4-4-19 cells were unaffected by depletion of MLN64 (Figure 3.33 B). Despite reducing cholesterol transport to the inner mitochondrial membrane, depletion of MLN64 had no effect on total mitochondrial cholesterol levels in wildtype CHO cells (Figure 3.33 C). However, depletion of MLN64 reduced cholesterol levels in mitochondria isolated from 4-4-19 cells (Figure 3.33 C). Together these results suggested that CHO cells were able to maintain basal levels of mitochondrial cholesterol in the absence of MLN64; however, MLN64 transported excess cholesterol to mitochondria in NPC1-deficient cells.

3.3.5 NPC2 contributes to the transport of cholesterol to mitochondria independent of NPC1

Previous work in our lab showed that siRNA-mediated depletion of NPC2 decreased pregnenolone production and that this decrease was not further reduced by co-depletion of MLN64 [267]. This finding suggested that NPC2 and MLN64 acted in common pathway to transport cholesterol to mitochondria. NPC2 is known to mobilize cholesterol from the inner membranes of multivesicular endosomes to the N-terminal lumenal domain of NPC1 for subsequent distribution to endoplasmic reticulum and plasma membrane [125]. However, because cholesterol is transported to mitochondria independently of NPC1, NPC2 must have additionally deliver cholesterol to MLN64.

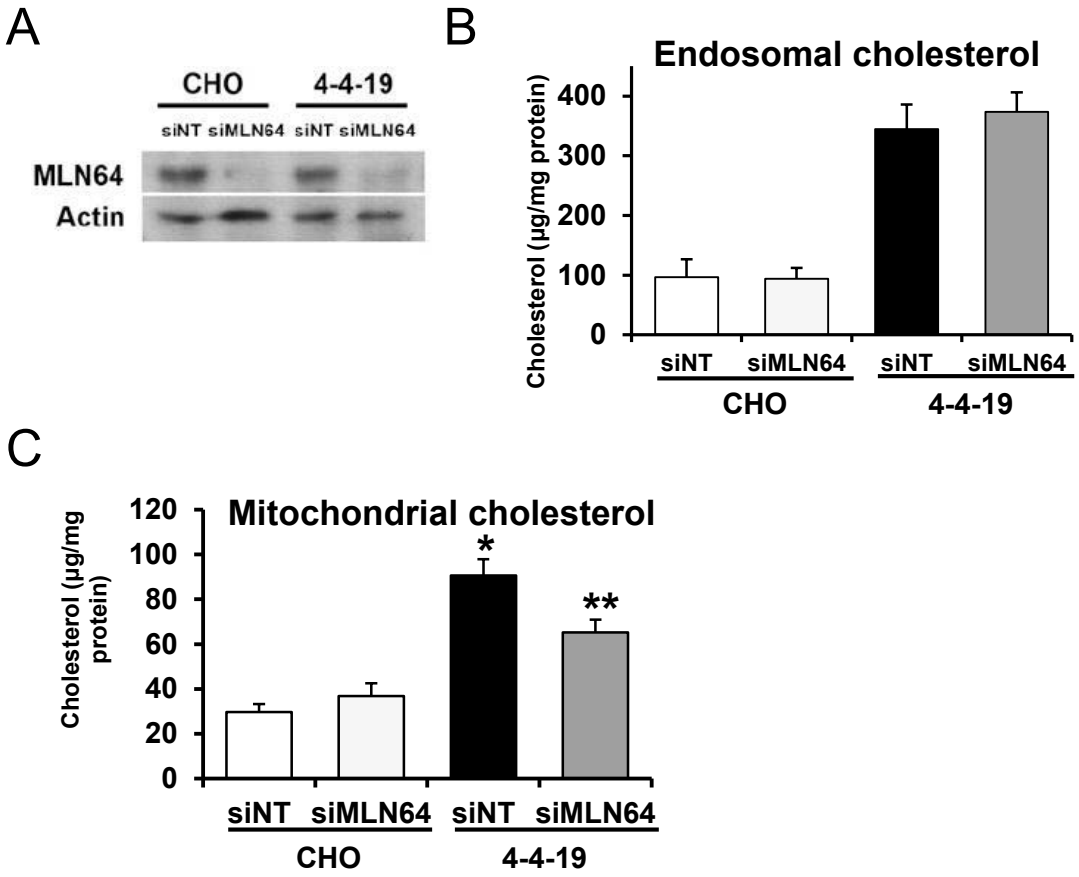

Figure 3.33 Mitochondrial cholesterol content is decreased following depleted of MLN64 in 4-4-19 cells

Mitochondria were isolated from CHO and 4-4-19 cells transfected with non-targeting siRNA (siNT) or siRNA directed against MLN64 (siMLN64) and grown in serum-containing medium for 3 days. A) Immunoblot of cell lysates using anti-MLN64 antibodies. Actin was used as loading control. Shown is one immunoblot representative of three independent experiments. B, C) Unesterified cholesterol determined with the Amplex Red assay in lysosomes/endosomes (B) and mitochondria (C) isolated by Percoll gradient centrifugation. Data are standardized to mitochondrial protein and represent the means ± SEM of three independent experiments. * $P < 0.05$. Data were derived from three independent experiments.

To investigate the role of NPC2 in transport of cholesterol to mitochondria we used previously described NPC2 mutations known to disrupt either the sterol binding site or the ability to transfer cholesterol to NPC1 [125]. Two known point mutations in NPC2, $NPC2^{V81D}$ and $NPC2^{V81A}$, prevent cholesterol transport between NPC2 and NPC1 [125]. $NPC2^{Y119S}$ is unable to bind cholesterol or transfer it to NPC1 [125]. To create a system in which the mutants were expressed but endogenous wildtype NPC2 was depleted we co-transfected F2-CHO cells with siRNA against hamster NPC2 and vectors encoding RNAi resistant human NPC2 mutants. Expression of the human NPC2 mutants was confirmed by reverse transcriptase PCR, and immunoblotting confirmed that the three human NPC2 mutants were expressed at similar levels (Figure 3.34 A, C). Immunoblot and qPCR analysis showed depletion of endogenous hamster NPC2 (Figure 3.34 B, C). Depletion of hamster NPC2 decreased cholesterol ester formation (Figure 3.34 D). As expected from previous reports, expression of human wildtype NPC2 restored cholesterol ester formation in cells depleted of hamster NPC2, while, expression of $NPC2^{V81D}$, $NPC2^{V81A}$, or $NPC2^{Y119S}$ had no effect on cholesterol ester formation in the NPC2-deficient cells (Figure 3.34 D)[125]. Expression of wildtype or any mutant NPC2 in cells transfected with non-targeting siRNA also had no effect on cholesterol ester formation (Figure 3.34 D). These results confirmed that cholesterol transfer from NPC2 to NPC1 was required for endosomal cholesterol transport to endoplasmic reticulum.

To determine whether $NPC2^{V81D}$ could restore cholesterol transport to mitochondria, we measured pregnenolone production in F2-CHO cells. Consistent with previous findings, depletion of endogenous NPC2 alone decreased pregnenolone

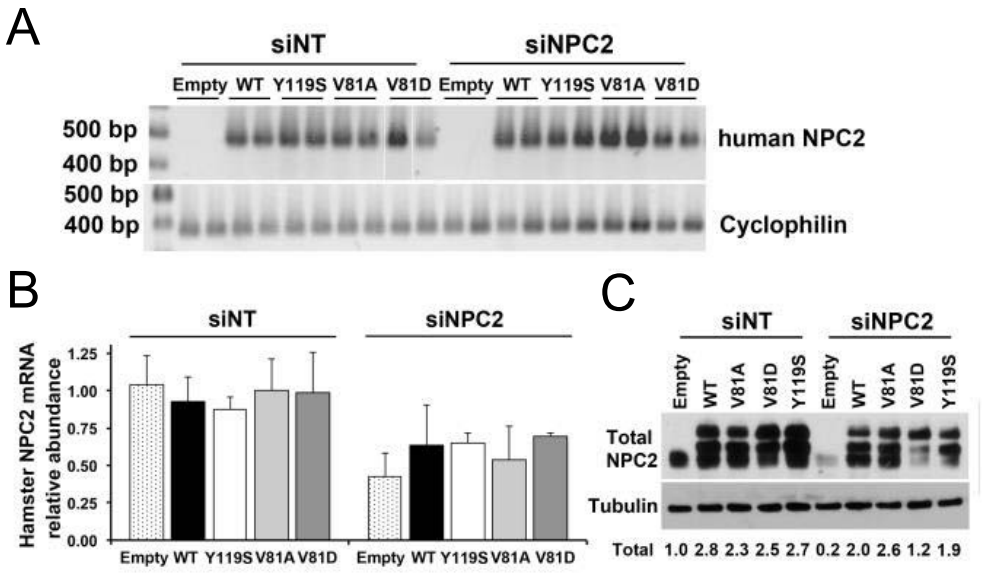
A
siNT
siNPC2
Empty WT Y119S V81A V81D Empty WT Y119S V81A V81D
500 bp
400 bp
human NPC2
500 bp
400 bp
Cyclophilin
B
siNT
siNPC2
Hamster NPC2 mRNA relative abundance
1.25
1.00
0.75
0.50
0.25
0.00
Empty WT Y119S V81A V81D Empty WT Y119S V81A V81D
C
siNT
siNPC2
Empty WT V81A V81D Y119S Empty WT V81A V81D Y119S
Total NPC2
Tubulin
Total 1.0 2.8 2.3 2.5 2.7 0.2 2.0 2.6 1.2 1.9
D
Cholesterol ester
14C-CE (% of siNT empty)
140
120
100
80
60
40
20
0
Empty WT Y119S V81A V81D
siNT
siNPC2
E
Pregnenolone
Pregnenolone/prote in (% of siNT empty)
140
120
100
80
60
40
20
0
siNT
siNPC2

Figure 3.34 Expression of NPC2 with a point mutation in the NPC1-interaction domain normalizes cholesterol transport to mitochondria in F2-CHO cells depleted of endogenous NPC2

CHO cells were cotransfected with non-targeting siRNA (siNT) or siRNA against hamster NPC2 (siNPC2) and with plasmids encoding empty vector (Empty), human flag-tagged NPC2 (WT), human flag-tagged NPC2 with a point mutation in the sterol binding domain (Y119S) or a point mutation in the NPC1-interaction domain (V81A and V81D). A) RT-PCR analysis of expression of human flag-tagged NPC2 and cyclophilin. B) Hamster *Npc2* mRNA levels measured by qPCR standardized to *Ppia* and expressed as percent siNT-Empty. Data are means ± SEM of one representative experiment in triplicate. C) Immunoblot using antibodies that recognize human and hamster NPC2 and antibodies against tubulin as a loading control. Numbers below the blot are the ratio of total NPC2 to tubulin immunoreactivity standardized to siNT-Empty. D) Cholesterol transport to the ER measured as cholesterol ester formation from [^{3}H]oleate and LDL-derived cholesterol. Data are expressed as percent of siNT-empty and represent means ± SEM from two independent experiments in triplicate. *$P < 0.05$ by ANOVA; significantly different from the corresponding condition in siNT. E) Cells were incubated in LPDS medium for 24 h. Serum-free import medium containing LDL was added for 24 h, then collected and analyzed for pregnenolone. Data are calculated as ng pregnenolone/mg protein/24 h and expressed as percentage of siNT-Empty. Data represent means ± SEM from five independent experiments in triplicate. *$P < 0.05$ by ANOVA; compared to corresponding condition in siNT.

production (Figure 3.34 E) [267]. As expected, expression of wildtype NPC2 restored pregnenolone production whereas expression of $NPC2^{Y119S}$ had no effect on pregnenolone production (Figure 3.34 E). In contrast, expression of $NPC2^{V81D}$ and $NPC2^{V81A}$ in NPC2-depleted cells restored pregnenolone formation, suggesting that sterol binding by NPC2 but not sterol transfer to NPC1 was required to transport cholesterol to mitochondria (Figure 3.34 E). Expression of wildtype NPC2 or NPC2 mutants had no effect on pregnenolone production in cells transfected with non-targeting siRNA (Figure 3.34 E).

The expression of NPC2 mutants (summarized in table 3.2) provided us with a model system to alter endosomal and mitochondrial cholesterol. To determine total mitochondrial cholesterol levels, we isolated mitochondria from the NPC2 mutant cells by density gradient ultracentrifugation and measured mitochondrial cholesterol. Since the measurement of mitochondrial cholesterol requires a large number of cells, we generated lentiviral vectors that encode non-targeting shRNA (shNT) or shRNA against hamster NPC2 (shNPC2) and one NPC2 mutant, wildtype NPC2, or the red fluorescent protein mCherry. CHO cells were infected with the lentiviral vectors and mRNA expression analysis confirmed the depletion of endogenous hamster NPC2 by shNPC2 and expression of human NPC2 (Figure 3.35 A). Mitochondria were isolated by ultracentrifugation over a Percoll gradient; lack of endosome or endoplasmic reticulum markers confirmed the purity of the mitochondrial fractions (Figure 3.35 B). The depletion of NPC2 alone had no effect on mitochondrial cholesterol levels compared to control cells (Figure 3.35 C). Expression of wildtype NPC2 and $NPC2^{Y119S}$ also had no effect on mitochondrial cholesterol levels (Figure 3.35 C). In contrast, the expression of

A

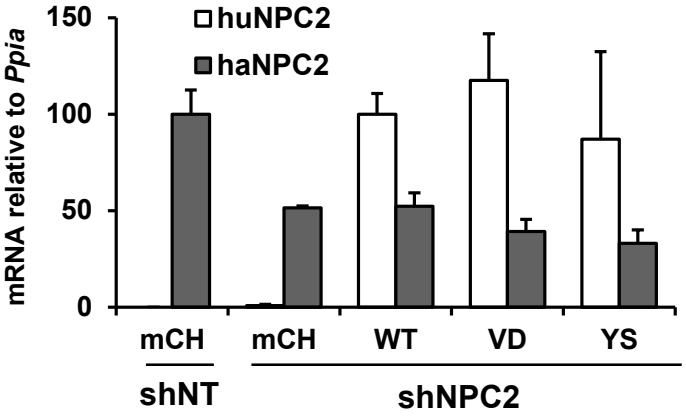
150
100
50
0
mRNA relative to Ppia
huNPC2
haNPC2
mCH
mCH
WT
VD
YS
shNT
shNPC2

B

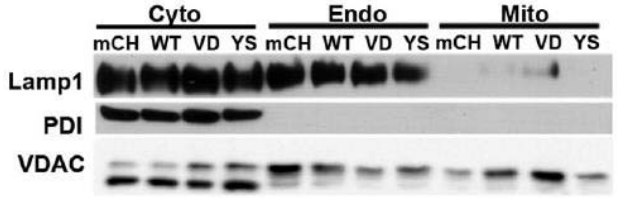
Cyto
Endo
Mito
mCH WT VD YS mCH WT VD YS mCH WT VD YS
Lamp1
PDI
VDAC

C

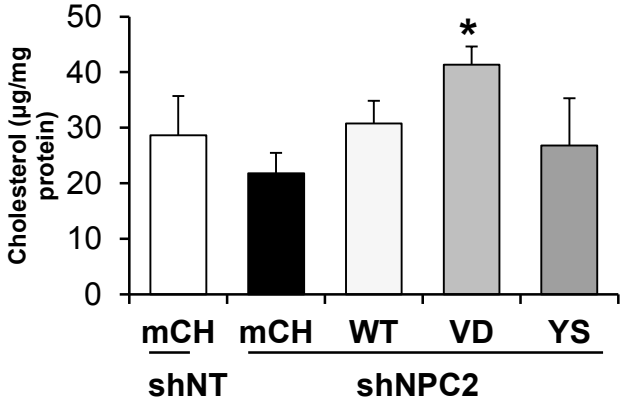
50
40
30
20
10
0
Cholesterol (µg/mg protein)
*
mCH
mCH
WT
VD
YS
shNT
shNPC2

Figure 3.35 Expression of NPC2 with a point mutation in the NPC1-interaction domain increases mitochondrial cholesterol levels in CHO cells depleted of endogenous NPC2

A) RNA was prepared from CHO cells expressing non-targeting shRNA (shNT) or shRNA targeting hamster NPC2 (shNPC2) and expressing mCherry (mCh), wildtype NPC2 (WT), $NPC2^{V81D}$ (VD), or $NPC2^{Y119S}$ (YS). Target gene mRNA levels were analyzed by qPCR using primers against hamster NPC2 (*haNpc2*) or by RT-PCR using primers against human NPC2 (*huNpc2*) standardized to *Ppia*. B) Immunoblot for protein disulfide-isomerase (PDI), lysosome-associated membrane protein 1 (LAMP1), and mitochondrial voltage-dependent anion channel 1 (VDAC1) in cytosolic (cyto) and endosomal (endo) fractions and in enriched mitochondria (mito) prepared from cells expressing non-targeting shRNA (shNT) or shRNA targeting hamster NPC2 (shNPC2) and expressing mCherry (mCh), wildtype NPC2 (WT), $NPC2^{V81D}$ (VD), or $NPC2^{Y119S}$ (YS). The lower band in the VDAC1 immunoblot is an unspecific band that appeared when the membrane was probed with other antibodies. C) Cholesterol levels ± SEM of mitochondria isolated from cells expressing shNT or shNPC2 and mCH, WT, VD, or YS. * $p < 0.05$ vs. shNPC2 mCH. Data were derived from four independent experiments in triplicate.

Table 3.2 Summary of mitochondrial cholesterol levels, lactate production, and *Nfe2l2* expression in CHO cells

Genotype/ phenotype	Pregnenolone (compare to WT)	Mito cholesterol (compared to WT)	Lactate levels (compared to WT)	*Nfe2l2* mRNA levels (compared to WT)
WT	-	-	-	-
Npc1$^{-/-}$	-	↑	↑	↑
Mln64$^{-/-}$	↓	-	-	-
Npc1$^{-/-}$/ siMln64	↓	-	-	-
Npc2$^{-/-}$	↓	-	-	-
Npc2$^{-/-}$ + NPC2^{WT}	-	-	-	-
Npc2$^{-/-}$ + NPC2^{V81D}	-	↑	↑	↑
Npc2$^{-/-}$ + NPC2^{Y119S}	↓	-	-	-

$NPC2^{V81D}$ caused an accumulation of mitochondrial cholesterol in NPC2-depleted cells (Figure 3.35 C). Together these results suggested that both a functional NPC2 sterol-binding site and endosomal cholesterol accumulation were required to increase mitochondrial cholesterol levels.

3.4 Effects of increased mitochondrial cholesterol levels on energy metabolism in NPC1-deficient CHO cells

With the exception of some preliminary data or data not published, the work in chapter 3.4 was published in J Biol Chem. 2014 Jun 6;289(23):16278-16289 [316]. In addition to myself, Dr. Barbara Karten and membranes from Dr. Wolfgang Graier's lab at the Medical University of Graz (Austria) including Corina Madreiter, Neelanjan Vishnu, and Dr. Roland Malli contributed to the work presented. I was involved in the conceptualization of all data and performed the experiments in all figures with the exception of figures 3.40 and 3.43, which were performed by members of Dr. Wolfgang Graier's lab at the Medical University of Graz.

The above findings established mechanisms to manipulate mitochondrial cholesterol levels by genetically altering NPC1, MLN64, and NPC2 expression (findings summarized in Table 3.2). Next, we determined whether increased mitochondrial cholesterol levels affect mitochondrial function and energy metabolism in NPC1-deficient CHO cells.

3.4.1 Depletion of MLN64 to prevent the increased lactate production by NPC1-depleted CHO cells

Similar to *Npc1*$^{-/-}$ cerebellum and cortex, CHO cells produced more lactate upon depletion of NPC1 by RNA interference in the presence of glucose (Figure 3.36 A, B).

A

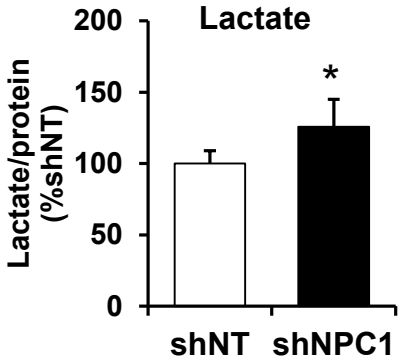
Lactate
Lactate/protein (%shNT)
200
150
100
50
0
*
shNT
shNPC1

B

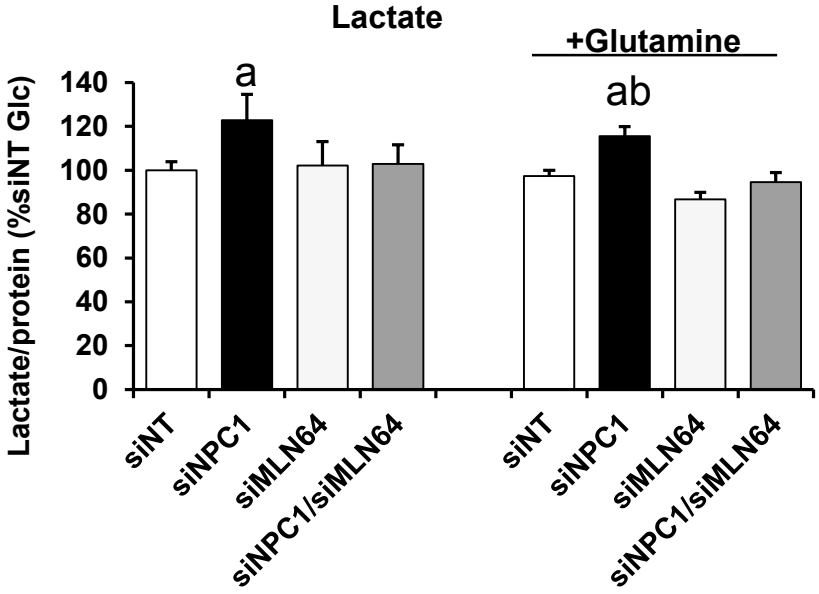
Lactate
+Glutamine
Lactate/protein (%siNT Glc)
140
120
100
80
60
40
20
0
a
ab
siNT
siNPC1
siMLN64
siNPC1/siMLN64
siNT
siNPC1
siMLN64
siNPC1/siMLN64

Figure 3.36 Increased lactate secretion in NPC1-depleted cells is prevented by co-depletion of MLN64

A) CHO cells were transfected with non-targeting shRNA (shNT) or shRNA targeting NPC1 (shNPC1) and selected with puromycin for 10 days. Lactate levels in incubation medium containing 2.5 mM glucose and incubated for 30 min with CHO cells expressing shNT or shNPC1. Data are means ± SEM of three independent experiments in triplicate (* $p < 0.05$). B) CHO cells were transfected with non-targeting siRNA (siNT) or with siRNA targeting NPC1 (siNPC1), MLN64 (siMLN64) or a combination of both (siNPC1/siMLN64). Lactate concentrations incubation medium containing 2.5 mM glucose (Glc) ± 1 mM glutamine and incubated for 30 min with CHO cells as indicated. Data are means ± SEM of three independent experiments in triplicate (^{a} $p < 0.05$ vs. siNT Glucose; ^{b} $p < 0.05$ vs. siNT Glutamine).

To determine whether blocking the transport of cholesterol from endosomes to mitochondria can prevent increased lactate production in NPC1-depleted cells, cells were co-transfected with a mixture of siRNAs targeting both NPC1 and MLN64. Co-depletion of NPC1 and MLN64 prevented the increase in lactate production (Figure 3.36 B). Depletion of MLN64 alone had no effect on lactate production (Figure 3.36 B). Because glutamate oxidation appeared increased in *Npc1*$^{-/-}$ brains and therefore likely contributes to energy metabolism we also determined whether the addition of glutamine caused altered glycolysis by measuring lactate production. In the presence of glutamine and glucose, NPC1-depleted cells again produced more lactate compared to control cells and co-depletion of NPC1 and MLN64 prevented increased lactate production (Figure 3.36 B). Together these results suggest that increased lactate production by NPC1-depleted cells is caused by increased mitochondrial cholesterol levels.

To investigate the mechanism leading to increased lactate production by NPC1-depleted cells I incubated cells in the presence of additional metabolites or inhibitors. Inhibition of ATP synthase with oligomycin increased lactate production in control and NPC1-depleted cells to a similar extent suggesting that both cells are synthesizing ATP by ATP synthase (Figure 3.37 A). Inhibition of aspartate aminotransferase with AOA treatment had no effect on lactate production in NPC1-deficient or control cells grown in the presence or absence of glutamine further showing that glutamate oxidation had no effect on lactate production under these conditions (Figure 3.37 B). Similarly, addition of alanine to increase intracellular pyruvate levels without changing the NADH/NAD^+ ratio had no effect on lactate production in NPC1-deficient or control cells suggesting that

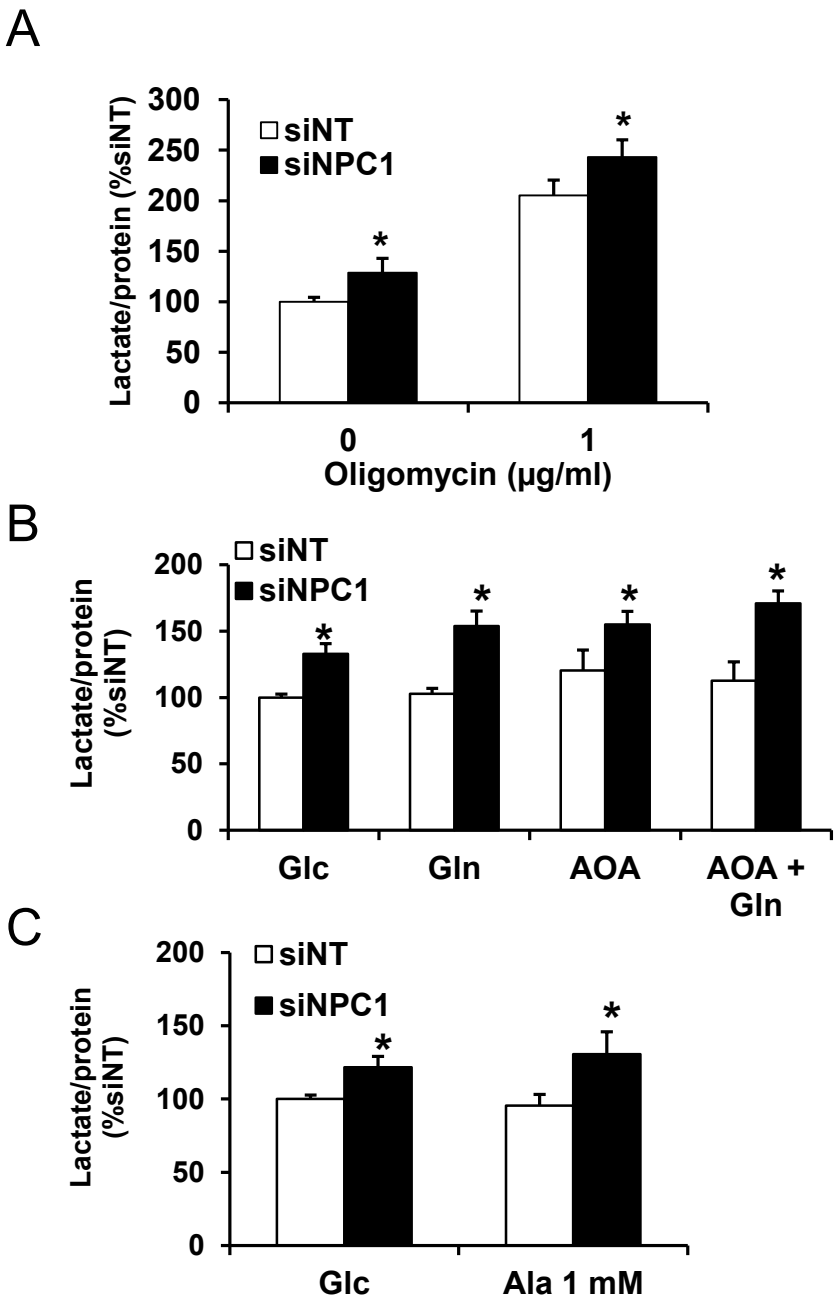

Figure 3.37 Altered lactate production by NPC1-depleted CHO cells
A-C) CHO cells were transfected with non-targeting siRNA (siNT) or with siRNA targeting NPC1 (siNPC1). Lactate concentrations in incubation medium containing 2.5 mM glucose (Glc) ± 1 µg/ml oligomycin, ± 1 mM glutamine (gln), ± 0.5 mM aminooxyacetate (AOA), ± 1 mM alanine (ala) and incubated for 30 min with CHO cells. Data are means ± SEM of three independent experiments in triplicate (* $p < 0.05$ vs. siNT of the same treatment).

increased lactate was not caused by increased activity of lactate dehydrogenase (Figure 3.37 C).

3.4.2 CHO cells depleted of both NPC1 and MLN64 have decreased glucose uptake in response to glutamine

To further characterize the mechanism behind increased lactate production by NPC1-depleted cells, we measured glucose uptake as an indicator of glycolysis. Glucose uptake was similar in cells transfected with siNT, siNPC1, and/or siMLN64 (Figure 3.38). Addition of glutamine decreased glucose uptake in cells transfected with siNT, siMLN64, or co-transfected with siNPC1 and siMLN64, suggesting glutamine was used an additional energy source (Figure 3.38). In contrast, NPC1-depleted cells did not downregulate glucose uptake in the presence of glutamine suggesting a lack of glutamine oxidation (Figure 3.38). This effect appears to be dependent on mitochondrial cholesterol accumulation since blocking cholesterol transport by depletion of MLN64 normalized the decrease in glucose uptake in response to glutamine addition.

3.4.3 Decreased oxygen consumption by NPC1-depleted cells in the presence of glutamine compared to control cells and cells co-depleted of MLN64 and NPC1

To determine whether NPC1-depleted cells had a defect in glutamine oxidation we measured oxygen consumption rates (OCR) in the presence or absence of glutamine with a Seahorse analyzer (Seahorse Bioscience) in collaboration with Dr. Wolfgang

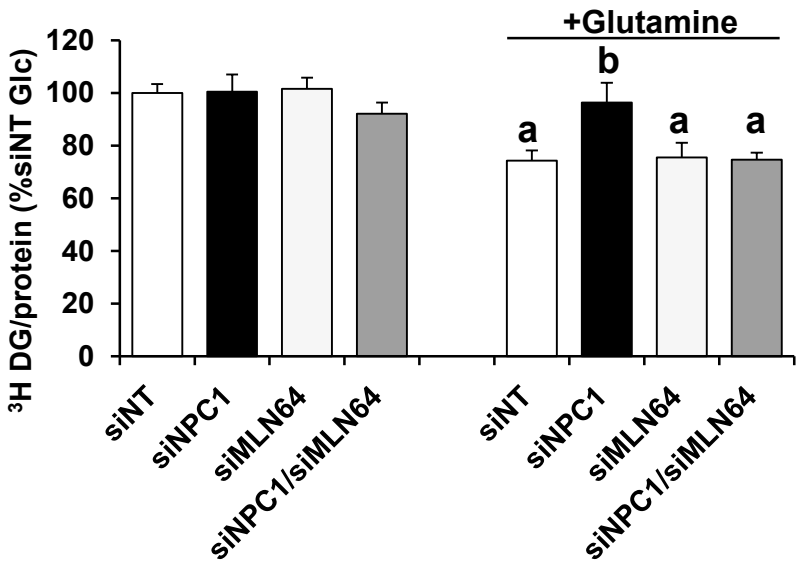

Figure 3.38 Glutamine-mediated downregulation of glucose uptake is disrupted in NPC1-depleted cells and normalized by co-depletion of MLN64

A) Cell-associated radioactivity in cells transfected with siNT, siNPC1, and/or siMLN64 after 30 min incubation with [^{3}H]-2-deoxyglucose, 2.5 mM glucose, and ± 1 mM glutamine. Data are means ± SEM of three independent experiments in triplicate (^{a} $p < 0.05$ vs. siNT Glucose; ^{b} $p < 0.05$ vs. siNT Glutamine).

Graier (Medical University of Graz, Austria). OCR were measured during the consecutive addition of oligomycin, the uncoupling agent carbonyl cyanide-p-trifluoromethoxyphenylhydrazone (FCCP), and complex III inhibitor antimycin A to obtain the basal OCR, ATP-synthase-dependent OCR, maximal respiratory capacity, and non-mitochondrial respiration (summarized in Figure 3.39)[321]. In the presence of glucose alone, there were no differences in any of these aspects in cells transfected with non-targeting siRNA or siRNA against MLN64 and/or NPC1 (Figure 3.40 A-D). However, under these conditions, OCR were very low in all cells (Figure 3.40 A). Low oxygen consumption in the presence of glucose alone is consistent with the high glucose uptake by all CHO cells (Figure 3.38) and suggests that under these conditions cells are highly glycolytic. This observation is consistent with previous reports of CHO cells and means that a mitochondrial defect may not become apparent when glucose is the only energy source [322, 323]. Addition of glutamine increased basal OCR, ATP synthase-dependent OCR, and maximal OCR in cells transfected with non-targeting siRNA, siRNA-targeting MLN64, and cells co-depleted of MLN64 and NPC1 compared to OCR in the presence of glucose alone (Figure 3.40 E). In contrast, basal OCR, ATP synthase-dependent OCR, and maximal OCR did not increase upon the addition of glutamine in NPC1-depleted cells and were all significantly lower compared to control and cells co-depleted of NPC1 and MLN64 in the presence of glutamine (Figure 3.40 E-H). Non-mitochondrial respiration was similar in all cells, demonstrating that decreased OCR were due to decreased mitochondrial respiration in NPC1-deficient cells (Figure 3.40 A, E). Altogether, these results suggest that increased mitochondrial cholesterol levels in NPC1-depleted cells caused impaired glutamine oxidation.

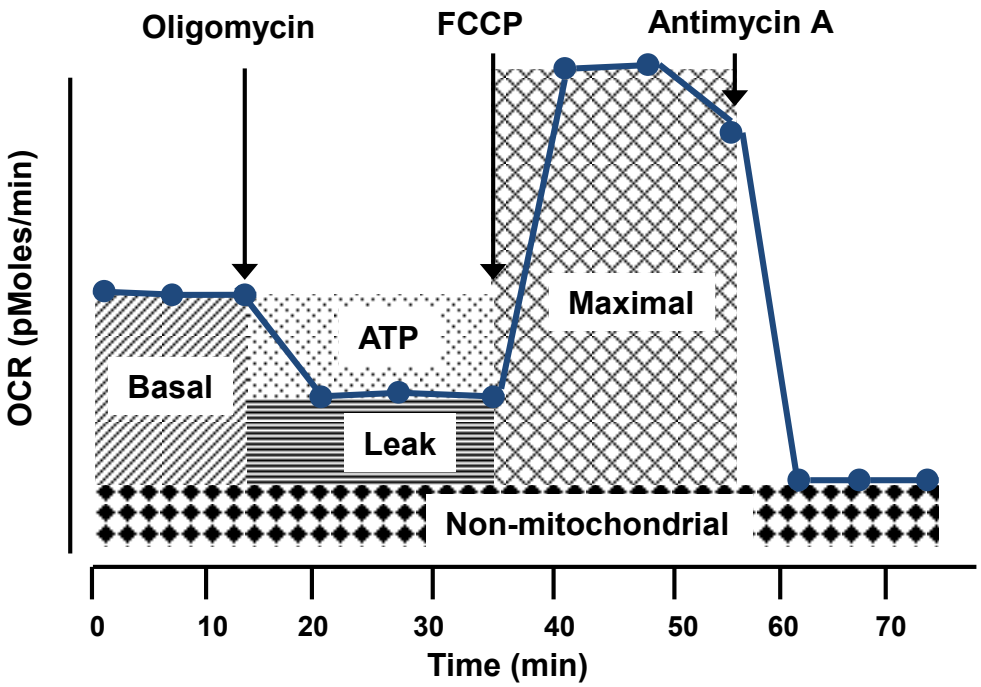

Figure 3.39 Schematic of oxygen consumption rates (OCR) measurements by a Seahorse Bioanalyzer XF and inhibitor treatments

OCR are measured during the consecutive addition of oligomycin, the uncoupling agent carbonyl cyanide-p-trifluoromethoxyphenylhydrazone (FCCP), and complex III inhibitor antimycin A to obtain the basal OCR, ATP-synthase-dependent OCR (ATP), proton leak-dependent OCR (Leak), maximal respiratory capacity (Maximal), and non-mitochondrial respiration.

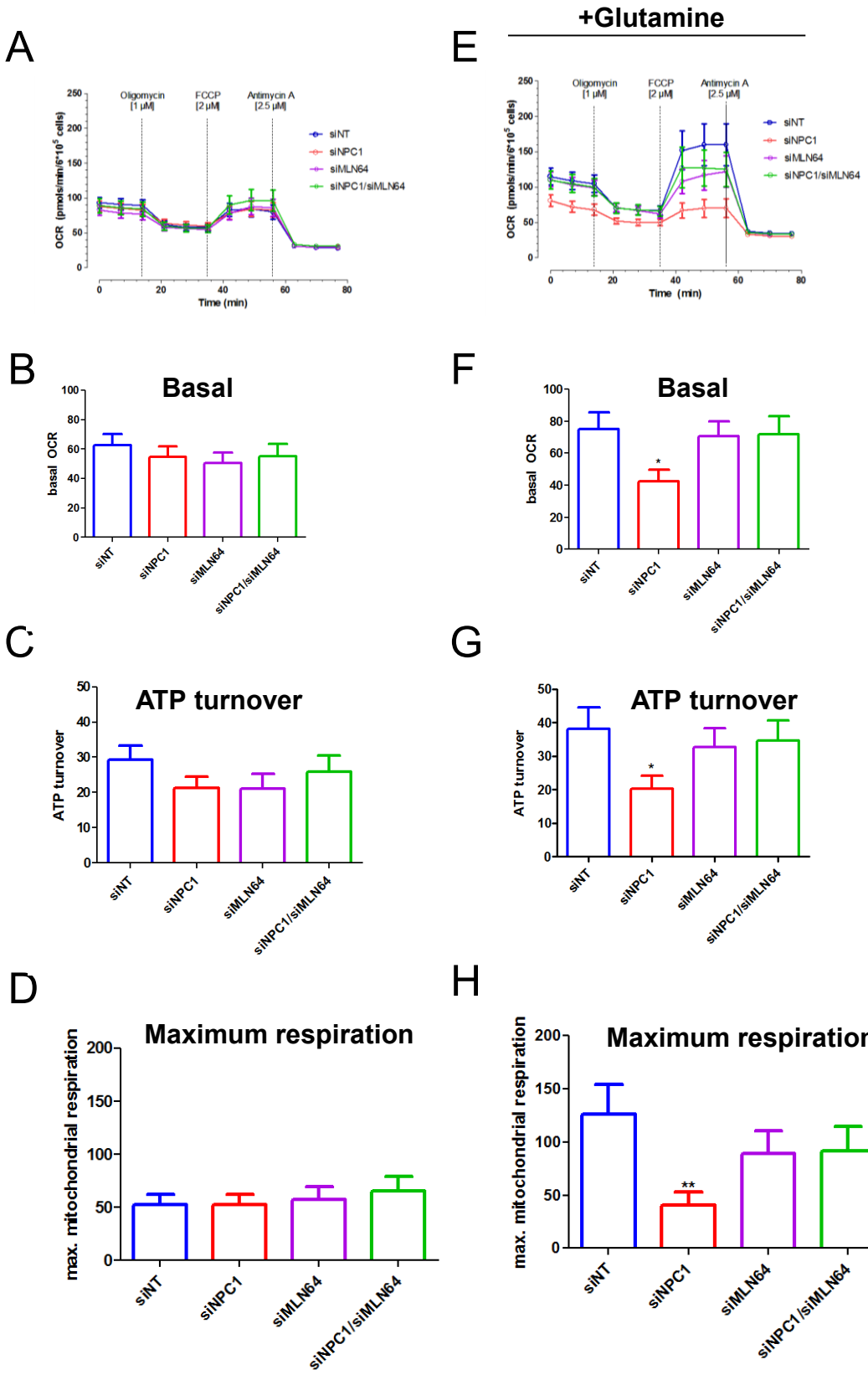
A
Oligomycin [1 µM]
FCCP [2 µM]
Antimycin A [2.5 µM]
siNT
siNPC1
siMLN64
siNPC1/siMLN64
OCR (pmols/min/6*10^5 cells)
Time (min)
E
+Glutamine
B
Basal
basal OCR
F
C
ATP turnover
G
D
Maximum respiration
max. mitochondrial respiration
H

Figure 3.40 Impaired glutamine-dependent mitochondrial respiration in NPC1-depleted cells is prevented by co-depletion of MLN64

A-H) Oxygen consumption rates (OCR) of CHO cells transfected with non-targeting siRNA (siNT) or with siRNA targeting NPC1 (siNPC1), MLN64 (siMLN64) or a combination of both (siNPC1/siMLN64) were measured using a Seahorse Bioanalyzer XF96 in the presence of glucose alone (A to D) or in the presence of glucose and glutamine (E to H) during the consecutive addition of 1 μM oligomycin, 2 μM FCCP, and 2.5 μM antimycin as indicated. A and E) OCR monitored over 77 min in cells transfected with siNT, siNPC1, siMLN64, siNPC1/siMLN64. B and F) Average basal OCR prior to the addition of oligomycin; C and G) ATP turnover calculated as the difference between basal OCR and the OCR in the presence of oligomycin. D and H) Maximum respiratory rates; OCR in the presence of FCCP. All data are means ± SEM (* $p < 0.05$; ** $p < 0.01$).

Decreased OCR in the presence of glutamine show that NPC1-depleted CHO cells have decreased oxidation of glutamine/glutamate. To further characterize glutamate oxidation, I measured mRNA levels of several key enzymes. Aspartate aminotransferase (*Got2*) and glutamine synthetase (*Glu1*) mRNA levels were unchanged in NPC1-depleted cells (Figure 3.41 A, B), while glutamate dehydrogenase (*Glud1*) mRNA levels were increased (Figure 3.41 C). Because we have shown that glutamine is not oxidized increased *Glud1* mRNA levels could suggest that GLUD1 is operating in reverse, generating glutamate from alpha ketoglutarate. However, without a flux study the direction and significance of increased *Glud1* is unknown.

3.4.4 NPC1-depleted CHO cells have increased ATP levels in the presence of glutamine

Next, to determine whether energy levels were affected we measured ATP levels in NPC1-deficient. Total ATP levels in the presence of glucose alone were similar among all cells (Figure 3.42 A). In contrast, total ATP levels were higher in NPC1-depleted cells compared to cells transfected with non-targeting siRNA, siRNA against MLN64, or cells co-depleted of NPC1 and MLN64 in the presence of glutamine (Figure 3.42 A). The increased ATP levels coincide with decreased respiration and increased glycolysis, suggesting that the increased ATP levels in NPC1-depleted cells were likely generated by glycolysis. Consistent with an increased ATP production from glycolysis, inhibition of glycolysis by a brief 2-deoxyglucose treatment in the presence of glutamine decreased ATP levels to a similar level in control and NPC1-depleted CHO cells (Figure 3.42 A).

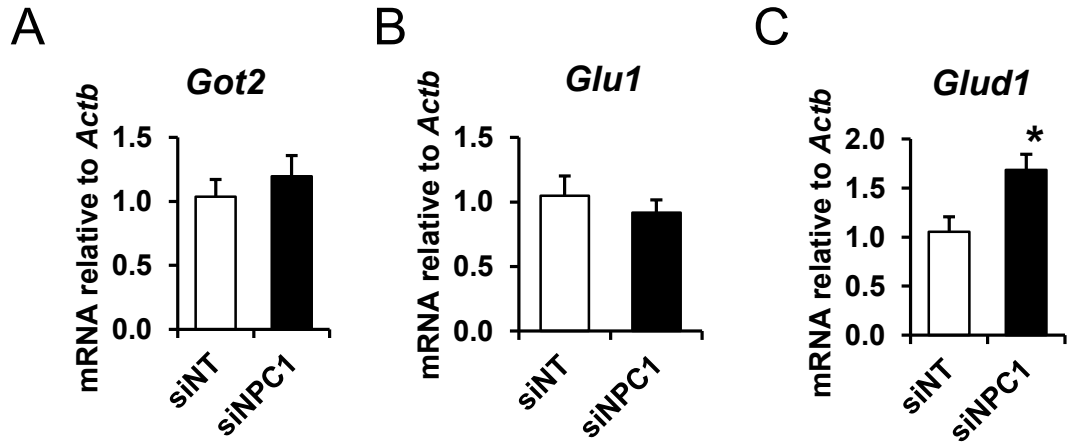

Figure 3.41 Glutamate metabolism-related gene expression in NPC1-depleted CHO cells

A-C) RNA was prepared from CHO cells transfected with non-targeting siRNA (siNT) and siRNA against NPC1 (siNPC1). Target genes mRNA levels were analyzed by qPCR using primers against aspartate aminotransferase 2 (*Got2*), glutamine synthetase 1 (*Glu1*), glutamate dehydrogenase 1 (*Glud1*), standardized to *Ppia*. Data in bar graphs are shown as means ± SEM. Data are derived from two independent experiments in triplicate. * $p < 0.05$.

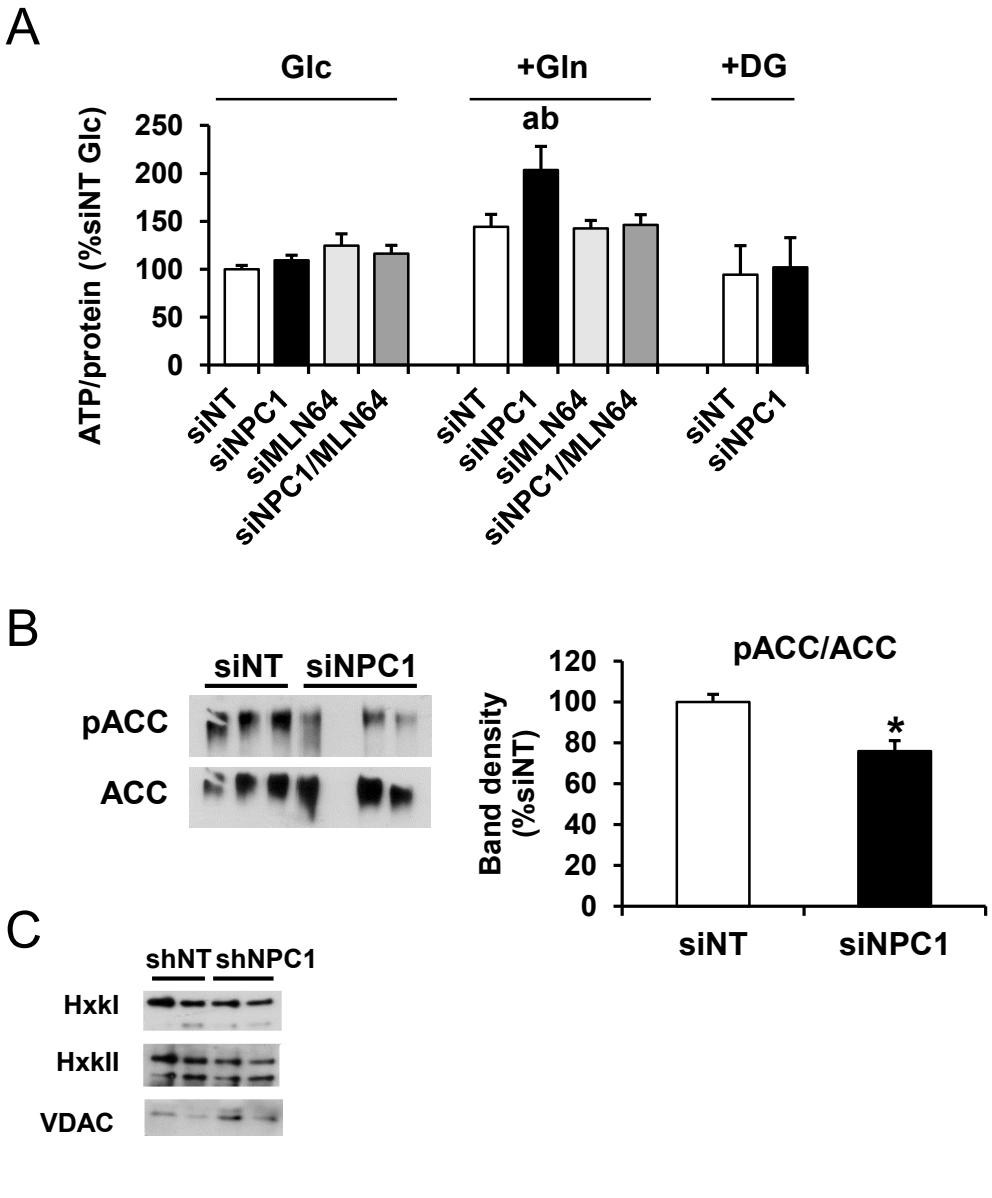
A
Glc
+Gln
+DG
ab
ATP/protein (%siNT Glc)
250
200
150
100
50
0
siNT
siNPC1
siMLN64
siNPC1/MLN64
siNT
siNPC1
siMLN64
siNPC1/MLN64
siNT
siNPC1
B
siNT
siNPC1
pACC
ACC
pACC/ACC
Band density (%siNT)
120
100
80
60
40
20
0
*
siNT
siNPC1
C
shNT
shNPC1
HxkI
HxkII
VDAC

Figure 3.42 Increased ATP levels in NPC1-depleted CHO cells in the presence of glutamine

Total cellular ATP levels in CHO cells transfected with non-targeting siRNA (siNT) or with siRNA targeting NPC1 (siNPC1), MLN64 (siMLN64) or a combination of both (siNPC1/siMLN64) and incubated in media containing 2.5 mM glucose (Glc) ± 1 mM glutamine (Gln) and 1 mM 2-deoxyglucose (DG) ± 1 μg/ml oligomycin (oligo) for 30 min, standardized to protein and expressed as percent of the average of siNT (A). B) Immunoblot of CHO cell transfected with siNT or siNPC1 using antibodies against phosphorylated acetyl-CoA carboxylase (pACC) or acetyl-CoA carboxylase (ACC). Bar graph shows the ratio of band intensity of pACC to ACC expressed as percent siNT. C) Preliminary immunoblot of mitochondria isolated from CHO cells transfected with non-targeting shRNA (shNT) or shRNA against NPC1 (shNPC1) using antibodies that recognize hexokinase I (HxkI), hexokinase II (HxkII), or voltage-dependent anion channel (VDAC) as a loading control. Data are means ± SEM of three independent experiments in triplicate (^{a} $p < 0.05$ vs. siNT Glucose; ^{b} $p < 0.05$ vs. siNT Glutamine; * $p < 0.05$ vs. siNT).

Another indicator of energy levels in cells is the activity of AMPK. Low ATP/AMP levels activate AMPK, which catalyzes the phosphorylation of acetyl-CoA carboxylase (ACC). In line with their increased ATP levels, NPC1-depleted cells had a decreased ratio of phosphorylated ACC per total ACC compared to control cells (Figure 3.42 B).

In synaptic mitochondria isolated from WT and *Npc1*$^{-/-}$ murine brain we observed an increased interaction of hexokinase I with mitochondria. However, in a preliminary experiment we observed similar levels of hexokinase I and hexokinase II bound to mitochondria isolated from CHO cells transfected with shNT or shNPC1 suggesting that this was not the cause of increased glycolysis in NPC1-depleted CHO cells (Figure 3.42 C).

3.4.5 Impaired ATP transport into mitochondria in NPC1-depleted cells

Total ATP levels represent several different aspects of synthesis (from glycolysis or oxidative phosphorylation) and breakdown. To further characterize differences between wildtype and NPC1-depleted cells, we (in collaboration with Dr. Wolfgang Graier (Medical University of Graz, Austria)) used a genetically encoded mitochondrial fluorescent resonance energy transfer (FRET) sensor (mtAT1.03) to measure mitochondrial ATP levels in live cells [282, 324]. CHO cells stably expressing non-targeting shRNA or shRNA against NPC1 were transfected with mtAT1.03. The basal ratio of the FRET mitochondrial-targeted ATP probe was not significantly different between NPC1-depleted cells and control cells indicating that mitochondrial ATP levels were similar (Figure 3.43 A). Inhibition of ATP synthase by oligomycin caused a large decrease in mitochondrial ATP levels in both cells and shortly after continuous oligomycin treatment, mitochondrial ATP levels recovered through import of cytosolic

A

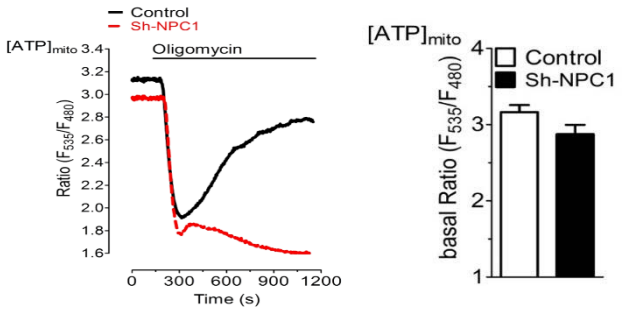
Control
Sh-NPC1
[ATP]mito
Oligomycin
Ratio (F535/F480)
Time (s)
basal Ratio (F535/F480)

B

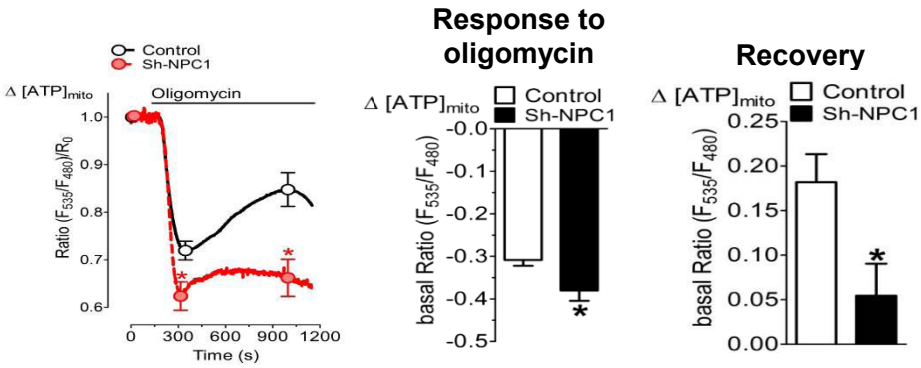
Control
Sh-NPC1
Δ [ATP]mito
Oligomycin
Ratio (F535/F480)/R0
Time (s)
Response to oligomycin
Recovery
basal Ratio (F535/F480)

C

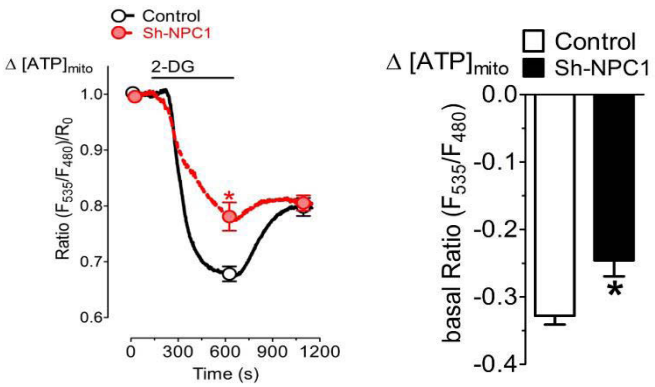
Control
Sh-NPC1
Δ [ATP]mito
2-DG
Ratio (F535/F480)/R0
Time (s)
basal Ratio (F535/F480)

Figure 3.43 Impaired mitochondrial ATP transport in NPC1-deficient cells
CHO cells expressing non-targeting shRNA (shNT) or shRNA against NPC1 (shNPC1) were transiently transfected with the FRET-based ATP sensor mtAT1.03. MitoATP levels ([ATP]mito) were measured as the ratio of emission at 535 nm/480 nm (ratio (F535nm/F480nm)), with excitation at 435 nm in the presence of glucose and glutamine. A) MitoATP levels in shNT and shNPC1 cells during addition of 1 µM oligomycin. The ratio (F535nm/F480nm) was measured for 2.5 min prior to addition of oligomycin (basal ratio (F535nm/F480nm)) and continued in the presence of oligomycin. The bar graph shows basal [ATP]mito as means ± SEM. B) Changes in ATP levels (Δ[ATP]mito) were calculated from the measurements shown in panel A as the ratio (F535 nm/F480 nm)/R0 with R0 as the ratio (F535nm/F480nm) at the beginning of the measurement. Centre panel (+ Oligomycin): Maximum decrease in [ATP]mito following the addition of oligomycin, calculated as the difference between basal Ratio (F535nm/F480nm)/R0 and the lowest Ratio(F535nm/F480nm)/R0. Right panel (Recovery): Increase in [ATP]mito calculated as the difference between the lowest ratio (F535 nm/F480 nm)/R0 and the highest ratio (F535 nm/F480 nm)/R0 following the addition of oligomycin. The lowest and highest ratio (F535 nm/F480 nm)/R0 are indicated by the markers on the plot of Δ[ATP]mito over time. C) Changes in mitoATP levels (Δ[ATP]mito) in shNT and shNPC1 cells during addition of 2-deoxyglucose calculated as the ratio (F535 nm/F480 nm)/R0. The ratio (F535 nm/F480 nm) was measured for 2.5 min prior to addition of 2-deoxyglucose and continued in the presence of 2-deoxyglucose. The bar graph shows the maximum decrease in [ATP]mito following the addition of 2-deoxyglucose, calculated as the difference between basal Ratio (F535 nm/F480 nm)/R0 and the lowest ratio (F535 nm/F480 nm)/R0. B) Data in bar graphs and markers are shown as means ± SEM. Data are derived from 3 independent experiments. * $p < 0.05$.

ATP into mitochondria in control cells (Figure 3.43 A). For a quantitative analysis of this effect, the FRET ratio measured overtime was normalized to the basal FRET ratio, the drop in ATP levels caused by oligomycin was significantly larger in NPC1-depleted cells compared to control (Figure 3.43 B). Furthermore, ATP levels in NPC1-depleted cells did not recover after continuous oligomycin treatment suggesting that ATP transport was defective (Figure 3.43 B). Inhibition of glycolytic ATP by 2-deoxyglucose treatment also decreased mitochondrial ATP in all cells (Figure 3.43 C). However, this decrease was not as pronounced in NPC1-depleted cells compared to control cells consistent with decreased transport of mitochondrial ATP into the cytosol (Figure 3.43 C).

3.4.6 Increased lactate production in CHO cells is not primarily caused by phosphorylation of pyruvate dehydrogenase

To investigate the role of PDH in NPC1-depleted CHO cells, we treated cells with the PDH kinase inhibitor, dichloroacetate (DCA), to activate pyruvate dehydrogenase (PDH) and measured lactate production. If PDH phosphorylation contributed to high lactate production we would expect DCA treatment to normalize lactate production in NPC1-deficient cells. As expected DCA treatment slightly reduced lactate production in all cells, and lactate production by NPC1-depleted cells was not significantly higher compared to control cells (Figure 3.44 A). However, we observed no differences in PDH phosphorylation or protein levels in NPC1-depleted CHO cells (Figure 3.44 B, C).

3.4.7 Increased antioxidant defense factor Nrf2 mRNA in NPC1-depleted cells is prevented by depletion of MLN64

I next measured the effect of mitochondrial cholesterol on oxidative stress in NPC1-depleted CHO cells. NPC1-depleted cells had increased *Nfe2l2* mRNA levels suggesting increased oxidative stress (Figure 3.45 A). Increased *Nfe2l2* expression was

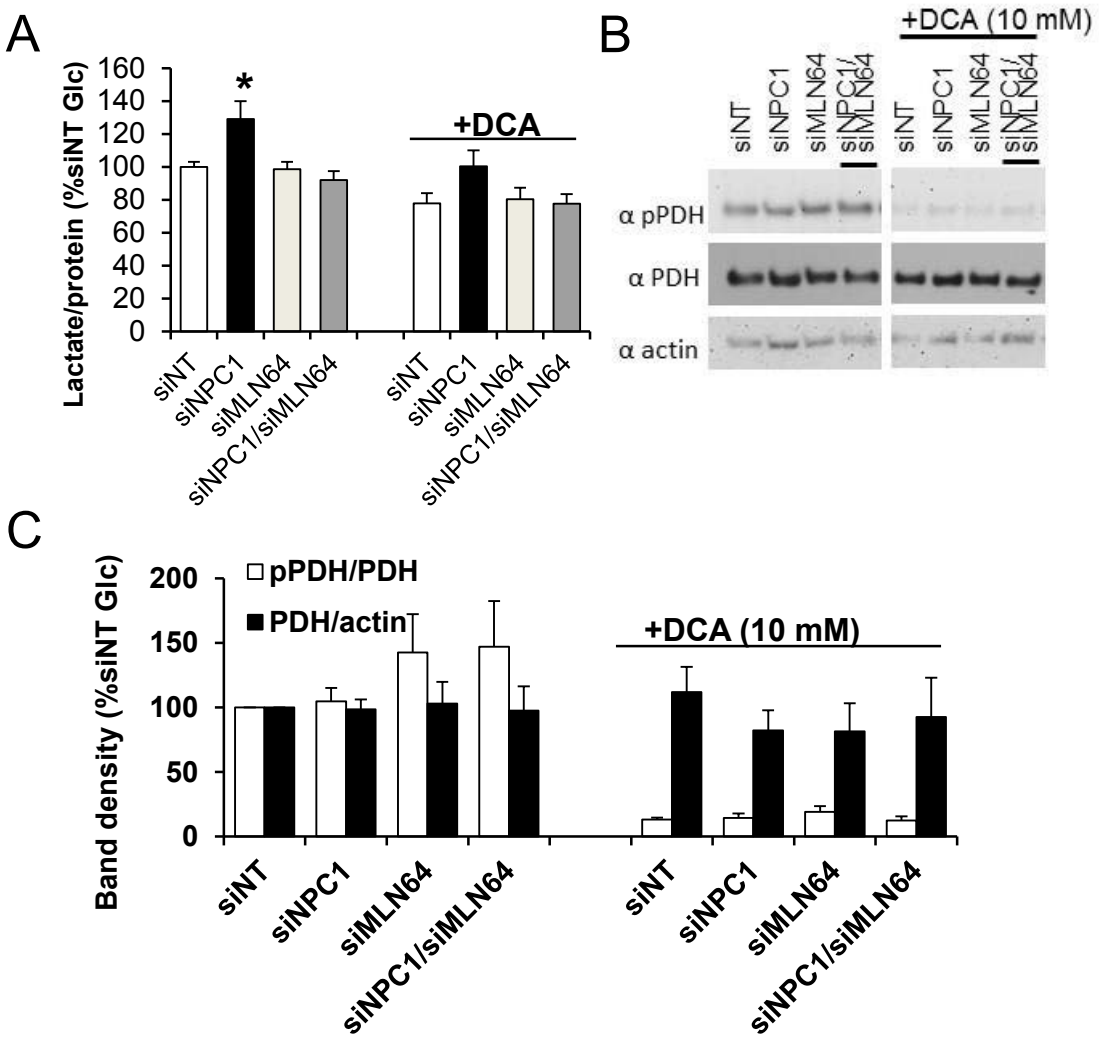
A
Lactate/protein (%siNT Glc)
160
140
120
100
80
60
40
20
0
*
+DCA
siNT
siNPC1
siMLN64
siNPC1/siMLN64
siNT
siNPC1
siMLN64
siNPC1/siMLN64
B
+DCA (10 mM)
siNT
siNPC1
siMLN64
siNPC1/siMLN64
siNT
siNPC1
siMLN64
siNPC1/siMLN64
α pPDH
α PDH
α actin
C
Band density (%siNT Glc)
200
150
100
50
0
pPDH/PDH
PDH/actin
+DCA (10 mM)
siNT
siNPC1
siMLN64
siNPC1/siMLN64
siNT
siNPC1
siMLN64
siNPC1/siMLN64

Figure 3.44 Total and phosphorylated pyruvate dehydrogenase (PDH) are unchanged in NPC1-depleted cells

A) Lactate concentration in incubation media supplemented with 2.5 mM glucose ± 10 mM dichloroacetate (DCA) and incubated for 30 min with CHO cells with non-targeting siRNA (siNT) or with siRNA targeting NPC1 (siNPC1), MLN64 (siMLN64) or a combination of both (siNPC1/siMLN64). B) Representative immunoblot of lysates prepared from cells used in panel A probed with antibodies against phosphorylated and total PDH and actin as a loading control. C) Density analysis of bands from immunoblot. Data shown are means ± SEM (n = 3). [a] $p < 0.05$ vs. siNT without DCA.

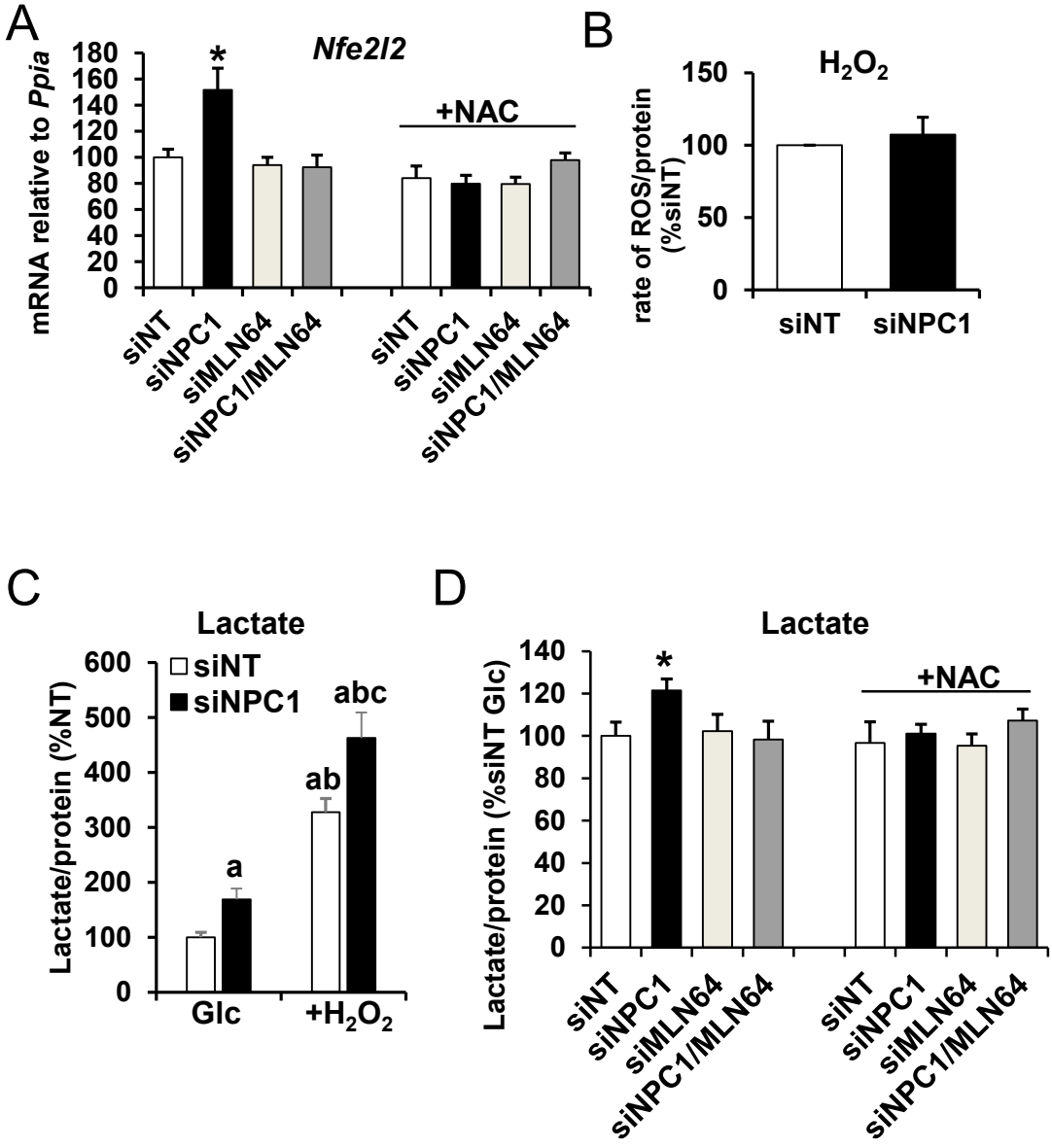
A
Nfe2l2
mRNA relative to Ppia
180
160
140
120
100
80
60
40
20
0
*
+NAC
siNT
siNPC1
siMLN64
siNPC1/MLN64
siNT
siNPC1
siMLN64
siNPC1/MLN64
B
H2O2
rate of ROS/protein (%siNT)
150
100
50
0
siNT
siNPC1
C
Lactate
siNT
siNPC1
Lactate/protein (%NT)
600
500
400
300
200
100
0
a
ab
abc
Glc
+H2O2
D
Lactate
Lactate/protein (%siNT Glc)
140
120
100
80
60
40
20
0
*
+NAC
siNT
siNPC1
siMLN64
siNPC1/MLN64
siNT
siNPC1
siMLN64
siNPC1/MLN64

Figure 3.45 Oxidative stress contributes to increased lactate production in NPC1-depleted cells

A) Nuclear factor (erythroid-derived 2)-like 2 (*Nfe2l2*) mRNA levels relative to cyclophilin (*Ppia*) in cells transfected with siNT, siNPC1, siMLN64 or siNPC1 and siMLN64, and incubated with or without N-acetylcysteine (NAC) for 48 hours. B) Reactive oxygen species (H_2O_2) production by CHO cells transfected with non-targeting siRNA (siNT) or siRNA against NPC1 (siNPC1). Data were derived from four independent experiments. C) Lactate concentration in incubation media supplemented with 2.5 mM glucose (Glc) and incubated for 30 min with CHO cells with non-targeting siRNA (siNT) or with siRNA targeting NPC1 (siNPC1) ± treatment with H_2O_2 for 24 hours. D) Lactate levels in incubation media supplemented with 2.5 mM glucose and incubated with cells transfected with siNT, siNPC1, and/or siMLN64 and treated with or without 1 mM NAC for 48 hours. *$p < 0.05$ vs. siNT without NAC, [a] $p < 0.05$ vs. siNT Glc, [b] $p < 0.05$ vs siNPC1 Glc, [c] $p < 0.05$ vs. siNT + H_2O_2.

not observed following co-depletion of NPC1 and MLN64 or treatment with the antioxidant N-acetylcysteine (NAC) (Figure 3.45 A). However, NPC1-depleted cells produced similar amounts of hydrogen peroxide levels as control cells (Figure 3.45 B).

To determine metabolic consequences of oxidative stress, we treated cells with hydrogen peroxide and measured lactate production. Treatment with low levels (50 uM) of hydrogen peroxide for 24 hours resulted in an approximately three-fold increase in lactate production by both control and NPC1-depleted cells indicating that oxidative stress caused increased lactate levels (Figure 3.45 C). Moreover, after hydrogen peroxide treatment, NPC1-depleted cells still produced more lactate than control cells suggesting that the consequences of oxidative stress on lactate production was similar between the cells (Figure 3.45 C). NPC1-depleted cells were treated with NAC for 24 hours and measured lactate production. Increased lactate production was prevented in NPC1-depleted cells treated with NAC (Figure 3.45 D). These results suggested that oxidative stress increased lactate production by NPC1-depleted cells.

3.4.8 Increased lactate production and upregulation of *Nfe2l2* correlate with mitochondrial cholesterol levels in the NPC2 mutant CHO system

Although the depletion of MLN64 alone had no effects on the metabolic parameters measured, it is still possible that MLN64 depletion had effects in addition to lowering mitochondrial cholesterol levels in NPC1-depleted cells. As a second model for elevated mitochondrial cholesterol levels, we depleted NPC2 and expressed NPC2 mutants in CHO cells as before (Figure 3.35). Depletion of NPC2 alone by siRNA had no effect on lactate production in the presence of glucose or total ATP levels in the presence of

glutamine (Figure 3.46 A, B). Similarly, depletion of endogenous NPC2 by shRNA and expression of mCherry, wildtype NPC2, or NPC2^{Y119S} (cannot bind or transfer cholesterol) had no effect on lactate production in the presence of glucose alone (Figure 3.46 C). Expression of NPC2^{V81D} (cannot transfer cholesterol to NPC1) in NPC2-depleted CHO cells increased lactate production (Figure 3.46 C). *Nfe2l2* mRNA levels were increased only in cells depleted of endogenous NPC2 and expressing NPC2^{V81D} (Figure 3.46 D). These results further support that increased mitochondrial cholesterol levels increased lactate and oxidative stress.

3.4.9 Increased ROS, ATP, and lactate levels in a long term model of NPC1-deficiency

To determine the effect of long term NPC1-deficiency we characterized 4-4-19 cells. Unlike the short-term models of NPC1-deficiency, 4-4-19 cells generated almost 60% more hydrogen peroxide levels than wildtype CHO cells (Figure 3.47 A). Preliminary results show increased glutathione levels in 4-4-19 cells compared to wildtype CHO cells suggesting that 4-4-19 cells had increased antioxidant defense (Figure 3.47 B). Inhibition of glutathione synthesis by 24 hour treatment with buthionine sulfoximine (BSO, selective inhibitor for glutamate-cysteine ligase) reduced glutathione levels to similar levels in both wildtype and 4-4-19 cells (Figure 3.47 B) [325]. 4-4-19 cells had increased ATP levels in the presence of both glucose and glutamine and produced more lactate in the presence of glucose than WT CHO cells (Figure 3.47 C, D). Preliminary results indicated that treatment with imipramine for either 24 or 48 hours reduced lactate production to similar levels in CHO and 4-4-19 cells (Figure 3.47 D). Because we showed that imipramine increases the mobilization of cholesterol to the inner

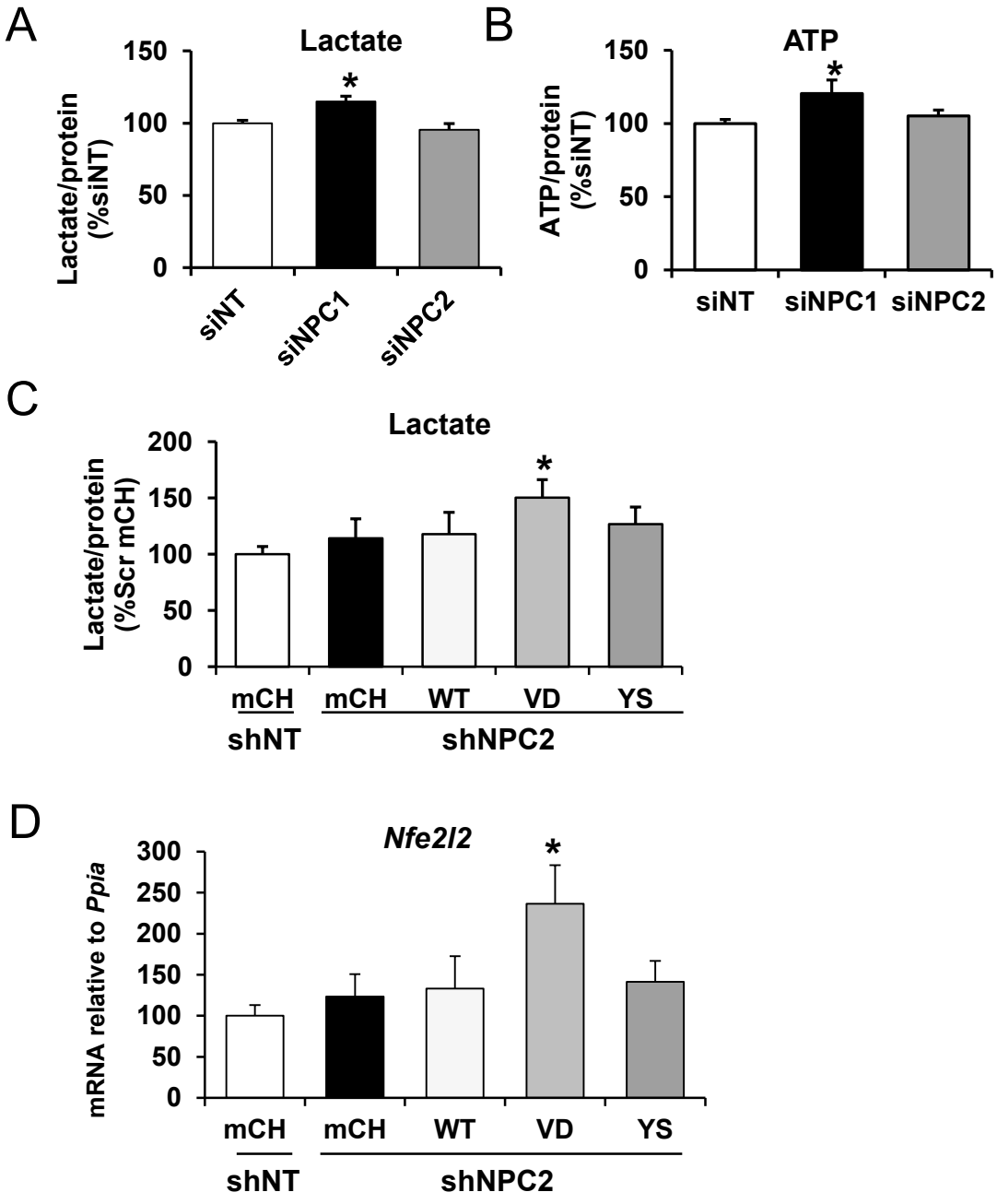
A
Lactate
Lactate/protein (%siNT)
150
100
50
0
*
siNT
siNPC1
siNPC2
B
ATP
ATP/protein (%siNT)
150
100
50
0
*
siNT
siNPC1
siNPC2
C
Lactate
Lactate/protein (%Scr mCH)
200
150
100
50
0
*
mCH
mCH
WT
VD
YS
shNT
shNPC2
D
Nfe2l2
mRNA relative to Ppia
300
250
200
150
100
50
0
*
mCH
mCH
WT
VD
YS
shNT
shNPC2

Figure 3.46 Increased mitochondrial cholesterol levels, lactate production, and *Nfe2l2* mRNA levels in cells depleted of NPC2 and expressing $NPC2^{V81D}$

A) Lactate concentration in incubation media supplemented with 2.5 mM glucose and incubated for 30 min with CHO cells with non-targeting siRNA (siNT), siRNA targeting NPC1 (siNPC1), or siRNA targeting NPC2 (siNPC2) expressed as percent of the average of siNT. B) Total cellular ATP levels in CHO cells transfected with siNT, siNPC1, siNPC2 that were incubated with media containing 2.5 mM glucose + 1 mM glutamine for 30 min, standardized to protein and expressed as percent of the average of siNT. C) Lactate levels in media containing 2.5 mM glucose and incubated with CHO cells expressing non-targeting shRNA (shNT) or shRNA targeting hamster NPC2 (shNPC2) and expressing mCherry (mCh), wildtype NPC2 (WT), $NPC2^{V81D}$ (VD), or $NPC2^{Y119S}$ (YS) and expressed as percent of the average of shNT mCH. D) *Nfe2l2* mRNA levels relative to cyclophilin in cells expressing shNT or shNPC2 and mCH, WT, VD, or YS and expressed as percent of the average of shNT mCH. Bar graphs show the means ± SEM. * $p < 0.05$ vs. shNPC2 mCH.

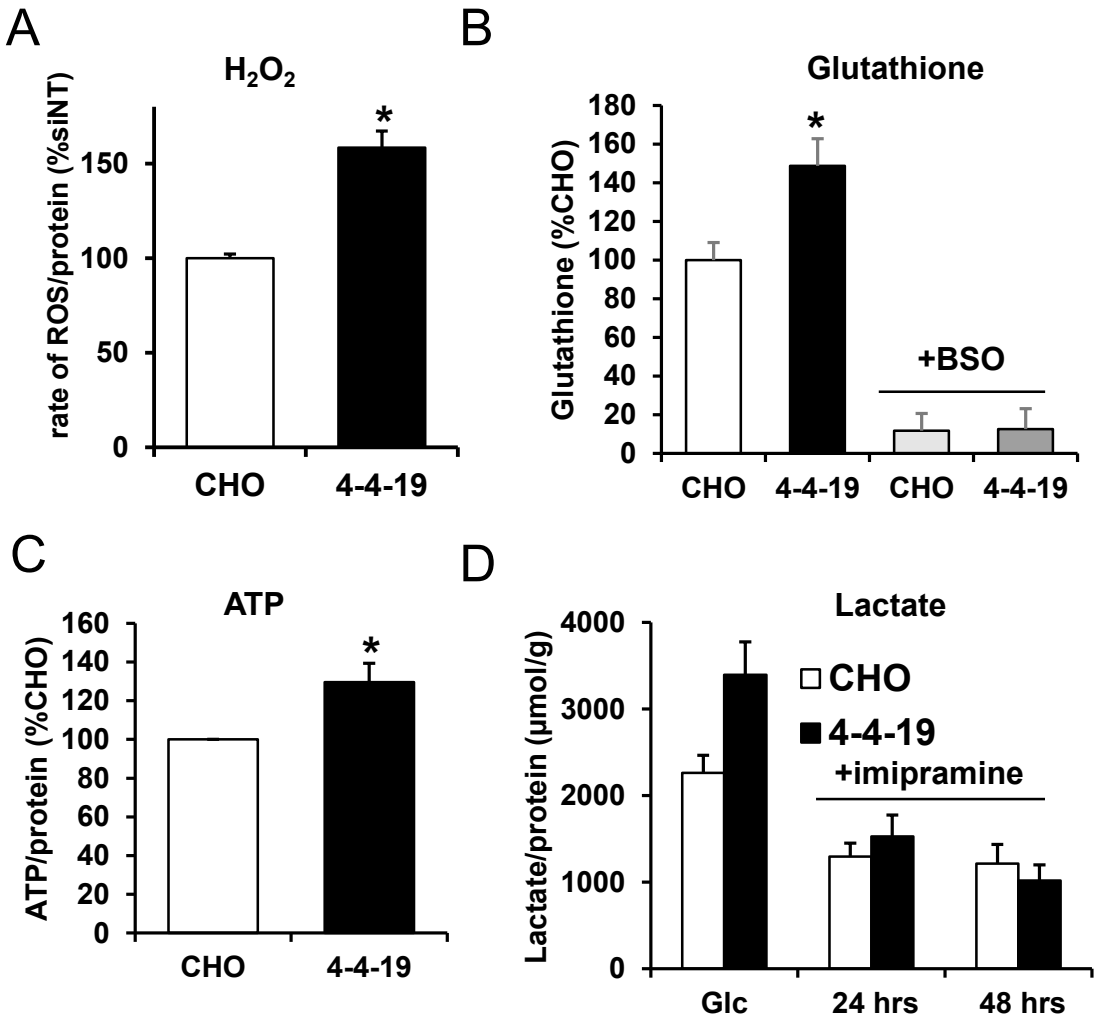

Figure 3.47 Increased ROS production and ATP levels in 4-4-19 cells
A) Reactive oxygen species (H_2O_2) production by wildtype CHO cells and 4-4-19 cells expressed as percent of the average of CHO cells. B) Cellular reduced glutathione levels in CHO and 4-4-19 cells pretreated with buthionine sulfoximine (BSO) for 24 hours expressed as percent CHO. Data were derived from one experiment in triplicate. C) Total cellular ATP levels in CHO and 4-4-19 cells that were incubated with media containing 2.5 mM glucose + 1 mM glutamine for 30 min, standardized to protein and expressed as percent of the average of CHO cells. Data were derived from seven independent experiments in duplicate. D) Lactate levels in media containing 2.5 mM glucose (Glc) and incubated with CHO and 4-4-19 cells that were or were not pretreated with 40 µM imipramine for 24 or 48 hours expressed as percent of the average of CHO. Data were derived from one experiment in triplicate. Bar graphs shows the mean ± SEM. * $p < 0.05$ vs. CHO Glc.

mitochondrial membrane, the effect of imipramine on lactate production could suggest that increasing the mobilization of cholesterol from the outer to the inner mitochondrial membrane normalizes mitochondrial function in NPC1-deficient CHO cells.

Cyclodextrin is a cholesterol binding complex carbohydrate that is endocytosed into cells and increases mobilization of endosomal cholesterol in NPC1-deficient cells [326]. Treatment with 2-hydroxypropyl-beta-cyclodextrin (HPCD) for 48 hours ameliorated endosomal cholesterol accumulation as shown by filipin staining but had no effect on hydrogen peroxide production in 4-4-19 cells suggesting that either HPCD treatment did not normalize mitochondrial cholesterol levels or that underlying damage was already present and therefore could not be reversed by HPCD treatment (Figure 3.48 A, B). Further experiments will be required to determine whether HPCD affected mitochondrial cholesterol or whether irreversible mitochondrial changes had occurred.

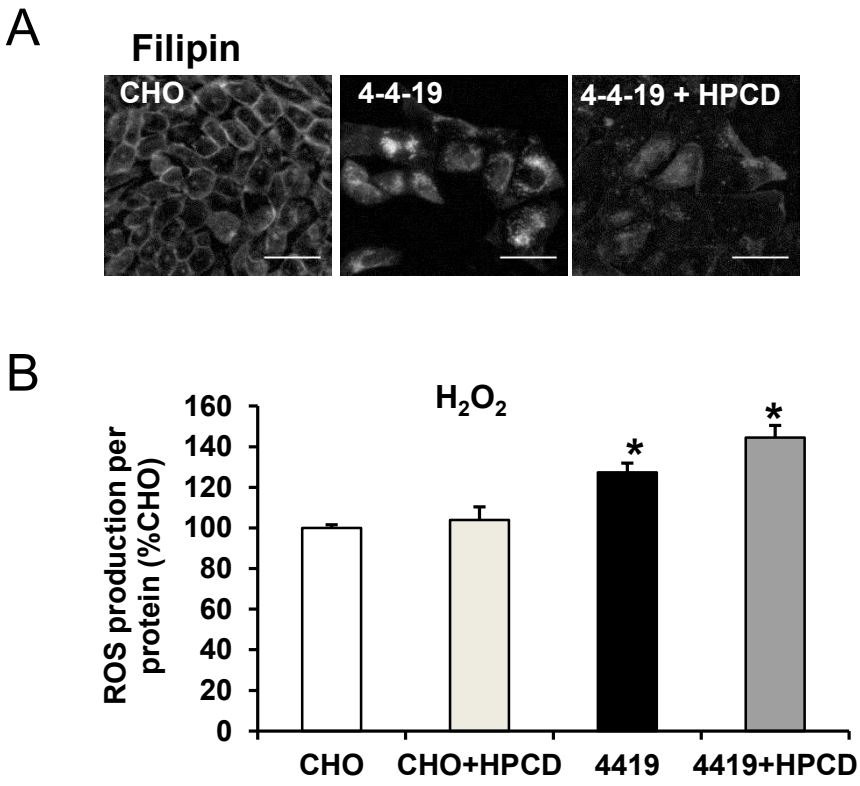

Figure 3.48 HPCD treatment reduced endosomal cholesterol accumulation but not H_2O_2 production in 4-4-19 cells

A) Filipin stain of CHO and 4-4-19 cells pretreated with or without HPCD for 72 hours. B) Reactive oxygen species (H_2O_2) production by wildtype CHO cells and 4-4-19 cells pretreated with or without HPCD for 72 hours expressed as percent of the average of CHO cells. Scale bars = 50 μm. Data were derived from four independent experiment in triplicate. * $p < 0.05$ vs. CHO without HPCD.

CHAPTER 4 Discussion

In addition to the well-known accumulation of endosomal cholesterol, mitochondrial cholesterol is also increased in NPC1-deficient cells. The consequences of increased mitochondrial cholesterol in NPC pathogenesis are unknown. Here, I have investigated the mechanisms of cholesterol accumulation and found that cholesterol is transported from endosomes to mitochondria by a pathway that involves two endosomal proteins, NPC2 and MLN64. By blocking this transport pathway in NPC1-depleted CHO cells I show that several aspects of energy metabolism and mitochondrial function were normalized under these conditions including oxidative stress, decreased glutamine oxidation, and increased glycolysis suggesting that increased mitochondrial cholesterol caused mitochondrial dysfunction in NPC1-depleted CHO cells. I also investigated brain energy metabolism in a murine model of NPC disease using unbiased metabolomics and targeted gene expression analyses. I found 1) alterations in glucose and pyruvate metabolism that suggested an early symptomatic decrease in the oxidative metabolism of glucose in *Npc1*$^{-/-}$ murine cerebellum, 2) pre-symptomatic activation of an antioxidant response system that suggested early oxidative stress in *Npc1*$^{-/-}$ murine cerebellum, and 3) an *Npc1*$^{-/-}$ brain region-specific pattern of energy metabolism suggesting global alterations in metabolism. My work in NPC1-depleted CHO cells suggests that oxidative stress and increased glycolysis may be caused by increased mitochondrial cholesterol levels in *Npc1*$^{-/-}$ murine brain.

4.1 Mitochondrial dysfunction and altered energy metabolism in *Npc1*$^{-/-}$ brain

In the following section I will develop a model of metabolic alterations in *Npc1*$^{-/-}$ murine brain, compare our findings with the current literature on NPC disease, and discuss how mitochondrial dysfunction and altered energy metabolism may contribute to NPC disease pathogenesis.

4.1.1 Model of mitochondrial dysfunction and altered energy metabolism in *Npc1*$^{-/-}$ brain

Mitochondrial dysfunction and oxidative stress

Recently, several groups have reported markers of oxidative damage in the CSF of NPC human patients, in late-stage disease *Npc1*$^{-/-}$ mice, and in NPC-deficient cells [144, 240-252]. However, it was unclear whether oxidative damage occurred early in disease progression or was a late defect. Here, we measured mRNA levels of several antioxidant defense genes at different disease stages of *Npc1*$^{-/-}$ murine cerebellum. We detected increased *Nfe2l2*, *Hmox1*, *Sod1*, *Ucp2* mRNA, increased SOD2 protein levels, and increased phosphorylation of JNK in 3-week-old *Npc1*$^{-/-}$ cerebellum (Figure 3.01 and 3.02). Together these results suggest that oxidative stress precedes the onset of symptoms in *Npc1*$^{-/-}$ cerebellum. Because *Hmox1*, *Sod1*, and *Sod2* are all Nrf2 targets [287, 288], it is likely that Nrf2 is activated in *Npc1*$^{-/-}$ cerebellum. Under stress conditions, high JNK phosphorylation/activation is maintained by inhibition of oxidative-stress sensitive JNK phosphatases [289-291, 299]. In *Npc1*$^{-/-}$ cerebellum, early development of oxidative stress likely causes the activation of Nrf2, upregulation of

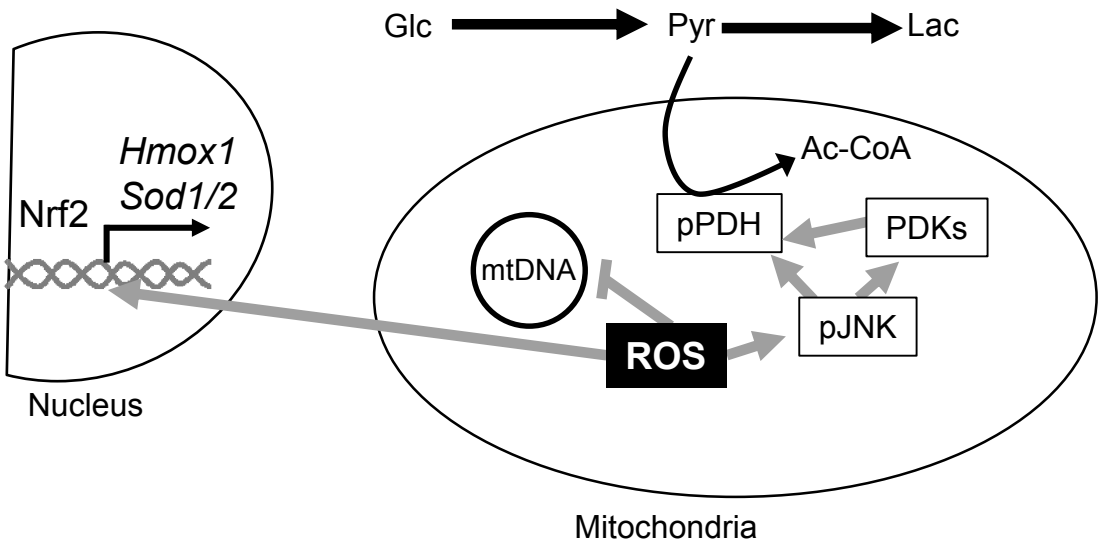

Figure 4.01 Consequences of oxidative stress in *Npc1*$^{-/-}$ murine cerebellum
Increased ROS 1) upregulates Nrf2 expression and translocation into nucleus, where Nrf2 acts as a transcription factor, 2) causes mutations in mtDNA leading to decreased mtDNA copy number, 3) leads to increased activation/phosphorylation of JNK. pJNK activates PDKs, which lead to phosphorylation and inhibition of PDH. Inhibition of PDH forces pyruvate metabolism to lactate and away from Ac-CoA. Black arrows represent metabolic flux with the darker arrows representing the areas of greatest flux. Grey arrows represent activation and grey inhibitory line represents inhibition. pPDH: phosphorylated/inhibited Pyruvate Dehydrogenase, PDKs: Pyruvate dehydrogenase kinases, pJNK: phosphorylated/activated Jun-N-terminal kinase, mtDNA: mitochondrial DNA, ROS: Reactive oxygen species, Nrf2: Nuclear factor erythroid 2-related factor, Hmox1: Heme oxygenase 1, Sod1/2: Superoxide dismutase 1/2, grey double stranded helix: DNA, Glc: glucose, Pyr: pyruvate, Lac: lactate.

antioxidant defense genes, and JNK phosphorylation/activation (Figure 4.01 describes a model of oxidative stress in *Npc1*$^{-/-}$ cerebellum).

Surprisingly, I detected no changes in hydrogen peroxide production by mitochondria isolated from 3- or 7-week-old *Npc1*$^{-/-}$ murine brain in the presence of succinate (Figure 3.04 A, B). The lack of increased ROS production could be explained by: 1) mitochondrial antioxidant defenses (catalase and superoxide dismutase) preventing increased production of hydrogen peroxide [327, 328], 2) ROS in *Npc1*$^{-/-}$ murine brain being produced by complex I of the electron transport chain, which would not be detected in the presence of succinate [230, 231, 329], 3) ROS production by the cerebellum was masked by the presence of other brain regions, or 4) ROS not being mitochondria-derived. It is unlikely that isolation of mitochondria from whole brain masked a brain region-specific defect because *Nfe2l2* mRNA levels were upregulated in 5-week-old *Npc1*$^{-/-}$ cortex and hippocampus (Figure 3.01 C, D). Although this work does not identify the source of ROS production, it is clear from the upregulation of antioxidant genes that oxidative stress develops presymptomatically in *Npc1*$^{-/-}$ cerebellum. Further work would be required to determine the role of complex I and non-mitochondrial production of ROS in *Npc1*$^{-/-}$ murine brain.

ROS have several consequences on cellular function by damaging proteins, lipids, and nucleotides. One example is decreased mtDNA copy number, by ROS damage of the mitochondrial DNA polymerase binding site (D loop), which is particularly sensitive to oxidative damage [293, 330-333]. We detected decreased levels of mtDNA in 5-week-old *Npc1*$^{-/-}$ cerebellum (Figure 3.03 A). Consistent with a loss of mtDNA, decreased mRNA levels of mtDNA encoded mitochondrial cytochrome c oxidase I (the major subunit of

complex IV) were found in 5- and 7-week-old *Npc1*$^{-/-}$ cerebellum. Thus, ROS may lead to decreased expression of certain electron transport chain components.

Another possible consequence of increased ROS production is the inhibition of PDH either by direct damage to the enzyme or through increased phosphorylation of PDH. The ratio of phosphorylated PDH to total PDH levels was increased in *Npc1*$^{-/-}$ cerebellum at 5 weeks of age and lactate levels were increased at all ages (Figures 3.06 B and 3.08). These results indicate decreased activity of PDH in *Npc1*$^{-/-}$ cerebellum. Two groups of kinases phosphorylate PDH; PDKs and JNKs. Increased JNK phosphorylation and increased mRNA levels of *Pdk1/2* in 5-week-old *Npc1*$^{-/-}$ cerebellum suggest that both groups of kinases are activated at 5 weeks of age (Figure 3.02 and 3.06). *Pdk1/2* expression is upregulated by the Hif1alpha transcription factor [334]. Hif1alpha is commonly active during hypoxia but it is also activated by ROS during normoxic conditions suggesting that Hif1alpha may be active in *Npc1*$^{-/-}$ cerebellum [335]. However, I did not succeed in detecting Hif1alpha by immunoblot in *Npc1*$^{-/-}$ murine brain. In addition, PDK1/2 are activated by JNK phosphorylation [336]. *Pdk1* and *Pdk2* are predominantly expressed in neurons and astrocytes, respectively; suggesting that PDH inhibition occurred in both cell types in *Npc1*$^{-/-}$ cerebellum [194]. The majority of astrocytic PDH is phosphorylated even under normal conditions [194], therefore, the increased phosphorylated PDH is representative of neuronal PDH. Mitochondria isolated from 3-week-old *Npc1*$^{-/-}$ murine brain produced less ATP in the presence of pyruvate and malate than control mitochondria (Figure 3.05), but showed no difference in ATP production in the presence of succinate, suggesting normal electron transport chain function and oxidative phosphorylation downstream of complex II. The decreased ATP

production in the presence of pyruvate and malate suggested that the defect was at a step between the oxidative decarboxylation of pyruvate and complex I. Together these results suggest a model in which early oxidative stress leads to the phosphorylation and inhibition of PDH resulting in decreased pyruvate oxidation and ATP production in *Npc1*$^{-/-}$ cerebellar neurons (Figure 4.01).

Increased glycolysis

Increased glycolysis n *Npc1*$^{-/-}$ cerebellum was indicated by several measures including increased lactate levels beginning at 3 weeks of age (Figure 3.08), increased mRNA levels of the astrocyte-specific enzymes *Ldha* and *Eno1* in 3- and 5-week-old *Npc1*$^{-/-}$ cerebellum (Figure 3.13 A, E), increased protein levels of the astrocytic GLUT1 in 7-week-old cerebellum (Figure 3.12 A), and increased mRNA levels of three neuronal and astrocytic isoforms of phosphofructokinase and protein levels of PFKp at 5 weeks of age (Figure 3.12 E)[337-340]. Even though the increased mRNA and protein levels are not conclusive proof, the findings strongly suggest that glycolysis is increased in *Npc1*$^{-/-}$ cerebellar astrocytes and neurons.

Several cell signaling pathways could lead to the upregulation of glycolysis in *Npc1*$^{-/-}$ cerebellum. One of these pathways is AMP kinase (AMPK), which is activated by high AMP to ATP ratios leading to the activation of several glycolytic proteins. However, the levels of total and phosphorylated AMPK were unchanged in 3-, 4-, and 5-week-old *Npc1*$^{-/-}$ cerebellum suggesting that AMP to ATP ratios were unchanged (Figure 3.14 A-C). ROS can also upregulate glycolysis, for example, *Pfk1m* expression is downregulated by micro RNA 320; hydrogen peroxide causes increased expression of *Pfk1m* and increased lactate production by damaging miRNA320, which normally

downregulates *Pfk1m* [341]. Additionally, Hif1alpha, which is activated by ROS, leads to upregulation of glycolytic genes [335]. Although further investigation on the cause of increased glycolytic gene expression in *Npc1*$^{-/-}$ brain is required, these findings suggest that oxidative stress and not energy deprivation is the likely cause in *Npc1*$^{-/-}$ cerebellum (Figure 4.02 describes a model of glycolysis in *Npc1*$^{-/-}$ cerebellum).

Altered glutamate metabolism

Glutamate is important in neurotransmission, ammonium detoxification, and energy metabolism in the brain. Therefore, even small alterations in glutamate metabolism could have consequences on neuronal health. Although glutamate and glutamine levels were unchanged in *Npc1*$^{-/-}$ cerebellum, we observed alterations in several genes involved in the glutamate-glutamine cycle suggesting that glutamate metabolism was altered (the glutamate-glutamine cycle is described in Figure 1.09). In the glutamate-glutamine cycle, glutamate is released by neurons at the synaptic terminus where it acts as an excitatory neurotransmitter. Glutamate is then taken up by neighboring astrocytes, converted to glutamine and shuttled back to neurons. In neurons glutamine is converted back into glutamate and the cycle continues. Glutamate can alternatively be oxidized as an energy source. For example, during hypoglycemia, increased glutamate is oxidized as an energy source in the brain [342-344]. I hypothesize that impaired glucose oxidation leads to increased glutamate oxidation in *Npc1*$^{-/-}$ cerebellum.

Several of our findings, including increased glutamine synthetase, glutaminase 2, glutamate dehydrogenase, aspartate aminotransferase, alanine aminotransferase 2, and neuronal branched chain aminotransferase 1 mRNA supports an increased flux to glutamate in neurons and increased glutamate oxidation in *Npc1*$^{-/-}$ cerebellum (Figure

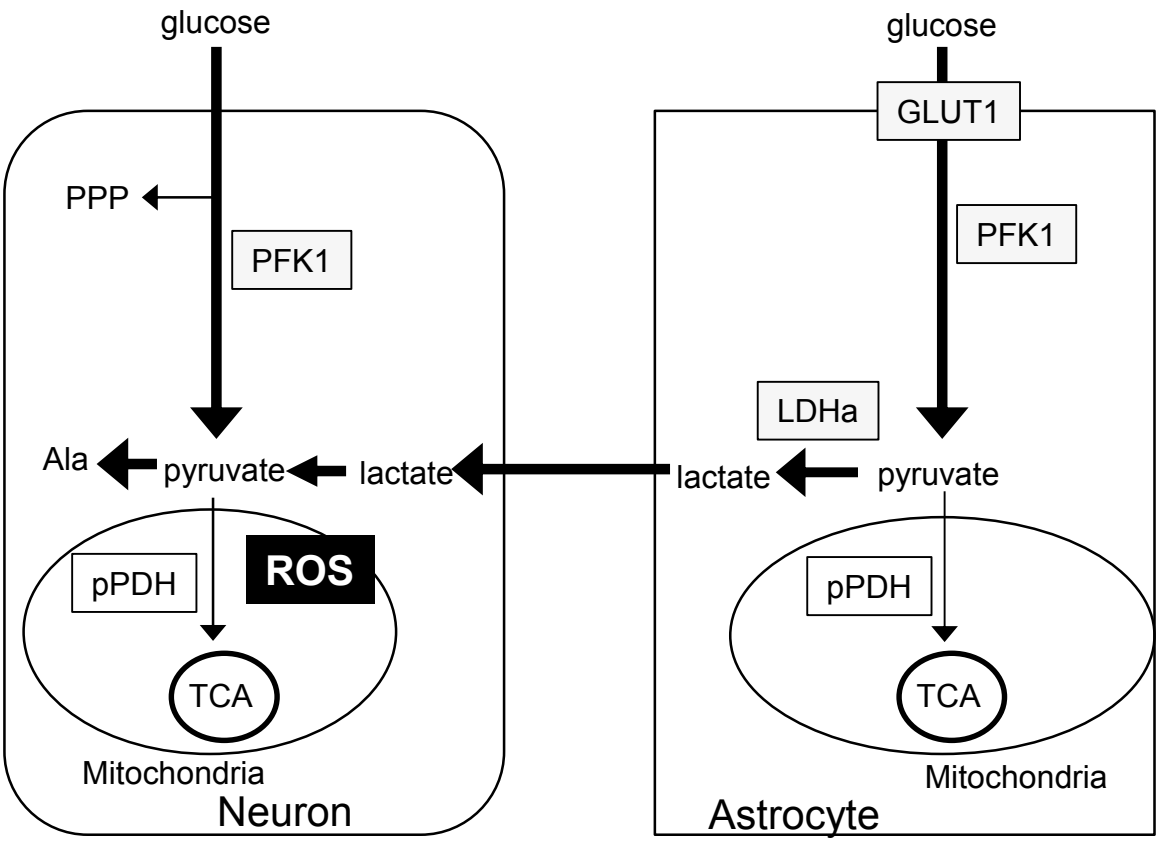

Figure 4.02 Model of glycolysis in *Npc1*$^{-/-}$ murine cerebellum
ROS causes increased phosphorylation of PDH, which leads to increased glycolysis and decreased oxidation of pyruvate. Black arrows represent metabolic flux with the darker arrows representing the areas of greatest flux. Grey boxes represent enzymes that are increased in protein and/or mRNA levels in *Npc1*$^{-/-}$ cerebellum. pPDH: phosphorylated/inhibited Pyruvate Dehydrogenase, ROS: Reactive oxygen species, GLUT1: astrocytic glucose transporter 3, PFK1: phosphofructokinase 1, LDHa: astrocytic lactate dehydrogenase a, TCA: tricarboxylic acid cycle, PPP: pentose phosphate pathway.

3.18). These increases in aminotransferase mRNA levels along with increased alanine, branched chain amino acids amino acids (leucine, valine, and isoleucine), and asparagine (synthesized from aspartate and glutamine in a reaction catalyzed by asparagine synthetase) supported increased conversion of glutamate to alpha-ketoglutarate in *Npc1*$^{-/-}$ cerebellum (Figures 3.08 and 3.22). Furthermore, the addition of glutamate decreased glucose uptake to a much greater extent in *Npc1*$^{-/-}$ neurons suggesting that *Npc1*$^{-/-}$ neurons preferred glutamate to glucose as an energy source (Figure 3.27 A) (Figure 4.03).

If pyruvate oxidation is inhibited in *Npc1*$^{-/-}$cerebellum glutamate oxidation can only occur in a truncated TCA cycle. A truncated TCA cycles have been observed in rat brains during hypoglycemia and in murine small intestine after fasting [345, 346]. In this pathway, glutamate and oxaloacetate are converted to alpha ketoglutarate and aspartate by aspartate aminotransferase (GOT2). Alpha-ketoglutarate is subsequently converted back to oxaloacetate in a five-step enzymatic TCA cycle reaction, resulting in the reduction of two NAD+ molecules to NADH and the generation of one GTP per glutamate molecule (Figure 4.04) and allowing cells to generate energy without the need of pyruvate oxidation. Increased mRNA levels of GOT2 and increased levels of asparagine in *Npc1*$^{-/-}$ cerebellum support truncated TCA cycle.

The signaling mechanisms that might cause such alterations in glutamate metabolism in *Npc1*$^{-/-}$ cerebellum are unknown. Several of the genes that were upregulated in *Npc1*$^{-/-}$ are regulated by p53, which can be activated by oxidative stress [347, 348], namely *Glud1*, *Got2*, and *Gls2*. However, while Gls2 is upregulated by p53, Glud1 and Got2 are negatively regulated by p53 [349, 350]. The increase of *Glud1*, *Got2*,

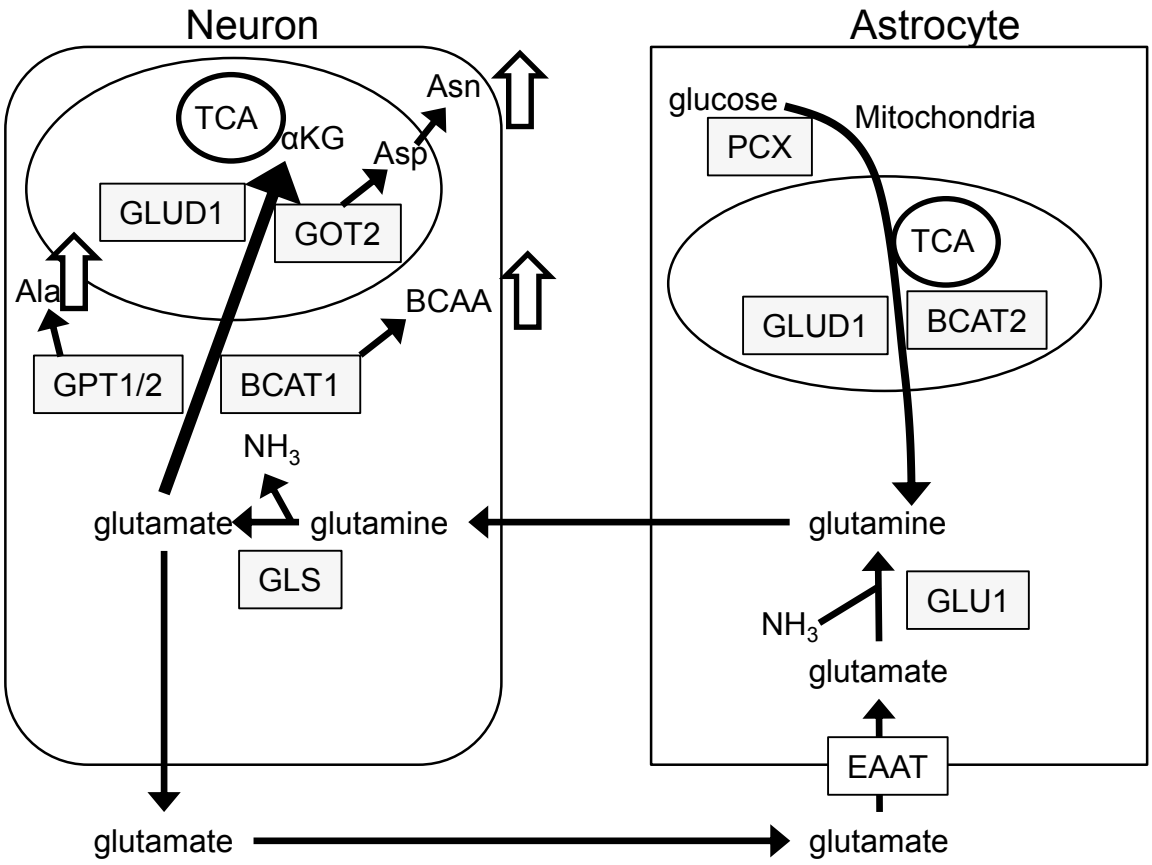

Figure 4.03 Model of glutamate metabolism in *Npc1*$^{-/-}$ murine cerebellum
Increased glutamate conversion to αKG in *Npc1*$^{-/-}$ cerebellum compared to WT results in increased levels of Asn, Ala, and BCAAs. Black arrows represent metabolic flux with the darker arrows representing the areas of greatest flux. Grey boxes represent enzymes that are increased in protein and/or mRNA levels in *Npc1*$^{-/-}$ cerebellum. White arrows represent increases in indicated metabolite levels. GLU1: glutamine synthetase, GLS2: glutaminase 2, GOT2: aspartate aminotransferase 2, GLUD1: glutamate dehydrogenase, BCAT1/2: branched-chain aminotransferase 1/2, GPT2: alanine aminotransferase 2, TCA: tricarboxylic acid cycle, αKG: alpha ketoglutarate, BCAA: branched chain amino acids, PCX: pyruvate carboxylase.

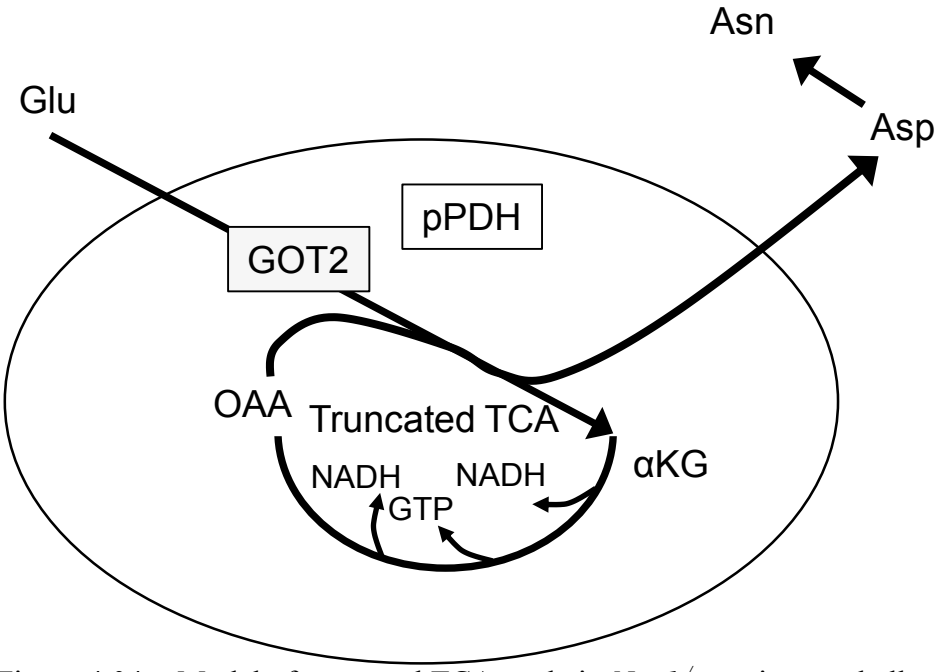

Figure 4.04 Model of truncated TCA cycle in *Npc1*$^{-/-}$ murine cerebellum
Black arrows represent metabolic flux. Grey boxes represent enzymes that are increased in protein and/or mRNA levels in *Npc1*$^{-/-}$ cerebellum. GOT2: aspartate aminotransferase 2, TCA: tricarboxylic acid cycle, αKG: alpha ketoglutarate, OAA: oxaloacetate pPDH: phosphorylated/inhibited pyruvate dehydrogenase.

and *Gls2* mRNA levels in *Npc1*$^{-/-}$ cerebellum does not clearly align with either an activation or inactivation of p53. Interestingly, the p53 e3 ligase mRNA levels, which negatively regulates p53 protein levels, are increased in 7-week-old *Npc1*$^{-/-}$ liver suggesting that p53 protein levels may be decreased [351]. Other genes including *Glu1* are regulated by ammonium levels [221, 352]; however, whether ammonium levels are increased in *Npc1*$^{-/-}$ cerebellum is unknown.

Altered energy metabolism in cortex and hippocampus

Our most extensive characterization of *Npc1*$^{-/-}$ brains was of the cerebellum, however, NPC disease affects all brain regions including the cerebral cortex and the hippocampus. We found increased oxidative stress markers and significant alterations in gene expression and metabolite levels in both *Npc1*$^{-/-}$ cortex and hippocampus. However, each brain region showed a distinct pattern of changes. Similar to cerebellum, *Npc1*$^{-/-}$ cortex had increased levels of phosphorylated PDH, increased *Pdk1* mRNA levels, decreased acetate levels, increased lactate levels, and increased *Pfkp* mRNA levels consistent with increased glycolysis and decreased pyruvate oxidation in 5-week-old *Npc1*$^{-/-}$ murine cortex (Figures 3.09 and 3.15). Whether glutamate oxidation was also increased will require further investigation including an analysis of amino acids, although the increased *Glud1* and *Bcat2* mRNA levels suggested altered glutamate metabolism in *Npc1*$^{-/-}$ murine cortex (Figure 3.20). However, the differences gene expression in cerebellum and cortex including for example decreased mRNA levels of *Glu1* in *Npc1*$^{-/-}$ cortex (mRNA levels were increased in *Npc1*$^{-/-}$ cerebellum) suggested that glutamate metabolism may differ from *Npc1*$^{-/-}$ murine cerebellum (Figure 3.20).

Similar to cerebellum and cortex, *Nfe2l2* and *Pfkm* mRNA levels were increased in *Npc1*$^{-/-}$ murine hippocampus suggesting increased glycolysis and oxidative stress. However, the normal lactate and alanine levels, increased PDH protein levels, and the lack of an increase in phosphorylated PDH suggested normal or higher PDH activity in *Npc1*$^{-/-}$ murine hippocampus. The decreased acetyl-CoA levels would then suggest increased metabolism of acetyl-CoA; the four main pathways of acetyl-CoA metabolism are cholesterol biosynthesis in glia, fatty acid synthesis in glia, acetylcholine synthesis in cholinergic neurons, or entry into TCA cycle. Acetyl-CoA is not likely used as a substrate for cholesterol biosynthesis because cholesterol biosynthesis is decreased in *Npc1*$^{-/-}$ brain [353]. Acetylcholine is a neurotransmitter that is synthesized by the transfer of the acetyl group from acetyl-CoA to choline mediated by choline acetyltransferase. Interestingly, we detected decreased choline levels in all *Npc1*$^{-/-}$ brain regions including hippocampus (Figure 3.08-3.10). Decreased acetyl-CoA and choline levels would be consistent with increased acetylcholine synthesis. Recently, two groups have found evidence that the cholinergic system is altered in NPC1-deficiency, including increased choline acetyltransferase protein levels in 8-week-old *Npc1*$^{-/-}$ mouse hippocampus [354]. Also, a clinical neurophysiologic study concluded that the cholinergic system was dysfunctional in human NPC patients based on analysis of cognitive abilities [355]. Alternatively, acetyl-CoA could be metabolized by the TCA cycle. However, preliminary results showed decreased KGDH protein levels in *Npc1*$^{-/-}$ hippocampus suggesting a block in the TCA cycle (Figure 3.16). Further work is required to determine the mechanisms leading to the decreased acetyl-CoA levels in *Npc1*$^{-/-}$ hippocampus.

4.1.2 Other reports of mitochondrial dysfunction and altered energy metabolism in NPC disease

Recently, several groups have analyzed large datasets of *Npc1*$^{-/-}$ tissues or cells, including gene expression analysis of *Npc1*$^{-/-}$ murine liver [351], *Npc1*$^{-/-}$ human fibroblasts [247, 250], *Npc2*$^{-/-}$ human fibroblasts [356], 3-week-old *Npc1*$^{-/-}$ murine cerebellum [357], 7-week-old *Npc1*$^{-/-}$ murine cerebellum and liver [245], and proteomic analysis of *Npc1*$^{-/-}$ murine cerebellum [358]. In addition to these studies, other smaller scale studies reported differences in mRNA levels or protein levels of genes involved in energy metabolic pathways. In this section I will discuss how findings from these studies compare to our study.

Oxidative stress

Several studies found markers of oxidative stress in 7-week-old *Npc1*$^{-/-}$ mouse brain and in CSF of symptomatic human NPC disease patients [240, 241, 243-245, 351]. Moreover, SOD1 and UCP2 protein levels are increased in human NPC patient CSF, and mRNA levels are increased beginning at 1 week of age in *Npc1*$^{-/-}$ murine livers [351, 358]. Furthermore, total glutathione levels were decreased in 7-week-old *Npc1*$^{-/-}$ mouse livers [245]. Whereas total glutathione levels in *Npc1*$^{-/-}$ mouse whole brain were unaltered, mitochondrial glutathione levels were decreased in 7-week-old *Npc1*$^{-/-}$ murine brain [146]. Several components of the glutathione S-transferase family are upregulated as early as 1 week of age in *Npc1*$^{-/-}$ mouse cerebellum and in CSF of human NPC patient, suggesting activation of the glutathione antioxidant pathway [358]. Together with our findings, these results clearly show that oxidative stress occurs in *Npc1*$^{-/-}$ mice and NPC human patients.

Mitochondrial function

Similar to our findings, other studies have shown evidence that pyruvate oxidation is disrupted in *Npc1*$^{-/-}$ mice, including decreased PDH subunit b mRNA levels and increased pyruvate dehydrogenase kinase 3 mRNA levels in pre-symptomatic *Npc1*$^{-/-}$ liver [351]. Also, a proteomic analysis 1-week-old *Npc1*$^{-/-}$ cerebellum found decreased PDH subunit E1 protein levels [358]. Additionally, there is a non-significant trend to higher pyruvate levels in 1-week-old *Npc1*$^{-/-}$ cerebellum [358].

Mitochondria isolated from 9-week-old *Npc1*$^{-/-}$ murine brains produce less ATP in the absence of energy substrates [144], and have low rates of ATP hydrolysis, indicating a defect in ATP synthase activity [144]. Supporting a decrease in ATP synthase activity, mRNA and protein levels of the ATP synthase beta subunit were decreased as early as 1 week of age in *Npc1*$^{-/-}$ cerebellum [245, 358]. Conversely, we found lower rates of ATP synthesis only mitochondria isolated from 3-week-old *Npc1*$^{-/-}$ murine brain in the presence of pyruvate and malate, while mitochondria isolated from 7-week-old *Npc1*$^{-/-}$ murine brain appeared normal (Figure 3.05). We proposed that the defect in ATP generation is caused by PDH inhibition rather than a defect in ATP synthase. Differences between these studies include the age of the mice and the energy substrate used. Furthermore, data from our NPC1-depleted CHO cells showed that ATP/ADP exchange across the mitochondrial membranes was defective, which could also explain the defect in ATP synthase activity observed by Yu et al. (Figure 3.43)[144]. Together these results suggest that mitochondrial ATP production is decreased possibly as early as 3 weeks of age in *Npc1*$^{-/-}$ murine brain; however, determination of the mechanism of decreased ATP will require further investigation.

Glycolysis

In the literature there are several reports in support of increased glycolysis and conversely other reports that support decreased glycolysis in *Npc1*$^{-/-}$ cells and brain. For example, *in vivo* glucose uptake in the brain of NPC patients appears to depend on the brain region and disease stage; in a 33-year-old NPC disease patient, glucose uptake was decreased in cerebellum, cortex, and thalamus [359]; in 6-year-old twins with NPC disease, glucose uptake was decreased only in frontal cortex [360]; in a 22-year-old NPC patient, glucose uptake was decreased in frontal cortex and thalamus but increased in cerebellum and pons [361]. Additionally, glucose uptake is decreased in *Npc1*$^{-/-}$ human fibroblasts incubated in the absence of alternative metabolites [358]. This latter finding is in contrast to our finding that *Npc1*$^{-/-}$ cortical neurons have increased glucose uptake in the absence of alternative energy metabolites and also differs from our findings that NPC1-depleted CHO cells had normal glucose uptake in the absence of alternative metabolites, showing that glucose uptake is dependent on the cell type in *Npc1*$^{-/-}$ cells (Figure 3.27).

Cluzeau et al. detected increased mRNA levels of several glycolytic genes in *Npc1*$^{-/-}$ murine liver [351]. These genes included *Ldhb*, aldolase A and C beginning at 1 week of age; hexokinase I, II, and III, enolase II, and *Pkm2* beginning at 3 weeks of age; glucose-6-phosphate isomerase and *Pfkp* beginning at 5 weeks of age [351]. Conversely, in a proteomic analysis of *Npc1*$^{-/-}$ cerebellum found decreased glycolytic enzymes including PKM1/2 beginning at 1 week of age and triosephosphate isomerase I beginning at 5 weeks of age [358]. Results from these two studies suggest that glycolysis is upregulated in *Npc1*$^{-/-}$ murine livers but downregulated in *Npc1*$^{-/-}$ cerebellum. The

downregulation of glycolysis is in contrast to our findings of increased expression of several glycolytic enzymes including PFK1 at 5 weeks and increased lactate levels at all ages in *Npc1*$^{-/-}$ cerebellum (Figures 3.08 and 3.12). The contrasting conclusions from these two studies emphasize the difficulties in studying energy metabolism in the brain because of the complex factors contributing to regulation of energy metabolism and the contributions to energy metabolism by the two metabolically distinct cell types (neurons and astrocytes).

Glutamate metabolism

Few studies have addressed glutamate metabolism in *Npc1*$^{-/-}$ cells. Consistent with our findings, Yadid et al. found that glutamate and glutamine levels were unchanged in 50-day-old *Npc1*$^{-/-}$ cerebellum [57]. Proteomic analysis on 8-week-old *Npc1*$^{-/-}$ hippocampus revealed decreased protein expression astrocytic glutamate transporter, excitatory amino acid-carrier-1, and increased glutamic acid decarboxylase (GAD-6) protein levels [56]. Increased GAD-6 protein is in line with increased *Gad1* mRNA levels that we detected in 5-week-old *Npc1*$^{-/-}$ hippocampus (Figure 3.21). The significance of these alterations in hippocampal glutamate metabolism are unknown.

4.1.3 Detrimental and compensatory pathways

Here, I have characterized mitochondrial function, glucose and glutamate metabolism in *Npc1*$^{-/-}$ murine brain. Without intervention in pathways and observation of the resulting phenotype the consequences of the metabolic alterations remain unknown. Nevertheless, studies of these pathways in different contexts can give us clues to which pathways in which cell types are likely detrimental, and therefore potential therapeutic targets, and which are compensatory. The relative contribution of neurons and astrocytes

to NPC pathogenesis has been addressed in several studies by using cell-specific expression of NPC1. Expression of NPC1 only in Purkinje cells of *Npc1*$^{-/-}$ mice (site of the majority of neurodegeneration in NPC disease) prevents weight loss, neurological ataxia, and extends life span by approximately 25% [253, 362]. Depletion of NPC1 of Purkinje cells of wildtype mice caused Purkinje cell death and loss of motor function beginning at postnatal day 6 but not the weight loss or premature death characteristic for *Npc1*$^{-/-}$ mice [363]. Expression of NPC1 in neurons of *Npc1*$^{-/-}$ mice prevented neuron degeneration and ameliorated the disease, whereas, depletion of NPC1 in non-Purkinje neurons result in a similar phenotype as *Npc1*$^{-/-}$ mice [362, 364]. Together these findings suggest that Purkinje cell death causes ataxia but is not solely responsible for the neuropathology and premature death of *Npc1*$^{-/-}$ mice, and that neuronal abnormalities in all regions of the brain caused neuropathology and premature death of *Npc1*$^{-/-}$ mice.

Supporting a role for glial in NPC disease is that expression of NPC1 in glia (mediated by the glial fibrillary acidic protein (GFAP) promoter) caused decreased cholesterol accumulation in neurons, decreased neurodegeneration, and prolonged lifespan of *Npc1*$^{-/-}$ mice by 3 times [365]. However, there was some doubt about the specificity of the promoter and other studies showed much less contribution of astrocytes to NPC disease pathogenesis. For example, Lopez et al. found that expression of NPC1 in astrocytes only (driven by GFAP promoter) does not improve life span compared to *Npc1*$^{-/-}$ mice [362]. Also, transgenic mice with depletion of NPC1 in astrocytes beginning at 6 weeks of age do not display any symptoms of NPC pathology [364]. Furthermore, death of *Npc1*$^{-/-}$ Purkinje cells is not prevented by surrounding wildtype astrocytes or conversely, wildtype Purkinje cells are not killed by surrounding NPC1-deficient cells in

chimeric mice with selective expression NPC1 only in some cells [253]. Depletion of NPC1 in oligodendrocytes, results in delayed myelination at early postnatal stages, decreases performance on a balance beam suggesting loss of muscle control, Purkinje cell death, although at a much later age than *Npc1*$^{-/-}$mice (between 7 and 23 weeks of age), but no premature death [366]. These latter findings suggest that NPC disease pathogenesis is not caused by loss of NPC1 in astrocytes and expression of NPC1 in astrocytes is not sufficient to rescue NPC1-deficient neurons.

The apparent lack of involvement of astrocytes in NPC disease surprising considering the significant alterations in astrocytic energy metabolism that we observed and the activation of astrocytes early in disease progression [52]. One possible explanation would be that the alterations in *Npc1*$^{-/-}$ astrocytes are compensatory pathways that are actually beneficial for *Npc1*$^{-/-}$ neurons. In addition to providing neurons with lactate and glutamine for energy, astrocytes also play a role in antioxidant defense by providing glutamine and cysteine for the synthesis of glutathione in neurons in an Nrf2-dependent mechanism [367-370]. It may be worth considering that alterations in *Npc1*$^{-/-}$ astrocytes are beneficial and therefore would not be a potential target for treatment.

One potential target for treatment in *Npc1*$^{-/-}$ murine brain is oxidative stress. Oxidative stress is known to contribute to neurodegeneration, axonal deterioration, and several other defects leading to brain dysfunction in other neurological disorders [371]. Furthermore, because markers of oxidative stress were increased at presymptomatic ages it is likely to be an initial defect in NPC disease progression. Several antioxidant therapeutic treatments have been attempted in *Npc1*$^{-/-}$ mice to mixed success. Treatment with two antioxidants, vitamin E and tamoxifen, at 3 weeks of age delayed loss of motor

function and weight loss in *Npc1*$^{-/-}$ mice [372]. Daily treatment with curcumin (a potent activation of antioxidant defense genes) at weaning prolonged *Npc1*$^{-/-}$ mouse survival by 35% [373, 374]. However, treatment of *Npc1*$^{-/-}$ mice at week 6 with the antioxidant vitamin C had no effect on survival [375]. Treatment with the antioxidant NAC beginning at week 6 had minimal effects in the brain but presented liver damage in *Npc1*$^{-/-}$ mice [245]. Together these findings suggest that antioxidant treatment is beneficial to *Npc1*$^{-/-}$ mice, however, treatment must be started early in disease progression. With our findings that markers of oxidative stress are already increased at 3 weeks of age in *Npc1*$^{-/-}$ cerebellum, I propose that antioxidant treatment should be started presymptomatically in NPC patients.

Another potential factor in NPC pathology is an upregulation of glycolysis in neurons. Increased usage of glucose by glycolysis can decrease the availability of glucose for the pentose phosphate pathway, which generates NADPH (required for the reduction of glutathione mediated by glutathione reductase) [185]. Experimental upregulation of glycolysis in cultured neurons causes neurodegeneration by oxidative damage [183, 184]. Decreased flux through the pentose phosphate pathway in *Npc1*$^{-/-}$ cerebellum is supported by our findings of decreased G6pd mRNA levels at 3 weeks of age (Figure 3.13 F).

On the other hand, evidence supporting a beneficial role for glycolysis in the survival of Purkinje cells is found in factors contributing to Purkinje cell survival and neuronal function. Purkinje cells die in a complex pattern in *Npc1*$^{-/-}$ mice; the first Purkinje cells that die have a distinct protein expression profile including the lack of the glycolytic protein aldolase C, then as the disease progresses (by day 45) the majority of remaining Purkinje cells die [376, 377]. The significance of altered expression of aldolase

C in Purkinje cell death by NPC1-deficiency is unknown. One possible explanation would be that aldolase C-negative Purkinje cells are less capable of compensating for loss of mitochondria-generated ATP because of decreased glycolytic capability. Supporting this hypothesis is that ischemia, specifically causes death of specifically aldolase C negative Purkinje cells in rats [378]. Together these findings suggest that *Npc1*$^{-/-}$ Purkinje cells require increased glycolysis for survival, possibly to compensate for loss of energy production by mitochondria; however increased glycolysis could have a negative long-term effect.

PDH deficiency in humans is linked to ataxia and death of Purkinje cells, as well as poor weight gain, cognitive delay, seizures, and early death, suggesting that PDH deficiency causes global neuronal abnormalities [379]. Together these findings suggest that inhibition of PDH in *Npc1*$^{-/-}$ cerebellum contribute to Purkinje cell death, ataxia, and other brain abnormalities that lead to premature death of *Npc1*$^{-/-}$ mice.

4.2 Cholesterol transport to mitochondria

4.2.1 Increased mitochondrial cholesterol levels

To investigate the cause of mitochondrial dysfunction and altered energy metabolism in *Npc1*$^{-/-}$ murine brain we focused on the role of mitochondrial cholesterol. Similar to findings from several other groups we found increased mitochondrial cholesterol levels in 5- and 7-week-old *Npc1*$^{-/-}$ brain (Figure 3.28)[144-146]. Additionally, mitochondrial cholesterol levels were increased in Npc1-deficient CHO cells suggesting that this phenomenon was not unique to brain (Figures 3.29). In CHO cells we determined that cholesterol accumulated in mitochondria within 10 days of

NPC1-depletion, suggesting that cholesterol may accumulate early in NPC disease progression (Figure 3.30).

4.2.2 Cholesterol source

To investigate the effect of increased mitochondrial cholesterol on mitochondrial function we determined both the source of cholesterol and mechanisms to lower mitochondrial cholesterol. One method used to decrease mitochondrial cholesterol levels is the treatment with statin to inhibit cholesterol biosynthesis. Inhibition of cholesterol synthesis by statins (lovastatin, atorvastatin, simvastatin) decreases mitochondrial cholesterol levels in several models of mitochondrial cholesterol accumulation, including acetaldehyde-treated human hepatoblastoma cell, hepatocytes from *ob/ob* mice, and murine heptoma cells exposed to insulin [145, 155, 159, 380], suggesting that newly synthesized cholesterol from the endoplasmic reticulum is a source of increased mitochondrial cholesterol in these models. One possible mechanism of cholesterol transport between the endoplasmic reticulum and mitochondrial is through the specialized domains of the endoplasmic reticulum called mitochondria-associated membranes (MAM). Because MAM are cholesterol-rich and contain enzymes involved in cholesterol synthesis it has been proposed that cholesterol is transported to mitochondria at these sites [381, 382]. However, cholesterol biosynthesis is generally lower in NPC1-deficient cells compared to wildtype cells suggesting that the endoplasmic reticulum is not the source for increased mitochondrial cholesterol [90, 353, 383]. Previous work in our lab investigated the source of mitochondrial cholesterol in F2-CHO cells by incubating cells with or without exogenously supplied cholesterol and measuring pregnenolone production as an indication of cholesterol delivery to mitochondria. This study showed

that refeeding with cholesterol by addition of LDL to cholesterol starved NPC1-deficient F2-CHO cells decreased cholesterol biosynthesis by 2-fold but increased pregnenolone production by 30% pointing to endosomes as a source for mitochondrial cholesterol [147]. A similar increase in pregnenolone production occurred after LDL treatment of control and NPC1-deficient F2-CHO cells showed that this pathway was not inhibited by loss of NPC1 [147]. The transport of exogenously-derived cholesterol to mitochondria is also in line with the known stimulation of oxysterol production by lipoproteins [90]. Together these findings suggest 1) cholesterol is transported from endosome to mitochondria in an NPC1-independent mechanism and 2) exogenously-derived cholesterol and not newly synthesized cholesterol was the source for accumulating mitochondrial cholesterol in NPC1-deficient CHO cells.

In a second study we further investigated whether cholesterol was transported directly from endosomes to mitochondria [267]. We developed an assay to measure cholesterol delivery to mitochondria in the absence of cytosolic transfer proteins, ATP, and/or GTP [267]. We showed that digitonin-treated semi-permeabilized F2-4-4-19 cells produced pregnenolone, and that pregnenolone levels were increased by a pre-incubation with lipoprotein-containing serum, suggesting that cholesterol was transported from endosomes to mitochondria in a mechanism independent of cytosolic transport proteins [267].

The mechanism of cholesterol transport between endosomes and mitochondria is unknown; however, several studies showing the transport of other substrates from endosomes to mitochondria. For example, iron is directly transported from endosome to mitochondria in developing erythroid cells; by direct contact sites visualized by electron

microscopy [384]. Contact sites were also found between endosomes and mitochondria following treatment with *H. pylori* toxin [385]. Further investigation is required to determine whether cholesterol transport between endosomes and mitochondria involves direct, possibly transient contact between the organelles.

4.2.3 MLN64

To investigate the mechanism of cholesterol transport between endosomes and mitochondria we measured the effect of RNAi-depletion of candidate endosomal proteins on mitochondrial cholesterol levels and pregnenolone production. Depletion of MLN64 reduced pregnenolone production by F2-CHO cells and mitochondrial cholesterol levels in NPC1-depleted CHO cells suggesting that MLN64 was involved in the transport of endosomal cholesterol to mitochondria and contributed to mitochondrial cholesterol accumulation in NPC1-depleted CHO cells (Figure 3.33 C). These findings are in line with previous studies showing that addition of the soluble START domain of MLN64 increased the production of steroids by placental mitochondria [386, 387]. The mechanism of MLN64 dependent cholesterol delivery is unknown. Bose et al. found that normal placenta expresses an N-terminally cleaved, cytosol MLN64 and suggested that this cleaved MLN64 delivers cholesterol in a mechanism similar to the StAR protein [171, 387]. However, findings in semi-permeabilized cells that cytosolic proteins were not necessary, speak against a general requirement for cleavage of MLN64 to transport cholesterol to mitochondria [267]. Two MLN64 domains bind cholesterol: the transmembrane MENTAL domain of MLN64 and the cytosolic START domain [169]. Therefore, one possible mechanism is that cholesterol is delivered to the transmembrane domain and subsequently passed to the cytosolic START domain from where cholesterol

is then delivered directly to an acceptor on the outer mitochondrial membrane. On the other hand, a recent study has shown that MLN64 forms a tether between late endosomes and endoplasmic reticulum [388]. It is difficult to envision all three organelles (endosomes, endoplasmic reticulum, and mitochondria) interacting together therefore it is likely that MLN64 only interacts with one organelle at a time. Further work is required to determine whether the endoplasmic reticulum acceptor and the mitochondrial acceptor compete for a common site in MLN64 and also under what conditions these may differ or whether it is a two-step mechanism.

Although MLN64 delivers cholesterol to mitochondria in NPC1-deficient cells leading to mitochondrial cholesterol accumulation, the flux of cholesterol through this pathway in wildtype cells is unknown. While depletion of MLN64 decreased pregnenolone production in both wildtype and NPC1-deficient cells, mitochondrial cholesterol levels were only decreased in NPC1-depleted cells suggesting that depletion of MLN64 had much less of an effect in wildtype cells compared to NPC1-deficient cells. Furthermore, expression of MLN64 with a loss of function mutation in its START domain in mice caused only minimal effects on plasma lipid levels, liver lipid content and expression of genes involved in sterol metabolism [389]. However, primary cultures of granulosa cells from these *Mln64* mutant mice had reduced conversion of cholesterol to steroids further supporting that MLN64 transports cholesterol to mitochondria [389]. Although depletion of MLN64 may have minimal effects in wildtype cells and mice, it may contribute to other pathogenic conditions.

4.2.4 NPC2

We found that depletion of NPC2 decreased cholesterol transport to mitochondria (Figure 3.34 E). NPC2 transfers endosomal cholesterol from internal membranes to the endosome perimeter membrane [122, 390-393]. However, the only known protein acceptor of cholesterol at the endosome perimeter from NPC2 is NPC1. Our findings that endosomal cholesterol was transported to mitochondria independently of NPC1 suggested that NPC2 delivers cholesterol to mitochondria independently of NPC1. To answer this question we generated expression vectors encoding mutated NPC2 proteins that were previously described to be unable to bind cholesterol ($NPC2^{Y119S}$) or unable to transfer cholesterol to NPC1 ($NPC2^{V81A/V81D}$) [125]. The expression of $NPC2^{V81A/V81D}$ restored pregnenolone production (Figure 3.34) and caused an accumulation of mitochondrial cholesterol in NPC2-depleted cells (Figure 3.35 C). Suggesting that transfer to NPC1 was not necessary for endosome to mitochondria cholesterol trafficking and that mitochondrial cholesterol can accumulate under conditions when endosomal cholesterol is high and endosome-to-mitochondrial transport is possible. Altogether these finding suggest a model in which NPC2 contributes to the transport of cholesterol from the endosome to mitochondrial independently of NPC1 possibly through MLN64. Whether NPC2 delivers cholesterol directly to MLN64 requires further investigation (Figure 4.05 shows my proposed model of cholesterol transport between endosomes and mitochondria).

4.2.5 NPC2 vs NPC1

Our results suggest different roles for NPC1 and NPC2 in cholesterol transport to mitochondria. The current model of NPC1 and NPC2 is that the two proteins function in

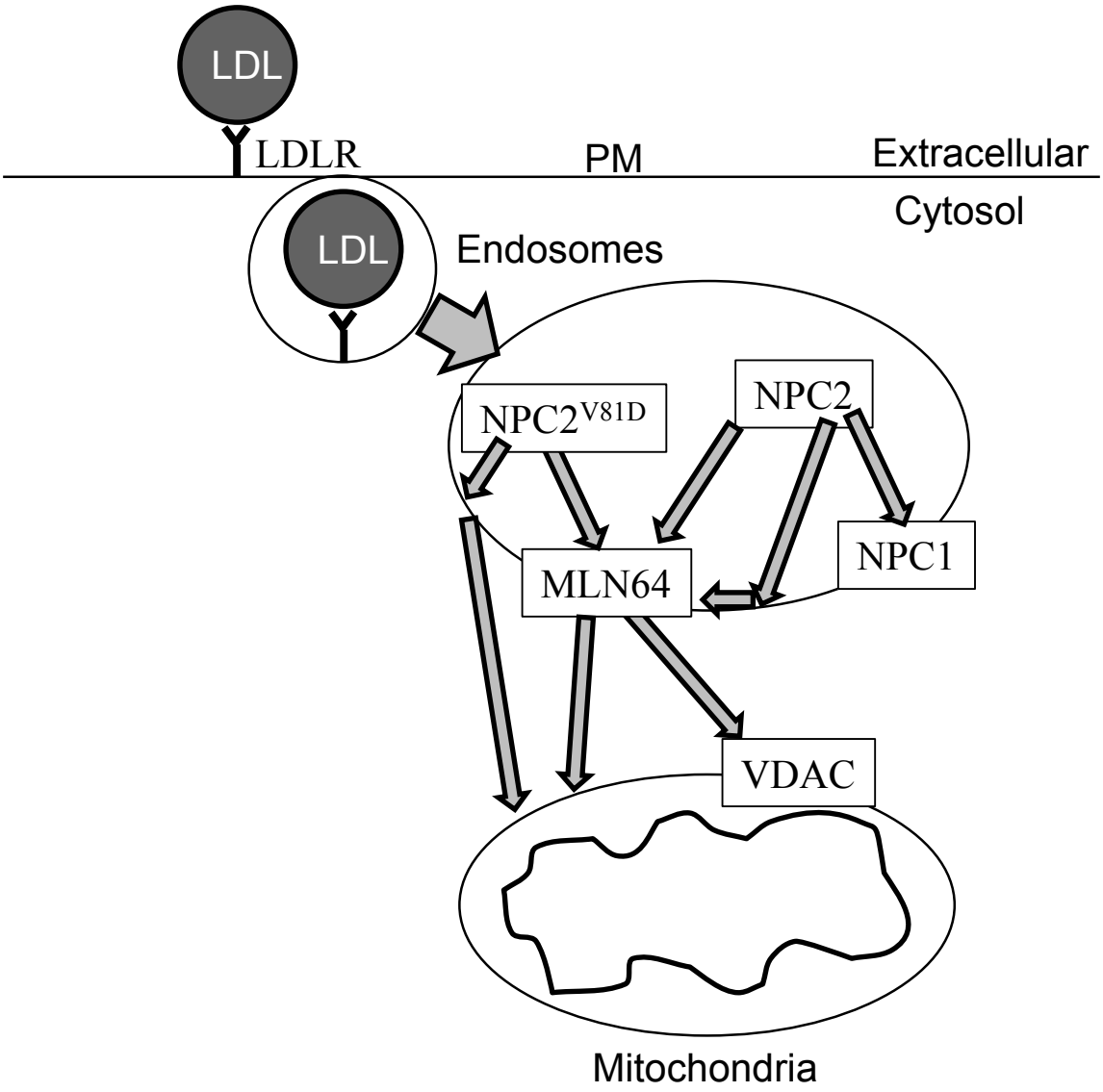

Figure 4.05 Model of endosomal cholesterol transport to mitochondria
Exogenously-derived cholesterol is transported to mitochondria by NPC2, independently of NPC1. NPC2 transports cholesterol to mitochondria in an unknown mechanism but likely involves MLN64. NPC2 may transport cholesterol directly to MLN64 or indirectly through the perimeter membrane. MLN64 transports cholesterol to mitochondria in an unknown mechanism but possibly through VDAC. Large grey arrow represent the direction of cholesterol transport. PM: plasma membrane, LDL: low density lipoprotein, LDLR: LDL receptor, VDAC: voltage-dependent anion channel, MLN64: metastatic lymph node 64.

the same cholesterol transport pathway. NPC2 transports cholesterol to the N-terminal domain through interaction with the second lumenal domain of NPC1 presents cholesterol to cytosolic cholesterol carrier proteins [124, 125]. Several studies have identified biochemical differences between cells lacking NPC1 and cells lacking NPC2. For example, fibroblasts depleted of both NPC1 and NPC2 secreted less dextran (previously shown to accumulate in endosomes of NPC1-deficient cells [394]) than fibroblasts depleted of NPC1 or NPC2 [395]. In the same study, the retrograde fusion of lysosomes with endosomes in fibroblasts was prevented by depletion of NPC1 but not NPC2 [395]. Additionally, NPC2, but not NPC1, was required for ATP-binding cassette A1 (ABCA1)-mediated cholesterol mobilization from endosomes in human fibroblasts [396]. NPC2 has also been associated with the regulation of cell differentiation in adipocytes and fibroblasts; a role that has not been described for NPC1 [397, 398]. These findings may not necessarily support our proposed model for NPC2-dependent/NPC1-independent cholesterol transport to mitochondria but they show that NPC2 and NPC1 have distinct functions in addition to their activity in a common pathway, something that is not fully appreciated in the current model of endosomal cholesterol trafficking.

Our findings show that mitochondrial cholesterol levels accumulate in NPC1-deficient CHO cells and are unchanged in NPC2-depleted cells. If elevated mitochondrial cholesterol levels contribute to disease pathogenesis we would expect differences between NPC1-deficient and NPC2-deficient mice. Two different murine models of NPC2-deficiency have been characterized. Sleat et al. generated *Npc2*-hypomorph mice, which express between 0 and 4% of wildtype NPC2 and compared these mice to both $Npc1^{-/-}$ mice and $Npc1^{-/-}$ mice crossed with the NPC2 hypomorphs [61]. Although all

mutant mice die prematurely, have Purkinje cell death, and suffer from ataxia, NPC2 hypomorphs have delayed onset of symptoms including weight loss and a 40% longer lifespan compared to *Npc1*$^{-/-}$ mice, whereas double mutant (*Npc1*$^{-/-}$/*Npc2*$^{-/-}$) mice were indistinguishable from *Npc1*$^{-/-}$ mice [61]. The difference in onset of symptoms and age of death between *Npc1*$^{-/-}$ mice and NPC2 hypomorph mice would agree with my hypothesis that mitochondrial cholesterol accumulation contributes to disease phenotype, although the authors attributed the difference to the remaining expression of NPC2 in the NPC2 hypomorphs or possibly the strain background. More recently, Dixit et al. generated NPC2 hypomorph mice on identical background (BALB/c) as *Npc1*$^{-/-}$ mice [63]. Again, NPC2 hypomorphs mice survive on average 110 days compared to *Npc1*$^{-/-}$ mice that survive on average 73 days suggesting that the difference between NPC2 hypomorphs and *Npc1*$^{-/-}$ mice was not caused by strain differences [63]. Mice lacking both NPC1 and NPC2 survive on average 83 days, which was not significantly different from the *Npc1*$^{-/-}$ mice. NPC2 hypomorphs mice have several similar symptoms as *Npc1*$^{-/-}$ mice and die prematurely, thus increased mitochondrial cholesterol levels are not the main cause of neurodegeneration and premature death; however, the delay in symptoms in NPC2-hypomorph mice suggests that either the remaining expression of NPC2 or possibly mitochondrial cholesterol may contribute to NPC disease. A complete NPC2 null mouse has been recently generated however a comparison with *Npc1*$^{-/-}$ mice was not completed or life span was not measured [62].

4.3 CHO cell energy metabolism and effects of increased mitochondrial cholesterol levels

4.3.1 Altered energy metabolism in NPC1-deficient CHO cells

To determine the effect of cholesterol on mitochondrial function and energy metabolism in NPC1-deficient cells we genetically manipulated the endosome to mitochondria cholesterol transport pathway and measured several aspects of energy metabolism. Since the characterization of energy metabolism was completed in *Npc1*$^{-/-}$ murine brain, we first had to characterize energy metabolism in NPC1-deficient CHO cells. Similar to the brain, depletion of NPC1 in CHO cells led to significant changes in energy metabolism and mitochondrial function. Increases of lactate production in the presence or absence of glutamine suggest increased glycolysis in NPC1-depleted CHO cells (Figure 3.36), one likely associated with increased glucose uptake. An increase in glycolytic flux is consistent with the observed higher steady-state ATP levels in NPC1-deficient compared to wildtype CHO cells in the presence of glutamine (Figure 3.42). In *Npc1*$^{-/-}$ cerebellum, the increase in lactate levels was associated with increased phosphorylated PDH. Following DCA treatment to inhibit PDKs and activate PDH, the lactate production was not significantly different in NPC1-depleted and wildtype CHO cells suggesting that inhibition of PDH contributed to increased lactate production (Figure 3.44 A). However, PDH phosphorylation was not increased in NPC1-deficient CHO cells compared to control, PDH inhibition was unlikely the primary reason for the increased lactate production (Figure 3.44). The normalization of lactate production following pre-treatment with NAC suggests that oxidative stress contributes to increased lactate production (Figure 3.45 D).

To further investigate mitochondrial function in NPC1-deficient CHO cells we measured oxygen consumption rates (OCR) in the presence and absence of glutamine. In the presence of glucose, OCR were similar and generally low between control and NPC1-depleted CHO cells (Figure 3.40 A-D). The normal OCR were probably due to relatively low levels of mitochondrial respiration and is consistent with high glycolytic flux of proliferating CHO cells [322, 323]. In the presence of glutamine, the basal OCR, ATP turnover, and the maximal OCR were all decreased in NPC1-depleted cells indicating a defect in mitochondrial respiration (Figure 3.40 E-H). Basal OCR are controlled by three components: ATP turnover, substrate oxidation, and proton leak [321]. ATP turnover is further controlled by ATP synthase activity, ATP/ADP exchange, and turnover of ATP in the cytosol [321]. Substrate oxidation involves substrate uptake, metabolism of substrate, and electron transport chain activity [321]. Maximal OCR represent the maximal rate of substrate uptake, metabolism of substrate, and electron transport chain activity [321]. Since all components were lower than normal in NPC1-deficient CHO cells it was difficult to narrow down the dysfunction site causing the defect in mitochondrial respiration. Further investigation using a genetically encoded mitochondrial ATP sensor revealed deficiencies in ATP transport across mitochondrial membranes (Figure 3.43). Transport of ATP across mitochondrial membranes occurs in exchange for ADP and is mediated by the adenosine nucleotide translocase (ANT) in the inner mitochondrial membrane and by the voltage-dependent anion channel (VDAC) in the outer mitochondrial membrane [399, 400]. Defects in the transport of ATP across the mitochondrial membrane would limit the availability of ADP for ATP synthase and thereby decrease basal OCR and ATP turnover in NPC1-deficient CHO cells. Together

these results suggest that a defect in ATP/ADP exchange across the mitochondrial membranes causes decreased oxidation of glutamine, leading to upregulation of glycolysis to compensate for loss of energy production in NPC1-depleted CHO cells (Figure 4.06).

Further evidence of mitochondrial dysfunctional in NPC1-depleted CHO cells were the increased mRNA levels of *Nfe2l2* (Figure 3.45 A). Furthermore, the long established cell line, 4-4-19, produced more hydrogen peroxide than wildtype cells (Figure 3.47 A), while the short term depletion of NPC1 did not upregulate hydrogen peroxide production, suggesting that the upregulation of antioxidant defense system initially prevents accumulation of ROS.

4.3.2 How mitochondrial cholesterol affects energy metabolism

To determine the effect of increased mitochondrial cholesterol levels on mitochondrial dysfunction in NPC1-depleted CHO cell, we manipulated cholesterol transport from endosomes to mitochondria using depletion of MLN64. Depletion of MLN64 in wildtype cells did not affect mitochondrial cholesterol levels and had no effects on energy metabolism or mitochondrial function. Depletion of MLN64 in NPC1-depleted cells normalized lactate levels, glucose uptake, OCR in the presence of glutamine, and *Nfe2l2* expression, suggesting that mitochondrial cholesterol accumulation caused mitochondrial dysfunction in NPC1-deficient cells.

The findings in CHO cells expressing NPC2 mutants further supported the hypothesis that increased mitochondrial cholesterol levels caused mitochondrial dysfunction. Depletion of NPC2 had no effect on lactate production or *Nfe2l2* mRNA levels (Figure 3.46 A, C). Expression of $NPC2^{V81D}$ in NPC2-depleted cells (which led to increased

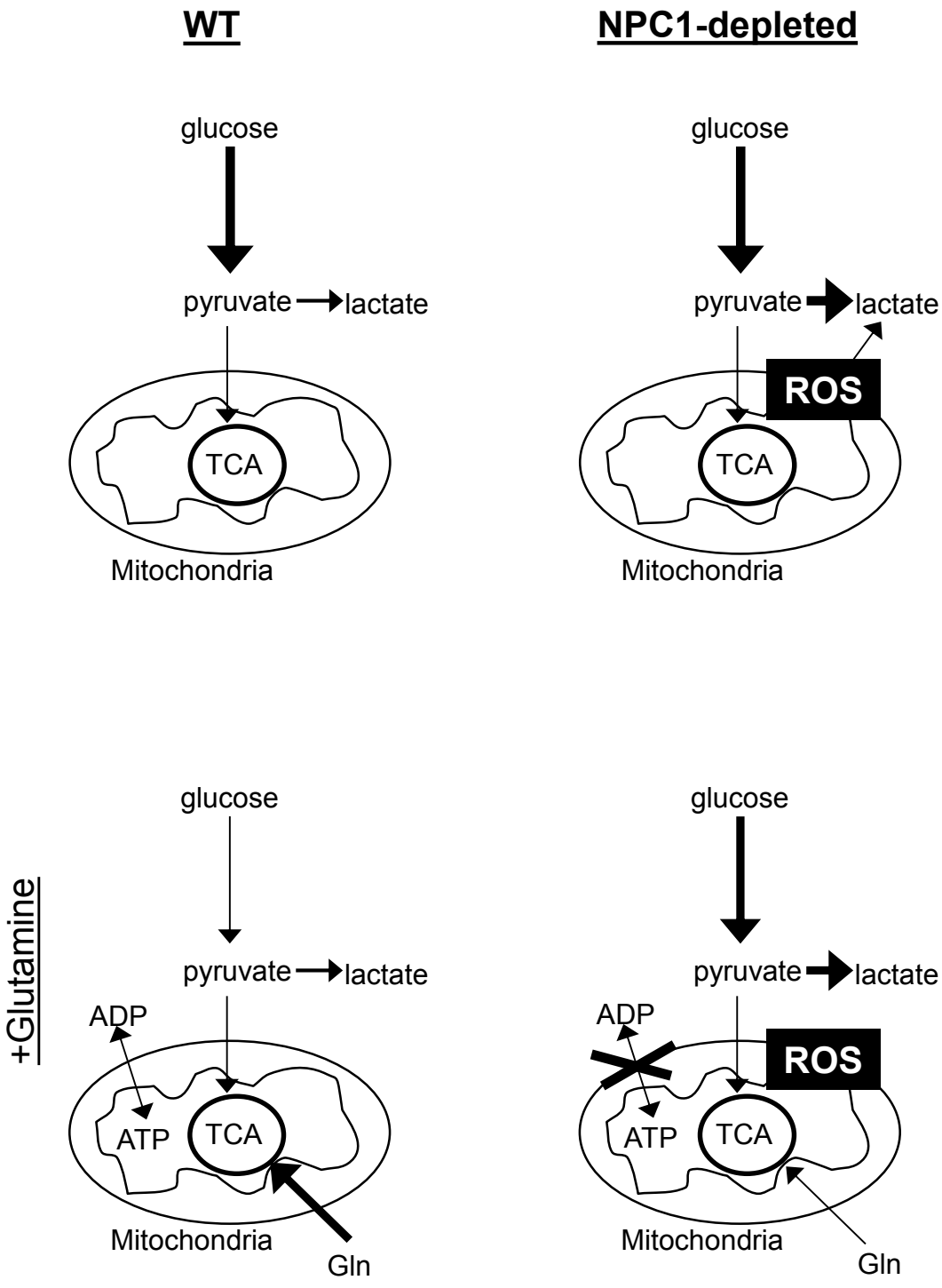
WT
NPC1-depleted
glucose
pyruvate
lactate
TCA
Mitochondria
ROS
+Glutamine
ADP
ATP
Gln

Figure 4.06 Model of energy metabolism in NPC1-depleted CHO cells in presence or absence of glutamine

In the absence of glutamine, NPC1-deficient CHO cells have increased glycolysis, which may be caused by ROS compared to WT cells. In the presence of glutamine, NPC1-deficient cells have increased glycolysis, decreased oxidation of glutamine, and decreased transport of ATP across the mitochondrial membrane. Black arrows represent metabolic flux with the darker arrows representing the areas of greatest flux. Left side represents CHO cells transfected with non-targeting siRNA (WT), right side represents NPC1-depleted CHO cells. ROS: Reactive oxygen species, TCA: tricarboxylic acid cycle, X= blocked.

mitochondrial cholesterol levels) also caused increased lactate production and *Nfe2l2* expression (Figure 3.46 D). This mitochondrial cholesterol accumulation caused oxidative stress, which increased lactate production, and a decreased capacity to oxidize glutamine, possibly because of a defect in ATP/ADP transport (Figure 4.07).

Our findings that increased cholesterol levels causes mitochondrial dysfunction are consistent with several other studies. When mitochondria isolated from hepatocytes are incubated with cholesterol complexed to cyclodextrin to increase mitochondrial cholesterol levels, ROS production complex I increases [159]. Several other models of mitochondrial cholesterol accumulation also show have increased oxidative stress. For example, Mari et al. found that mitochondrial cholesterol levels increase in liver from rats fed a high cholesterol diet within one day of the beginning of the diet [145]. Hepatocytes from high cholesterol fed rats generated more ROS and were more susceptible to apoptosis after treatment with TNF alpha compared to hepatocytes from chow-fed rats [145]. Moreover, mitochondrial but not cytosolic levels of reduced glutathione were decreased in hepatocytes from high cholesterol-fed rats [145]. Similarly, hepatocytes from *Npc1*$^{-/-}$ mice had increased mitochondrial cholesterol, were more susceptible to TNF alpha-mediated cell death, and had decreased mitochondrial glutathione levels [145]. TNF alpha-induced ROS production and cell death were prevented by treatment of hepatocytes with vitamin E or a membrane permeable form of glutathione (GSH ethyl ester) suggesting that the depletion of mitochondrial glutathione caused the susceptibility to TNF alpha [145]. Another study by Fernández et al. showed that mitochondrial cholesterol levels were increased in the brains of mice overexpressing SREBP-2, in a common murine model for Alzheimer disease, which expresses mutant amyloid precursor

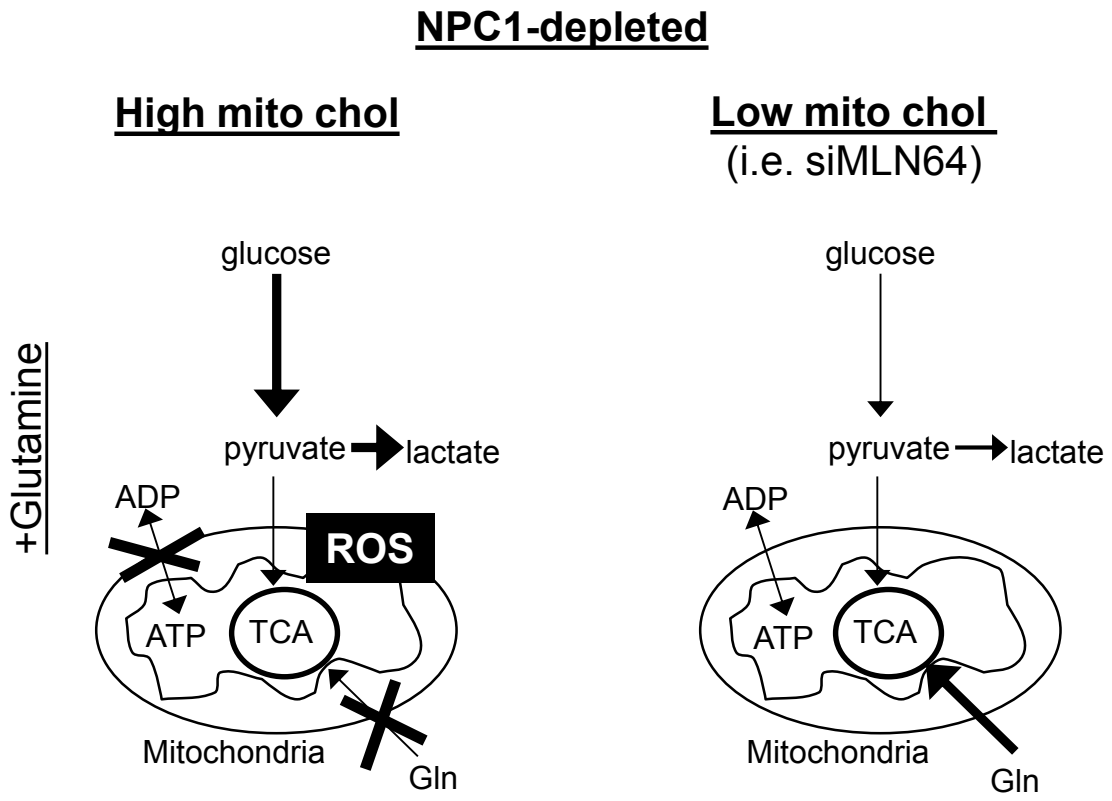

Figure 4.07 Effect of blocking endosomes-to-mitochondria cholesterol transport pathway on energy metabolism in NPC1-depleted CHO cells

Depletion of MLN64 in NPC1-depleted cells normalizes glycolysis and glutamine oxidation. Black arrows represent metabolic flux with the darker arrows representing the areas of greatest flux. Left side represents NPC1-depleted cells, right side represents NPC1-depleted CHO cells with low mitochondrial (mito) cholesterol (chol) (induced by depletion of MLN64). ROS: Reactive oxygen species, TCA: tricarboxylic acid cycle, X= blocked.

protein and mutant human presenilin-1 (APP/PS1 mice) at 10 months of age [146]. Mitochondrial glutathione levels were decreased in all three models [146], and mitochondria from the transgenic mice overexpressing SREBP-2 or from *Npc1*$^{-/-}$ brain generated approximately 2-fold higher ROS compared to control after exposure to human amyloid beta [146]. Treatment with GSH ethyl ester protected against neurodegeneration in the SREBP-2 overexpressing transgenic mice against neurodegeneration induced by amyloid beta [146]. Similar to our findings, mitochondria increased cholesterol levels (including mitochondria from *Npc1*$^{-/-}$ mice) produced similar levels of ROS compared to control under basal (not treated with TNF alpha or amyloid beta) conditions suggesting that additional stress is required for increased ROS production (Figure 3.04). Together these findings suggest that decreased GSH levels cause increased ROS and cell death in response to a stress signal such as TNF alpha or amyloid beta. Amyloid beta levels and TNF alpha signaling are increased in *Npc1*$^{-/-}$ murine brain [42, 254, 401], and the decreased mitochondrial glutathione levels would make *Npc1*$^{-/-}$ brain very susceptible to oxidative damage, neuronal dysfunction, and neurodegeneration.

Glutathione import into mitochondria is mediated by the inner mitochondrial membrane dicarboxylate and 2-oxoglutarate carriers [402-405]. The mode of glutathione transport across the outer mitochondrial membrane is unclear. A defect in VDAC1 but not VDAC2 caused accumulation of glutathione in yeast mitochondria possibly suggesting that VDAC1 played a role in transport of glutathione [237]. Because lipid composition affects membrane viscosity one possibility is that increased mitochondrial cholesterol levels would inhibit import of glutathione. Treatment with a fatty acid derivative (2-(2-methoxyethoxy) ethyl 8-(cis-2-n-octylcyclopropyl) octanoate) that

intercalates into the lipid bilayer and results in fluidization without changing cholesterol content, normalizes mitochondrial glutathione import suggesting that the decreased fluidity of mitochondrial membranes caused by cholesterol accumulation negatively affects glutathione import [380, 406-408].

Several other studies have also manipulated mitochondrial cholesterol levels to reduce oxidative stress. Myocardial ischemia in rats causes oxidative stress and an accumulation of mitochondrial cholesterol levels in heart cells [149]. TSPO is an outer mitochondrial membrane protein that mediates the transport of cholesterol to mitochondria [162]. Administration of the TSPO ligand 4'-chlorodiazepam to these rats 10 min prior to induction of ischemia prevented mitochondrial cholesterol accumulation and oxidative stress [149]. Ha et al. showed that macrophages have increased mitochondrial cholesterol levels, increased ROS, and decreased mitochondrial glutathione levels, and increased cell death after treatment with the anthrax lethal toxin [409]. Similar to our findings in NPC1-deficient cells, siRNA-mediated depletion of MLN64 prevented increased ROS and cell death in macrophages treated with anthrax lethal toxin [409]. These results suggest that blocking cholesterol transport to mitochondria in models of mitochondrial cholesterol accumulation, prevents oxidative stress.

Elevated mitochondrial cholesterol levels have also been linked to impairment of several additional aspects of mitochondrial function, for example impaired pyruvate import [410], decreased phosphate carrier activity [411, 412], more citrate export from mitochondria [152], and decreased ATP generation [144]. Yu et al. reported that mitochondria isolated from 9-week-old *Npc1*$^{-/-}$ mouse brain had increased mitochondrial

cholesterol levels and decreased rates of ATP hydrolysis and synthesis and proposed that ATP synthase was impaired [144]. Incubation of mitochondria isolated from *Npc1*$^{-/-}$ murine brain with methyl-beta-cyclodextrin reduced mitochondrial cholesterol levels and restored ATP generation in that study [144]. ATPase activity is also decreased by addition of cholesterol complexed to BSA to mitochondria isolated from rat liver and from pig hearts after myocardial ischemia ATPase [148, 157]. However, because ATP synthase activity is also dependent on ATP/ADP transport across the mitochondrial membrane it is unclear whether increased mitochondrial cholesterol directly caused ATP synthase dysfunction or rather inhibited ATP/ADP transport as we observed in NPC1-deficient CHO cells (Figure 3.43). In contrast, to our findings, enrichment of cholesterol in rat liver mitochondria by incubation with cholesterol/BSA complexes had no effect on the initial rate of ^{14}C ADP uptake [164]. The effect of mitochondrial cholesterol levels on ADP/ATP exchange mat depend on the distribution of cholesterol between inner mitochondrial membrane and outer mitochondrial membrane. In NPC1-deficient CHO cells we propose that cholesterol accumulates in the outer but not the inner mitochondrial membrane based on the increased total mitochondrial cholesterol levels and normal pregnenolone production. However, Yu et al. reported that cholesterol levels are increased in both the inner (mitoplasts) and the outer mitochondrial membranes in *Npc1*$^{-/-}$ brain at 9 weeks of age [144]. The consequences of cholesterol accumulation in the inner vs. the outer mitochondrial membrane may be very different especially with regards to ATP/ADP transport.

Although several studies suggest a connection between mitochondrial cholesterol and mitochondrial function there is one study that found no effects of increasing cholesterol

levels. Prabhu et al. found that treatment of a human prostate cancer cell line with cholesterol complexed with cyclodextrin increased mitochondrial cholesterol levels but had no effect on OCR [413]. This result emphasizes that the exact consequences of increased mitochondrial cholesterol levels are likely dependent on cell type and cholesterol distribution.

4.4 Role of mitochondrial cholesterol in *Npc1*$^{-/-}$ murine brain

In this study we showed that blocking cholesterol transport from endosomes to mitochondria normalized mitochondrial defects in NPC1-deficient CHO cells suggesting that increased mitochondrial cholesterol levels caused mitochondrial dysfunction. We also showed that NPC1-deficient CHO cells and *Npc1*$^{-/-}$ murine brain have increased mitochondrial cholesterol levels and several common defects in mitochondrial function and energy metabolism. The following section will discuss findings from NPC1-deficient CHO cells and *Npc1*$^{-/-}$ brain, with the goal of developing a model of how increased mitochondrial cholesterol levels contribute to NPC pathogenesis in mice.

Our hypothesis is that increased mitochondrial cholesterol levels cause mitochondrial dysfunction in *Npc1*$^{-/-}$ mice. Although we have yet to measure mitochondrial cholesterol levels in *Npc1*$^{-/-}$ mice younger than 5 weeks of age, mitochondrial cholesterol levels accumulate in CHO cells within 10 days of transfection with shNPC1, suggesting that mitochondrial cholesterol accumulates shortly after NPC1-depletion. Furthermore our model of cholesterol transport to mitochondria suggests that an accumulation of cholesterol in endosomes leads to mitochondrial cholesterol accumulation in the presence of a functional endosome-to-mitochondria cholesterol transport pathway. Together with findings by Reid et al. that endosomal cholesterol

accumulates in *Npc1*$^{-/-}$ murine brain within postnatal day 9 days our finding would support an early accumulation of mitochondrial cholesterol [60].

In NPC1-deficient CHO cells increased mitochondrial cholesterol levels clearly caused oxidative stress (Figure 3.45 A). It is therefore likely that oxidative stress in *Npc1*$^{-/-}$ murine brain is also at least partially caused by mitochondrial cholesterol. Furthermore, the increased mitochondrial cholesterol levels led to increased lactate production, which was prevented by treatment with the antioxidant NAC also prevented increased lactate production in NPC1-depleted cells suggesting that oxidative stress caused increased lactate levels (Figure 3.45 D). Together our findings suggest that increased mitochondrial cholesterol levels decreased the anti-oxidant capacity and increased ROS production, leading to increased lactate production. As proposed in our model of mitochondrial dysfunction in *Npc1*$^{-/-}$ murine cerebellum, oxidative stress likely contributes to increased lactate production through JNK-mediated phosphorylation and inhibition of PDH (Figure 4.01). In NPC1-depleted CHO cells dephosphorylation of PDH by DCA treatment decreased lactate levels to control levels. However, under basal conditions pPDH levels were unchanged maybe because of increased Nrf2 suggesting that increased lactate levels are not fully accounted for by PDH inhibition in NPC1-depleted CHO (Figure 3.44).

In *Npc1*$^{-/-}$ brain, increased levels of *Glud1* and aminotransferase mRNA and increased levels of BCAAs suggested that glutamate oxidation was increased (Figures 3.18 and 3.22). However, NPC1-deficient CHO cells were unable to oxidize glutamate as indicated by high glucose uptake and lower oxygen consumption in the presence of glutamine (Figures 3.38 and 3.40). We propose that decreased glutamate oxidation was caused by inhibition of ATP/ADP exchange across the mitochondrial membranes in

NPC1-depleted CHO cells. Whether ATP/ADP exchange is affected in *Npc1*$^{-/-}$ murine brain is unknown, but finding of decreased ATP generation by mitochondria isolated from 9-week-old *Npc1*$^{-/-}$ murine brain is consistent with both a defect in ATP synthase or a defect in ATP/ADP exchange [144]. Further work is required to determine whether ATP/ADP exchange across mitochondrial membranes is inhibited in *Npc1*$^{-/-}$ murine brain.

Together these results suggest that mitochondrial cholesterol accumulates early in *Npc1*$^{-/-}$ mice, causing increased oxidative stress. Increased oxidative stress likely causes inhibition of PDH resulting in a shift to glycolysis and increased lactate production in *Npc1*$^{-/-}$ cerebellum. One difference between the two models is that *Npc1*$^{-/-}$ cerebellum had increased oxidation of glutamate to compensate for the loss of energy whereas NPC1-depleted CHO cells are unable to oxidize glutamate because of a defect in ATP/ADP exchange across the mitochondrial membrane. A future experiment of interest would be to determine the effect of depleting MLN64 in *Npc1*$^{-/-}$ murine brain on mitochondrial function and disease pathogenesis.

4.5 Similarities between NPC and Alzheimer diseases

Alzheimer disease is a common neurodegenerative disease that affects all brain regions and is characterized by the build-up of extracellular deposits of amyloid-beta plaques. Although the cause of sporadic Alzheimer disease is unknown, one current hypothesis is that the accumulation of amyloid beta is an early event that causes a multitude of neuronal defects including mitochondrial dysfunction leading to neurodegeneration [414]. There are several links between Alzheimer disease and Niemann-Pick type C disease in which have been addressed in several reviews [415,

416]. For example, in *Npc1*$^{-/-}$ mice, the level of amyloid beta, the amyloid precursor protein, and two enzymes involved in the processing of amyloid beta (gamma-secretase and beta-secretase) are elevated in the cerebellum and hippocampus beginning at 7 weeks of age [401]. Haploinsufficiency of *Npc1* causes a more rapid accumulation of amyloid beta in APP/PS1 Alzheimer disease model mice [417]. Furthermore, two single-nucleotide polymorphisms (SNP) alleles in the *Npc1* gene are linked to sporadic late onset Alzheimer disease in a Polish population suggesting that altered NPC1 function may contribute to Alzheimer disease [418].

Altered cholesterol homeostasis has been linked to Alzheimer disease. For example, the apolipoprotein E4 allele is genetically associated with both sporadic and familiar forms of Alzheimer disease [419-421], and numerous studies have shown that increases in cholesterol levels cause increase processing and accumulation of amyloid beta (reviewed by Burns and Rebeck [422]). Furthermore, a recent study has reported increased mitochondrial cholesterol levels in 10-month-old APP/PS1 mice [146].

Multiple lines of evidence support the involvement of mitochondrial dysfunction in Alzheimer disease. Similar to our findings in *Npc1*$^{-/-}$ mice, markers of oxidative stress are increased early in Alzheimer disease progression [reviewed in [423, 424]. Furthermore, oxidative stress-induced mutations in mtDNA are common occurrences in mouse models and post-mortem brain of Alzheimer disease patients [425-430]. Amyloid beta treatment also causes an inhibition of PDH activity in isolated mitochondria and neuronal cell cultures, and postmortem human brains have decreased activity of PDH [431-436]. In human patients, mouse models, and cellular models of Alzheimer disease, ATP synthase activity and ATP levels are decreased [437, 438]. A proteomics study in

the brain of Alzheimer disease patients showed that the alpha subunit of ATP synthase was damaged by oxidative stress [437]. Similar to *Npc1*$^{-/-}$ cerebellum, these findings show that Alzheimer diseased brains have increased oxidative stress, defects in mtDNA, and inhibition of PDH. Because I have shown that many of these defects are caused by increased mitochondrial cholesterol levels in NPC1-deficient cells, it would be interesting to determine consequences of lowering mitochondrial cholesterol levels in Alzheimer disease models.

4.6 Similarities between cancer and NPC disease

Cancer is a collection of diseases that together is the number one cause of death in the Western world. Cancer is characterized by uncontrollable cell growth, resistance to apoptosis, and high aerobic glycolysis (also known as the Warburg effect). At first glance, NPC disease and cancer have little in common. NPC disease is characterized by cell death, whereas cancer cells are characterized by resistance to cell death. However, upon further investigation these two diseases have much more in common than originally thought (reviewed in [439]). Both diseases have oxidative stress and, based on our findings, glycolysis appears increased in *Npc1*$^{-/-}$ brain. Furthermore, similar to *Npc1*$^{-/-}$ brain, mitochondrial cholesterol levels are increased in some cancers [150-155, 440]. The exact mechanism of cholesterol transport to mitochondria in these cancer cells is unknown. However, MLN64 and NPC2 are highly expressed in multiple cancers, possibly suggesting that the endosomal-to-mitochondrial cholesterol transport pathway is upregulated [167, 441-443].

Two other commonalities between NPC disease and cancer are increased phosphorylation of PDH and increased glutamate oxidation. Increased

phosphorylation/inhibition of PDH occurs in several cancer cells both *in vitro* and *in vivo* [444-446]. Cancer cells are also well known to have high levels of glutamate oxidation, likely to compensate for inhibition of PDH [447, 448]. As far as I am aware there are no studies that link increased mitochondrial cholesterol with PDH inhibition or increased glutamate oxidation in cancer, however, based on our findings in NPC disease I propose that increased mitochondrial cholesterol may cause these alterations and therefore may be a target in cancer studies.

4.7 Conclusion

With this study I hope to have provided new information to the research field of NPC disease that will one day contribute to a cure for the disease. I have elucidated a novel cholesterol transport pathway between endosomes and mitochondria that involves NPC2 and MLN64 and contributes to mitochondrial cholesterol accumulation in NPC1-deficient cells. Interestingly, this points to a model in which NPC1 and NPC2 function differently and so that the deficiency of each protein likely has different consequences on mitochondrial function and disease pathogenesis. We also performed a characterization of energy metabolism in *Npc1*$^{-/-}$ murine brain that revealed several alterations, including presymptomatic oxidative stress, and early symptomatic increases in glycolysis, glutamate oxidation, and decreased pyruvate oxidation. These alterations likely contribute to NPC pathogenesis and are therefore targets for potential treatments. I also show evidence that blocking the endosome to mitochondria cholesterol transport pathway in NPC1-deficient cells normalized several aspects of mitochondrial dysfunction, including increased lactate production, oxidative stress, and defects in glutamate oxidation suggesting a potential therapeutic target in NPC disease. Finally, because

mitochondrial cholesterol levels are increased in other diseases including cancer and a murine model of Alzheimer disease, I propose that my findings could have wider application to other related diseases.

BIBLIOGRAPHY

1. Niemann, A., *Ein unbekanntes Krankheitsbild.* Jahrbuch fuer Kinderheilkunde und physische Erziehung, 1914. **79**: p. 1-10.
2. Crocker, A.C., *The cerebral defect in Tay-Sachs disease and Niemann-Pick disease.* J Neurochem, 1961. **7**: p. 69-80.
3. Crocker, A.C. and S. Farber, *Niemann-Pick disease: a review of eighteen patients.* Medicine (Baltimore), 1958. **37**(1): p. 1-95.
4. Klenk, E., *Über die Natur der Phosphatide der Milz bei der Niemann-Pickschen Krankheit.* Hoppe-Seyler´s Zeitschrift für physiologische Chemie, 1934. **229**(4-6): p. 125-277.
5. Greer, W.L., et al., *The Nova Scotia (type D) form of Niemann-Pick disease is caused by a G3097-->T transversion in NPC1.* Am J Hum Genet, 1998. **63**(1): p. 52-4.
6. Carstea, E.D., et al., *Niemann-Pick C1 disease gene: homology to mediators of cholesterol homeostasis.* Science, 1997. **277**(5323): p. 228-31.
7. Naureckiene, S., et al., *Identification of HE1 as the second gene of Niemann-Pick C disease.* Science, 2000. **290**(5500): p. 2298-301.
8. Vanier, M.T., et al., *Genetic heterogeneity in Niemann-Pick C disease: a study using somatic cell hybridization and linkage analysis.* Am J Hum Genet, 1996. **58**(1): p. 118-25.
9. Carstea, E.D., et al., *Linkage of Niemann-Pick disease type C to human chromosome 18.* Proc Natl Acad Sci U S A, 1993. **90**(5): p. 2002-4.
10. Pentchev, P.G., et al., *A defect in cholesterol esterification in Niemann-Pick disease (type C) patients.* Proc Natl Acad Sci U S A, 1985. **82**(23): p. 8247-51.
11. Liscum, L., *Niemann-Pick type C mutations cause lipid traffic jam.* Traffic, 2000. **1**(3): p. 218-25.
12. Steinberg, S.J., D. Mondal, and A.H. Fensom, *Co-cultivation of Niemann-Pick disease type C fibroblasts belonging to complementation groups alpha and beta stimulates LDL-derived cholesterol esterification.* J Inherit Metab Dis, 1996. **19**(6): p. 769-74.
13. Pentchev, P.G., et al., *A genetic storage disorder in BALB/C mice with a metabolic block in esterification of exogenous cholesterol.* J Biol Chem, 1984. **259**(9): p. 5784-91.
14. Brady, R.O., et al., *The metabolism of sphingomyelin. II. Evidence of an enzymatic deficiency in Niemann-Pick diseae.* Proc Natl Acad Sci U S A, 1966. **55**(2): p. 366-9.
15. Ferlinz, K., R. Hurwitz, and K. Sandhoff, *Molecular basis of acid sphingomyelinase deficiency in a patient with Niemann-Pick disease type A.* Biochem Biophys Res Commun, 1991. **179**(3): p. 1187-91.
16. Levran, O., R.J. Desnick, and E.H. Schuchman, *Niemann-Pick disease: a frequent missense mutation in the acid sphingomyelinase gene of Ashkenazi Jewish type A and B patients.* Proc Natl Acad Sci U S A, 1991. **88**(9): p. 3748-52.

17. Levran, O., R.J. Desnick, and E.H. Schuchman, *Identification and expression of a common missense mutation (L302P) in the acid sphingomyelinase gene of Ashkenazi Jewish type A Niemann-Pick disease patients.* Blood, 1992. **80**(8): p. 2081-7.
18. Takahashi, T., et al., *Identification of a missense mutation (S436R) in the acid sphingomyelinase gene from a Japanese patient with type B Niemann-Pick disease.* Hum Mutat, 1992. **1**(1): p. 70-1.
19. Takahashi, T., et al., *Identification and expression of five mutations in the human acid sphingomyelinase gene causing types A and B Niemann-Pick disease. Molecular evidence for genetic heterogeneity in the neuronopathic and non-neuronopathic forms.* J Biol Chem, 1992. **267**(18): p. 12552-8.
20. Schuchman, E.H., *Two new mutations in the acid sphingomyelinase gene causing type a Niemann-pick disease: N389T and R441X.* Hum Mutat, 1995. **6**(4): p. 352-4.
21. Schuchman, E.H. and S.R. Miranda, *Niemann-Pick disease: mutation update, genotype/phenotype correlations, and prospects for genetic testing.* Genet Test, 1997. **1**(1): p. 13-9.
22. Vanier, M.T. and G. Millat, *Niemann-Pick disease type C.* Clin Genet, 2003. **64**(4): p. 269-81.
23. Spiegel, R., et al., *The clinical spectrum of fetal Niemann-Pick type C.* Am J Med Genet A, 2009. **149A**(3): p. 446-50.
24. Vanier, M.T., et al., *Niemann-Pick disease group C: clinical variability and diagnosis based on defective cholesterol esterification. A collaborative study on 70 patients.* Clin Genet, 1988. **33**(5): p. 331-48.
25. Trendelenburg, G., et al., *Niemann-Pick type C disease in a 68-year-old patient.* J Neurol Neurosurg Psychiatry, 2006. **77**(8): p. 997-8.
26. Sevin, M., et al., *The adult form of Niemann-Pick disease type C.* Brain, 2007. **130**(Pt 1): p. 120-33.
27. Iturriaga, C., et al., *Niemann-Pick C disease in Spain: clinical spectrum and development of a disability scale.* J Neurol Sci, 2006. **249**(1): p. 1-6.
28. Imrie, J., et al., *The natural history of Niemann-Pick disease type C in the UK.* J Inherit Metab Dis, 2007. **30**(1): p. 51-9.
29. Garver, W.S., et al., *The National Niemann-Pick C1 disease database: report of clinical features and health problems.* Am J Med Genet A, 2007. **143A**(11): p. 1204-11.
30. Solomon, D., et al., *Niemann-Pick type C disease in two affected sisters: ocular motor recordings and brain-stem neuropathology.* Ann N Y Acad Sci, 2005. **1039**: p. 436-45.
31. Kandt, R.S., et al., *Cataplexy in variant forms of Niemann-Pick disease.* Ann Neurol, 1982. **12**(3): p. 284-8.
32. Oyama, K., et al., *Niemann-Pick disease type C: cataplexy and hypocretin in cerebrospinal fluid.* Tohoku J Exp Med, 2006. **209**(3): p. 263-7.
33. Group, N.-C.G.W., et al., *Recommendations on the diagnosis and management of Niemann-Pick disease type C.* Mol Genet Metab, 2009. **98**(1-2): p. 152-65.
34. Vanier, M.T., *Niemann-Pick disease type C.* Orphanet J Rare Dis, 2010. **5**: p. 16.

35. Hsu, Y.S., et al., *Niemann-Pick disease type C (a cellular cholesterol lipidosis) treated by bone marrow transplantation.* Bone Marrow Transplant, 1999. **24**(1): p. 103-7.
36. Gartner, J.C., Jr., et al., *Progression of neurovisceral storage disease with supranuclear ophthalmoplegia following orthotopic liver transplantation.* Pediatrics, 1986. **77**(1): p. 104-6.
37. Walkley, S.U. and K. Suzuki, *Consequences of NPC1 and NPC2 loss of function in mammalian neurons.* Biochim Biophys Acta, 2004. **1685**(1-3): p. 48-62.
38. Morris, M.D., et al., *Lysosome lipid storage disorder in NCTR-BALB/c mice. I. Description of the disease and genetics.* Am J Pathol, 1982. **108**(2): p. 140-9.
39. Shio, H., et al., *Lysosome lipid storage disorder in NCTR-BALB/c mice. II. Morphologic and cytochemical studies.* Am J Pathol, 1982. **108**(2): p. 150-9.
40. Loftus, S.K., et al., *Murine model of Niemann-Pick C disease: mutation in a cholesterol homeostasis gene.* Science, 1997. **277**(5323): p. 232-5.
41. Voikar, V., H. Rauvala, and E. Ikonen, *Cognitive deficit and development of motor impairment in a mouse model of Niemann-Pick type C disease.* Behav Brain Res, 2002. **132**(1): p. 1-10.
42. Li, H., et al., *Molecular, anatomical, and biochemical events associated with neurodegeneration in mice with Niemann-Pick type C disease.* J Neuropathol Exp Neurol, 2005. **64**(4): p. 323-33.
43. Yan, X., et al., *Decreased expression of myelin gene regulatory factor in Niemann-Pick type C 1 mouse.* Metab Brain Dis, 2011. **26**(4): p. 299-306.
44. Weintraub, H., et al., *Neurological mutation characterized by dysmyelination in NCTR-Balb/C mouse with lysosomal lipid storage disease.* J Neurochem, 1985. **45**(3): p. 665-72.
45. Weintraub, H., et al., *Dysmyelination in NCTR-Balb/C mouse mutant with a lysosomal storage disorder. Morphological survey.* Acta Neuropathol, 1987. **74**(4): p. 374-81.
46. Takikita, S., et al., *Perturbed myelination process of premyelinating oligodendrocyte in Niemann-Pick type C mouse.* J Neuropathol Exp Neurol, 2004. **63**(6): p. 660-73.
47. Walterfang, M., et al., *White and gray matter alterations in adults with Niemann-Pick disease type C: a cross-sectional study.* Neurology, 2010. **75**(1): p. 49-56.
48. Loftus, S.K., et al., *Rescue of neurodegeneration in Niemann-Pick C mice by a prion-promoter-driven Npc1 cDNA transgene.* Hum Mol Genet, 2002. **11**(24): p. 3107-14.
49. Higashi, Y., et al., *Cerebellar degeneration in the Niemann-Pick type C mouse.* Acta Neuropathol, 1993. **85**(2): p. 175-84.
50. Ong, W.Y., et al., *Neurodegeneration in Niemann-Pick type C disease mice.* Exp Brain Res, 2001. **141**(2): p. 218-31.
51. Byun, K., et al., *Alteration of the CNS pathway to the hippocampus in a mouse model of Niemann-Pick, type C disease.* J Chem Neuroanat, 2011. **42**(1): p. 39-44.
52. Pressey, S.N., et al., *Early glial activation, synaptic changes and axonal pathology in the thalamocortical system of Niemann-Pick type C1 mice.* Neurobiol Dis, 2012. **45**(3): p. 1086-100.

53. D'Arcangelo, G., et al., *Glutamatergic neurotransmission in a mouse model of Niemann-Pick type C disease.* Brain Res, 2011. **1396**: p. 11-9.
54. Xu, S., et al., *Defects of synaptic vesicle turnover at excitatory and inhibitory synapses in Niemann-Pick C1-deficient neurons.* Neuroscience, 2010. **167**(3): p. 608-20.
55. Hawes, C.M., et al., *Pre-synaptic defects of NPC1-deficient hippocampal neurons are not directly related to plasma membrane cholesterol.* J Neurochem, 2010. **114**(1): p. 311-22.
56. Byun, K., et al., *Alteration of the glutamate and GABA transporters in the hippocampus of the Niemann-Pick disease, type C mouse using proteomic analysis.* Proteomics, 2006. **6**(4): p. 1230-6.
57. Yadid, G., et al., *Neurochemical alterations in the cerebellum of a murine model of Niemann-Pick type C disease.* Brain Res, 1998. **799**(2): p. 250-6.
58. German, D.C., et al., *Neurodegeneration in the Niemann-Pick C mouse: glial involvement.* Neuroscience, 2002. **109**(3): p. 437-50.
59. Baudry, M., et al., *Postnatal development of inflammation in a murine model of Niemann-Pick type C disease: immunohistochemical observations of microglia and astroglia.* Exp Neurol, 2003. **184**(2): p. 887-903.
60. Reid, P.C., et al., *A novel cholesterol stain reveals early neuronal cholesterol accumulation in the Niemann-Pick type C1 mouse brain.* J Lipid Res, 2004. **45**(3): p. 582-91.
61. Sleat, D.E., et al., *Genetic evidence for nonredundant functional cooperativity between NPC1 and NPC2 in lipid transport.* Proc Natl Acad Sci U S A, 2004. **101**(16): p. 5886-91.
62. Nielsen, G.K., et al., *Protein replacement therapy partially corrects the cholesterol-storage phenotype in a mouse model of Niemann-Pick type C2 disease.* PLoS One, 2011. **6**(11): p. e27287.
63. Dixit, S.S., et al., *Loss of Niemann-Pick C1 or C2 protein results in similar biochemical changes suggesting that these proteins function in a common lysosomal pathway.* PLoS One, 2011. **6**(8): p. e23677.
64. Simons, K. and R. Ehehalt, *Cholesterol, lipid rafts, and disease.* J Clin Invest, 2002. **110**(5): p. 597-603.
65. Brown, M.S. and J.L. Goldstein, *A proteolytic pathway that controls the cholesterol content of membranes, cells, and blood.* Proc Natl Acad Sci U S A, 1999. **96**(20): p. 11041-8.
66. Osborne, T.F., et al., *Operator constitutive mutation of 3-hydroxy-3-methylglutaryl coenzyme A reductase promoter abolishes protein binding to sterol regulatory element.* J Biol Chem, 1988. **263**(7): p. 3380-7.
67. Brown, M.S. and J.L. Goldstein, *The SREBP pathway: regulation of cholesterol metabolism by proteolysis of a membrane-bound transcription factor.* Cell, 1997. **89**(3): p. 331-40.
68. Herz, J. and H.H. Bock, *Lipoprotein receptors in the nervous system.* Annu Rev Biochem, 2002. **71**: p. 405-34.

69. Goldstein, J.L. and M.S. Brown, *Binding and degradation of low density lipoproteins by cultured human fibroblasts. Comparison of cells from a normal subject and from a patient with homozygous familial hypercholesterolemia.* J Biol Chem, 1974. **249**(16): p. 5153-62.
70. Anderson, R.A. and G.N. Sando, *Cloning and expression of cDNA encoding human lysosomal acid lipase/cholesteryl ester hydrolase. Similarities to gastric and lingual lipases.* J Biol Chem, 1991. **266**(33): p. 22479-84.
71. Goldstein, J.L., S.E. Dana, and M.S. Brown, *Esterification of low density lipoprotein cholesterol in human fibroblasts and its absence in homozygous familial hypercholesterolemia.* Proc Natl Acad Sci U S A, 1974. **71**(11): p. 4288-92.
72. Dietschy, J.M. and S.D. Turley, *Thematic review series: brain Lipids. Cholesterol metabolism in the central nervous system during early development and in the mature animal.* J Lipid Res, 2004. **45**(8): p. 1375-97.
73. Orth, M. and S. Bellosta, *Cholesterol: its regulation and role in central nervous system disorders.* Cholesterol, 2012. **2012**: p. 292598.
74. Guo, J., et al., *Effects of cholesterol levels on the excitability of rat hippocampal neurons.* Mol Membr Biol, 2008. **25**(3): p. 216-23.
75. Slezak, M. and F.W. Pfrieger, *New roles for astrocytes: regulation of CNS synaptogenesis.* Trends Neurosci, 2003. **26**(10): p. 531-5.
76. Mauch, D.H., et al., *CNS synaptogenesis promoted by glia-derived cholesterol.* Science, 2001. **294**(5545): p. 1354-7.
77. Argmann, C.A., et al., *Regulation of macrophage cholesterol efflux through hydroxymethylglutaryl-CoA reductase inhibition: a role for RhoA in ABCA1-mediated cholesterol efflux.* J Biol Chem, 2005. **280**(23): p. 22212-21.
78. LaDu, M.J., et al., *Nascent astrocyte particles differ from lipoproteins in CSF.* J Neurochem, 1998. **70**(5): p. 2070-81.
79. Nakai, M., et al., *Expression of apolipoprotein E mRNA in rat microglia.* Neurosci Lett, 1996. **211**(1): p. 41-4.
80. Bassett, C.N., et al., *Cerebrospinal fluid lipoproteins in Alzheimer's disease.* Microsc Res Tech, 2000. **50**(4): p. 282-6.
81. Pfrieger, F.W., *Cholesterol homeostasis and function in neurons of the central nervous system.* Cell Mol Life Sci, 2003. **60**(6): p. 1158-71.
82. Posse De Chaves, E.I., et al., *Uptake of lipoproteins for axonal growth of sympathetic neurons.* J Biol Chem, 2000. **275**(26): p. 19883-90.
83. Offe, K., et al., *The lipoprotein receptor LR11 regulates amyloid beta production and amyloid precursor protein traffic in endosomal compartments.* J Neurosci, 2006. **26**(5): p. 1596-603.
84. Pitas, R.E., et al., *Astrocytes synthesize apolipoprotein E and metabolize apolipoprotein E-containing lipoproteins.* Biochim Biophys Acta, 1987. **917**(1): p. 148-61.
85. Sokol, J., et al., *Type C Niemann-Pick disease. Lysosomal accumulation and defective intracellular mobilization of low density lipoprotein cholesterol.* J Biol Chem, 1988. **263**(7): p. 3411-7.

86. Treiber-Held, S., et al., *Spatial and temporal distribution of intracellular free cholesterol in brains of a Niemann-Pick type C mouse model showing hyperphosphorylated tau protein. Implications for Alzheimer's disease.* J Pathol, 2003. **200**(1): p. 95-103.
87. Xie, C., et al., *Cholesterol balance and metabolism in mice with loss of function of Niemann-Pick C protein.* Am J Physiol, 1999. **276**(2 Pt 1): p. E336-44.
88. Liscum, L. and J.R. Faust, *Low density lipoprotein (LDL)-mediated suppression of cholesterol synthesis and LDL uptake is defective in Niemann-Pick type C fibroblasts.* J Biol Chem, 1987. **262**(35): p. 17002-8.
89. Liscum, L., R.M. Ruggiero, and J.R. Faust, *The intracellular transport of low density lipoprotein-derived cholesterol is defective in Niemann-Pick type C fibroblasts.* J Cell Biol, 1989. **108**(5): p. 1625-36.
90. Frolov, A., et al., *NPC1 and NPC2 regulate cellular cholesterol homeostasis through generation of low density lipoprotein cholesterol-derived oxysterols.* J Biol Chem, 2003. **278**(28): p. 25517-25.
91. Benarroch, E.E., *Brain cholesterol metabolism and neurologic disease.* Neurology, 2008. **71**(17): p. 1368-73.
92. Taniguchi, M., et al., *Sites and temporal changes of gangliosides GM1/GM2 storage in the Niemann-Pick disease type C mouse brain.* Brain Dev, 2001. **23**(6): p. 414-21.
93. Davies, J.P., F.W. Chen, and Y.A. Ioannou, *Transmembrane molecular pump activity of Niemann-Pick C1 protein.* Science, 2000. **290**(5500): p. 2295-8.
94. Ogata, S. and M. Fukuda, *Lysosomal targeting of Limp II membrane glycoprotein requires a novel Leu-Ile motif at a particular position in its cytoplasmic tail.* J Biol Chem, 1994. **269**(7): p. 5210-7.
95. Davies, J.P. and Y.A. Ioannou, *Topological analysis of Niemann-Pick C1 protein reveals that the membrane orientation of the putative sterol-sensing domain is identical to those of 3-hydroxy-3-methylglutaryl-CoA reductase and sterol regulatory element binding protein cleavage-activating protein.* J Biol Chem, 2000. **275**(32): p. 24367-74.
96. Ohgami, N., et al., *Binding between the Niemann-Pick C1 protein and a photoactivatable cholesterol analog requires a functional sterol-sensing domain.* Proc Natl Acad Sci U S A, 2004. **101**(34): p. 12473-8.
97. Millard, E.E., et al., *The sterol-sensing domain of the Niemann-Pick C1 (NPC1) protein regulates trafficking of low density lipoprotein cholesterol.* J Biol Chem, 2005. **280**(31): p. 28581-90.
98. Infante, R.E., et al., *Purified NPC1 protein: II. Localization of sterol binding to a 240-amino acid soluble luminal loop.* J Biol Chem, 2008. **283**(2): p. 1064-75.
99. Patel, S.C., et al., *Localization of Niemann-Pick C1 protein in astrocytes: implications for neuronal degeneration in Niemann- Pick type C disease.* Proc Natl Acad Sci U S A, 1999. **96**(4): p. 1657-62.
100. Higgins, M.E., et al., *Niemann-Pick C1 is a late endosome-resident protein that transiently associates with lysosomes and the trans-Golgi network.* Mol Genet Metab, 1999. **68**(1): p. 1-13.
101. Garver, W.S., et al., *Localization of the murine Niemann-Pick C1 protein to two distinct intracellular compartments.* J Lipid Res, 2000. **41**(5): p. 673-87.

102. Karten, B., et al., *The Niemann-Pick C1 protein in recycling endosomes of presynaptic nerve terminals.* J Lipid Res, 2006. **47**(3): p. 504-14.
103. Prasad, A., et al., *Regional and developmental expression of the Npc1 mRNA in the mouse brain.* J Neurochem, 2000. **75**(3): p. 1250-7.
104. Falk, T., et al., *Expression of Niemann-Pick type C transcript in rodent cerebellum in vivo and in vitro.* Brain Res, 1999. **839**(1): p. 49-57.
105. Yamamoto, T., et al., *NPC1 gene mutations in Japanese patients with Niemann-Pick disease type C.* Hum Genet, 1999. **105**(1-2): p. 10-6.
106. Millat, G., et al., *Niemann-Pick C1 disease: the I1061T substitution is a frequent mutant allele in patients of Western European descent and correlates with a classic juvenile phenotype.* Am J Hum Genet, 1999. **65**(5): p. 1321-9.
107. Sun, X., et al., *Niemann-Pick C variant detection by altered sphingolipid trafficking and correlation with mutations within a specific domain of NPC1.* Am J Hum Genet, 2001. **68**(6): p. 1361-72.
108. Millat, G., et al., *Niemann-Pick C1 disease: correlations between NPC1 mutations, levels of NPC1 protein, and phenotypes emphasize the functional significance of the putative sterol-sensing domain and of the cysteine-rich luminal loop.* Am J Hum Genet, 2001. **68**(6): p. 1373-85.
109. Yamamoto, T., et al., *Genotype-phenotype relationship of Niemann-Pick disease type C: a possible correlation between clinical onset and levels of NPC1 protein in isolated skin fibroblasts.* J Med Genet, 2000. **37**(9): p. 707-12.
110. Bauer, P., et al., *NPC1: Complete genomic sequence, mutation analysis, and characterization of haplotypes.* Hum Mutat, 2002. **19**(1): p. 30-8.
111. Park, W.D., et al., *Identification of 58 novel mutations in Niemann-Pick disease type C: correlation with biochemical phenotype and importance of PTC1-like domains in NPC1.* Hum Mutat, 2003. **22**(4): p. 313-25.
112. Yang, C.C., et al., *Six novel NPC1 mutations in Chinese patients with Niemann-Pick disease type C.* J Neurol Neurosurg Psychiatry, 2005. **76**(4): p. 592-5.
113. Wenger, D.A., G. Barth, and J.H. Githens, *Nine cases of sphingomyelin lipidosis, a new variant in Spanish-American Children. Juvenile variant of Niemann-Pick Disease with foamy and sea-blue histiocytes.* Am J Dis Child, 1977. **131**(9): p. 955-61.
114. Greer, W.L., et al., *Linkage disequilibrium mapping of the Nova Scotia variant of Niemann-Pick disease.* Clin Genet, 1999. **55**(4): p. 248-55.
115. Kirchhoff, C., et al., *Cloning and analysis of mRNAs expressed specifically in the human epididymis.* Int J Androl, 1990. **13**(2): p. 155-67.
116. Larsen, L.B., et al., *Primary structure of EPV20, a secretory glycoprotein containing a previously uncharacterized type of domain.* Eur J Biochem, 1997. **243**(1-2): p. 437-41.
117. Okamura, N., et al., *A porcine homolog of the major secretory protein of human epididymis, HE1, specifically binds cholesterol.* Biochim Biophys Acta, 1999. **1438**(3): p. 377-87.
118. Xu, S., et al., *Structural basis of sterol binding by NPC2, a lysosomal protein deficient in Niemann-Pick type C2 disease.* J Biol Chem, 2007. **282**(32): p. 23525-31.

119. Friedland, N., et al., *Structure of a cholesterol-binding protein deficient in Niemann-Pick type C2 disease.* Proc Natl Acad Sci U S A, 2003. **100**(5): p. 2512-7.
120. Ko, D.C., et al., *The integrity of a cholesterol-binding pocket in Niemann-Pick C2 protein is necessary to control lysosome cholesterol levels.* Proc Natl Acad Sci U S A, 2003. **100**(5): p. 2518-25.
121. Liou, H.L., et al., *NPC2, the protein deficient in Niemann-Pick C2 disease, consists of multiple glycoforms that bind a variety of sterols.* J Biol Chem, 2006. **281**(48): p. 36710-23.
122. Cheruku, S.R., et al., *Mechanism of cholesterol transfer from the Niemann-Pick type C2 protein to model membranes supports a role in lysosomal cholesterol transport.* J Biol Chem, 2006. **281**(42): p. 31594-604.
123. Infante, R.E., et al., *NPC2 facilitates bidirectional transfer of cholesterol between NPC1 and lipid bilayers, a step in cholesterol egress from lysosomes.* Proc Natl Acad Sci U S A, 2008. **105**(40): p. 15287-92.
124. Kwon, H.J., et al., *Structure of N-terminal domain of NPC1 reveals distinct subdomains for binding and transfer of cholesterol.* Cell, 2009. **137**(7): p. 1213-24.
125. Wang, M.L., et al., *Identification of surface residues on Niemann-Pick C2 essential for hydrophobic handoff of cholesterol to NPC1 in lysosomes.* Cell Metab, 2010. **12**(2): p. 166-73.
126. Deffieu, M.S. and S.R. Pfeffer, *Niemann-Pick type C 1 function requires lumenal domain residues that mediate cholesterol-dependent NPC2 binding.* Proc Natl Acad Sci U S A, 2011. **108**(47): p. 18932-6.
127. Li, H., et al., *GM2/GD2 and GM3 gangliosides have no effect on cellular cholesterol pools or turnover in normal or NPC1 mice.* J Lipid Res, 2008. **49**(8): p. 1816-28.
128. Rosenbaum, A.I., et al., *Endocytosis of beta-cyclodextrins is responsible for cholesterol reduction in Niemann-Pick type C mutant cells.* Proc Natl Acad Sci U S A, 2010. **107**(12): p. 5477-82.
129. Davidson, C.D., et al., *Chronic cyclodextrin treatment of murine Niemann-Pick C disease ameliorates neuronal cholesterol and glycosphingolipid storage and disease progression.* PLoS One, 2009. **4**(9): p. e6951.
130. Liu, B., et al., *Reversal of defective lysosomal transport in NPC disease ameliorates liver dysfunction and neurodegeneration in the npc1-/- mouse.* Proc Natl Acad Sci U S A, 2009. **106**(7): p. 2377-82.
131. Aqul, A., et al., *Unesterified cholesterol accumulation in late endosomes/lysosomes causes neurodegeneration and is prevented by driving cholesterol export from this compartment.* J Neurosci, 2011. **31**(25): p. 9404-13.
132. Liu, B., et al., *Genetic variations and treatments that affect the lifespan of the NPC1 mouse.* J Lipid Res, 2008. **49**(3): p. 663-9.
133. Matsuo, M., et al., *Effects of cyclodextrin in two patients with Niemann-Pick Type C disease.* Mol Genet Metab, 2013. **108**(1): p. 76-81.
134. Pritchard, K.A., Jr., et al., *Effect of low-density lipoprotein on endothelial cell membrane fluidity and mononuclear cell attachment.* Am J Physiol, 1991. **260**(1 Pt 1): p. C43-9.

135. Yeagle, P.L., *Cholesterol and the cell membrane.* Biochim Biophys Acta, 1985. **822**(3-4): p. 267-87.
136. Bastiaanse, E.M., K.M. Hold, and A. Van der Laarse, *The effect of membrane cholesterol content on ion transport processes in plasma membranes.* Cardiovasc Res, 1997. **33**(2): p. 272-83.
137. Hu, M.C., et al., *Steroid deficiency syndromes in mice with targeted disruption of Cyp11a1.* Mol Endocrinol, 2002. **16**(8): p. 1943-50.
138. Yang, X., et al., *Inherited congenital adrenal hyperplasia in the rabbit is caused by a deletion in the gene encoding cytochrome P450 cholesterol side-chain cleavage enzyme.* Endocrinology, 1993. **132**(5): p. 1977-82.
139. Roff, C.F., et al., *The murine Niemann-Pick type C lesion affects testosterone production.* Endocrinology, 1993. **133**(6): p. 2913-23.
140. Griffin, L.D., et al., *Niemann-Pick type C disease involves disrupted neurosteroidogenesis and responds to allopregnanolone.* Nat Med, 2004. **10**(7): p. 704-11.
141. Chen, G., et al., *Decreased estradiol release from astrocytes contributes to the neurodegeneration in a mouse model of Niemann-Pick disease type C.* Glia, 2007. **55**(15): p. 1509-18.
142. Fluegel, M.L., T.J. Parker, and L.J. Pallanck, *Mutations of a Drosophila NPC1 gene confer sterol and ecdysone metabolic defects.* Genetics, 2006. **172**(1): p. 185-96.
143. Liao, G., et al., *Allopregnanolone treatment delays cholesterol accumulation and reduces autophagic/lysosomal dysfunction and inflammation in Npc1-/- mouse brain.* Brain Res, 2009. **1270**: p. 140-51.
144. Yu, W., et al., *Altered cholesterol metabolism in Niemann-Pick type C1 mouse brains affects mitochondrial function.* J Biol Chem, 2005. **280**(12): p. 11731-9.
145. Mari, M., et al., *Mitochondrial free cholesterol loading sensitizes to TNF- and Fas-mediated steatohepatitis.* Cell Metab, 2006. **4**(3): p. 185-98.
146. Fernandez, A., et al., *Mitochondrial cholesterol loading exacerbates amyloid beta peptide-induced inflammation and neurotoxicity.* J Neurosci, 2009. **29**(20): p. 6394-405.
147. Charman, M., et al., *MLN64 mediates egress of cholesterol from endosomes to mitochondria in the absence of functional Niemann-Pick Type C1 protein.* J Lipid Res, 2010. **51**(5): p. 1023-34.
148. Rouslin, W., et al., *Mitochondrial cholesterol content and membrane properties in porcine myocardial ischemia.* Am J Physiol, 1982. **242**(2): p. H254-9.
149. Paradis, S., et al., *Cardioprotection by the TSPO ligand 4'-chlorodiazepam is associated with inhibition of mitochondrial accumulation of cholesterol at reperfusion.* Cardiovasc Res, 2013. **98**(3): p. 420-7.
150. Feo, F., et al., *Effect of cholesterol content on some physical and functional properties of mitochondria isolated from adult rat liver, fetal liver, cholesterol-enriched liver and hepatomas AH-130, 3924A and 5123.* Biochim Biophys Acta, 1975. **413**(1): p. 116-34.
151. Sabine, J.R., *Defective control of lipid biosynthesis in cancerous and precancerous liver.* Prog Biochem Pharmacol, 1975. **10**: p. 269-307.

152. Parlo, R.A. and P.S. Coleman, *Enhanced rate of citrate export from cholesterol-rich hepatoma mitochondria. The truncated Krebs cycle and other metabolic ramifications of mitochondrial membrane cholesterol.* J Biol Chem, 1984. **259**(16): p. 9997-10003.
153. Coleman, P.S., *Membrane cholesterol and tumor bioenergetics.* Ann N Y Acad Sci, 1986. **488**: p. 451-67.
154. Baggetto, L.G., E. Clottes, and C. Vial, *Low mitochondrial proton leak due to high membrane cholesterol content and cytosolic creatine kinase as two features of the deviant bioenergetics of Ehrlich and AS30-D tumor cells.* Cancer Res, 1992. **52**(18): p. 4935-41.
155. Montero, J., et al., *Mitochondrial cholesterol contributes to chemotherapy resistance in hepatocellular carcinoma.* Cancer Res, 2008. **68**(13): p. 5246-56.
156. Ziolkowski, W., et al., *Exercise-induced heart mitochondrial cholesterol depletion influences the inhibition of mitochondrial swelling.* Exp Physiol, 2013.
157. Echegoyen, S., et al., *Cholesterol increase in mitochondria: its effect on inner-membrane functions, submitochondrial localization and ultrastructural morphology.* Biochem J, 1993. **289 (Pt 3)**: p. 703-8.
158. Fernandez-Checa, J.C. and N. Kaplowitz, *Hepatic mitochondrial glutathione: transport and role in disease and toxicity.* Toxicol Appl Pharmacol, 2005. **204**(3): p. 263-73.
159. Mei, S., et al., *Prolonged exposure to insulin induces mitochondrion-derived oxidative stress through increasing mitochondrial cholesterol content in hepatocytes.* Endocrinology, 2012. **153**(5): p. 2120-9.
160. Clark, B.J., et al., *The purification, cloning, and expression of a novel luteinizing hormone-induced mitochondrial protein in MA-10 mouse Leydig tumor cells. Characterization of the steroidogenic acute regulatory protein (StAR).* J Biol Chem, 1994. **269**(45): p. 28314-22.
161. Miller, W.L. and H.S. Bose, *Early steps in steroidogenesis: intracellular cholesterol trafficking.* J Lipid Res, 2011. **52**(12): p. 2111-35.
162. Hauet, T., et al., *Peripheral-type benzodiazepine receptor-mediated action of steroidogenic acute regulatory protein on cholesterol entry into leydig cell mitochondria.* Mol Endocrinol, 2005. **19**(2): p. 540-54.
163. Bose, M., et al., *Steroidogenic activity of StAR requires contact with mitochondrial VDAC1 and phosphate carrier protein.* J Biol Chem, 2008. **283**(14): p. 8837-45.
164. Colell, A., et al., *Cholesterol impairs the adenine nucleotide translocator-mediated mitochondrial permeability transition through altered membrane fluidity.* J Biol Chem, 2003. **278**(36): p. 33928-35.
165. Furukawa, A., et al., *Steroidogenic acute regulatory protein (StAR) transcripts constitutively expressed in the adult rat central nervous system: colocalization of StAR, cytochrome P-450SCC (CYP XIA1), and 3beta-hydroxysteroid dehydrogenase in the rat brain.* J Neurochem, 1998. **71**(6): p. 2231-8.
166. Lavaque, E., et al., *Steroidogenic acute regulatory protein in the brain.* Neuroscience, 2006. **138**(3): p. 741-7.

167. Moog-Lutz, C., et al., *MLN64 exhibits homology with the steroidogenic acute regulatory protein (STAR) and is over-expressed in human breast carcinomas.* Int J Cancer, 1997. **71**(2): p. 183-91.
168. Alpy, F., et al., *MENTHO, a MLN64 homologue devoid of the START domain.* J Biol Chem, 2002. **277**(52): p. 50780-7.
169. Alpy, F., et al., *Functional characterization of the MENTAL domain.* J Biol Chem, 2005. **280**(18): p. 17945-52.
170. Watari, H., et al., *MLN64 contains a domain with homology to the steroidogenic acute regulatory protein (StAR) that stimulates steroidogenesis.* Proc Natl Acad Sci U S A, 1997. **94**(16): p. 8462-7.
171. Bose, H.S., et al., *N-218 MLN64, a protein with StAR-like steroidogenic activity, is folded and cleaved similarly to StAR.* Biochemistry, 2000. **39**(38): p. 11722-31.
172. King, S.R., et al., *Characterization of the putative cholesterol transport protein metastatic lymph node 64 in the brain.* Neuroscience, 2006. **139**(3): p. 1031-8.
173. King, S.R., et al., *The steroidogenic acute regulatory protein is expressed in steroidogenic cells of the day-old brain.* Endocrinology, 2004. **145**(10): p. 4775-80.
174. Attwell, D. and S.B. Laughlin, *An energy budget for signaling in the grey matter of the brain.* J Cereb Blood Flow Metab, 2001. **21**(10): p. 1133-45.
175. Alle, H., A. Roth, and J.R. Geiger, *Energy-efficient action potentials in hippocampal mossy fibers.* Science, 2009. **325**(5946): p. 1405-8.
176. Nehlig, A., *Brain uptake and metabolism of ketone bodies in animal models.* Prostaglandins Leukot Essent Fatty Acids, 2004. **70**(3): p. 265-75.
177. van Hall, G., et al., *Blood lactate is an important energy source for the human brain.* J Cereb Blood Flow Metab, 2009. **29**(6): p. 1121-9.
178. Zielke, H.R., C.L. Zielke, and P.J. Baab, *Direct measurement of oxidative metabolism in the living brain by microdialysis: a review.* J Neurochem, 2009. **109 Suppl 1**: p. 24-9.
179. Ruderman, N.B., et al., *Regulation of glucose and ketone-body metabolism in brain of anaesthetized rats.* Biochem J, 1974. **138**(1): p. 1-10.
180. Lovatt, D., et al., *The transcriptome and metabolic gene signature of protoplasmic astrocytes in the adult murine cortex.* J Neurosci, 2007. **27**(45): p. 12255-66.
181. Bouzier-Sore, A.K., et al., *Competition between glucose and lactate as oxidative energy substrates in both neurons and astrocytes: a comparative NMR study.* Eur J Neurosci, 2006. **24**(6): p. 1687-94.
182. Boumezbeur, F., et al., *Altered brain mitochondrial metabolism in healthy aging as assessed by in vivo magnetic resonance spectroscopy.* J Cereb Blood Flow Metab, 2010. **30**(1): p. 211-21.
183. Herrero-Mendez, A., et al., *The bioenergetic and antioxidant status of neurons is controlled by continuous degradation of a key glycolytic enzyme by APC/C-Cdh1.* Nat Cell Biol, 2009. **11**(6): p. 747-52.
184. Rodriguez-Rodriguez, P., et al., *Excitotoxic stimulus stabilizes PFKFB3 causing pentose-phosphate pathway to glycolysis switch and neurodegeneration.* Cell Death Differ, 2012. **19**(10): p. 1582-9.

185. Kaplowitz, N., T.Y. Aw, and M. Ookhtens, *The regulation of hepatic glutathione.* Annu Rev Pharmacol Toxicol, 1985. **25**: p. 715-44.
186. Qu, H., et al., *(13)C MR spectroscopy study of lactate as substrate for rat brain.* Dev Neurosci, 2000. **22**(5-6): p. 429-36.
187. Boumezbeur, F., et al., *The contribution of blood lactate to brain energy metabolism in humans measured by dynamic 13C nuclear magnetic resonance spectroscopy.* J Neurosci, 2010. **30**(42): p. 13983-91.
188. Serres, S., et al., *Ex vivo NMR study of lactate metabolism in rat brain under various depressed states.* J Neurosci Res, 2005. **79**(1-2): p. 19-25.
189. Bolanos, J.P., A. Almeida, and S. Moncada, *Glycolysis: a bioenergetic or a survival pathway?* Trends Biochem Sci, 2010. **35**(3): p. 145-9.
190. Itoh, Y., et al., *Dichloroacetate effects on glucose and lactate oxidation by neurons and astroglia in vitro and on glucose utilization by brain in vivo.* Proc Natl Acad Sci U S A, 2003. **100**(8): p. 4879-84.
191. Bittner, C.X., et al., *High resolution measurement of the glycolytic rate.* Front Neuroenergetics, 2010. **2**.
192. Pellerin, L. and P.J. Magistretti, *Glutamate uptake into astrocytes stimulates aerobic glycolysis: a mechanism coupling neuronal activity to glucose utilization.* Proc Natl Acad Sci U S A, 1994. **91**(22): p. 10625-9.
193. Magistretti, P.J., et al., *Energy on demand.* Science, 1999. **283**(5401): p. 496-7.
194. Halim, N.D., et al., *Phosphorylation status of pyruvate dehydrogenase distinguishes metabolic phenotypes of cultured rat brain astrocytes and neurons.* Glia, 2010. **58**(10): p. 1168-76.
195. Escartin, C., et al., *Neuron-astrocyte interactions in the regulation of brain energy metabolism: a focus on NMR spectroscopy.* J Neurochem, 2006. **99**(2): p. 393-401.
196. Delgado-Esteban, M., A. Almeida, and J.P. Bolanos, *D-Glucose prevents glutathione oxidation and mitochondrial damage after glutamate receptor stimulation in rat cortical primary neurons.* J Neurochem, 2000. **75**(4): p. 1618-24.
197. DiNuzzo, M., et al., *Changes in glucose uptake rather than lactate shuttle take center stage in subserving neuroenergetics: evidence from mathematical modeling.* J Cereb Blood Flow Metab. **30**(3): p. 586-602.
198. Pellerin, L., *Brain energetics (thought needs food).* Curr Opin Clin Nutr Metab Care, 2008. **11**(6): p. 701-5.
199. Chuquet, J., et al., *Predominant enhancement of glucose uptake in astrocytes versus neurons during activation of the somatosensory cortex.* J Neurosci, 2010. **30**(45): p. 15298-303.
200. Porras, O.H., A. Loaiza, and L.F. Barros, *Glutamate mediates acute glucose transport inhibition in hippocampal neurons.* J Neurosci, 2004. **24**(43): p. 9669-73.
201. Parpura-Gill, A., D. Beitz, and E. Uemura, *The inhibitory effects of beta-amyloid on glutamate and glucose uptakes by cultured astrocytes.* Brain Res, 1997. **754**(1-2): p. 65-71.
202. Rouach, N., et al., *Astroglial metabolic networks sustain hippocampal synaptic transmission.* Science, 2008. **322**(5907): p. 1551-5.

203. Schmidt, S., et al., *Neuronal functions, feeding behavior, and energy balance in Slc2a3+/- mice.* Am J Physiol Endocrinol Metab, 2008. **295**(5): p. E1084-94.
204. Stuart, C.A., et al., *Brain glucose transporter (Glut3) haploinsufficiency does not impair mouse brain glucose uptake.* Brain Res, 2011. **1384**: p. 15-22.
205. Wang, D., et al., *A mouse model for Glut-1 haploinsufficiency.* Hum Mol Genet, 2006. **15**(7): p. 1169-79.
206. Bittar, P.G., et al., *Selective distribution of lactate dehydrogenase isoenzymes in neurons and astrocytes of human brain.* J Cereb Blood Flow Metab, 1996. **16**(6): p. 1079-89.
207. Fonnum, F., *Glutamate: a neurotransmitter in mammalian brain.* J Neurochem, 1984. **42**(1): p. 1-11.
208. van den Berg, C.J. and D. Garfinkel, *A stimulation study of brain compartments. Metabolism of glutamate and related substances in mouse brain.* Biochem J, 1971. **123**(2): p. 211-8.
209. Benjamin, A.M. and J.H. Quastel, *Locations of amino acids in brain slices from the rat. Tetrodotoxin-sensitive release of amino acids.* Biochem J, 1972. **128**(3): p. 631-46.
210. Ottersen, O.P., N. Zhang, and F. Walberg, *Metabolic compartmentation of glutamate and glutamine: morphological evidence obtained by quantitative immunocytochemistry in rat cerebellum.* Neuroscience, 1992. **46**(3): p. 519-34.
211. Fillenz, M., *Physiological release of excitatory amino acids.* Behav Brain Res, 1995. **71**(1-2): p. 51-67.
212. Rothman, S., *Synaptic release of excitatory amino acid neurotransmitter mediates anoxic neuronal death.* J Neurosci, 1984. **4**(7): p. 1884-91.
213. Rothman, S.M., *The neurotoxicity of excitatory amino acids is produced by passive chloride influx.* J Neurosci, 1985. **5**(6): p. 1483-9.
214. Meldrum, B.S., *The role of glutamate in epilepsy and other CNS disorders.* Neurology, 1994. **44**(11 Suppl 8): p. S14-23.
215. Tanaka, K., *Expression cloning of a rat glutamate transporter.* Neurosci Res, 1993. **16**(2): p. 149-53.
216. Pines, G., et al., *Cloning and expression of a rat brain L-glutamate transporter.* Nature, 1992. **360**(6403): p. 464-7.
217. Kanai, Y. and M.A. Hediger, *Primary structure and functional characterization of a high-affinity glutamate transporter.* Nature, 1992. **360**(6403): p. 467-71.
218. Rothstein, J.D., et al., *Knockout of glutamate transporters reveals a major role for astroglial transport in excitotoxicity and clearance of glutamate.* Neuron, 1996. **16**(3): p. 675-86.
219. Tanaka, K., et al., *Epilepsy and exacerbation of brain injury in mice lacking the glutamate transporter GLT-1.* Science, 1997. **276**(5319): p. 1699-702.
220. Martinez-Hernandez, A., K.P. Bell, and M.D. Norenberg, *Glutamine synthetase: glial localization in brain.* Science, 1977. **195**(4284): p. 1356-8.
221. Suarez, I., G. Bodega, and B. Fernandez, *Glutamine synthetase in brain: effect of ammonia.* Neurochem Int, 2002. **41**(2-3): p. 123-42.
222. Broer, A., et al., *The astroglial ASCT2 amino acid transporter as a mediator of glutamine efflux.* J Neurochem, 1999. **73**(5): p. 2184-94.

223. Varoqui, H., et al., *Cloning and functional identification of a neuronal glutamine transporter.* J Biol Chem, 2000. **275**(6): p. 4049-54.
224. Daikhin, Y. and M. Yudkoff, *Compartmentation of brain glutamate metabolism in neurons and glia.* J Nutr, 2000. **130**(4S Suppl): p. 1026S-31S.
225. Cooper, A.J., *13N as a tracer for studying glutamate metabolism.* Neurochem Int, 2011. **59**(4): p. 456-64.
226. McKenna, M.C., *Glutamate dehydrogenase in brain mitochondria: do lipid modifications and transient metabolon formation influence enzyme activity?* Neurochem Int, 2011. **59**(4): p. 525-33.
227. Lin, M.T. and M.F. Beal, *Mitochondrial dysfunction and oxidative stress in neurodegenerative diseases.* Nature, 2006. **443**(7113): p. 787-95.
228. Liu, Y., G. Fiskum, and D. Schubert, *Generation of reactive oxygen species by the mitochondrial electron transport chain.* J Neurochem, 2002. **80**(5): p. 780-7.
229. Indo, H.P., et al., *Evidence of ROS generation by mitochondria in cells with impaired electron transport chain and mitochondrial DNA damage.* Mitochondrion, 2007. **7**(1-2): p. 106-18.
230. Chance, B., H. Sies, and A. Boveris, *Hydroperoxide metabolism in mammalian organs.* Physiol Rev, 1979. **59**(3): p. 527-605.
231. Raha, S. and B.H. Robinson, *Mitochondria, oxygen free radicals, disease and ageing.* Trends Biochem Sci, 2000. **25**(10): p. 502-8.
232. Orrenius, S., V. Gogvadze, and B. Zhivotovsky, *Mitochondrial oxidative stress: implications for cell death.* Annu Rev Pharmacol Toxicol, 2007. **47**: p. 143-83.
233. Sies, H., *Strategies of antioxidant defense.* Eur J Biochem, 1993. **215**(2): p. 213-9.
234. Simon, H.U., A. Haj-Yehia, and F. Levi-Schaffer, *Role of reactive oxygen species (ROS) in apoptosis induction.* Apoptosis, 2000. **5**(5): p. 415-8.
235. McCord, J.M. and I. Fridovich, *Superoxide dismutase. An enzymic function for erythrocuprein (hemocuprein).* J Biol Chem, 1969. **244**(22): p. 6049-55.
236. Martensson, J., J.C. Lai, and A. Meister, *High-affinity transport of glutathione is part of a multicomponent system essential for mitochondrial function.* Proc Natl Acad Sci U S A, 1990. **87**(18): p. 7185-9.
237. Cummings, B.S., et al., *Role of voltage-dependent anion channels in glutathione transport into yeast mitochondria.* Biochem Biophys Res Commun, 2000. **276**(3): p. 940-4.
238. Garcia-Ruiz, C., et al., *Evidence that the rat hepatic mitochondrial carrier is distinct from the sinusoidal and canalicular transporters for reduced glutathione. Expression studies in Xenopus laevis oocytes.* J Biol Chem, 1995. **270**(27): p. 15946-9.
239. Adibhatla, R.M. and J.F. Hatcher, *Altered lipid metabolism in brain injury and disorders.* Subcell Biochem, 2008. **49**: p. 241-68.
240. Fu, R., et al., *Oxidative stress in Niemann-Pick disease, type C.* Mol Genet Metab, 2010. **101**(2-3): p. 214-8.
241. Porter, F.D., et al., *Cholesterol oxidation products are sensitive and specific blood-based biomarkers for Niemann-Pick C1 disease.* Sci Transl Med, 2010. **2**(56): p. 56ra81.

242. Jiang, X., et al., *A sensitive and specific LC-MS/MS method for rapid diagnosis of Niemann-Pick C1 disease from human plasma.* J Lipid Res, 2011. **52**(7): p. 1435-45.
243. Vazquez, M.C., et al., *Oxidative stress: a pathogenic mechanism for Niemann-Pick type C disease.* Oxid Med Cell Longev, 2012. **2012**: p. 205713.
244. Klein, A., et al., *Oxidative stress activates the c-Abl/p73 proapoptotic pathway in Niemann-Pick type C neurons.* Neurobiol Dis, 2011. **41**(1): p. 209-18.
245. Vazquez, M.C., et al., *Alteration of gene expression profile in Niemann-Pick type C mice correlates with tissue damage and oxidative stress.* PLoS One, 2011. **6**(12): p. e28777.
246. Schedin, S., et al., *Peroxisomal impairment in Niemann-Pick type C disease.* J Biol Chem, 1997. **272**(10): p. 6245-51.
247. Reddy, J.V., I.G. Ganley, and S.R. Pfeffer, *Clues to neuro-degeneration in Niemann-Pick type C disease from global gene expression profiling.* PLoS One, 2006. **1**: p. e19.
248. Beal, M.F., *Mitochondria and neurodegeneration.* Novartis Found Symp, 2007. **287**: p. 183-92; discussion 192-6.
249. Petrozzi, L., et al., *Mitochondria and neurodegeneration.* Biosci Rep, 2007. **27**(1-3): p. 87-104.
250. De Windt, A., et al., *Gene set enrichment analyses revealed several affected pathways in Niemann-pick disease type C fibroblasts.* DNA Cell Biol, 2007. **26**(9): p. 665-71.
251. Kim, S.J., et al., *Impaired functions of neural stem cells by abnormal nitric oxide-mediated signaling in an in vitro model of Niemann-Pick type C disease.* Cell Res, 2008. **18**(6): p. 686-94.
252. Zampieri, S., et al., *Oxidative stress in NPC1 deficient cells: protective effect of allopregnanolone.* J Cell Mol Med, 2009. **13**(9B): p. 3786-96.
253. Ko, D.C., et al., *Cell-autonomous death of cerebellar purkinje neurons with autophagy in Niemann-Pick type C disease.* PLoS Genet, 2005. **1**(1): p. 81-95.
254. Wu, Y.P., et al., *Apoptosis accompanied by up-regulation of TNF-alpha death pathway genes in the brain of Niemann-Pick type C disease.* Mol Genet Metab, 2005. **84**(1): p. 9-17.
255. Alvarez, A.R., et al., *Imatinib therapy blocks cerebellar apoptosis and improves neurological symptoms in a mouse model of Niemann-Pick type C disease.* FASEB J, 2008. **22**(10): p. 3617-27.
256. Pacheco, C.D., R. Kunkel, and A.P. Lieberman, *Autophagy in Niemann-Pick C disease is dependent upon Beclin-1 and responsive to lipid trafficking defects.* Hum Mol Genet, 2007. **16**(12): p. 1495-503.
257. Pacheco, C.D., M.J. Elrick, and A.P. Lieberman, *Tau deletion exacerbates the phenotype of Niemann-Pick type C mice and implicates autophagy in pathogenesis.* Hum Mol Genet, 2009. **18**(5): p. 956-65.
258. Ordonez, M.P., et al., *Disruption and therapeutic rescue of autophagy in a human neuronal model of Niemann Pick type C1.* Hum Mol Genet, 2012. **21**(12): p. 2651-62.

259. Sattler, W., D. Mohr, and R. Stocker, *Rapid isolation of lipoproteins and assessment of their peroxidation by high-performance liquid chromatography postcolumn chemiluminescence.* Methods Enzymol, 1994. **233**: p. 469-89.
260. Karten, B., et al., *Cholesterol accumulates in cell bodies, but is decreased in distal axons, of Niemann-Pick C1-deficient neurons.* J Neurochem, 2002. **83**(5): p. 1154-63.
261. Karten, B., et al., *Generation and function of astroglial lipoproteins from Niemann-Pick type C1-deficient mice.* Biochem J, 2005. **387**(Pt 3): p. 779-88.
262. Dahl, N.K., et al., *Isolation and characterization of Chinese hamster ovary cells defective in the intracellular metabolism of low density lipoprotein-derived cholesterol.* J Biol Chem, 1992. **267**(7): p. 4889-96.
263. Wojtanik, K.M. and L. Liscum, *The transport of low density lipoprotein-derived cholesterol to the plasma membrane is defective in NPC1 cells.* J Biol Chem, 2003. **278**(17): p. 14850-6.
264. Harikrishna, J.A., et al., *Construction and function of fusion enzymes of the human cytochrome P450scc system.* DNA Cell Biol, 1993. **12**(5): p. 371-9.
265. Huang, M.C. and W.L. Miller, *Creation and activity of COS-1 cells stably expressing the F2 fusion of the human cholesterol side-chain cleavage enzyme system.* Endocrinology, 2001. **142**(6): p. 2569-76.
266. Kanoksilapatham, W., J.M. Gonzalez, and F.T. Robb, *Directed-Mutagenesis and Deletion Generated through an Improved Overlapping-Extension PCR Based Procedure.* Silpakorn University Science and Technology Journal, 2007. **1**(2): p. 7-12.
267. Kennedy, B.E., M. Charman, and B. Karten, *Niemann-Pick Type C2 protein contributes to the transport of endosomal cholesterol to mitochondria without interacting with NPC1.* J Lipid Res, 2012. **53**(12): p. 2632-42.
268. Pfaffl, M.W., *A new mathematical model for relative quantification in real-time RT-PCR.* Nucleic Acids Res, 2001. **29**(9): p. e45.
269. Guo, W., et al., *DNA extraction procedures meaningfully influence qPCR-based mtDNA copy number determination.* Mitochondrion, 2009. **9**(4): p. 261-5.
270. Amthor, H., et al., *Lack of myostatin results in excessive muscle growth but impaired force generation.* Proc Natl Acad Sci U S A, 2007. **104**(6): p. 1835-40.
271. Kristian, T., et al., *Isolation of mitochondria with high respiratory control from primary cultures of neurons and astrocytes using nitrogen cavitation.* J Neurosci Methods, 2006. **152**(1-2): p. 136-43.
272. Vives-Bauza, C., L. Yang, and G. Manfredi, *Assay of mitochondrial ATP synthesis in animal cells and tissues.* Methods Cell Biol, 2007. **80**: p. 155-71.
273. Armstrong, J.S. and M. Whiteman, *Measurement of reactive oxygen species in cells and mitochondria.* Methods Cell Biol, 2007. **80**: p. 355-77.
274. Wu, H., et al., *High-throughput tissue extraction protocol for NMR- and MS-based metabolomics.* Anal Biochem, 2008. **372**(2): p. 204-12.
275. Soanes, K.H., et al., *Molecular characterization of zebrafish embryogenesis via DNA microarrays and multiplatform time course metabolomics studies.* J Proteome Res, 2011. **10**(11): p. 5102-17.

276. Zhou, M., et al., *A stable nonfluorescent derivative of resorufin for the fluorometric determination of trace hydrogen peroxide: applications in detecting the activity of phagocyte NADPH oxidase and other oxidases.* Anal Biochem, 1997. **253**(2): p. 162-8.
277. Shapiro, F. and N. Silanikove, *Rapid and accurate determination of d- and l-lactate, lactose and galactose by enzymatic reactions coupled to formation of a fluorochromophore: Applications in food quality control.* Food Chemistry, 2010. **119**(2): p. 829-833.
278. Potts, G.O., et al., *Trilostane, an orally active inhibitor of steroid biosynthesis.* Steroids, 1978. **32**(2): p. 257-67.
279. Papadopoulos, V., et al., *Pregnenolone biosynthesis in C6-2B glioma cell mitochondria: regulation by a mitochondrial diazepam binding inhibitor receptor.* Proc Natl Acad Sci U S A, 1992. **89**(11): p. 5113-7.
280. Goldstein, J.L., S.K. Basu, and M.S. Brown, *Receptor-mediated endocytosis of low-density lipoprotein in cultured cells.* Methods Enzymol, 1983. **98**: p. 241-60.
281. Kristiana, I., H. Yang, and A.J. Brown, *Different kinetics of cholesterol delivery to components of the cholesterol homeostatic machinery: implications for cholesterol trafficking to the endoplasmic reticulum.* Biochim Biophys Acta, 2008. **1781**(11-12): p. 724-30.
282. Imamura, H., et al., *Visualization of ATP levels inside single living cells with fluorescence resonance energy transfer-based genetically encoded indicators.* Proc Natl Acad Sci U S A, 2009. **106**(37): p. 15651-6.
283. Waldeck-Weiermair, M., et al., *Leucine zipper EF hand-containing transmembrane protein 1 (Letm1) and uncoupling proteins 2 and 3 (UCP2/3) contribute to two distinct mitochondrial Ca2+ uptake pathways.* J Biol Chem, 2011. **286**(32): p. 28444-55.
284. Shapiro, S.S. and M.B. Wilk, *An analysis of variance test for normality (complete samples).* Biometrika, 1965. **52**(3-4): p. 591-611.
285. Kennedy, B.E., et al., *Pre-symptomatic activation of antioxidant responses and alterations in glucose and pyruvate metabolism in niemann-pick type c1-deficient murine brain.* PLoS One, 2013. **8**(12): p. e82685.
286. Li, H., et al., *Effect of glutathione depletion on Nrf2/ARE activation by deltamethrin in PC12 Cells.* Arh Hig Rada Toksikol, 2013. **64**(1): p. 87-97.
287. Ma, Q., *Role of nrf2 in oxidative stress and toxicity.* Annu Rev Pharmacol Toxicol, 2013. **53**: p. 401-26.
288. Lee, J.M., et al., *Identification of the NF-E2-related factor-2-dependent genes conferring protection against oxidative stress in primary cortical astrocytes using oligonucleotide microarray analysis.* J Biol Chem, 2003. **278**(14): p. 12029-38.
289. Davis, R.J., *Signal transduction by the JNK group of MAP kinases.* Cell, 2000. **103**(2): p. 239-52.
290. Camps, M., A. Nichols, and S. Arkinstall, *Dual specificity phosphatases: a gene family for control of MAP kinase function.* FASEB J, 2000. **14**(1): p. 6-16.
291. Chen, Y.R., A. Shrivastava, and T.H. Tan, *Down-regulation of the c-Jun N-terminal kinase (JNK) phosphatase M3/6 and activation of JNK by hydrogen peroxide and pyrrolidine dithiocarbamate.* Oncogene, 2001. **20**(3): p. 367-74.

292. McCubrey, J.A., M.M. Lahair, and R.A. Franklin, *Reactive oxygen species-induced activation of the MAP kinase signaling pathways.* Antioxid Redox Signal, 2006. **8**(9-10): p. 1775-89.
293. Taanman, J.W., *The mitochondrial genome: structure, transcription, translation and replication.* Biochim Biophys Acta, 1999. **1410**(2): p. 103-23.
294. Robin, E.D. and R. Wong, *Mitochondrial DNA molecules and virtual number of mitochondria per cell in mammalian cells.* J Cell Physiol, 1988. **136**(3): p. 507-13.
295. Virbasius, J.V. and R.C. Scarpulla, *Activation of the human mitochondrial transcription factor A gene by nuclear respiratory factors: a potential regulatory link between nuclear and mitochondrial gene expression in organelle biogenesis.* Proc Natl Acad Sci U S A, 1994. **91**(4): p. 1309-13.
296. Mambo, E., et al., *Electrophile and oxidant damage of mitochondrial DNA leading to rapid evolution of homoplasmic mutations.* Proc Natl Acad Sci U S A, 2003. **100**(4): p. 1838-43.
297. Lee, H.C., et al., *Somatic mutations in the D-loop and decrease in the copy number of mitochondrial DNA in human hepatocellular carcinoma.* Mutat Res, 2004. **547**(1-2): p. 71-8.
298. Puigserver, P. and B.M. Spiegelman, *Peroxisome proliferator-activated receptor-gamma coactivator 1 alpha (PGC-1 alpha): transcriptional coactivator and metabolic regulator.* Endocr Rev, 2003. **24**(1): p. 78-90.
299. Zhou, Q., et al., *c-Jun N-terminal kinase regulates mitochondrial bioenergetics by modulating pyruvate dehydrogenase activity in primary cortical neurons.* J Neurochem, 2008. **104**(2): p. 325-35.
300. Korotchkina, L.G. and M.S. Patel, *Site specificity of four pyruvate dehydrogenase kinase isoenzymes toward the three phosphorylation sites of human pyruvate dehydrogenase.* J Biol Chem, 2001. **276**(40): p. 37223-9.
301. Cabiscol, E., et al., *Oxidative stress promotes specific protein damage in Saccharomyces cerevisiae.* J Biol Chem, 2000. **275**(35): p. 27393-8.
302. Humphries, K.M., Y. Yoo, and L.I. Szweda, *Inhibition of NADH-linked mitochondrial respiration by 4-hydroxy-2-nonenal.* Biochemistry, 1998. **37**(2): p. 552-7.
303. Chinopoulos, C., L. Tretter, and V. Adam-Vizi, *Depolarization of in situ mitochondria due to hydrogen peroxide-induced oxidative stress in nerve terminals: inhibition of alpha-ketoglutarate dehydrogenase.* J Neurochem, 1999. **73**(1): p. 220-8.
304. Niculescu, M.D. and S.H. Zeisel, *Diet, methyl donors and DNA methylation: interactions between dietary folate, methionine and choline.* J Nutr, 2002. **132**(8 Suppl): p. 2333S-2335S.
305. Cornford, E.M., S. Hyman, and B.E. Swartz, *The human brain GLUT1 glucose transporter: ultrastructural localization to the blood-brain barrier endothelia.* J Cereb Blood Flow Metab, 1994. **14**(1): p. 106-12.
306. Yu, S., et al., *Immunohistochemical localization of glucose transporters (GLUT1 and GLUT3) in the rat hypothalamus.* Obes Res, 1995. **3 Suppl 5**: p. 753S-76S.

307. Sprengers, E.D., A.H. Koenderman, and G.E. Staal, *Mitochondrial and cytosolic hexokinase from rat brain: one and the same enzyme?* Biochim Biophys Acta, 1983. **755**(1): p. 112-8.
308. Van Schaftingen, E., et al., *A kinetic study of pyrophosphate: fructose-6-phosphate phosphotransferase from potato tubers. Application to a microassay of fructose 2,6-bisphosphate.* Eur J Biochem, 1982. **129**(1): p. 191-5.
309. Sudakin, V., et al., *The cyclosome, a large complex containing cyclin-selective ubiquitin ligase activity, targets cyclins for destruction at the end of mitosis.* Mol Biol Cell, 1995. **6**(2): p. 185-97.
310. Gupta, V. and R.N. Bamezai, *Human pyruvate kinase M2: a multifunctional protein.* Protein Sci, 2010. **19**(11): p. 2031-44.
311. Gui, D.Y., C.A. Lewis, and M.G. Vander Heiden, *Allosteric regulation of PKM2 allows cellular adaptation to different physiological states.* Sci Signal, 2013. **6**(263): p. pe7.
312. Frigerio, F., et al., *Deletion of glutamate dehydrogenase 1 (Glud1) in the central nervous system affects glutamate handling without altering synaptic transmission.* J Neurochem, 2012. **123**(3): p. 342-8.
313. Schousboe, A., L.K. Bak, and H.S. Waagepetersen, *Astrocytic Control of Biosynthesis and Turnover of the Neurotransmitters Glutamate and GABA.* Front Endocrinol (Lausanne), 2013. **4**: p. 102.
314. Gamberino, W.C., et al., *Role of pyruvate carboxylase in facilitation of synthesis of glutamate and glutamine in cultured astrocytes.* J Neurochem, 1997. **69**(6): p. 2312-25.
315. Hassel, B. and A. Brathe, *Neuronal pyruvate carboxylation supports formation of transmitter glutamate.* J Neurosci, 2000. **20**(4): p. 1342-7.
316. Kennedy, B.E., et al., *Adaptations of energy metabolism associated with increased levels of mitochondrial cholesterol in Niemann-Pick type C1-deficient cells.* J Biol Chem, 2014.
317. Roff, C.F., et al., *Type C Niemann-Pick disease: use of hydrophobic amines to study defective cholesterol transport.* Dev Neurosci, 1991. **13**(4-5): p. 315-9.
318. Butler, J.D., et al., *Progesterone blocks cholesterol translocation from lysosomes.* J Biol Chem, 1992. **267**(33): p. 23797-805.
319. Jefcoate, C.R., E.R. Simpson, and G.S. Boyd, *Spectral properties of rat adrenal-mitochondrial cytochrome P-450.* Eur J Biochem, 1974. **42**(2): p. 539-51.
320. Toaff, M.E., H. Schleyer, and J.F. Strauss, 3rd, *Metabolism of 25-hydroxycholesterol by rat luteal mitochondria and dispersed cells.* Endocrinology, 1982. **111**(6): p. 1785-90.
321. Brand, M.D. and D.G. Nicholls, *Assessing mitochondrial dysfunction in cells.* Biochem J, 2011. **435**(2): p. 297-312.
322. Ahn, W.S. and M.R. Antoniewicz, *Metabolic flux analysis of CHO cells at growth and non-growth phases using isotopic tracers and mass spectrometry.* Metab Eng, 2011. **13**(5): p. 598-609.
323. Ahn, W.S. and M.R. Antoniewicz, *Parallel labeling experiments with [1,2-(13)C]glucose and [U-(13)C]glutamine provide new insights into CHO cell metabolism.* Metab Eng, 2013. **15**: p. 34-47.

324. Vishnu, N., et al., *ATP increases within the lumen of the endoplasmic reticulum upon intracellular Ca2+ release.* Mol Biol Cell, 2014. **25**(3): p. 368-79.
325. Drew, R. and J.O. Miners, *The effects of buthionine sulphoximine (BSO) on glutathione depletion and xenobiotic biotransformation.* Biochem Pharmacol, 1984. **33**(19): p. 2989-94.
326. Camargo, F., et al., *Cyclodextrins in the treatment of a mouse model of Niemann-Pick C disease.* Life Sci, 2001. **70**(2): p. 131-42.
327. Esworthy, R.S., Y.S. Ho, and F.F. Chu, *The Gpx1 gene encodes mitochondrial glutathione peroxidase in the mouse liver.* Arch Biochem Biophys, 1997. **340**(1): p. 59-63.
328. Bai, J. and A.I. Cederbaum, *Mitochondrial catalase and oxidative injury.* Biol Signals Recept, 2001. **10**(3-4): p. 189-99.
329. Tejero-Taldo, M.I., et al., *Antioxidant properties of pyruvate mediate its potentiation of beta-adrenergic inotropism in stunned myocardium.* J Mol Cell Cardiol, 1999. **31**(10): p. 1863-72.
330. Ropp, P.A. and W.C. Copeland, *Cloning and characterization of the human mitochondrial DNA polymerase, DNA polymerase gamma.* Genomics, 1996. **36**(3): p. 449-58.
331. Hance, N., M.I. Ekstrand, and A. Trifunovic, *Mitochondrial DNA polymerase gamma is essential for mammalian embryogenesis.* Hum Mol Genet, 2005. **14**(13): p. 1775-83.
332. Liu, C.S., et al., *Oxidative stress-related alteration of the copy number of mitochondrial DNA in human leukocytes.* Free Radic Res, 2003. **37**(12): p. 1307-17.
333. Lee, H.C. and Y.H. Wei, *Mitochondrial biogenesis and mitochondrial DNA maintenance of mammalian cells under oxidative stress.* Int J Biochem Cell Biol, 2005. **37**(4): p. 822-34.
334. Kim, J.W., et al., *HIF-1-mediated expression of pyruvate dehydrogenase kinase: a metabolic switch required for cellular adaptation to hypoxia.* Cell Metab, 2006. **3**(3): p. 177-85.
335. Bonello, S., et al., *Reactive oxygen species activate the HIF-1alpha promoter via a functional NFkappaB site.* Arterioscler Thromb Vasc Biol, 2007. **27**(4): p. 755-61.
336. Zhou, Q., et al., *Activation of c-Jun-N-terminal kinase and decline of mitochondrial pyruvate dehydrogenase activity during brain aging.* FEBS Lett, 2009. **583**(7): p. 1132-40.
337. Firestein, B.L. and D.S. Bredt, *Interaction of neuronal nitric-oxide synthase and phosphofructokinase-M.* J Biol Chem, 1999. **274**(15): p. 10545-50.
338. Kinni, H., et al., *Cerebral metabolism after forced or voluntary physical exercise.* Brain Res, 2011. **1388**: p. 48-55.
339. Mor, I., E.C. Cheung, and K.H. Vousden, *Control of glycolysis through regulation of PFK1: old friends and recent additions.* Cold Spring Harb Symp Quant Biol, 2011. **76**: p. 211-6.
340. Bigl, M., et al., *Changes of activity and isozyme pattern of phosphofructokinase in the brains of patients with Alzheimer's disease.* J Neurochem, 1996. **67**(3): p. 1164-71.

341. Tang, H., et al., *Oxidative stress-responsive microRNA-320 regulates glycolysis in diverse biological systems.* FASEB J, 2012. **26**(11): p. 4710-21.
342. Dawson, R.M., *Studies on the glutamine and glutamic acid content of the rat brain during insulin hypoglycaemia.* Biochem J, 1950. **47**(4): p. 386-91.
343. Lewis, L.D., et al., *Changes in carbohydrate substrates, amino acids and ammonia in the brain during insulin-induced hypoglycemia.* J Neurochem, 1974. **23**(4): p. 659-71.
344. Terpstra, M., et al., *Changes in human brain glutamate concentration during hypoglycemia: insights into cerebral adaptations in hypoglycemia-associated autonomic failure in type 1 diabetes.* J Cereb Blood Flow Metab, 2014. **34**(5): p. 876-82.
345. Sutherland, G.R., R.L. Tyson, and R.N. Auer, *Truncation of the krebs cycle during hypoglycemic coma.* Med Chem, 2008. **4**(4): p. 379-85.
346. Sokolovic, M., et al., *Fasting induces a biphasic adaptive metabolic response in murine small intestine.* BMC Genomics, 2007. **8**: p. 361.
347. Han, E.S., et al., *The in vivo gene expression signature of oxidative stress.* Physiol Genomics, 2008. **34**(1): p. 112-26.
348. Brown, J.M. and B.G. Wouters, *Apoptosis, p53, and tumor cell sensitivity to anticancer agents.* Cancer Res, 1999. **59**(7): p. 1391-9.
349. Fiorini, A., et al., *Lack of p53 affects the expression of several brain mitochondrial proteins: insights from proteomics into important pathways regulated by p53.* PLoS One, 2012. **7**(11): p. e49846.
350. Hu, W., et al., *Glutaminase 2, a novel p53 target gene regulating energy metabolism and antioxidant function.* Proc Natl Acad Sci U S A, 2010. **107**(16): p. 7455-60.
351. Cluzeau, C.V., et al., *Microarray expression analysis and identification of serum biomarkers for Niemann-Pick disease, type C1.* Hum Mol Genet, 2012. **21**(16): p. 3632-46.
352. Shen, F., et al., *Glutamate-induced glutamine synthetase expression in retinal Muller cells after short-term ocular hypertension in the rat.* Invest Ophthalmol Vis Sci, 2004. **45**(9): p. 3107-12.
353. Schedin, S., et al., *Alterations in the biosynthesis of cholesterol, dolichol and dolichyl-P in the genetic cholesterol homeostasis disorder, Niemann-Pick type C disease.* Biochim Biophys Acta, 1998. **1394**(2-3): p. 177-86.
354. Cabeza, C., et al., *Cholinergic abnormalities, endosomal alterations and up-regulation of nerve growth factor signaling in Niemann-Pick type C disease.* Mol Neurodegener, 2012. **7**: p. 11.
355. Manganelli, F., et al., *Central cholinergic dysfunction in the adult form of Niemann Pick disease type C: a further link with Alzheimer's disease?* J Neurol, 2014. **261**(4): p. 804-8.
356. Frolov, A., et al., *Niemann-pick type C2 deficiency in human fibroblasts confers robust and selective activation of prostaglandin E2 biosynthesis.* J Biol Chem, 2013. **288**(33): p. 23696-703.
357. Liao, G., et al., *Abnormal gene expression in cerebellum of Npc1-/- mice during postnatal development.* Brain Res, 2010. **1325**: p. 128-40.

358. Cologna, S.M., et al., *Quantitative proteomic analysis of Niemann-Pick disease, type C1 cerebellum identifies protein biomarkers and provides pathological insight.* PLoS One, 2012. **7**(10): p. e47845.
359. Battisti, C., et al., *Adult onset Niemann-Pick type C disease: A clinical, neuroimaging and molecular genetic study.* Mov Disord, 2003. **18**(11): p. 1405-9.
360. Kumar, A. and H.T. Chugani, *Niemann-Pick disease type C: unique 2-deoxy-2[(1)(8)F] fluoro-D-glucose PET abnormality.* Pediatr Neurol, 2011. **44**(1): p. 57-60.
361. Huang, J.Y., et al., *Neuroimaging findings in a brain with Niemann-Pick type C disease.* J Formos Med Assoc, 2011. **110**(8): p. 537-42.
362. Lopez, M.E., et al., *Anatomically defined neuron-based rescue of neurodegenerative Niemann-Pick type C disorder.* J Neurosci, 2011. **31**(12): p. 4367-78.
363. Elrick, M.J., et al., *Conditional Niemann-Pick C mice demonstrate cell autonomous Purkinje cell neurodegeneration.* Hum Mol Genet, 2010. **19**(5): p. 837-47.
364. Yu, T., et al., *Temporal and cell-specific deletion establishes that neuronal Npc1 deficiency is sufficient to mediate neurodegeneration.* Hum Mol Genet, 2011. **20**(22): p. 4440-51.
365. Zhang, M., et al., *Astrocyte-only Npc1 reduces neuronal cholesterol and triples life span of Npc1-/- mice.* J Neurosci Res, 2008. **86**(13): p. 2848-56.
366. Yu, T. and A.P. Lieberman, *Npc1 acting in neurons and glia is essential for the formation and maintenance of CNS myelin.* PLoS Genet, 2013. **9**(4): p. e1003462.
367. Dringen, R., *Metabolism and functions of glutathione in brain.* Prog Neurobiol, 2000. **62**(6): p. 649-71.
368. Drukarch, B., et al., *Astrocyte-mediated enhancement of neuronal survival is abolished by glutathione deficiency.* Brain Res, 1997. **770**(1-2): p. 123-30.
369. Gras, G., et al., *The glutamate-glutamine cycle as an inducible, protective face of macrophage activation.* J Leukoc Biol, 2006. **80**(5): p. 1067-75.
370. Belanger, M., I. Allaman, and P.J. Magistretti, *Brain energy metabolism: focus on astrocyte-neuron metabolic cooperation.* Cell Metab, 2011. **14**(6): p. 724-38.
371. Reynolds, A., et al., *Oxidative stress and the pathogenesis of neurodegenerative disorders.* Int Rev Neurobiol, 2007. **82**: p. 297-325.
372. Bascunan-Castillo, E.C., et al., *Tamoxifen and vitamin E treatments delay symptoms in the mouse model of Niemann-Pick C.* J Appl Genet, 2004. **45**(4): p. 461-7.
373. Balogun, E., et al., *Curcumin activates the haem oxygenase-1 gene via regulation of Nrf2 and the antioxidant-responsive element.* Biochem J, 2003. **371**(Pt 3): p. 887-95.
374. Lloyd-Evans, E., et al., *Niemann-Pick disease type C1 is a sphingosine storage disease that causes deregulation of lysosomal calcium.* Nat Med, 2008. **14**(11): p. 1247-55.
375. Smith, D., et al., *Beneficial effects of anti-inflammatory therapy in a mouse model of Niemann-Pick disease type C1.* Neurobiol Dis, 2009. **36**(2): p. 242-51.
376. Sarna, J.R., et al., *Patterned Purkinje cell degeneration in mouse models of Niemann-Pick type C disease.* J Comp Neurol, 2003. **456**(3): p. 279-91.

377. Amritraj, A., et al., *Increased activity and altered subcellular distribution of lysosomal enzymes determine neuronal vulnerability in Niemann-Pick type C1-deficient mice.* Am J Pathol, 2009. **175**(6): p. 2540-56.
378. Welsh, J.P., et al., *Why do Purkinje cells die so easily after global brain ischemia? Aldolase C, EAAT4, and the cerebellar contribution to posthypoxic myoclonus.* Adv Neurol, 2002. **89**: p. 331-59.
379. Prasad, C., T. Rupar, and A.N. Prasad, *Pyruvate dehydrogenase deficiency and epilepsy.* Brain Dev, 2011. **33**(10): p. 856-65.
380. Lluis, J.M., et al., *Acetaldehyde impairs mitochondrial glutathione transport in HepG2 cells through endoplasmic reticulum stress.* Gastroenterology, 2003. **124**(3): p. 708-24.
381. Rusinol, A.E., et al., *A unique mitochondria-associated membrane fraction from rat liver has a high capacity for lipid synthesis and contains pre-Golgi secretory proteins including nascent lipoproteins.* J Biol Chem, 1994. **269**(44): p. 27494-502.
382. Hayashi, T., et al., *MAM: more than just a housekeeper.* Trends Cell Biol, 2009. **19**(2): p. 81-8.
383. Zhang, J.R., et al., *Niemann-Pick C1 protects against atherosclerosis in mice via regulation of macrophage intracellular cholesterol trafficking.* J Clin Invest, 2008. **118**(6): p. 2281-90.
384. Sheftel, A.D., et al., *Direct interorganellar transfer of iron from endosome to mitochondrion.* Blood, 2007. **110**(1): p. 125-32.
385. Calore, F., et al., *Endosome-mitochondria juxtaposition during apoptosis induced by H. pylori VacA.* Cell Death Differ, 2010. **17**(11): p. 1707-16.
386. Zhang, M., et al., *MLN64 mediates mobilization of lysosomal cholesterol to steroidogenic mitochondria.* J Biol Chem, 2002. **277**(36): p. 33300-10.
387. Bose, H.S., M.A. Baldwin, and W.L. Miller, *Evidence that StAR and MLN64 act on the outer mitochondrial membrane as molten globules.* Endocr Res, 2000. **26**(4): p. 629-37.
388. Alpy, F., et al., *STARD3 or STARD3NL and VAP form a novel molecular tether between late endosomes and the ER.* J Cell Sci, 2013. **126**(Pt 23): p. 5500-12.
389. Kishida, T., et al., *Targeted mutation of the MLN64 START domain causes only modest alterations in cellular sterol metabolism.* J Biol Chem, 2004. **279**(18): p. 19276-85.
390. Abdul-Hammed, M., et al., *Role of endosomal membrane lipids and NPC2 in cholesterol transfer and membrane fusion.* J Lipid Res, 2010. **51**(7): p. 1747-60.
391. Gallala, H.D., B. Breiden, and K. Sandhoff, *Regulation of the NPC2 protein-mediated cholesterol trafficking by membrane lipids.* J Neurochem, 2011. **116**(5): p. 702-7.
392. Storch, J. and Z. Xu, *Niemann-Pick C2 (NPC2) and intracellular cholesterol trafficking.* Biochim Biophys Acta, 2009. **1791**(7): p. 671-8.
393. Xu, Z., et al., *Regulation of sterol transport between membranes and NPC2.* Biochemistry, 2008. **47**(42): p. 11134-43.
394. Gong, Y., et al., *Niemann-Pick C1 protein facilitates the efflux of the anticancer drug daunorubicin from cells according to a novel vesicle-mediated pathway.* J Pharmacol Exp Ther, 2006. **316**(1): p. 242-7.

395. Goldman, S.D. and J.P. Krise, *Niemann-Pick C1 functions independently of Niemann-Pick C2 in the initial stage of retrograde transport of membrane-impermeable lysosomal cargo.* J Biol Chem, 2010. **285**(7): p. 4983-94.
396. Boadu, E., R.C. Nelson, and G.A. Francis, *ABCA1-dependent mobilization of lysosomal cholesterol requires functional Niemann-Pick C2 but not Niemann-Pick C1 protein.* Biochim Biophys Acta, 2012. **1821**(3): p. 396-404.
397. Csepeggi, C., et al., *Somatic cell plasticity and Niemann-Pick type C2 protein: fibroblast activation.* J Biol Chem, 2011. **286**(3): p. 2078-87.
398. Csepeggi, C., M. Jiang, and A. Frolov, *Somatic cell plasticity and Niemann-pick type C2 protein: adipocyte differentiation and function.* J Biol Chem, 2010. **285**(39): p. 30347-54.
399. Halestrap, A.P. and C. Brenner, *The adenine nucleotide translocase: a central component of the mitochondrial permeability transition pore and key player in cell death.* Curr Med Chem, 2003. **10**(16): p. 1507-25.
400. Rostovtseva, T.K. and S.M. Bezrukov, *ATP transport through a single mitochondrial channel, VDAC, studied by current fluctuation analysis.* Biophys J, 1998. **74**(5): p. 2365-73.
401. Kodam, A., et al., *Altered levels and distribution of amyloid precursor protein and its processing enzymes in Niemann-Pick type C1-deficient mouse brains.* Glia, 2010. **58**(11): p. 1267-81.
402. Chen, Z. and L.H. Lash, *Evidence for mitochondrial uptake of glutathione by dicarboxylate and 2-oxoglutarate carriers.* J Pharmacol Exp Ther, 1998. **285**(2): p. 608-18.
403. Chen, Z., D.A. Putt, and L.H. Lash, *Enrichment and functional reconstitution of glutathione transport activity from rabbit kidney mitochondria: further evidence for the role of the dicarboxylate and 2-oxoglutarate carriers in mitochondrial glutathione transport.* Arch Biochem Biophys, 2000. **373**(1): p. 193-202.
404. Wilkins, H.M., et al., *Mitochondrial glutathione transport is a key determinant of neuronal susceptibility to oxidative and nitrosative stress.* J Biol Chem, 2013. **288**(7): p. 5091-101.
405. Lash, L.H., *Mitochondrial glutathione transport: physiological, pathological and toxicological implications.* Chem Biol Interact, 2006. **163**(1-2): p. 54-67.
406. Kosower, E.M., N.S. Kosower, and P. Wegman, *Membrane mobility agents. IV. The mechanism of particle-cell and cell-cell fusion.* Biochim Biophys Acta, 1977. **471**(2): p. 311-29.
407. Coll, O., et al., *Sensitivity of the 2-oxoglutarate carrier to alcohol intake contributes to mitochondrial glutathione depletion.* Hepatology, 2003. **38**(3): p. 692-702.
408. Colell, A., et al., *Transport of reduced glutathione in hepatic mitochondria and mitoplasts from ethanol-treated rats: effect of membrane physical properties and S-adenosyl-L-methionine.* Hepatology, 1997. **26**(3): p. 699-708.
409. Ha, S.D., et al., *Cellular adaptation to anthrax lethal toxin-induced mitochondrial cholesterol enrichment, hyperpolarization, and reactive oxygen species generation through downregulating MLN64 in macrophages.* Mol Cell Biol, 2012. **32**(23): p. 4846-60.

410. Paradies, G. and F.M. Ruggiero, *Age-related changes in the activity of the pyruvate carrier and in the lipid composition in rat-heart mitochondria.* Biochim Biophys Acta, 1990. **1016**(2): p. 207-12.
411. Paradies, G., F.M. Ruggiero, and P. Dinoi, *The influence of hypothyroidism on the transport of phosphate and on the lipid composition in rat-liver mitochondria.* Biochim Biophys Acta, 1991. **1070**(1): p. 180-6.
412. Paradies, G. and F.M. Ruggiero, *Effect of aging on the activity of the phosphate carrier and on the lipid composition in rat liver mitochondria.* Arch Biochem Biophys, 1991. **284**(2): p. 332-7.
413. Prabhu, A.V., J.R. Krycer, and A.J. Brown, *Overexpression of a key regulator of lipid homeostasis, Scap, promotes respiration in prostate cancer cells.* FEBS Lett, 2013. **587**(7): p. 983-8.
414. Koepsell, T.D., et al., *Education, cognitive function, and severity of neuropathology in Alzheimer disease.* Neurology, 2008. **70**(19 Pt 2): p. 1732-9.
415. Nixon, R.A., *Niemann-Pick Type C disease and Alzheimer's disease: the APP-endosome connection fattens up.* Am J Pathol, 2004. **164**(3): p. 757-61.
416. Malnar, M., et al., *Bidirectional links between Alzheimer's disease and Niemann-Pick type C disease.* Neurobiol Dis, 2014.
417. Borbon, I.A. and R.P. Erickson, *Interactions of Npc1 and amyloid accumulation/deposition in the APP/PS1 mouse model of Alzheimer's.* J Appl Genet, 2011. **52**(2): p. 213-8.
418. Erickson, R.P., et al., *Variation in NPC1, the gene encoding Niemann-Pick C1, a protein involved in intracellular cholesterol transport, is associated with Alzheimer disease and/or aging in the Polish population.* Neurosci Lett, 2008. **447**(2-3): p. 153-7.
419. Corder, E.H., et al., *Gene dose of apolipoprotein E type 4 allele and the risk of Alzheimer's disease in late onset families.* Science, 1993. **261**(5123): p. 921-3.
420. Poirier, J., et al., *Apolipoprotein E polymorphism and Alzheimer's disease.* Lancet, 1993. **342**(8873): p. 697-9.
421. Rebeck, G.W., et al., *Apolipoprotein E in sporadic Alzheimer's disease: allelic variation and receptor interactions.* Neuron, 1993. **11**(4): p. 575-80.
422. Burns, M.P. and G.W. Rebeck, *Intracellular cholesterol homeostasis and amyloid precursor protein processing.* Biochim Biophys Acta, 2010. **1801**(8): p. 853-9.
423. Perry, G., A.D. Cash, and M.A. Smith, *Alzheimer Disease and Oxidative Stress.* J Biomed Biotechnol, 2002. **2**(3): p. 120-123.
424. Zhu, X., et al., *Causes of oxidative stress in Alzheimer disease.* Cell Mol Life Sci, 2007. **64**(17): p. 2202-10.
425. Grazina, M., et al., *Genetic basis of Alzheimer's dementia: role of mtDNA mutations.* Genes Brain Behav, 2006. **5 Suppl 2**: p. 92-107.
426. Lovell, M.A., et al., *Elevated thiobarbituric acid-reactive substances and antioxidant enzyme activity in the brain in Alzheimer's disease.* Neurology, 1995. **45**(8): p. 1594-601.
427. Marcus, D.L., et al., *Increased peroxidation and reduced antioxidant enzyme activity in Alzheimer's disease.* Exp Neurol, 1998. **150**(1): p. 40-4.
428. Aksenov, M.Y., et al., *Protein oxidation in the brain in Alzheimer's disease.* Neuroscience, 2001. **103**(2): p. 373-83.

429. Isobe, C., T. Abe, and Y. Terayama, *Levels of reduced and oxidized coenzyme Q-10 and 8-hydroxy-2'-deoxyguanosine in the CSF of patients with Alzheimer's disease demonstrate that mitochondrial oxidative damage and/or oxidative DNA damage contributes to the neurodegenerative process.* J Neurol, 2009.
430. Podlesniy, P., et al., *Low cerebrospinal fluid concentration of mitochondrial DNA in preclinical Alzheimer disease.* Ann Neurol, 2013. **74**(5): p. 655-68.
431. Casley, C.S., et al., *Beta-amyloid inhibits integrated mitochondrial respiration and key enzyme activities.* J Neurochem, 2002. **80**(1): p. 91-100.
432. Ishiguro, K., *[Involvement of tau protein kinase in amyloid-beta-induced neurodegeneration]*. Rinsho Byori, 1998. **46**(10): p. 1003-7.
433. Stacpoole, P.W., *The pyruvate dehydrogenase complex as a therapeutic target for age-related diseases.* Aging Cell, 2012. **11**(3): p. 371-7.
434. Blass, J.P., R.K. Sheu, and G.E. Gibson, *Inherent abnormalities in energy metabolism in Alzheimer disease. Interaction with cerebrovascular compromise.* Ann N Y Acad Sci, 2000. **903**: p. 204-21.
435. Bubber, P., et al., *Mitochondrial abnormalities in Alzheimer brain: mechanistic implications.* Ann Neurol, 2005. **57**(5): p. 695-703.
436. Butterworth, R.F. and A.M. Besnard, *Thiamine-dependent enzyme changes in temporal cortex of patients with Alzheimer's disease.* Metab Brain Dis, 1990. **5**(4): p. 179-84.
437. Terni, B., et al., *Mitochondrial ATP-Synthase in the Entorhinal Cortex Is a Target of Oxidative Stress at Stages I/II of Alzheimer's Disease Pathology.* Brain Pathol, 2009.
438. Hauptmann, S., et al., *Mitochondrial dysfunction: an early event in Alzheimer pathology accumulates with age in AD transgenic mice.* Neurobiol Aging, 2009. **30**(10): p. 1574-86.
439. Sosa, V., et al., *Oxidative stress and cancer: an overview.* Ageing Res Rev, 2013. **12**(1): p. 376-90.
440. Campbell, A.M. and S.H. Chan, *Mitochondrial membrane cholesterol, the voltage dependent anion channel (VDAC), and the Warburg effect.* J Bioenerg Biomembr, 2008. **40**(3): p. 193-7.
441. Alpy, F., et al., *Metastatic lymph node 64 (MLN64), a gene overexpressed in breast cancers, is regulated by Sp/KLF transcription factors.* Oncogene, 2003. **22**(24): p. 3770-80.
442. Stigliano, A., et al., *Increased metastatic lymph node 64 and CYP17 expression are associated with high stage prostate cancer.* J Endocrinol, 2007. **194**(1): p. 55-61.
443. Liao, Y.J., et al., *Characterization of Niemann-Pick Type C2 Protein Expression in Multiple Cancers Using a Novel NPC2 Monoclonal Antibody.* PLoS One, 2013. **8**(10): p. e77586.
444. McFate, T., et al., *Pyruvate dehydrogenase complex activity controls metabolic and malignant phenotype in cancer cells.* J Biol Chem, 2008. **283**(33): p. 22700-8.
445. Michelakis, E.D., et al., *Metabolic modulation of glioblastoma with dichloroacetate.* Sci Transl Med, 2010. **2**(31): p. 31ra34.

446. Bonnet, S., et al., *A mitochondria-K+ channel axis is suppressed in cancer and its normalization promotes apoptosis and inhibits cancer growth.* Cancer Cell, 2007. **11**(1): p. 37-51.
447. Zhao, Y., E.B. Butler, and M. Tan, *Targeting cellular metabolism to improve cancer therapeutics.* Cell Death Dis, 2013. **4**: p. e532.
448. DeBerardinis, R.J., et al., *Beyond aerobic glycolysis: transformed cells can engage in glutamine metabolism that exceeds the requirement for protein and nucleotide synthesis.* Proc Natl Acad Sci U S A, 2007. **104**(49): p. 19345-50.